CIVIL ENGINEERING JOURNAL

číslo 3/2021

Obsah:

CIVIL ENGINEERING JOURNAL

Article no. 45

THE CIVIL ENGINEERING JOURNAL 3-2021

ANALYSIS OF A LAYOUT SOLUTION OF DESIGN BY CTU STUDENTS – ÚŠTĚK RECTORY

Helena Hexnerová

Czech Technical University in Prague, Faculty of Civil Engineering, Department of Architecture, Prague, Thákurova 7, Czech Republic; helena.hexnerova@fsv.cvut.cz

ABSTRACT

The main objective of this paper is to compare student projects of café and restaurant interior in the preserved building of the rectory in a monument reservation in the centre of the town Úštěk. There are six projects dealing with suitability of café and restaurant in the building of the rectory. Students designed interiors and they also worked on the layout of the building with the adjacent courtyard and farm buildings, including their modifications. The article analyses and compares individual student works in terms of the use of areas for individual functions of operation and the number of seats for guests.

KEYWORDS

Rectory, Layout, Restaurant design, Comparative analyses

INTRODUCTION

This article deals with an analyses of student projects of layout solution of the building of the rectory in Úštěk and its use as a café and restaurant. The projects were done in cooperation with Úštěk town hall and Department of Architecture at CTU. Students should have designed interiors of the café and restaurant with kitchen in the former rectory building situated on the square in town Úštěk. The work was commissioned in 2019 in two subjects focused on interior design. First subject was an optional XIND, which is intended for fifth-year students of the Faculty of Civil Engineering in the field of Architecture and Civil Engineering. Second subject was INTERIOR – a part of the Erasmus program. There were two students from Bulgaria and one from Croatia within the Erasmus program who worked separately and five Czech students who worked in pairs and one student worked alone.

Úštěk is a town which was almost untouched by tourism until recent years. It was popular among film makers thanks to its genius loci. In recent years the seasonal attendance of Úštěk has begun to increase thanks to cultural events organized in cooperation with the townhall and as well as thanks to the entrepreneurship of citizens and the developing cycling. Due to the increased number of visitors, there was an acute shortage of urban amenities. In cooperation with the city council, teachers of the subjects mentioned above made a task for students to create a plan of the restaurant and the café in the building of the former rectory.

Initial assumptions

Students´ plans of the café and restaurant layout were evaluated by the method of analyses, compared and analysed. There were six plans and they were named as students' numbers 1-6. For all designs there were calculated: the total used areas, the areas of demolished structures projected into the layout of the areas of individual operations, the number of seats for guests and all of these were compared with each other to verify the operation.
The plans were also used as a background for the negotiation about the restaurant and café in the building with the monument care authority.

Goals of the work

The goal of the student works was to prove the possibilities of placing the restaurant and café into the building of the former rectory in Úštěk. It was necessary to check the capacity of the object during the winter as well as the summer opening and to design the possible ways of the layout. Second aim was to get the inspiration how to do the reconstruction of the building. The works should have shown the creativity in the ways how to use the object of the rectory without any limited factors. The final projects should have been used for the negotiation with the monument care office.

This article analyses and compares individual student works in terms of the use of space and number of seats for the guests of the restaurant.

Assignment of student works

The assignment was as follows: The content of the project is to design an interior of the restaurant/ café in the protected object of the former rectory, which is situated on the square next to the late Baroque church of St. Peter and Paul in Úštěk. Kitchen, restaurant with the bar counter, background and summer terrace should be on the ground floor. On the first floor there should be a multi-purpose hall for weddings, birthday celebrations etc. There are six rooms on the ground floor and a hall. Two rooms should have been used as a kitchen. The entrance to the building is not barrier-free.

Student works

The students had a lot of freedom in preparing the design. In addition to interior design, they also worked out the layout solution, including its modifications. There was still a chapel in operation during the research and the rectory made a request to the townhall not to place a bar to this part. The townhall gave this project also to the design company as well as to the students. This request was not binding for the students because the projects of the students should bring the investor as much inspiration as possible. The basis for the work was the construction focus of the rectory and photographic documentation, which students acquired during a visit to the city and a survey of the building.

INTRODUCTION TO THE TOPIC

The Czech Republic has a long history of heritage protection, but the scope and extent of the reconstruction – conservation are an issue. Worldwide, we can find places where are doubts whether to protect and reconstruct the historical buildings. The reasons are historical and also poor durability of building structures. However, even there, over the last fifty years, the approach to preserving immovable monuments has changed [1]. In the interests of conservation, it is always necessary to find a balance and take advantage of the inclusion of three basic sectors, public, private and civic, as discussed in the research of the Getty Institute. This research also describes criteria and three levels for successful sectoral cooperation. The Czech Republic is in the level „one“ which is the lowest of the levels [2].

The way how to use historical buildings is a topic which is crucial for monument restoration. Researches from all over the world deal with the method of finding new content for a protected building, with the help of various methodologies, as the extent and manner of preserving the heritage is a global issue and problem. Reconstruction and use of sacral buildings is a separate chapter [7, 8].

Due to the Australian research it is necessary to take into account following criteria for the final design of reconstructed building: physical, political, legal, social, economic, technological and functional [9]. Foster [10] studies economic criteria of reconstruction and use of the monuments.

History of town Úštěk

Úštěk, a picturesque historical town on a promontory, which is also a monument reserve, was first mentioned in 1361, when it was held by Petr z Michalovic who held also the surrounding estate, but it was probably founded in the second half of the 13th century. The name Úštěk as well as Ouštěk was used in the 19th century, till 1945 it was called Auscha. This name was used especially by German part of inhabitants [11].

There were also found remains of the pottery and late Slavic burial ground from the turn of the 9th and 10th centuries [12].

The urbanism of the town was set by the high sandstone promontory above the confluence of the streams where was the town placed. There was an important road going through the town that led from Litoměřice via Česká Lípa to Lausitz. The first strategically located settlement with a fortress was set up on the hill. Northern and southern side made a natural barrier for the town. The fortress was lately replaced by the independently fortified castle, which was the centre of the southern part. Thanks to the shape of the narrow promontory, a slightly curved street square was created, which widened in a funnel-like direction towards the center. The town was without developed street network. The burgher houses had narrow deep plots, around the perimeter of the square, with multi-storey cellars carved into sandstone. In some of them there were exit corridors. The burgher houses were often rebuilt in the late Gothic period, their character was still preserved. These were one-storey (two-storey) houses, on the ground floor with a stone farm arcade, on the two to four-axis floor. The ridge of the roofs was perpendicular to the square, the gable was steep and high[13]. Upper floors of the houses were made of wood, the roof was covered by shingle. Significant building modifications took place mainly after fires [11].

In 14th century the inner town and the church of Saint Michael with the cemetery were built. In the second half of the 14th century, the city was surrounded by walls with two small and two big gates. Western one called Litoměřická or Česká, eastern one called Leipzig or German, prevented the entry of carriages into the city. There were two smaller gates in the north and south. The southern one was called Roudnická. The Renaissance period meant a time of development for Úštěk. Most of the buildings, including the town gates, were rebuilt. The development of the city was also on the suburbs. The town hall was built and the castle palace was rebuilt. The town was confiscated in 1621 and handed over to Jesuits.

They built many important baroque buildings. In the 20s of the 17th century the brewery was also rebuilt. After the Jesuits were abolished the town was passed into hands of townspeople. They built a new school and also a courthouse. Many buildings were rebuilt due to two big fires in 1856 and 1859. In some places there is also a merging of plots, in the case of houses the ridge of roofs is parallel to the facade. This partially disrupts the order of the Gothic order of the houses. Part of the arcades were changed and used for shops. The town gates were demolished not to narrow the street profile, the gate called Litoměřická was destroyed in 1830, Lipská gate in 1859. In the second half of the 19th century, a residential colony of "ptačí domky" (bird houses) was built in Kamenná Street. In 1888 a railway connection was built to Velké Březno, in 1898 followed the railway from Litoměřice via Úštěk to Česká Lípa. At the turn of the 19th and 20th centuries, industrial enterprises were established, and gradually also new quarters of family villas. A pond called Chmelař was renewed [13], [14].

History and description of the rectory (Deanery No. 1)

One of the rectory buildings was firstly mentioned in the first half of the 16th century. It was situated on the Mírové square. Nowadays, there is a house number 67. The original building was one storey wooden house with two rooms, a cowshed, shed and a yard. A town paid its reconstruction in 1567 and a stable was added. In 1626 it was demolished and replaced by a new rectory and in 1628 a new barn was built. The building had been used till 1722 when a new rectory was built. There was no longer a suitable place for it by the city walls [11]. Church dedicated to St. Michal, dated to 1363 - 1756, was the first parish church with the original cemetery [13]. The

cemetery by the St. Michal church was closed in 1721 and it was moved to the new place close to the Church of the Holy Trinity (1668) [11]. This created a place where a new baroque building of the current rectory was built in the years 1720-1722 at the expense of the Jesuits of Liběšice. The new rectory was built into the square in terms of floor plan [14]. The rectory building was already made of bricks, the roofing was made with shingles. It was bought from the Liběšice nobility in 1725 by the City Hall [11]. The baroque building is situated on the Mírové square. It is situated opposite the church of Saint Peter and Paul, which was built after the demolition of the Church of St. Michal, in the years 1764-1972. The rectory stands also next to the castle. The two-storey building, symmetrically designed, with seven window axes and a three-axis central risalit, which is decorated with rustic in the corners, as well as both wings, was built in 1722. It is probably the work of the Litoměřice builder of Italian origin Octávio Broggio [13].

The rectory is a two-storey, partly basement, building with a hipped roof, with seven window axes towards the square. It has central corridor, a hall with stairs and entrance to the yard. The sanitary facilities are accessible from the hall too. Most of the rooms are accessible from the hall and you can go through one to another. Most of them have a vaulted ceiling. Upstairs there are rooms with stucco decoration. At the time of the survey, the ground floor of the rectory was used for occasional exhibitions, the chapel and its parish lobby and the first floor were rented by amateur actors. The basement as well as the attic were not used. The rectory building also has other related, original economic parts that are connected to the courtyard. The courtyard is accessible not only through the rectory building, but it also has a generous entrance through the original gate. The rectory was reconstructed in 2006.

Nowadays the rectory is owned by the town Úštěk. On the first floor there is a background for a group of amateur theatre actors called Pik-art. There was created also a place for meeting of pensioners, but it was not used [15].

Rectory from the point of view of the monument care

Cultural monuments register no. ÚSKP 42650/5-1902 – deanery, protected monument since 3. 5. 1958. Area monument protection - monument reservation register no. ÚSKP 1039 – Úštek protected since 1. 10. 1980.

STUDENT WORKS

Layout solution

Students have chosen different layout solutions. Mostly they interfere to the layout by the demolishing some walls or by opening vistas and passages in the load-bearing walls. The bar was mostly situated in the central widened corridor, once it was in the staircase hall and once in the chapel. The chapel and the farm building adjacent to the parish were most often used for the kitchen. In one case, the kitchen was located on the left side of the rectory.

Student No. 1 used the staircase hall for the bar. Kitchen and tasting room are in the left. The corridor widened by the demolishing of the walls and former chapel are designed as a dining room. Toilets are situated in the space behind the stairs. The outdoor part, adjacent to the rectory, is used as a summer dining room. Opposite farm house in the yard are designed as a warehouse and toilet for summer operation, when the yard is designed for summer seating Figure 1.

Student No. 2 placed the kitchen into the chapel and summer kitchen to the adjacent farming spaces. Bar is placed in the entrance part created by the widening of the corridor. Toilet is situated behind the staircase, other space is used as a dining room. The yard is used for sitting in the summer. Outdoor farming building is used as a warehouse and a toilet Figure 2.

Student No. 3 places the bar into the central entrance space. It makes a dominant part of all space. The kitchen is located to the adjoining outdoor annex which is connected to the hall with the staircase by the corridor. Other space is gently used as a dining space, toilet for disabled people

and guests is situated behind the staircase. Next toilet, souvenir shop and the storage are placed in the farm house.

Students No. 4, who worked in a pair, made a setup which makes maximum use of the space that was available. The main consideration of the design is the axiality of the building with a view across the entire building, where is also situated a bar in the entrance extended part. They placed the kitchen to the chapel. The kitchen has access to a warehouse and facilities for employees, as well as an outdoor bar and kitchen in the adjoining farm building. Other rooms are used for sitting. The supply is solved by a new entrance to the square. In the basement there are bathrooms, warehouses and a bar. The yard is used for sitting in the summer, the toilet is in the opposite farm building. There is also a multi-purpose hall and upstairs there is a simple accommodation for eight people. Part of the yard is covered by vegetation and there is also a sandpit with live wicker shading. The courtyard also maintains a connection with the castle courtyard Figure 4.

Student No. 5 placed a bar to the widened central corridor. The bar is followed by box seating and in the left part of the layout there are lounges. Kitchen is situated in the former chapel and outdoor kitchen is in the adjacent farm building. Toilet is behind the staircase. Supply is solved via the corridor which was made by breaking down the entrance from the square in the right part of the building. The yard is used for summer sitting. In the farm house there is a background for the summer terrace, toilet, storage for furniture a multi - purpose space Figure 5.

Students No. 6, who worked in a pair, situated the bar into the chapel. Kitchen is in the adjacent farmhouse. Main building is mainly used as a dining space, warehouses and toilets for employees and toilet for the disabled. The yard is used in summer, in the farmhouse, there is a storage space, meeting room and a bathroom Figure 6.

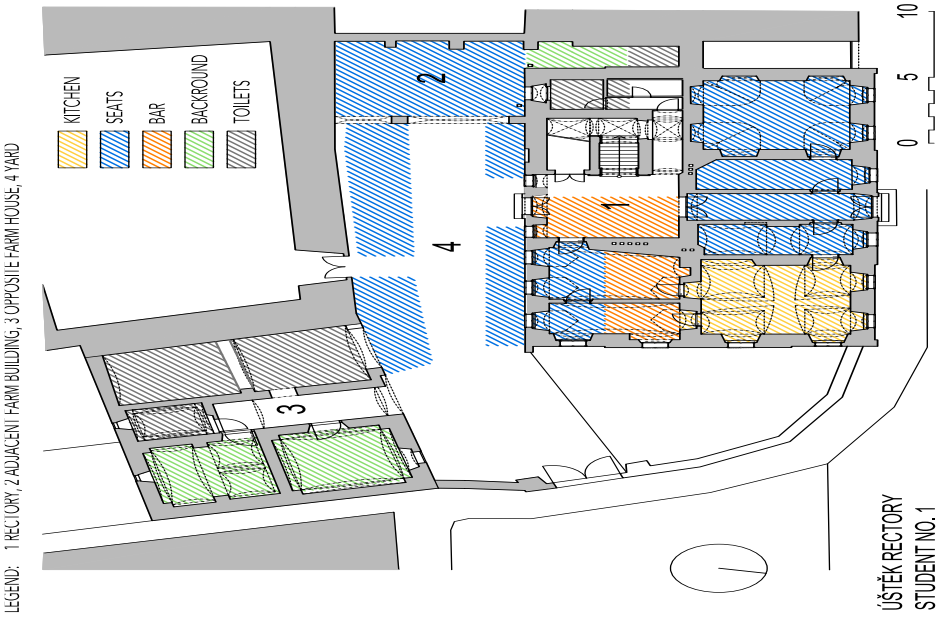

Fig. 1 – Layout of the building, Student No. 1

Fig. 2 – Layout of the building, Student No. 2

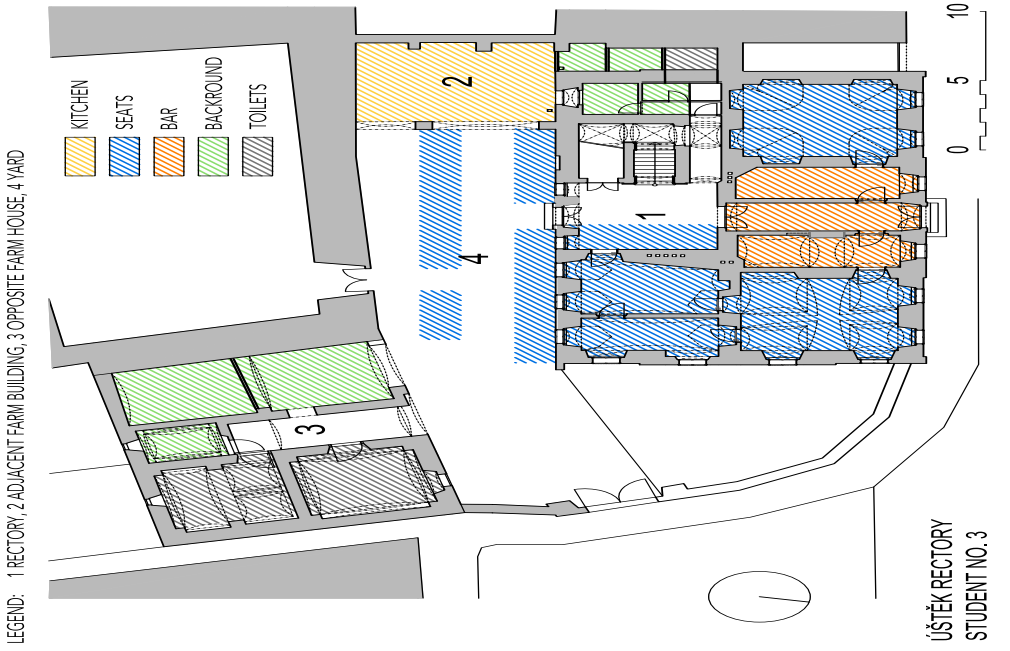

Fig. 3 – Layout of the building, Student No. 3

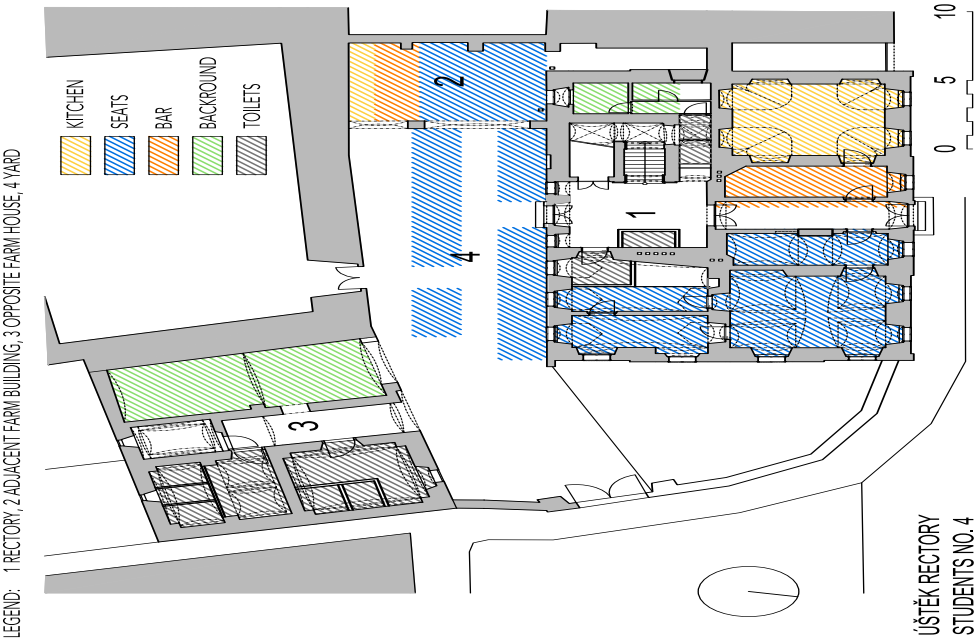

Fig. 4 – Layout of the building, Students No. 4

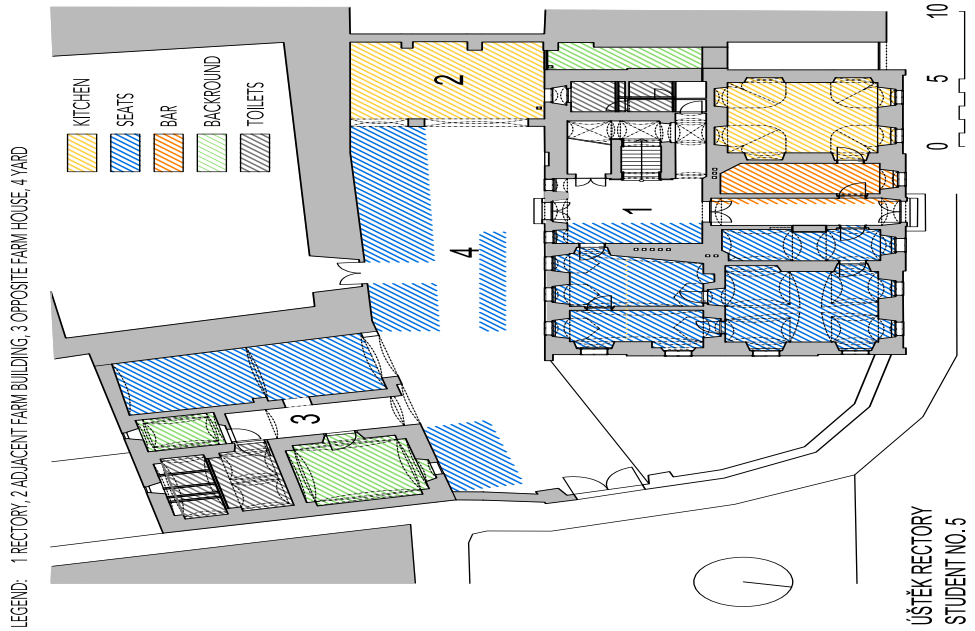

Fig. 5 – Layout of the building, Student No. 5

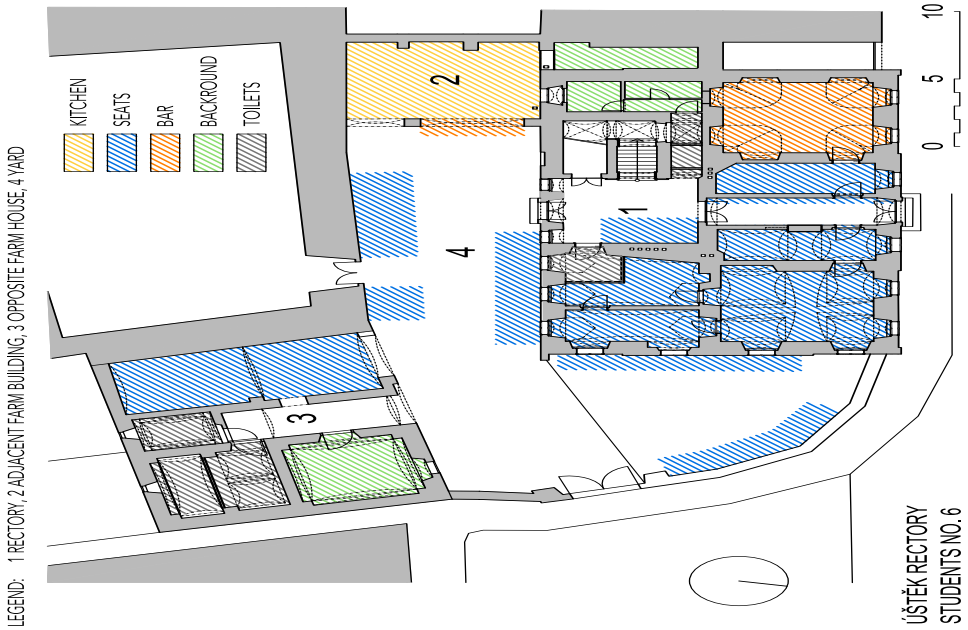

Fig. 6 – Layout of the building, Students No. 6

ANALYSIS OF THE USE OF OBJECT AREAS

Total used area of the object

Students had a different approach to the possible use of the object area. Individual projects vary in the way how the area is used also due to the different use of the seating area of the yard. Demolishing of constructions has a smallest influence on the differences in the using of the area. Most of the area used students No. 4, who used also a basement of the rectory and they also inhabited a first floor of the farm building. Other students covered to their plans only the area of the ground floors of all three buildings. It is interesting that the students who made biggest changes in the construction did not always use maximum of the space for the restaurant. The overall use of the area can be seen in the Figure 7.

Demolished constructions

The students intervened in the structures only to the necessary extent, taking into account that it was a listed building. Not all interventions were easy to make, however, the task was not limited by the budget. In the picture below, we can see highlighted constructions, that were demolished in all projects. Demolished structures were calculated in the area for simplified comparison. The areas of demolished constructions were between 6.27m^2 to 10.52m^2. Student No. 1 interfered the most to the constructions, student No. 3 changed the construction the least. Thanks to the sensitivity of the plans, individual proposes to demolition in the projects were not so big and in the area comparison they differ only slightly, see Figure 9.

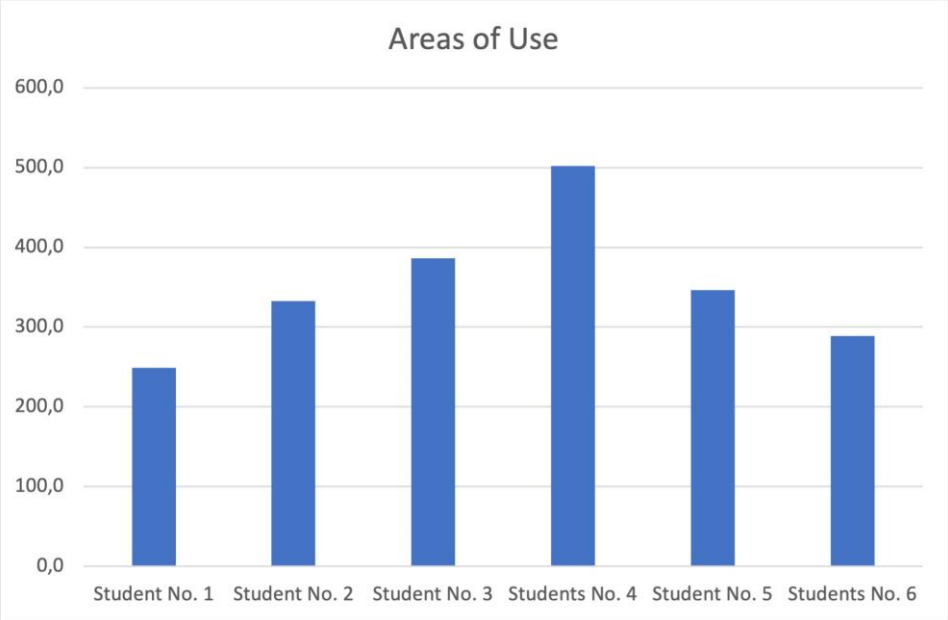

Fig. 7 – Overall use of the area in square meters

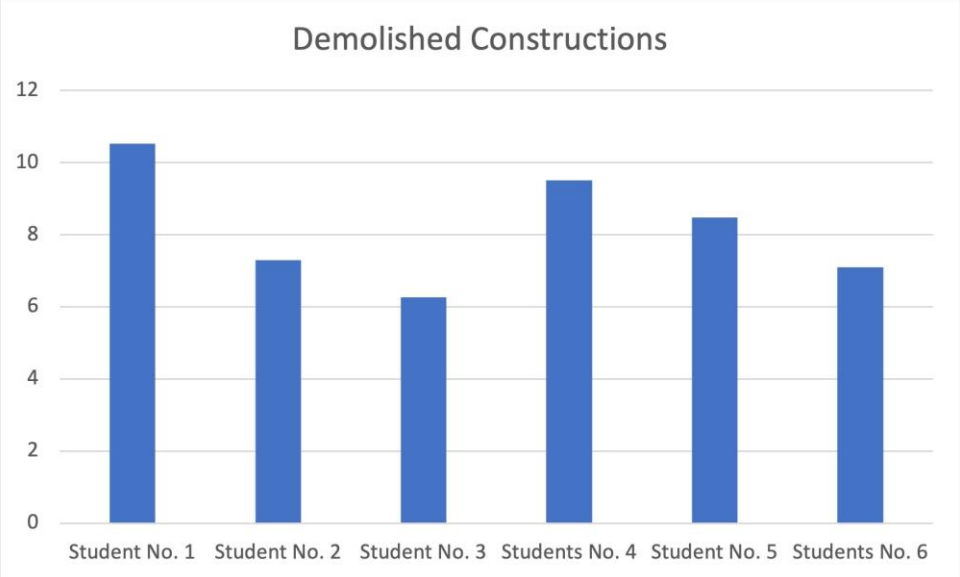

Fig. 8 – Overall demolished structures in m^2

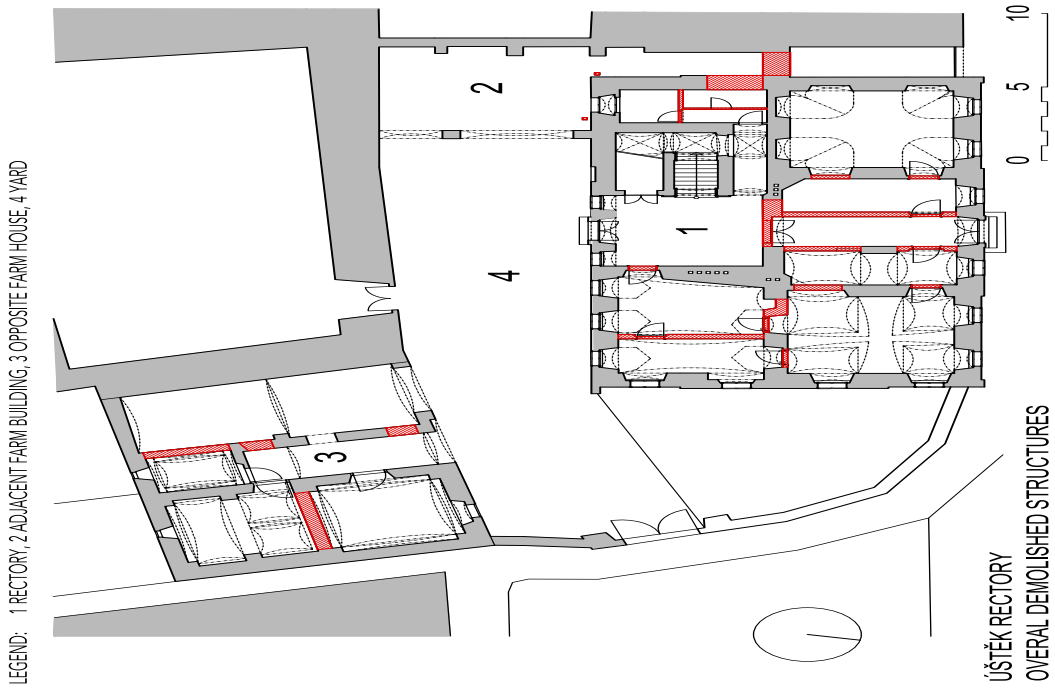

Fig. 9 – Graphical representation of the overall demolished structures

Placement of the main operating parts of the restaurant

Kitchen placement

The predominant agreement of student designs in the layout of the kitchen also examines the suitability of this placement. Student No. 1 located it in the southwest corner of the rectory. Student No. 2 designed a kitchen for the rectory in the room of the former chapel in the southeast corner and a summer kitchen in the outbuilding adjacent to the rectory. Student No. 3 situated the kitchen into the farmhouse adjacent to the rectory. Students No.4 placed the kitchen into the former chapel. Student No.5 designed the kitchens in the same way as student No. 2. Students 6 placed the kitchen to the farmhouse adjacent to the rectory, Figure 10.

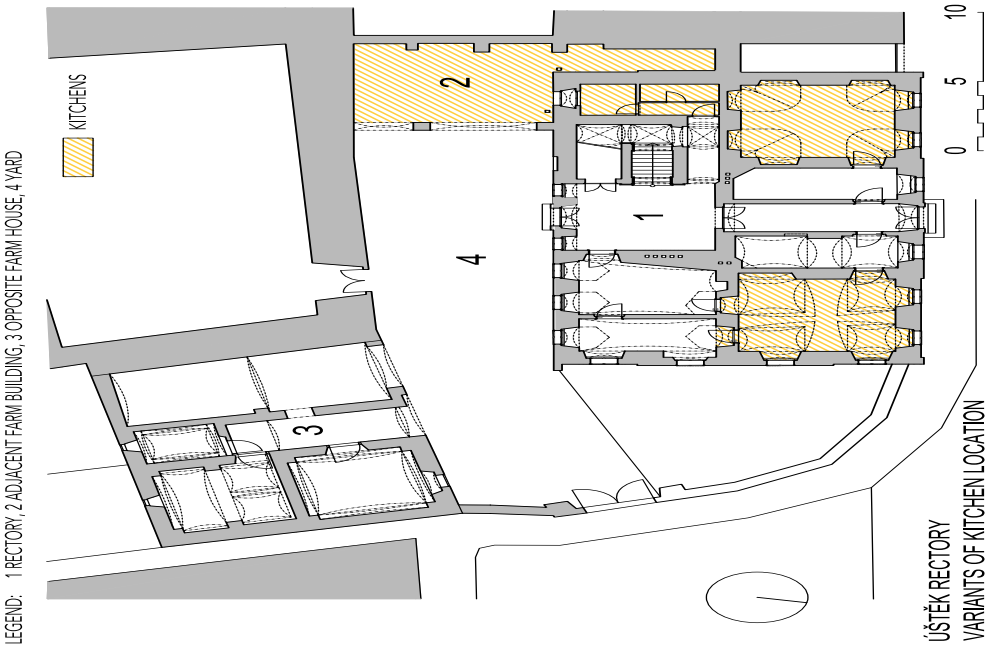

Fig. 10 – Floor plan with marked variants of kitchen location

Bar placement

Student No. 3 designed one bar that is in the central entrance room. Students No. 6 designed 2 bars, one in the former chapel and second is placed outside neighbouring with the outdoor kitchen situated in the farmhouse. Student No. 1 designed also 2 bars, one in the central part and second one – breakfast bar - in the north western part. Students No. 4 situated one bar to the central entrance part and second a summer bar to the farmhouse. Students No.2 and 5 situated the bar to the same place in the central entrance hall. Most of the students kept the demand of the conservationists not to place the bar to the former chapel. Only students No. 6 situated the bar bravely to the chapel. However, their design was very sensitive and referred to the original church use of the building, Figure 11.

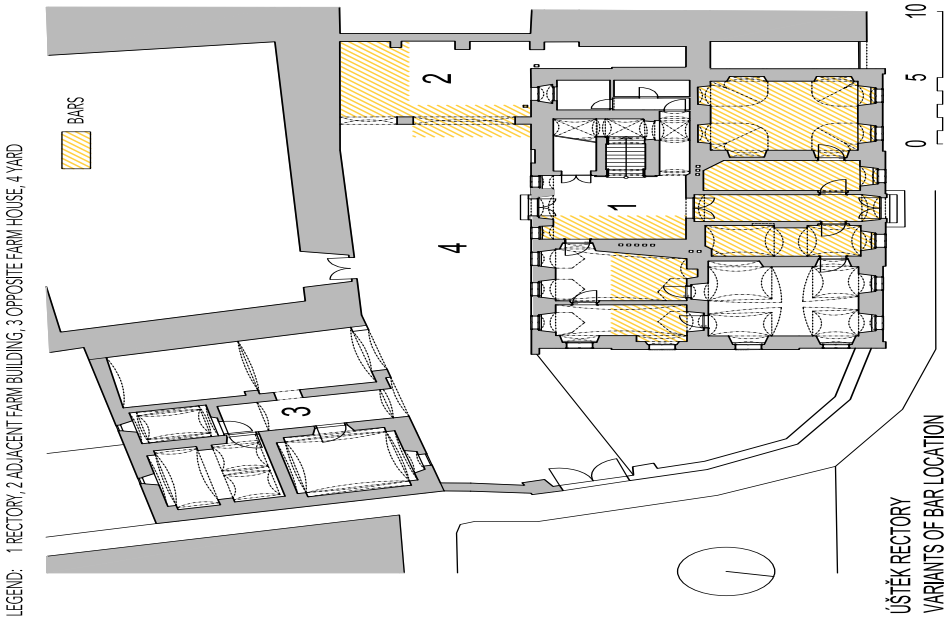

Fig. 11 – Floor plan with marked variants of bar location

Areas of the rooms

Use of the area

Due to the fact that the students used the space defined by the existing load-bearing masonry for the location of the kitchen, the students designed them in basically two sizes. The differences are only in the number of the kitchens in the individual plans, there is one kitchen or two. Second kitchen is always used for the summer terrace and therefore, it was placed in an outbuilding adjacent to the rectory.

Areas of the bars are different in individual projects because some students designed more than one bar. The bar areas do not include a separate bar-type seating, but only bar seating at staff bars.

Spaces used for the sitting of the guest are very different in single plans, student No. 1 used smallest space, the largest area is used by student No. 4. It is very interesting as both projects have similar size of the background.

Students No. 4 used the biggest area for the social facilities, the facilities are used also for the simple accommodation, which was designed in the attic of the farmhouse adjacent to the castle. Students have shown that the parish space is suitable for this form of use. A comparison of individual functional surfaces can be seen in Figure 13.

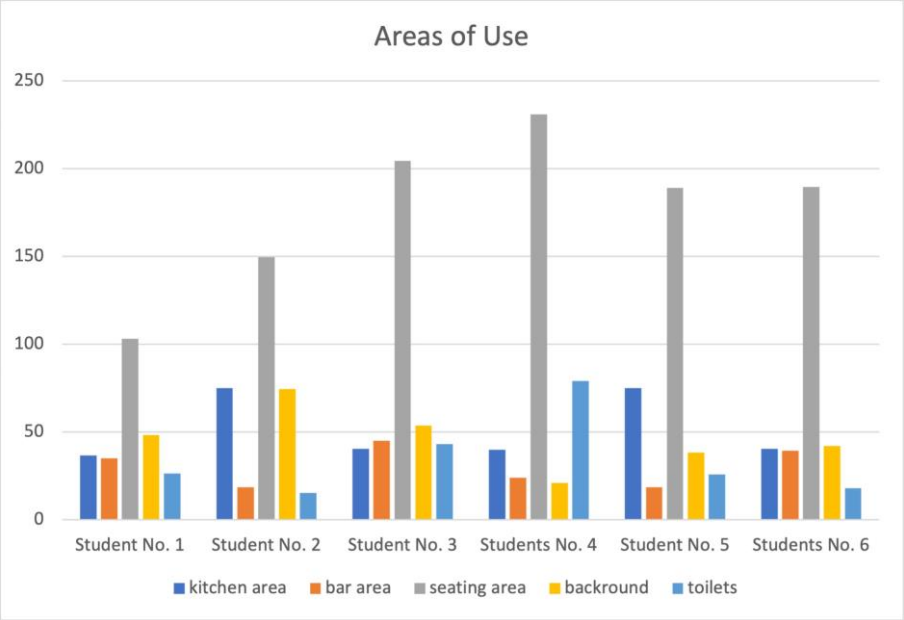

Fig. 12 – Resulting areas of use in m^2 in individual student projects

Number of seats

Numbers of seats are divided into seats inside, bar seats and seats in the summer garden. To compare the number of places between individual projects, this distribution was not taken into account and the total number of places was correlated. The comparison of number of seats in terms of students´ nationalities is interesting. Foreign students designed similar number of seats and similar number of sets was also in the projects of the Czech students. In total, foreign students proposed smaller number of seats than the Czech students. Student No. 1 has 89 seats, student No.2 90 seats, student No. 3 only 78. Student No. 4 have 130 seats and even 8 beds of occasional sleeping. Student No. 5 has 111 seats and students No. 6 have 119 seats. The ratio of the proposed places can be seen in Figure 13.

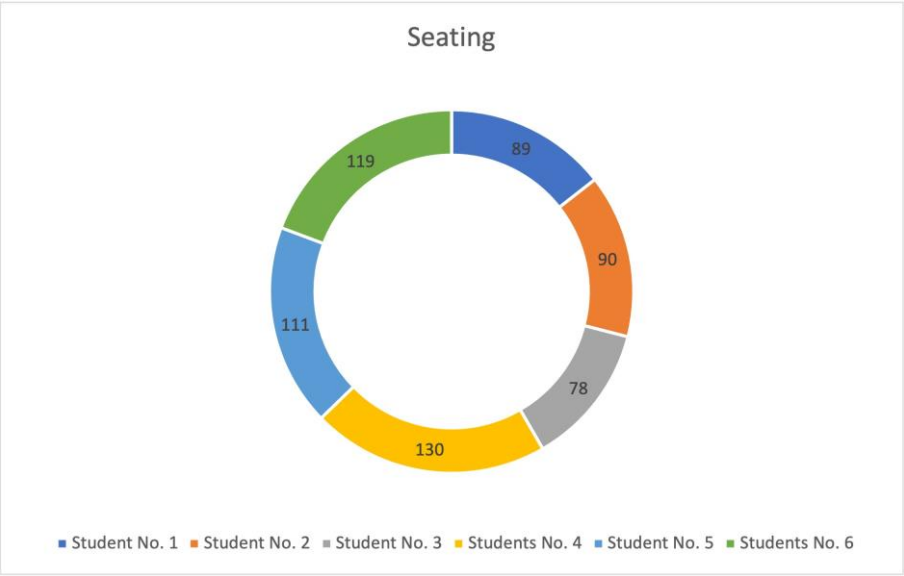

Fig. 13 – Number of seats in individual projects

CONCLUSION

Students´ works proved that a listed building of the rectory is suitable in terms of layout and capacity for the possible location of a restaurant with summer operation and a kitchen. Layout was solved in several possible plans. The objective of examining the possibility of operation has therefore been achieved.

Designs of interiors were various. Some inventively, imaginatively and exaggeratedly reflected the original use of the building, which they transferred to the newly designed interior projects. They followed up on the spiritual legacy of the original purpose of the building, even though the proposed content was problematic for the subjects of monument care, as they mainly assessed the ethical dimension of this use.

The use of church buildings as accommodation, restaurants, cafés is not unusual. Czech suitable examples can be Café Fara in Kletnice in South Moravia, Fara Hostinec in Loučná nad Desnou, residential restaurant in rectory in Kmetiněves or the almost historic Restaurant Na staré faře, in the original parish house near the church of St. Matěj in Prague 6.

The proposals were used as a basis for arguments during the meeting of the town hall management with the locally competent monument office. However, neither the intention of the city management nor the inspiring work of the students had any effect on the decision of the monument care. Their final opinion was the decision wording: "the operation of the restaurant would dishonour the building". The goal of positively influencing the decision of the locally competent authorities of monument care was therefore not achieved.

REFERENCES

[1] Farhanah N., Azhari N., Mohamed E., 2012. Public Perception: Heritage Building conservation in Kuala Lumpur. In: Proccedings of ASEAN Conference on Environment-Behaviour Studies, (Procedia - Social and Behavioral Sciences 50), 271 – 279, https://doi.org/10.1016/j.sbspro.2012.08.033

[2] Macdonald S., Cheong C., 2014. The Role of Public-Private Partnerships and the Third Sector in Conserving Heritage Buildings, Sites, and Historic Urban Areas (The Getty Conservation Institute, Los Angeles), http://hdl.handle.net/10020/gci_pubs/public_private_partnerships

[3] Elsorady D.A., 2014. Assessment of the compatibility of new uses for heritage buildings: The example of Alexandria National Museum, Alexandria, Egypt, (Journal of Cultural Heritage, Volume 15, Issue 5) 511-521, https://doi.org/10.1016/j.culher.2013.10.011

[4] Haroun H.-A.A.F, Bakr A.F., Hasan A.E.-S., 2019. Multi-criteria decision making for adaptive reuse of heritage buildings: Aziza Fahmy Palace, Alexandria, Egypt (Alexandria Engineering Journal Volume 58, Issue 2) 467-478, https://doi.org/10.1016/j.aej.2019.04.003

[5] Langston C., Shen l.-Y., 2007. Application of the adaptive reuse potential model in Hong Kong: A case study of Lui Seng Chun (International Journal of Strategic Property Management, 11:4) 193-207, https://doi.org/10.1080/1648715X.2007.9637569

[6] Mehr S.Y., 2019. Analysis of 19th and 20th Century Conservation Key Theories in Relation to Contemporary Adaptive Reuse of Heritage Buildings (Heritage 2(1)) 920-937, https://doi.org/10.3390/heritage2010061

[7] Kelly C. 2012. Socialist Churches: Heritage Preservation and ‘Cultic Buildings’ in Leningrad, 1924–1940 (Slavic Review, vol. 71, no. 4, 2012) 792–823, https://doi.org/10.5612/slavicreview.71.4.0792

[8] DeBlock E., Fredericks A., Peacock D., Skrzek A., 2013. St. Mary's Parish House: Reuse and Rehabilitaion Feasibility Report (Historic Preservation. Paper 9.)

[9] Conejos S., Langston C., Smith J., 2011. Improving the implementation of adaptive reuse strategies for historic buildings (In The IX International Forum of Studies: S.A.V.E. Heritage Institute of Sustainable) 1-10 pp.

[10] Foster G., 2020, Circular economy strategies for adaptive reuse of cultural heritage buildings to reduce environmental impacts (Resources, Conservation and Recycling Volume 152), https://doi.org/10.1016/j.resconrec.2019.104507

[11] Košťál B., 2015. Úštěk. (Baron, Hostivice)

[12] Gabriel, F., Kursová L., 2015. Město Úštěk a jeho dva hrady (Městský úřad, Úštěk) Kde se vzalo město Úštěk?

[13] Kibic, K., 1981. Paměť měst: městské památkové rezervace v Českých zemích, edited by Vladimíra Kašťáková 2. vyd. (Odeon, Praha)
[14] Kuča, K. 2011. Města a městečka v Čechách, na Moravě a ve Slezsku (Praha, Libri) part 7
[15] Košťál B., Sassmanová H., 2011. Úštěk Městská památková rezervace (Úštěk, Louny)

CIVIL ENGINEERING JOURNAL

Article no. 46

THE CIVIL ENGINEERING JOURNAL 3-2021

SEISMIC PERFORMANCE OF PRECAST COLUMNS CONNECTED WITH TWO DIFFERENT CONNECTION MODES

Chuanlin Wang

Department of Civil and Environmental Engineering, Shantou University, Guangdong Engineering Center for Structure Safety and Health Monitoring , Shantou, No. 243, Daxue Road, 515063, China; clwang@stu.edu.cn

ABSTRACT

The precast reinforced concrete building is made of precast components connected at the joints via reliable connection approaches. In this paper, experiments on two connection modes, i.e. corrugated pipe confined with spiral stirrup connection and steel sleeve connection, were carried out. The experimental tests consisted of six specimens, including one cast-in-situ specimen, three precast specimens using steel sleeve connection and two precast specimens using corrugated pipe confined with the spiral stirrup. The influence of artificially unbonded length at the connection joint was also studied. All specimens were tested under low-frequency cyclic repeated loading to analyze their seismic performance under different connection modes. The experimental results showed that the precast columns using the two proposed connections have a similar or even better seismic performance compared with the cast-in-situ column. The installation of proper unbonded treatment on the longitudinal reinforcement in the connection is beneficial in improving the seismic performance of precast columns and the length of 5 times of the longitudinal reinforcement's diameter is recommended.

KEYWORDS

Precast column, Steel sleeve connection, Corrugated pipe confined with spiral stirrup, Seismic behaviour Artificially unbonded treatment

INTRODUCTION

The precast concrete structure components are created, and cured off-site then lifted to their final resisting place and assembled securely at the construction site. The advantages of the precast building compared with cast-in-situ buildings include improving construction quality, increased construction speed, and saving material consumption and little impact on the environment [1,2]. The main shortcomings of precast structures are high-cost, lack of integrity and discontinuity of the connections. Therefore, the connections' quality and reliability are often suspected and doubted by consumers and some engineers. However, as defined in ACI 550 [3], if with emulative connections, the precast structure can achieve equivalent or even better seismic performance compared to the cast-in-situ structure. Biondini et al. [4,5] pointed out that the early brittle failures of the joint connections of precast frames can be avoided by a proper capacity design. Therefore, it is necessary to ensure that the load-bearing members, especially the connection joint in the precast structure have enough strength and energy dissipation capacity. The seismic design criteria for precast frame structures have extensively considered the role of the connections, which were further developed based on a series of European research projects (Ecoleader 2001-2003, Growth 2002-2006) over the last two decades [4-10]. In 2012, the European Commision has supported a project called SAFECLADDING research to investigate the design solutions for precast structures [11].

The two main types of precast reinforced concrete structure are precast shear wall system and precast frame system. As stated previously, no matter which type of structure, the critical problem is to guarantee the safety and reliability of the splice that connects the precast components. To develop an economical, simple and reliable connection, many researchers and engineers have proposed various connection approaches for the precast system, and the seismic behaviour of the precast components and the joint connection methods have been comprehensively studied [12-18]. Grouted sleeve, corrugated metal pipe, grouting-anchoring lap splice and steel sleeve are the most commonly used ones, illustrated in Figure 1. High strength cementitious grout is later poured into the reserved holes for these connections to provide connecting strength.

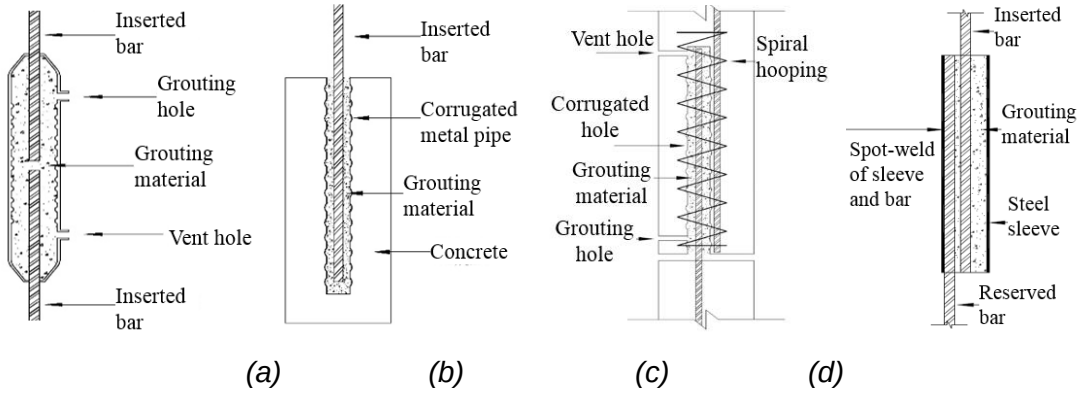

Fig. 1 - Different types of connection: (a) Grouted sleeve; (b) Grouting anchoring; (c) Corrugated pipe confined with spiral hoop; (d) Steel sleeve

Grouted sleeve connection (Figure 1 (a)) has been widely used in precast structures because of its high strength and easy implementation [19,20]. The precast components are connected by inserting the bars into the pre-embedded grouted sleeves, and then high-strength grouting material is injected into the sleeve. The typical failure type of this kind connection includes bar pull-out, bar fracture and sleeve fracture [21]. Though the grouted sleeve can effectively transfer the rebar stress, it is much more expensive than other types of connection, and its high precision and difficulty in processing have limited its widespread use [18]. Compared with grouted sleeve, grouting anchoring in a corrugated pipe (Figure 1 (b)) is much cheaper. However, the anchoring length should be considered to guarantee the mechanical performance of the connecting joint [22]. Therefore, the inserted bars are often lapped with the embedded bars, and spiral stirrup is proposed to install around the pipe to provide confinement and improve the robustness of the splices. It is strictly required that the newly formed connection joint must have a more robust performance than the longitudinal reinforcement no matter in what conditions [23], which means the corrugated pipe confined with spiral stirrup should fail later than the reinforcements it connected. Belleri and Riva [24] conducted an experimental study on the precast columns connected by corrugated steel grouting sleeve, and the results showed that this type of connection could effectively transfer steel stress. In the work of Jiang *et al*. [25], pull-out tests of precast concrete specimens with rebar embedded in corrugated pipe confined with spiral stirrup were carried out. The experimental results proved that this type of connection is simple, reliable and economical. Steel sleeve or metal duct grouted connector is often used in New Zealand to connect precast concrete components to their foundations [2,26]. The merit of using this type of connection is simple, but it also displayed the vulnerability, which has been revealed in several past studies [27,28]. In the work of Kim [28], the grouted metal duct connection presented a poor performance compared with cast-in-situ structure due to the pull-out of the longitudinal bar from the

metal duct. In the research of Riva [27], the energy dissipation and failure displacement were depended on the level of confinement provided to the connections as the column stiffness will decrease if large cracks occurred and spread around the metal ducts. As the corrugated pipe connection and steel sleeve connection is cheap and straightforward; therefore, it is necessary to investigate their seismic performance under different conditions, thus developing a safer and more reliable connection. In this research, the connection modes of corrugated pipe confined with spiral stirrup and steel sleeve are experimentally investigated and compared in the aspects of bearing capacity, fracture mode, ductility and energy dissipation capacity under low-frequency cyclic load.

Furthermore, Pandey and Mutsuyoshi [29] found that the installation of unbonded longitudinal reinforcement in the reinforced concrete structure improves its seismic performance. Wu *et al*. [30] made the same conclusion that some unbonded longitudinal bars in the column foot can enhance the column's seismic performance. Therefore, the influence of artificially unbonded treatment on the seismic performance of the precast column was also investigated in this research. To develop an easy and cheap construction system in the precast structure, the reserved hole will be placed on the foundation, and then the hole will be filled with high-strength grouting filler. After that, the extended longitudinal reinforcement in the precast concrete column will be inserted into the corrugated pipe and steel sleeve to make a rigid connection.

EXPERIMENTAL PROGRAM

Test specimens

In this research, six inverted T-shaped reinforced concrete specimens were cast, including a cast-in-situ reinforced concrete column, three precast RC columns with steel duct connection and two precast RC columns with corrugated pipe confined by spiral stirrup connection, which was then tested to determine their seismic performance. The precast columns were designed following the law of emulative connection suggested in the ACI 550 [3]. Specifically, the influence of unbonded length at the column base and joint connection type are considered and investigated in this research. Due to the limitation of experimental condition, i.e. the equipment in this experiment cannot provide too high axial pressure. Therefore, the appropriate column cross-section size will be chosen based on a 1/2 scale model experiment. The effect and efficiency of steel sleeve connection and corrugated pipe confined with spiral stirrup can be qualitatively investigated and obtained through the model test. Hence, the column's dimensions are 200mm×200mm, and the net height of the column is 1100mm. The horizontal loading point is located at 1000mm from the base of the column. Four longitudinal reinforcements with a diameter of 12mm are placed in the column. The foundation's dimension is 1200mm×340mm×360mm, four rebars with a diameter of 16mm and four rebars with a diameter of 8mm are used. The outer diameter and thickness of the steel duct are 50mm and 3mm, respectively. The diameter of the corrugated pipe is 40mm. The length of the steel duct and corrugated pipe are both 300mm. Based on the previous research carried out on the anchorage length, 300mm is enough to splice the rebars, though it is smaller than the Chinese Standard (355mm) and British Standard (340mm). The specimen's schematic illustration is shown in Figure 2, and the specimen details of precast columns are displayed in Figure 3.

The precast components were cast and cured first, and then the reserved hole was filled with high-strength grouting material. After that, the column and the foundation would be connected by inserting the extended rebars into the reserved holes. The grouting material would be spilt out and tiled on the surface between the column and the foundation, which exactly filled the gap between them and made a rigid connection. The detailed manufacturing process is illustrated in Figure 4. Furthermore, the artificially unbonded treatment is made by separating the longitudinal reinforcements from the concrete at the column base using insulating tape, shown in Figure 4 (a). The specific operation is carried out by binding the insulating tape around the reinforcement at the height from 300mm to 360mm. Based on the previous research, the unbonded treatment of 5d and

10d (d is the longitudinal bar's diameter) is considered. The details of each specimen are summarized in Table 1.

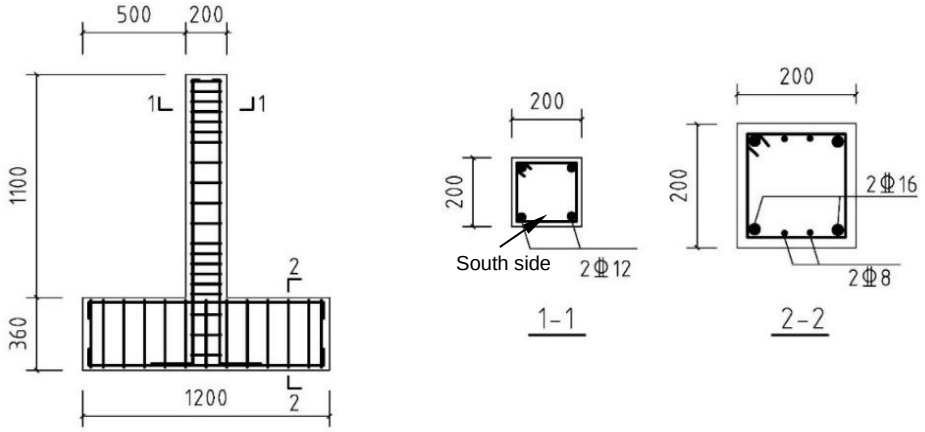

Fig. 2 - Specimen details

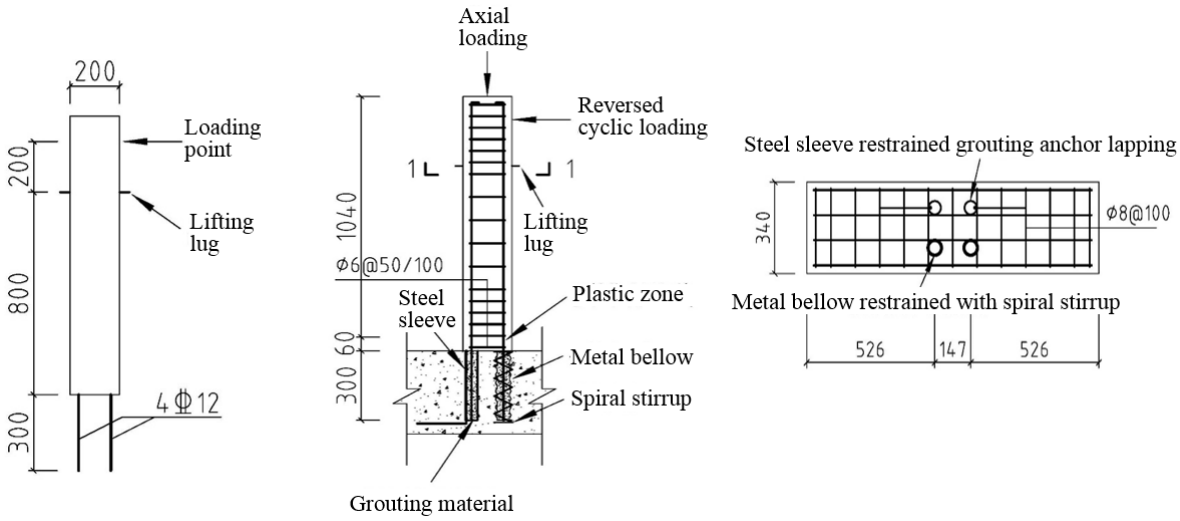

Fig. 3 - Specimen details of precast columns

(a) (b) (c)

Fig. 4 - Manufacturing process of the precast column: (a). Install of plastic hinge zone; (b). Hoisting of the column; (c). The precast column

Tab. 1: Experimental details of all specimens

No.	Longitudinal rebar	Reinforcement ratio	Axial force（KN）	Length of plastic hinge	Connection type
XJ-1	4ϕ12	1.13	458	0d	Cast-in place connection
YG-2	4ϕ12	1.13	458	0d	Steel sleeve connection
YG-3	4ϕ12	1.13	458	5d	
YG-4	4ϕ12	1.13	458	10d	
YL-1	4ϕ12	1.13	458	0d	Corrugated pipe confined with spiral stirrup connection
YL-2	4ϕ12	1.13	458	5d	

Material properties

The concrete samples were collected during the construction of specimens, and the grouting samples were taken after the grouting material poured into the reserved hole. The dimensions of the concrete samples are 100mm×100mm×100mm, and the dimensions of grout cube samples are 50mm×50mm×50mm. They were cast and cured at the same condition with the column specimens. The reinforcement samples were tested as well. The specific properties of the materials in terms of mean value are summarized in Tables 2 and 3.

Tab 2: Compressive strength of concrete and grout

Material	Compressive strength (MPa)
Concrete	55.74
Grout	63.33

Tab 3: Steel mechanical properties

d(mm)	E(GPa)	f_y(MPa)	f_u(MPa)	ε_u(%)
12	210	458.3	587.6	21%

Test setup

This study's experimental equipment includes an automatic data collecting system, a hydraulic jack, and a hydraulic actuator. The hydraulic jack was mounted on top of the column to provide axial compression. A pulley was installed between the rigid steel frame and the hydraulic jack to reduce friction between them. The hydraulic actuator was used to provide horizontal reversed-cyclic loading. Steel plates were placed around the column at the loading point to reduce stress concentration and make a good connection between the actuator and the column. After the specimen was lifted and placed in the right position, the foundation would be mounted to the rigid floor by steel anchors. After that, the axial compression force and the horizontal loading would be applied, respectively. The test setup is displayed in Figure 5.

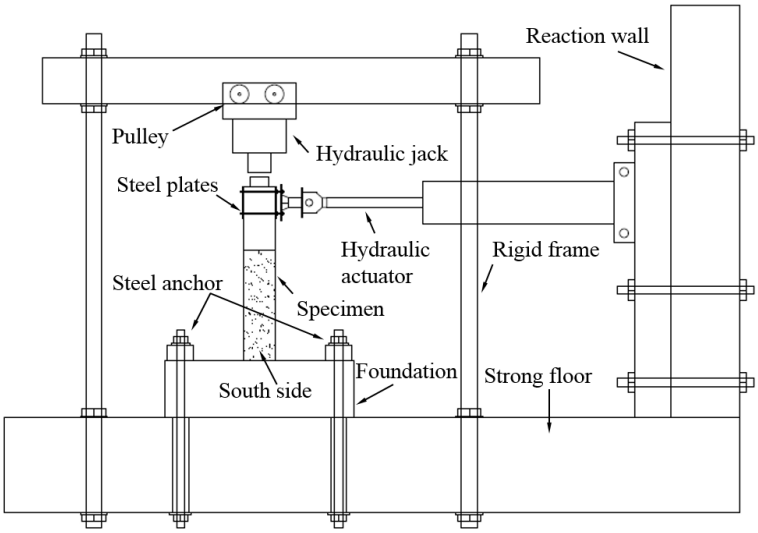

Fig 5 - Schematic illustration of the test setup

Loading procedure

In this study, low-frequency reversed cyclic loading protocol based on the Chinese Standard JGJ101 [31] was carried out at the Shantou University Structure's Laboratory in Shantou, China. In this standard, dual control of load-displacement is recommended for the loading procedure under low-frequency reversed cyclic loading. The standard recommends using multi-stage loading before crack and keeps loading with smaller increments before reaching its cracking stage. The loading procedure will be changed to displacement-controlled after cracks occurred. At the beginning of the test, a hydraulic jack was applied on the top of the column, and an axial load of 458kN was provided. The horizontal load should be applied based on its theoretical cracking loading. In this study, the theoretical cracking loading is about 38kN. The 38kN will be applied on the column with three increments, and each increment will be carried out in three reversed cycles. After the cracks occurred on the bottom of the column, the displacement Δ will be recorded, and displacement-controlled loading protocol will then be carried out. The increment of the displacement-controlled loading will be Δ, and each increment will be repeated three times. The

specimen will be termed as failed when the residual lateral load reached 80% of the peak load, and the loading process will be terminated. The lateral loading protocol is shown in Figure 6.

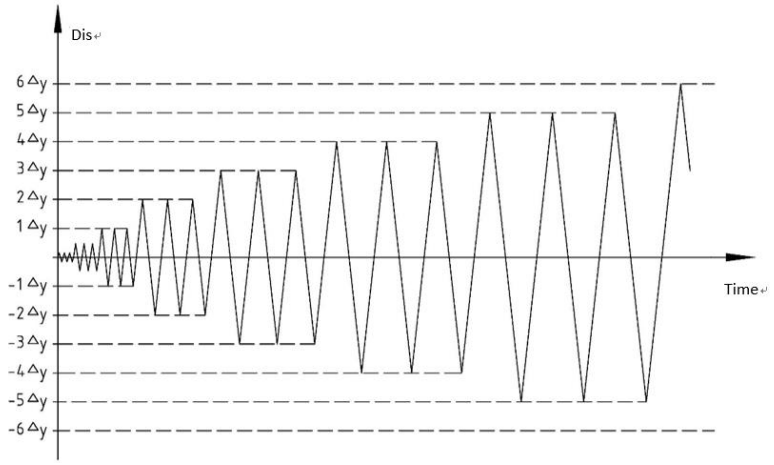

Fig. 6 - Lateral loading protocol

EXPERIMENTAL RESULTS

Crack patterns and failure modes

As the crack kept developing at different lateral displacement, the crack patterns and failure modes were recorded when the lateral displacement reached 5Δ to compare all specimens' crack patterns and failure modes. The specimens' crack patterns and failure modes are displayed in Figure 7, where all specimens are characterized by flexural failure. Under the low-frequency reversed cyclic loading, the development and progress of all specimens' failure can be grouped into three stages: elastic stage, yielding stage and failure stage. In the elastic stage, with the development of horizontal force, the deformation of the specimen increased almost linearly, and the residual deformation was minimal. When it came to the yielding stage, the loading protocol was changed to displacement controlled. With the increase of lateral displacement, the residual deformation accumulated gradually, and more cracks occurred on all sides of the column. There began to appear crushing and spalling at the base of the column. In the failure stage, the column base had been crushed, and later quit working entirely. The crack patterns of all specimen appeared quite similar. At the beginning of loading, horizontal penetrating cracks occurred on the east and west side (the loading direction) of the column at the location where stirrups were installed, and they kept propagating and reached to the south side. Short and horizontal cracks first appeared on the south side. With the development of deformation, the short and horizontal cracks on the south side started to develop diagonally and kept propagating until they intersected at the central place of the south side in the form of "X", displayed in Figures 7 (a), (c) and (e). As the bending moment reached the maximum at the column foot; therefore, the concrete at this place reached the ultimate compressive strain and was continually crushed and peeled off. The whole failure mode of specimens is typically large-eccentric compression failure.

(a) XJ-1 (South side) *(b) XJ-1 (East side)* *(c) YG-3 (South side)*

(d) YG-3 (East side) *(e) YL-2 (South side)* *(f) YL-2 (East side)*

Fig. 7 - Crack patterns and failure mode of the specimens at displacement of 5Δ

Hysteresis loops and skeleton curves

The hysteresis loops and skeleton curves of each specimen are illustrated in Figures 8 and 9, respectively. Hysteresis loop describes the relationship between the cyclic load and lateral displacement, reflecting the seismic performance. Figure 8 displays the development and evolution of the hysteresis loops, which are quite similar for all specimens. Under the load-controlled stage, there was no crack. Therefore, the specimens can be treated as a rigid body, and the rigidity barely changed. However, tiny and hairy cracks were produced inside the concrete, and minimal residual deformation still existed after unloading horizontal force, thus forming a tiny hysteresis loop. When it came to the displacement-controlled loading stage, concrete started to crack as it surpassed the ultimate strength. At the beginning of the displacement-controlled loading stage, although the concrete has cracked, and a small part was crushed and spalled, but it still kept working, and the stiffness of the specimens remained unchanged. In this stage, the peak horizontal load of the specimens raised with the increase of displacement, and the growth rate of peak horizontal load decreased with the improvement of displacement. At the end of the displacement-controlled loading stage, large pieces of concrete were crushed and peeled off, the stiffness declined rapidly, and the peak horizontal load decreased accordingly. Most of the hysteresis loops of the specimens are bow-shaped and have some pinching phenomenon. However, they are also fully shaped, which shows that the specimens have excellent seismic performance and ductility, and generally conform to the hysteretic curve characteristics of compression-bending members.

Compared of Figures 8 (a), (b) and (e), the hysteretic curve of the precast column YG-2 is fuller, which represents that precast column with steel sleeve connection has the similar bearing capacity, ductility and stiffness degradation with cast-in-situ column, while the seismic performance of the precast column using steel sleeve is better. After comparing the hysteretic curves of precast

column YL-1 using corrugated pipe confined with spiral stirrup with precast specimen YG-2 and cast-in-situ specimen XJ-1, the area of the hysteresis loop is smaller. Therefore, its seismic performance is worse than the other two types of specimens, though its bearing capacity is higher. The unbonded length of the three specimens displayed in Figures 8 (c), (d), and (f) are 5d, 10d and 5d, respectively. After compared with the ones without installation of unbonded treatment, the hysteretic loop of the specimens with unbonded treatment is fuller, which means using unbonded treatment could improve precast columns' seismic performance.

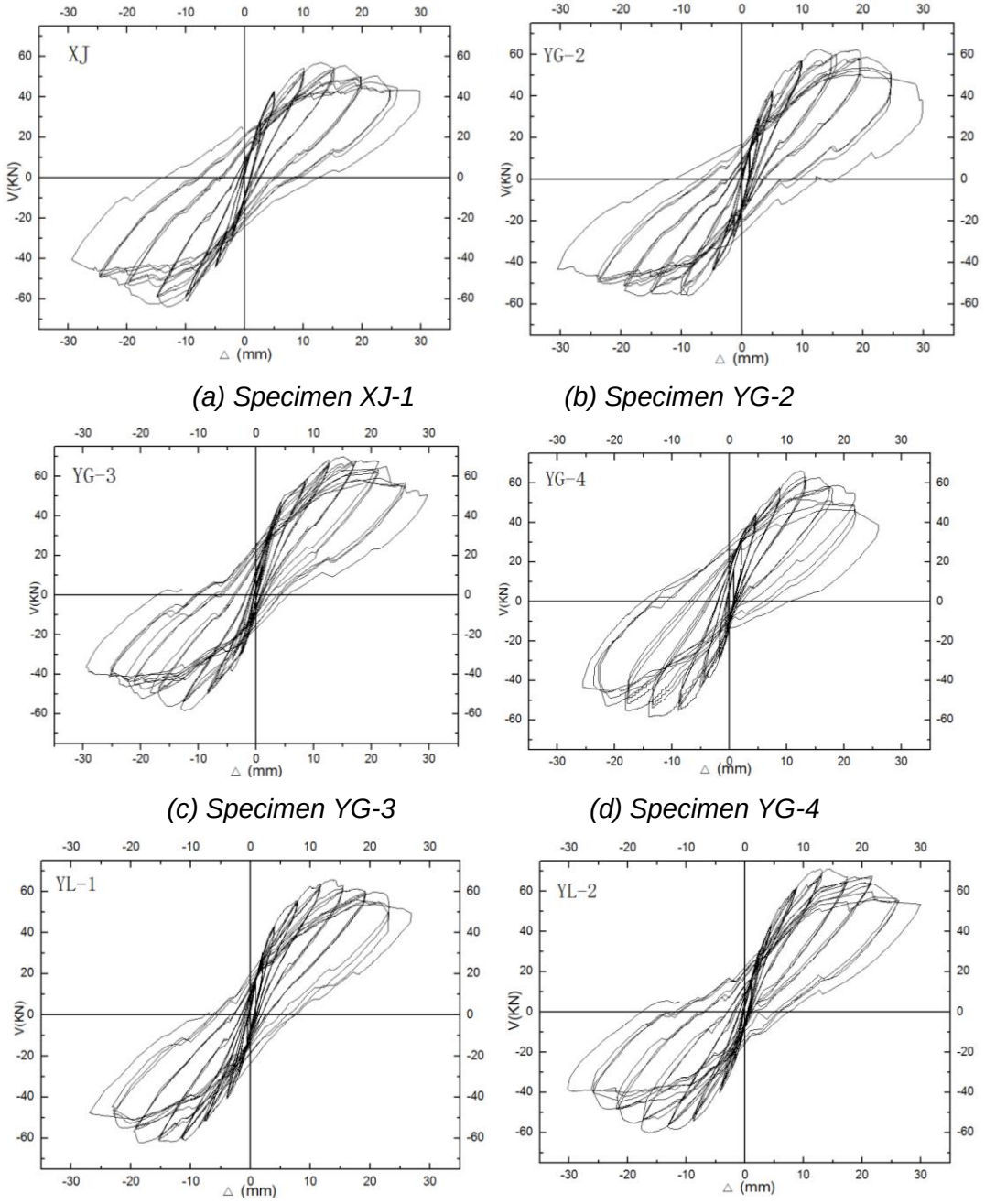

(a) Specimen XJ-1 *(b) Specimen YG-2*

(c) Specimen YG-3 *(d) Specimen YG-4*

(e) Specimen YL-1 *(f) Specimen YL-2*

Fig. 8 - Hysteresis loops of the specimens

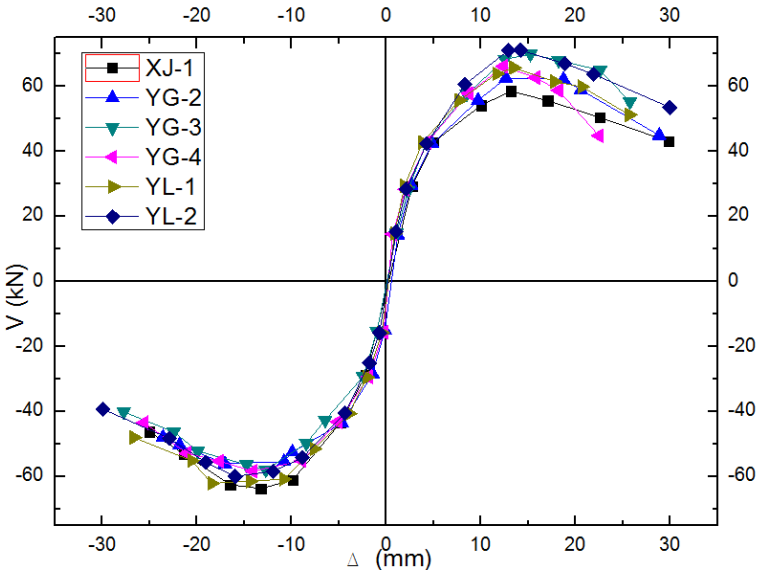

Fig. 9 - Skeleton curve of the specimens

Figure 9 shows that the increase of the horizontal force can be divided into three stages: the elastic stage, yielding stage, and failure stage. At the elastic stage, with the increase of lateral force, the precast column started to crack, and the slope of the skeleton curve began to decline gradually, which indicates that the increased speed of the lateral force slows down. When the lateral force reached the peak stage, the component reached its failure stage. After the peak stage, the lateral force decreased gradually, and more cracks occurred until the component failed finally. From the skeleton curves, it can be concluded that the cast-in-situ specimen and the precast specimens have the similar or even higher lateral resistance, which means that the proposed two types of connection are safe and reliable in connecting precast components. It also can be known that the implementation of artificially unbonded treatment helps improve the precast specimens' bearing capacity.

Bearing capacity and ductility

Table 4 displays the experimental results of the specimens. The yielding point is determined by the energy equivalence method [32]. The ultimate failure point is regarded when the lateral load dropped to 80% of the peak load. The ductility is defined by Equation (1), which represents the deformation capacity of the component after yielding.

$$\mu = \frac{\Delta_u}{\Delta_y} \quad (1)$$

Where Δ_u represents the displacement at the ultimate point and Δ_y at the yielding point. Table 4 shows that the precast specimens YG-2 and YL-2 have a similar bearing capacity with cast-in-situ specimen XJ-1, which can be concluded that the two types of connection could be used in the precast construction. Regarding the ductility, specimens YG-2 and YL-1 have been improved by about 13.09% and 20.32%, respectively, compared with specimen XJ-1, which indicates that these two types of connections could provide better deformation capacity, and the one with spiral stirrup performed much better. After comparing specimens YG-2, YG-3 and YG-4, and comparing specimens YL-1 and YL-2, the utilizing of unbonded treatment is beneficial to the precast specimens. However, it should be noticed that the too-long unbonded treatment could result in worse seismic performance as the ductility of specimen YG-4 (10d) is about 14.5% smaller than

the specimen YG-3 (5d). Therefore, the length of 5d (d is the longitudinal bars' diameters) is recommended in this research.

Tab 4: Test results of all specimens

Specimen	Direction	Yielding point		Critical point		Ultimate point		Vmax/KN	Ductility
		△y/mm	Vy/KN	△cr/mm	Vcr/KN	△u/mm	Vu/KN		
XJ-1	+	4.96	42.83	13.16	58.6	23.23	49.81	63.65	4.43
	-	-4.85	-43.37	-13.27	-63.65	-20.28	-54.10		
YG-2	+	4.84	42.43	12.63	62.58	23.96	53.19	62.58	5.01
	-	-4.68	-43.51	-17.05	-56	-23.74	-47.6		
YG-3	+	4.19	42.7	15.21	69.96	24.38	59.47	69.96	5.43
	-	-4.2	-32.49	-12.74	-57.87	-21.17	-49.19		
YG-4	+	4.32	42.83	12.34	66.19	20.96	56.26	66.19	4.64
	-	-5.12	-43.1	-14.09	-58.27	-22.64	-49.53		
YL-1	+	3.83	42.83	13.45	65.79	22.92	55.92	65.79	5.86
	-	-3.93	-40.95	-18.45	-62.03	-22.56	-52.73		
YL-2	+	4.26	42.43	14.15	71.16	24.49	60.486	71.16	5.33
	-	-4.38	-40.28	-15.99	-59.89	-21.51	-50.91		

Stiffness and strength degradation

Under the low-frequency cyclic loading, the components' stiffness declines with the increase of displacement, which is regarded as the stiffness degradation. The stiffness degradation can be calculated using Equation (2):

$$K_i^j = \frac{\left|+V_i^j\right|+\left|-V_i^j\right|}{\left|+\Delta_i^j\right|+\left|-\Delta_i^j\right|} \quad (2)$$

Where $+V_i^j$ and $-V_i^j$ is the positive and negative peak load of the i^{th} cyclic loading at the j^{th} displacement step, and Δ_i^j is the corresponding displacement. Figure 10 shows the stiffness degradation curve of each test specimen. It can be seen that the stiffness degraded with the increase of displacement, which all have a virtually identical decline trend, which indicates that stiffness deterioration of the two precast connection modes is similar to the cast-in-situ specimen and they both can be used to connect the precast components.

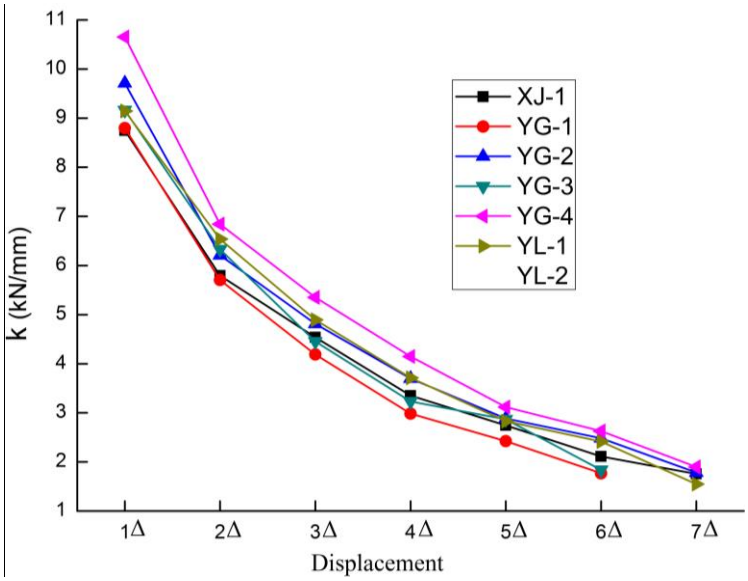

Fig. 10 - Stiffness degradation of the specimens

Energy dissipation

When the structure is subjected to cyclic loads, the area of the hysteretic loop is the energy dissipated by a cyclic load. Under the same condition, the fuller the hysteretic loop and the larger the area it contains, the higher the structure's energy dissipation capacity and the better the seismic performance. The energy dissipated in each cycle has been calculated, shown in Table 5, and presented in Figure 11. From the figure, the slope of each specimen's cumulative energy dissipation curve increases with the increase of displacement, which indicates that the larger the loading displacement, the faster the specimen's energy dissipation speed. Table 5 shows that precast columns' energy dissipation capacity using both types of connections is equivalent to the cast-in-situ specimens, which proves again that steel duct sleeve and corrugated pipe are confined with spiral stirrups can be used in precast construction. Moreover, the application of certain length unbonded treatment is beneficial in improving the energy dissipation capacity. However, it should be noted that too long unbonded treatment (10d in this research) is harmful to the precast specimens.

Tab 5: Energy dissipation (J)

Specimen	1Δ	2Δ	3Δ	4Δ	5Δ	6Δ	7Δ	Total×10^3
XJ-1	452.95	1260.91	2010.43	2507.28	2795.32	3137.15	/	12.16
YG-2	472.36	1239.98	1936.98	2445.3	2738.69	3214.44	/	12.05
YG-3	334.55	1082.72	1922.06	2423.16	2861.18	3131.28	3354.08	15.11
YG-4	465.82	1121.01	1840.87	2238.65	2513.87	2531.14	/	10.71
YL-1	343.82	946.09	1651.79	2244.04	2634.34	2802.22	3177.29	13.80
YL-2	386.56	1125.58	1929.65	2440.18	2791.19	3078.06	3352.75	15.10

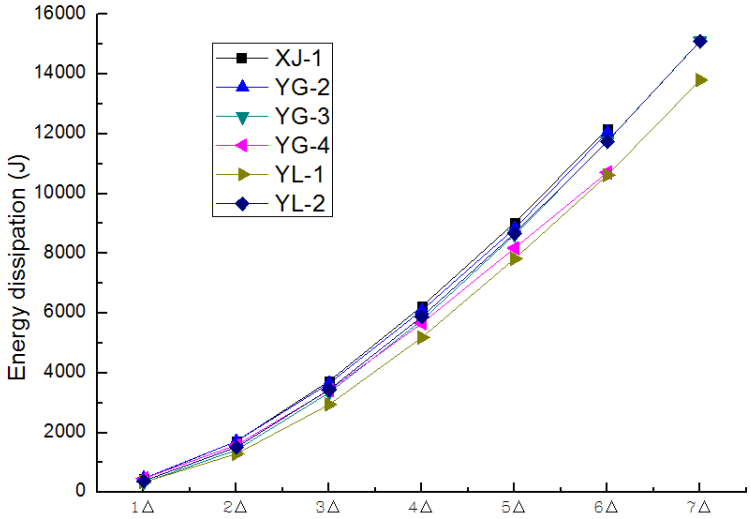

Fig. 11 - Energy dissipation of the specimens

Equivalent Viscous Damping Coefficient

In "Specification for the seismic test of buildings", the equivalent viscous damping coefficient is defined to analyze the structure's seismic performance, which is calculated through the following equation.

$$\zeta_{eq} = \frac{1}{2\pi} \bullet \frac{S_{(ABC+CDA)}}{S_{(OBE+ODF)}} \quad (3)$$

Where $S_{(ABC+CDA)}$ represents the hysteresis loop area in Figure 12 and $S_{(OBE+ODF)}$ indicates the area of triangles OBE and ODF.

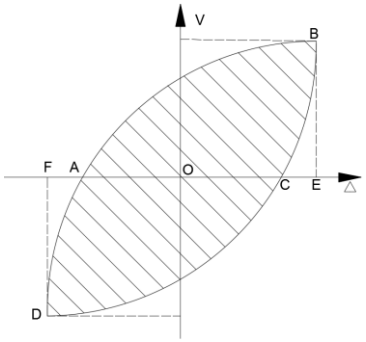

Fig. 12 - Schematic of the load-deformation hysteresis curve

The equivalent viscous damping coefficient of each specimen is calculated using the above equation and the results are displayed in Figure 13. It is known that the curves of equivalent viscous damping coefficients of all specimens show an upward trend, except the specimen of YG-4. Moreover, each specimen's equivalent viscous damping coefficient increases slowly with the increase of displacement before yielding. The specimens' equivalent viscous damping coefficient changed slightly after yielding, but the fluctuation range is small. Figure 13 shows that the equivalent viscous damping coefficient of specimen YG-4 is different from others, which indicates that the implementation of 10d unbonded treatment on the longitudinal reinforcement in specimen YG-4 is harmful.

Tab 6: Equivalent viscous damping coefficient ζ_{eq}

Specimen	Yielding	Critical	Ultimate
XJ-1	0.341	0.396	0.409
YG-2	0.368	0.444	0.422
YG-3	0.324	0.407	0.421
YG-4	0.365	0.358	0.381
YL-1	0.338	0.404	0.390
YL-2	0.344	0.395	0.384

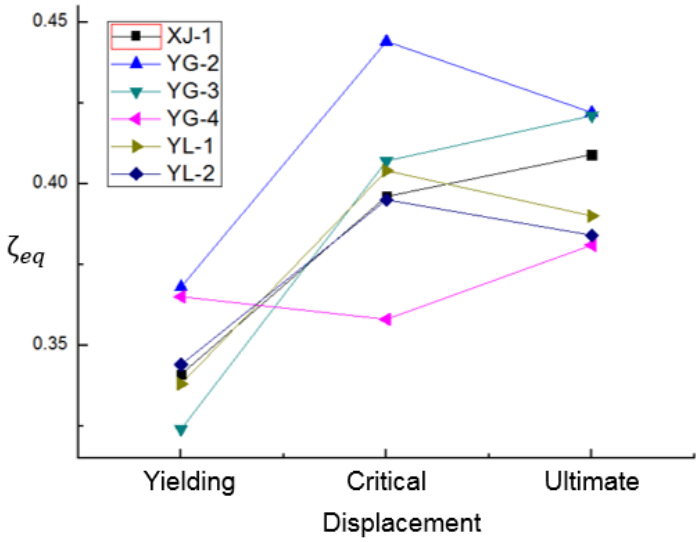

Fig. 13 - Equivalent viscous damping coefficients of the specimens

CONCLUSION

In this paper, a cast-in-situ reinforced column, three precast columns connected using steel sleeve, and two precast columns connected using corrugated pipe confined with spiral stirrup were tested. The tests were carried out under a combined constant vertical load and low-frequency cyclic horizontal load to determine their seismic performance. The seismic behaviour in terms of failure patterns, bearing capacity, ductility, stiffness, energy dissipation capacity and equivalent viscous damping coefficient are evaluated comprehensively. Based on the experimental results, the following conclusions can be made:

(1) The failure modes of precast column specimens and cast-in-situ column specimens are basically the same. At the beginning of loading, horizontal penetrating cracks occurred on the east and west side of the column at the location where stirrups were installed. On the south side of the column, the crack appeared in the form of "X". The concrete at the column base was crushed and peeled off. The whole failure mode of specimens belongs to large eccentric compression failure.

(2) The precast specimens using both types of connection presented a similar or even better seismic performance compared with the cast-in-situ column in terms of bearing capacity, ductility, energy dissipation and equivalent viscous damping coefficient.

(3) For both types of precast column specimens, the application of the artificially unbonded treatment on the longitudinal reinforcement could improve the bearing capacity, ductility, energy

dissipation as well as equivalent viscous damping coefficient. However, it is harmful if the unbonded length is too large. The recommended length of unbonded treatment in this paper is five times of the longitudinal reinforcement's diameter.

(4) The connection type of steel sleeve and corrugated pipe confined with spiral stirrup both can effectively connect precast components, and the seismic performance of the precast columns using the above two connection modes are much better than that of cast-in-situ column. Therefore, these two connection modes can be applied in practical precast structures.

In a further study, the same connection method will be used to test the specimens with larger cross-section. Moreover, the unbonded treatment of different lengths will be considered to determine the most suitable and beneficial unbonded length. Besides, some energy-dissipating steel bars will be installed at the joints to improve the prefabricated structures' seismic performance.

ACKNOWLEDGEMENTS

This research was supported by the Shantou University Research Start-Up Fund (NFT17011). The authors gratefully acknowledge its financial support.

REFERENCES

[1] Xu, L., Pan, J., and Cai, J., 2019. Seismic performance of precast RC and RC/ECC composite columns with grouted sleeve connections. Engineering Structures, Vol. 188:104-110

[2] Seifi, P., Henry, R., and Ingham, J., 2019. In-plane cyclic testing of precast concrete wall panels with grouted metal duct base connections. Engineering Structures, Vol.184: 85-98

[3] ACI 550., 2009. Guide to emulating cast-in-place detailing for seismic design of precast concrete structures, Farmington Hills, MI, USA.

[4] Biondini, F., and Toniolo, G., 2009. Probabilistic calibration and experimental validation of seismic design criteria for one storey concrete frames. J Earthq Eng, Vol. 13, No. 4: 426–462.

[5] Biondini, F., Toniolo, G., and Tsionis, G., 2010. Capacity design and seismic performance of multi-storey precast structures. Eur J Environ Civil Eng, Vol. 14, No. 1: 11–28.

[6] Kramar, M., Isaković, T., and Fischinger, M., 2012. Seismic collapse risk of precast industrial buildings with strong connections. Earthq Eng Struct Dyn, Vol.39, No.8: 847–868.

[7] Psycharis, I.N., and Mouzakis, H.P., 2012. Shear resistance of pinned connections of precast members to monotonic and cyclic loading. Eng Struct, Vol. 41: 413–427.

[8] Negro, P., Bournas, D.A., Molina, F.J., 2013. Pseudodynamic tests on a full-scale 3-storey precast concrete building: global response. Eng Struct, Vol. 57: 594–608.

[9] Dal Lago, B., Negro, P., and Dal Lago, A., 2018. Seismic design and performance of dry-assembled precast structures with adaptable joints. Soil Dyn Earthq Eng, Vol. 106: 182–195.

[10] Dal Lago, B., Biondini, F., and Toniolo, G., 2018. Seismic performance of precast concrete structures with energy dissipating cladding panel connection systems. Structural Concrete. Vol. 19, No. 4: 1-19.

[11] Colombo, A., Negro, P., and Toniolo, G.,2014. The influence of claddings on the seismic response of precast structures: The Safecladding project. Proceedings of the 2nd European conference on earthquake engineering and seismology. Istanbul, Turkey: European Association for Earthquake Engineering (EAEE), Paper No. 1877.

[12] Ling, J., Rahman, A., Ibrahim, I., and Hamid, Z., 2012. Behavior of grouted pipe splice under incremental tensile load. Construction and Building Materials, Vol. 33: 90-98

[13] Haber, Z. B., Saiidi, M. S., and Sanders, D. H., 2014. Seismic performance of precast columns with mechanically spliced column-footing connections. ACI Structural Journal. Vol. 111, No. 3: 639-650.

[14] Hosseinin, S. J. A. and Rahman, A. B. A., 2016. Effects of spiral confinement to the bond behavior of deformed reinforcement bars subjected to axial tension. Engineering Structures, Vol. 112: 1-13

[15] Hosseini, S. J. A., Rahman, A. B. A., Osman, M. H., Saim, A., and Adnan, A., 2015. Bond behavior of spirally confined splice of deformed bars in grout. Construction Building Material, Vol. 80: 180-194.

[16] Seo, S. Y., Nam, B. R., and Kim, S. K., 2016. Tensile strength of the grout-filled head-splice sleeve. Construction and Building Materials, Vol. 124: 155-66

[17] Rave-Arango, J., Blandon, C., Restrepo, J., and Carmona, F., 2018. Seismic performance of precast concrete column-to-column lap-splice connections. Engineering Structures, Vol. 172: 687-699

[18] Gu, Q., Dong, G., Wang, X., Jiang, H., and Peng, S., 2019. Research on pseudo-static cyclic tests of precast concrete shear walls with vertical rebar lapping in grout-filled constrained hole. Engineering Structures, Vol. 189: 396-410.

[19] Tullini, N. and Minghini, F., 2016. Grouted sleeve connections used in precast reinforced concrete construction-Experimental investigation of a column-to-column joint. Engineering Structures, Vol. 1279: 784-803

[20] Huang, Y., Zhu, Z., Naito, C., and Yi, W., 2017. Tensile behaviour of half grouted sleeve connections: experimental study and analytical modeling. Construction and Building Materials, Vol. 152: 96-104

[21] Jansson, P., 2008. Evaluation of grouted-filled mechanical splices for precast concrete construction. Report No R-1512, Michigan Department of Transportation, Lansing, MI, USA.

[22] Chen, J. and Xiao, Y., 2016. Experimental study on seismic behavior of precast concrete column with longitudinal reinforcement grouting-anchoring connections. China Civil Engineering Journal, Vol. 49, No.5: 1-11

[23] ACI 318., 2011. Building code requirements for structural concrete, Farmington Hills, MI, USA.

[24] Belleri, A. and Riva, P., 2017. Seismic performance and retrofit of precast concrete grouted sleeve connections. PCI Journal, Vol. 57, No. 1: 97-109

[25] Jiang, H., Zhang, H., Liu, W., and Yan, H., 2011. Experimental study on plug-in filling hole for steel bar anchorage of the PC structure. Journal of Harbin Institution Technology, Vol. 43, No. 10: 28-31

[26] Seifi, P., Henry, R., and Ingham, J., 2016. Panel connection details in existing New Zealand precast concrete buildings. Bulletin of the New Zealand Society for Earthquake Engineering, Vol. 49, No.2: 190-199.

[27] Riva, P., 2006. Seismic behaviour of precast column-to-foundation grouted sleeve connections. Advances in Engineering Structures, Mechanics & Construction, Springer, Dordrecht, Netherlands, pp. 121-128.

[28] Kim, Y., 2000. A study of pipe splice sleeves for use in precast beam-column connections, PhD thesis, University of Texas at Austin, Austin, USA.

[29] Pandey, G. R. and Mutsuyoshi, H., 2005. Seismic performance of reinforced concrete piers with bond-controlled reinforcements. ACI Structural Journal, Vol. 102, No. 2,: 295-304

[30] Wu, Y., Xiao, Y., and Anderson, J., 2009. Seismic behavior of PC column and steel beam composite. Journal of Structural Engineering, Vol. 135, No. 11: 1398-1407

[31] JGJ101-2015., 2015. Specification for seismic test of buildings, China Plan Press, Beijing, China.

[32] Yan, Q., Chen, T., and Xie, Z., 2018. Seismic experimental study on a precast concrete beam-column connection with grout sleeves. Engineering Structures, Vol. 115: 330-44

CIVIL ENGINEERING JOURNAL

Article no. 47

THE CIVIL ENGINEERING JOURNAL 3-2021

MECHANICAL PROPERTIES OF LIGHTWEIGHT FOAMED CONCRETE REINFORCED WITH RAW MESOCARP FIBRE

Md Azree Othuman Mydin

School of Housing, Building and Planning, Universiti Sains Malaysia, 11800, Penang, Malaysia; azree@usm.my

ABSTRACT

Lightweight foamed concrete (LFC) is recognised for its high flowability, minimal utilization of aggregates and superior heat insulation properties. LFC is excellent under compression but poor in tensile stress, as it produces multiple microcracks. LFC cannot withstand the tensile stress induced by applied forces without additional reinforcing elements. Hence, this study was conducted to examine the potential utilisation of oil palm pressed fibre (OPPF) reinforced LFC in terms of its mechanical properties. Two densities, 600kg/m^3 and 1200kg/m^3, were cast and tested with six different percentages of OPPF, which were 0.15%, 0.30%, 0.45% and 0.60%. The parameters evaluated were compressive strength, flexural strength and tensile strength. The results revealed that the inclusion of 0.45% of OPPF in LFC helps to give the best results for the compressive strength, flexural strength and splitting tensile strength. The OPPF facilitated to evade the promulgation of cracks in the plastic state in the cement matrix when the load was applied.

KEYWORDS

Foamed concrete, Pressed fibre, Compression, Flexural, Water absorption, Porosity

INTRODUCTION

Lightweight foamed concrete (LFC) is characterised as a light cellular concrete with random air bubbles produced from the process of mixing foaming agent into the mortar [1]. LFC is known for its high flowability, low cement content, minimal use of aggregates, and superior heat insulation [2]. Moreover, LFC is deemed an economical alternative in the manufacture of large-scale lightweight construction materials and products, such as structural components, partitions, filling grades and road embankment infills, owing to its simple manufacturing process [3], which covers all stages from manufacturing plants to the final position of the applications [4]. LFC has a high degree of thermal insulation, which is a perfect material for use in passive house design [5]. It is undeniable that foam concrete is not reinforced as easily as traditional concrete, due to its low resistance to concentrated stress [5] and the difficulty of ensuring a sufficient bond of reinforcement [6]. LFC has a wide range of densities, from 300kg/m^3 to 1900kg/m^3, depending on its composition and the production machine used [7].

Some natural fibre, namely oil palm pressed fibre, is used in composites to develop lightweight, thermally insulated cement composites [8]. Oil palm pressed fibre (OPPF), also known as palm pressed fibre (PPF), is the residue of biomass produced after palm fruits are pressed for the extraction of palm oil [9]. After oil extraction, approximately 11 per cent of the OPPF is produced from palm fruits [9]. OPPF is generally made up of fabric, broken kernels and shells [10]. In mills, OPPF is currently primarily used as fuel for steam boilers [11,12]. As a lignocellulosic substance, OPPF has drawn researchers' interest because of its potential use in the development of bio-composites [13]. Natural fibre-reinforced composites have many advantages, such as being light

weight, low-cost, highly durable, and with fair strength and rigidity [14,15]. OPPF acts as a reinforcement to improve its composites' behaviour [16].

There are some advantages of using fibre introduced into the concrete, such as the resulting composites offering more flexural strength compared to that of a reinforcement bar [17,18]. Besides, it will increase the impact toughness and post-failure integrity [19] and enhance the bending strength of the composites [20,21]. In addition, it will arrest the propagation of micro-cracks [22], the tensile strength of concrete increases and the air void and water voids reduce [23]. Hence, this research was carried out to determine the effect of the inclusion of OPPF on the mechanical properties of LFC.

METHODS

Materials

Cement

Ordinary Portland Cement was the cement used, in accordance with BS 12 Standard. Figure 3shows the OPC used in this research, which was supplied by YTL Castle Cement Marketing Sdn Bhd. All the cement used was in good condition and stored in a covered area. Table 1 shows the basic composition of OPC.

Tab. 1. - Composition of Ordinary Portland Cement (OPC) used in this study

Chemical	Component (%)
Calcium Oxide, CaO	62.91
Silicon Dioxide, SiO2	20.34
Aluminium (III) Oxide, Al2O3	4.47
Iron (III) Oxide, Fe2O3	4.58
Potassium Oxide, K2O	0.29
Magnesium Oxide, MgO	1.24
Sodium Oxide, Na2O	0.31
Sulphur Trioxide, SO3	2.58
Loss on ignition, LOI	3.27

Fine Sand

The fine aggregate used was natural fine sand obtained from a local distributor. It had to be prepared three days before casting, which meant that it had to be dried and sieved. If sand is ideally indicated in the blend design, it should be fine, with a maximum width of 2 mm and a 600-micron sieve, and a passage of 60% to 90%. The suitability of the sand had to follow BS822:1992. Figure 1 shows the sieve analysis result done on the fine sand utilized for this study.

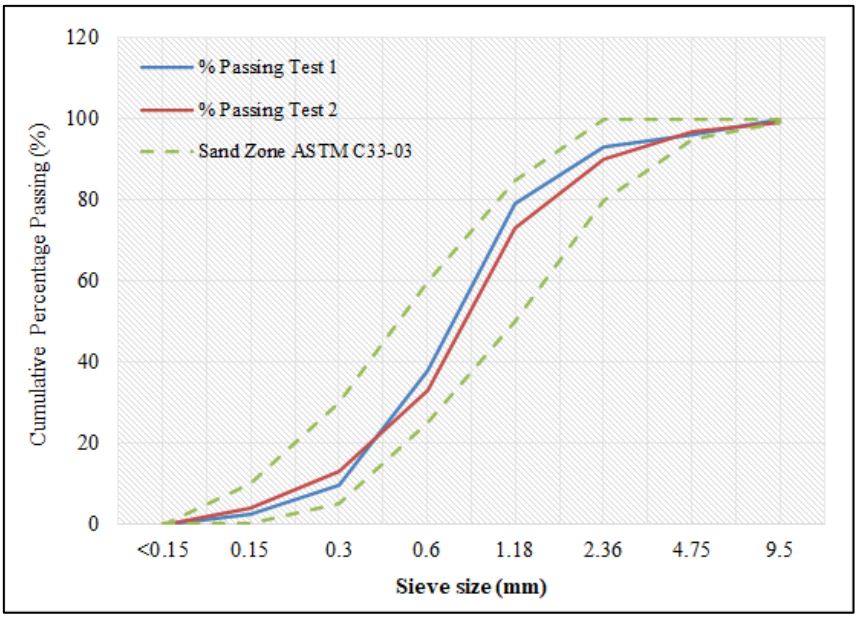

Fig. 1 - Sieve analysis result

Foaming agent

The foaming agent used in this study was a protein-based foaming agent, namely Noraite PA-1. The foam was produced by a portable foaming generator machine, namely the Portafoam TM-1 machine. Noraite PA-1 was chosen as the forming agent due to its stability and smaller bubbles, which create a stronger bubble bonding structure compared to a synthetic-based protein.

Water

The water used had to be clear and clean. Water was required for the preparation of the mortar, mixing the foam concrete and the curing work. The water-cement ratio used for this research was 0.45, because this ratio can achieve reasonable workability, based on previous research.

Oil Palm Pressed Fibre

The fibre used was OPPF, which was freshly collected from an industrial unit after processing. The OPPF was covered by a skin of grease which would cause fungus growth and spoilage. The fibre needed to be washed until it was free from the grease. The OPPF was placed under the sun to dry, as shown in Figure 2. Figure 3 visualizes the surface morphology details of OPPF structure.

Fig. 2 - OPPF was placed under the sun in the drying process

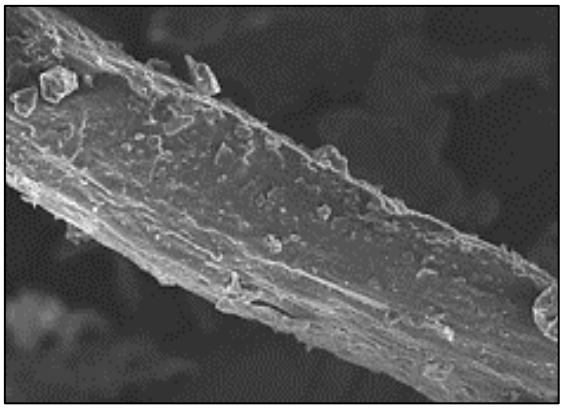

Fig. 3 – Surface morphology details of OPPF structure

The raw OPPF x-ray diffraction pattern is shown in Figure 4. It can be seen that the raw OPPF used for this research had diffraction patterns at around 2θ = 23 and 2θ = 18, which signified the crystalline and amorphous areas, correspondingly. Table 2 demonstrates the chemical composition and mechanical properties of single raw OPPF.

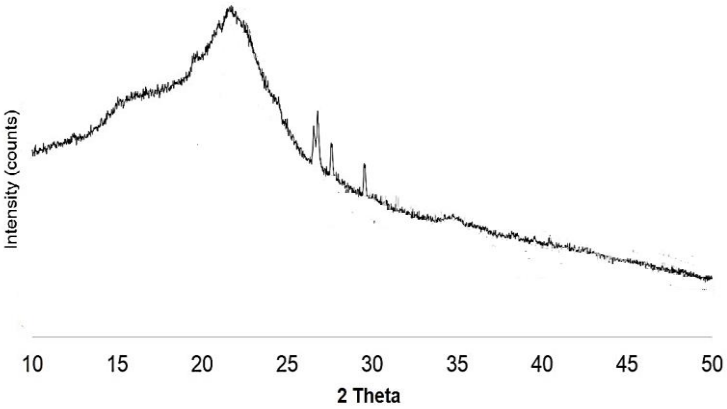

Fig. 4 - OPPF x-ray diffraction patterns

Tab. 2. - Chemical composition and mechanical properties of raw OPPF

Lignin (%)	31.4 ± 3.8
Cellulose (%)	26.2 ± 0.7
Hemicellulose (%)	31.7 ± 4.4
Extractives (%)	4.3± 0.2
Tensile strength (N/mm^2)	139.6
Young's modulus (kN/mm^2)	14.3
Elongation at break (%)	9.76

Mix Design

A total of 10 mixes and 2 densities, 600 kg/m^3 and 1200 kg/m^3, were prepared. The volume fractions of OPPF considered were 0.15%, 0.30%, 0.45% and 0.60%. For all the mixes, the sand-

cement ratio used was 1:1.5 and the water-cement ratio used was kept constant at 0.45. Table 3 shows the mix proportions of this study.

Tab. 3: Mix proportions

Mix	OPMP (%)	Density (kg/m^3)	Cement (kg)	Sand (kg)	Water (kg)	Mix Ratio (C:S:W)
1	-	600	20.72	31.09	9.32	1:1.5:0.45
2	0.15	600	20.72	31.09	9.32	1:1.5:0.45
3	0.30	600	20.72	31.09	9.32	1:1.5:0.45
4	0.45	600	20.72	31.09	9.32	1:1.5:0.45
5	0.60	600	20.72	31.09	9.32	1:1.5:0.45
6	-	1200	40.22	60.33	18.10	1:1.5:0.45
7	0.15	1200	40.22	60.33	18.10	1:1.5:0.45
8	0.30	1200	40.22	60.33	18.10	1:1.5:0.45
9	0.45	1200	40.22	60.33	18.10	1:1.5:0.45
10	0.60	1200	40.22	60.33	18.10	1:1.5:0.45

Testing

Tests were carried out investigating the mechanical and durability properties with the inclusion of OPPF. Destructive tests, which included compression tests, flexural tests and splitting tensile tests, were done to determine the mechanical properties of LFC. Table 4 shows the details of the specimens and standard codes referred to in these tests for the durability and mechanical properties. Figures 5, 6 and 7 demonstrate the setup for compression test, flexural test and splitting tensile test correspondingly.

Tab. 4: Mechanical properties tests

Type of Test	Specimen	Standard
Axial compression test	Cube (100mm x 100mm x 100mm)	BS EN 12390-3: 2001
Flexural test	Prism (100mm x 100mm x 500mm)	ASTM C 348
Splitting tensile test	Cylinder (100mm diameter x 200mm height)	ASTM C496/C 496M

Fig. 5 - Compression test setup according to BS EN 12390-3: 2001

Fig. 6 - Flexural test setup according to ASTM C 348

Fig. 7 - Splitting tensile test setup according to ASTM C496/C 496M

RESULTS AND DISCUSSION

Compressive Strength

Figures 8 and 9 show the results of the axial compressive strength test of both 600kg/m^3 and 1200kg/m^3 densities of LFC with the addition of different proportions of OPPF. There was an enhancement in the strength of the control until 0.45% of OPPF addition. The strength reduced when 0.60% of OPPF was added. The factor that led to the decreasing value of fibre reinforced LFC was the interruption of fibre presence. Next, the highest compressive strength for both densities was at day-56, compared to day-7 and day-28. For the density of 600kg/m^3, the highest compressive strength was 1.61N/mm^2 at day-56 with the addition of 0.45% of OPPF. The lowest compressive strength was 0.89N/mm^2 with the addition of 0.60% of OPPF at day-7. For the density of 1200kg/m^3, the highest compressive strength was 5.82 N/mm^2 at day-56 with the addition of 0.45% of OPPF. The lowest compressive strength was 3.22 N/mm^2, which was for plain LFC at day-7. At day-28, the strength of the control specimen of 600kg/m^3 density increased from 1.16N/mm^2 to 1.24N/mm^2, 1.30N/mm^2 and 1.44N/mm^2, when 0.15%, 0.30% and 0.45% of OPPF was added, respectively. For the 1200kg/m^3 density, the strength of the control specimen was 3.68N/mm^2, and it increased to 4.61N/mm^2, 4.77N/mm^2 and 5.35N/mm^2 when 0.15%, 0.30% and 0.45% of OPPF was added,

correspondingly. This shows that the addition of OPPF increases the compressive strength of LFC accordingly. There was a massive enhancement in strength from day-7 to day-90. When the OPPF volume fraction exceeds 0.45%, the compressive strength of LFC reduced intensely, as evidenced by other studies. According to Thakrele [24], the inclusion of high-volume fraction of natural fibre in LFC will impede the hydration process, consequently causing in low strength concrete. As LFC comprises void gaps of a wide range of sizes and shapes in the cement matrix and micro-cracks at the transition zone between the matrix, the inclusion of fibre can assist in the failure of the mode under compression stress [25].

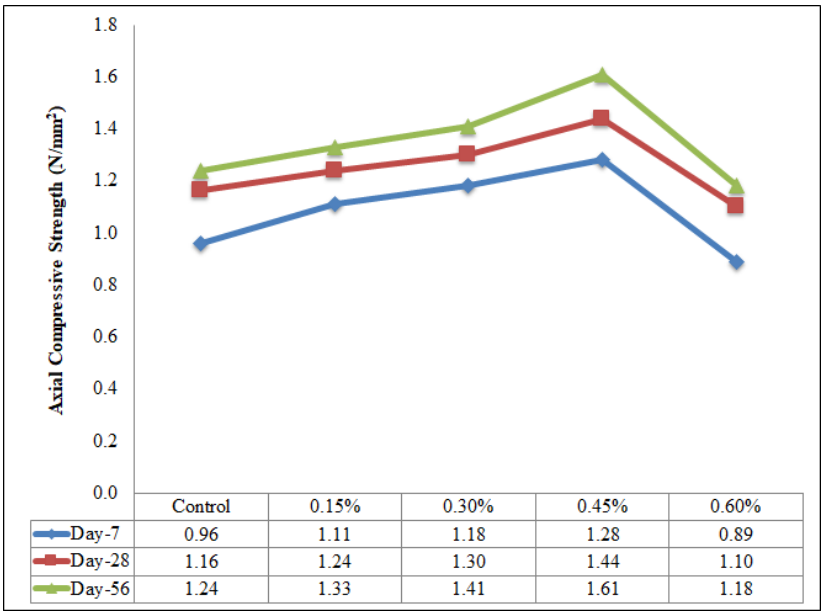

	Control	0.15%	0.30%	0.45%	0.60%
Day-7	0.96	1.11	1.18	1.28	0.89
Day-28	1.16	1.24	1.30	1.44	1.10
Day-56	1.24	1.33	1.41	1.61	1.18

Fig. 8 - Influence of different percentages of OPPF on axial compressive strength of 600 kg/m^3 density LFC

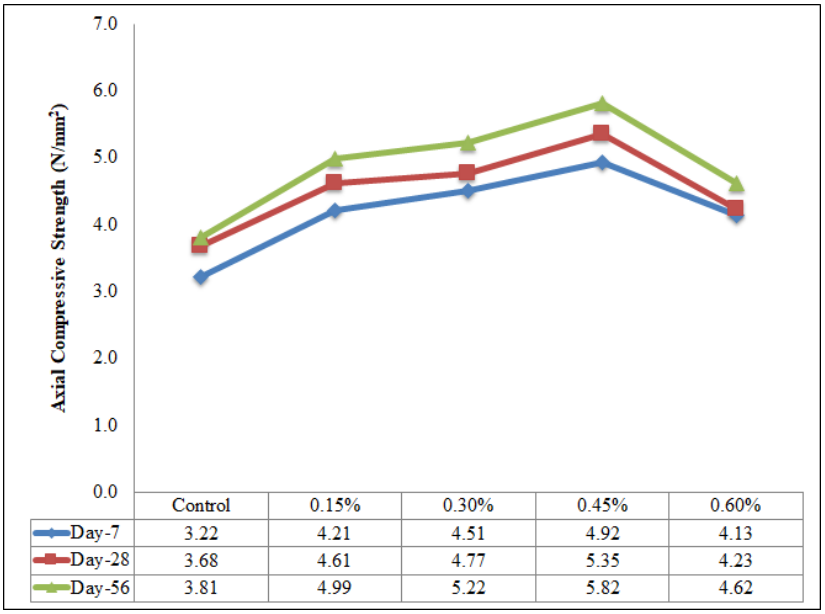

	Control	0.15%	0.30%	0.45%	0.60%
Day-7	3.22	4.21	4.51	4.92	4.13
Day-28	3.68	4.61	4.77	5.35	4.23
Day-56	3.81	4.99	5.22	5.82	4.62

Fig. 9 - Influence of different percentages of OPPF on axial compressive strength of 1200 kg/m^3 density LFC

Figure 10 shows the scanning electron microscopy result of fractured surface of LFC strengthened with OPPF. Although addition of OPPF plays and important role to enhance the interfacial adhesion between cement paste and the OPPF, the evidence of pull-out of fibre can be clearly seen under compressive load especially for lower density LFC (600 kg/m^3). Lower density which consists of large pores unable to withstand additional load under compressive due to poor adhesion. Anyhow, the addition of OPPF in LFC assisted in bounding the LFC matrix in lateral direction, thus improved the confinement effect and indirectly improved the compressive strength of LFC when the specimens were compressed.

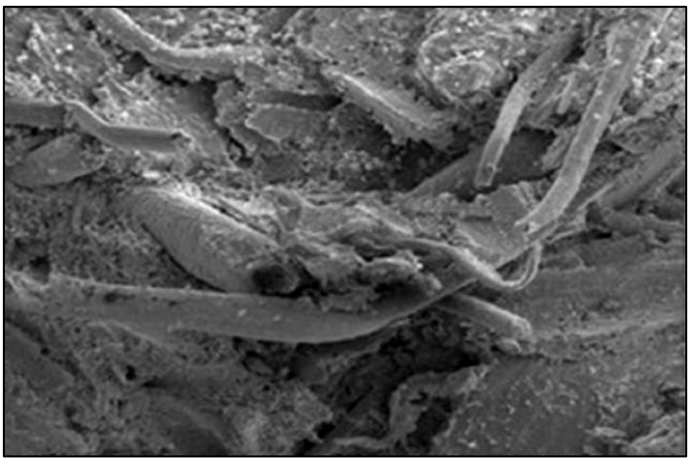

Fig. 10 - SEM image of fractured surface of 600kg/m^3 density LFC under compression load

Flexural Strength

Figure 11 and Figure 12 show the results of the flexural strength test of both densities of LFC, 600kg/m^3 and 1200kg/m^3. The flexural strength rose noticeably from the control up to the addition of 0.45% of OPPF. The improvement in the flexural strength of the LFC was attributed to the fact that the fibre behaves as a reinforcing layer that connects the grid of the cementitious matrix in a durable manner relative to the specimen, without any fibre being added in the tensile zone. Meanwhile, the flexural strength declined when 0.60% of OPPF was added. The reason for the decrease in the value of the fibre reinforced LFC was the interruption of fibre presence [26]. Next, the highest flexural strength was recorded for both densities at day-56, compared to day-7 and day-28. For the density of 600kg/m^3, the highest flexural strength was 0.37N/mm^2 at day-56 with the addition of 0.45% of OPPF. The lowest flexural strength was 0.9N/mm^2 without any proportion of OPPF at day-7. For the density of 1200kg/m^3, the highest flexural strength was 1.28N/mm^2 at day-56 with the addition of 0.45% of OPPF. The lowest flexural strength recorded was 0.72N/mm^2, which was found in the plain LFC at day-7. It can be seen that for both densities, plain LFC attained a lower flexural strength compared to the LFC with the addition of OPPF. The reason for the increase in flexural strength was the fracture process of the fibre, which derived from the progressive debonding of the fibre that slowed the crack propagation [27]. According to Musa et al. [28], the flexural strength of LFC ranges between 15% and 35% of its compressive strength. Whereas in the current research, the flexural strength of LFC is between 18-30% of its compressive strength. The OPPF in LFC is to strengthen FC mass and transfer the basic material character from brittle to ductile elastic-plastic. OPPF contributes towards enhancing the flexural strength of LFC. Though, disproportionate OPPF volume fraction may also lead to reducing bonding and deteriorating [29]. The use of a 0.45% volume fraction of OPPF can be considered an optimal percentage for this type of concrete based on the increment of flexural strength. The enhancement of flexural strength is compatible with the compressive strength upsurge. Elevated flexural strength is due to the reduction of porosity in LFC mixes.

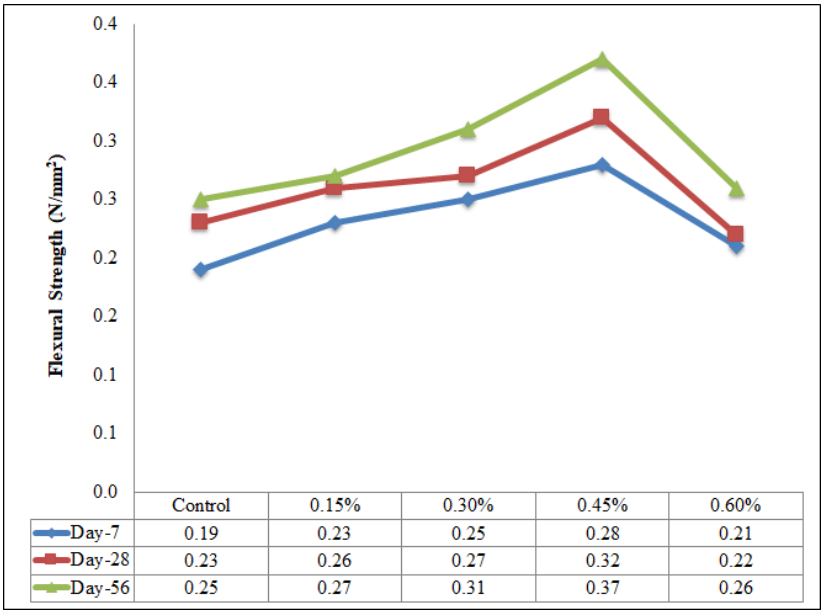

	Control	0.15%	0.30%	0.45%	0.60%
Day-7	0.19	0.23	0.25	0.28	0.21
Day-28	0.23	0.26	0.27	0.32	0.22
Day-56	0.25	0.27	0.31	0.37	0.26

Fig. 11 - Influence of different percentages of fibre on flexural strength of 600 kg/m^3 density

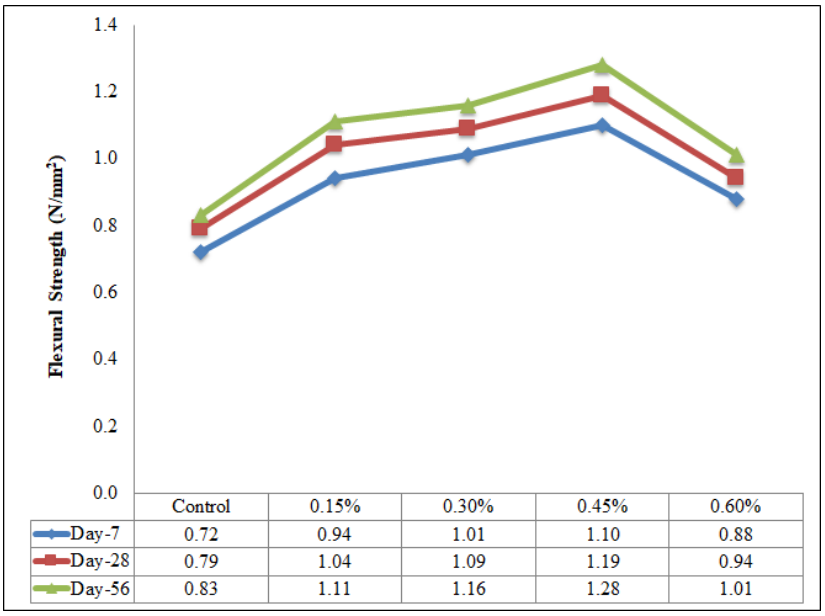

	Control	0.15%	0.30%	0.45%	0.60%
Day-7	0.72	0.94	1.01	1.10	0.88
Day-28	0.79	1.04	1.09	1.19	0.94
Day-56	0.83	1.11	1.16	1.28	1.01

Fig. 12 - Influence of different percentages of fibre on flexural strength of 1200 kg/m^3 density

Figure 13 visualizes the scanning electron microscopy result of fractured surface of LFC strengthened with OPPF under flexural load. As far as flexural load is concern, there was very little indication of OPPF retreat occurred signifying the stress which was transferred to the OPPF in the cementitious composite was stronger resulting in OPPF rupture rather than principally fibre pull-out.

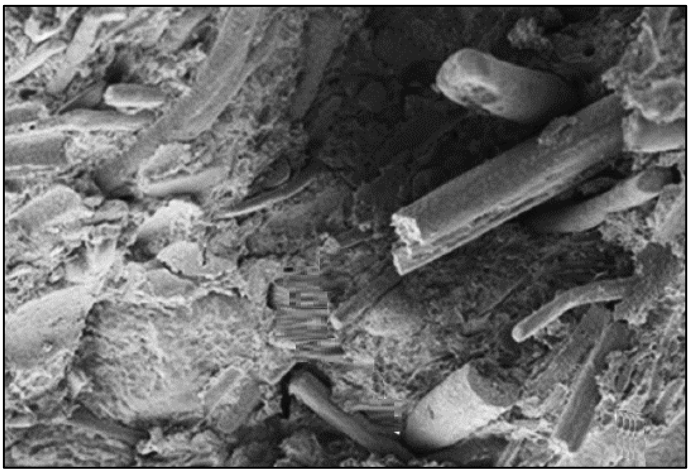

Fig. 13 - SEM image of fractured surface of 600 kg/m^3 density LFC under flexural load

Splitting Tensile Strength

Figures 14 and 15 display the trend concerning the development of the splitting tensile strength of LFC. The splitting tensile strength rose visibly from the control up to the inclusion of 0.45% of OPPF. The trend of the growth in the splitting tensile strength of LFC with the inclusion of OPPF was attributed to the elasticity of the fibre, which can stretch and bond strongly with the cement matrix to avoid cracking [30]. Subsequently, the splitting tensile strength dropped when 0.60% of OPPF was added. For the 600kg/m^3 density, the highest splitting tensile strength was 0.21N/mm^2, which was at day-56 with the inclusion of 0.45% OPPF. The lowest splitting tensile strength was 0.09N/mm^2, which was the plain LFC at day-7. For the 1200kg/m^3 density, the highest splitting tensile strength was 0.78N/mm^2 at day-56 with the addition of 0.45% OPPF. The lowest splitting tensile strength was 0.32N/mm^2, which was the plain LFC at day-7. The splitting tensile strength of LFC attained in this investigation is about 60% of its flexural strength. As shown in Table 1, the elongation at break for mesocarp fibre is considered minimal (9.76%), resulting in high tensile strength [31]. Elongation at break expresses the ability of fibre to resist changes of shape without crack formation. Natural fibre such as oil palm fibre is more rigid, thus contributes to enhancing the splitting tensile strength [32]. LFC is known to have low tensile strength and brittle nature. Though, based on the data recorded in this study, the tensile strength was shown to increase due to the presence of OPPF. The increase of tension strength is due to the increase in toughness of concrete due to the presence of OPPF where 0.45% of fibre content addition enhances the increment of tensile strength in FC by promoting optimum pozzolanic reaction with OPC content, thus producing denser and stronger concrete.

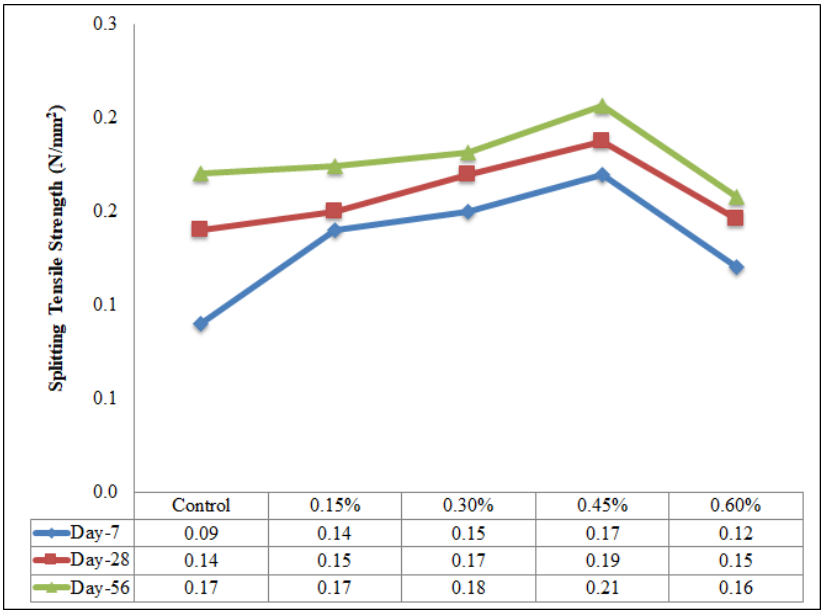

	Control	0.15%	0.30%	0.45%	0.60%
Day-7	0.09	0.14	0.15	0.17	0.12
Day-28	0.14	0.15	0.17	0.19	0.15
Day-56	0.17	0.17	0.18	0.21	0.16

Fig. 14 - Influence of different percentages of fibre on tensile strength of 600 kg/m^3 density LFC

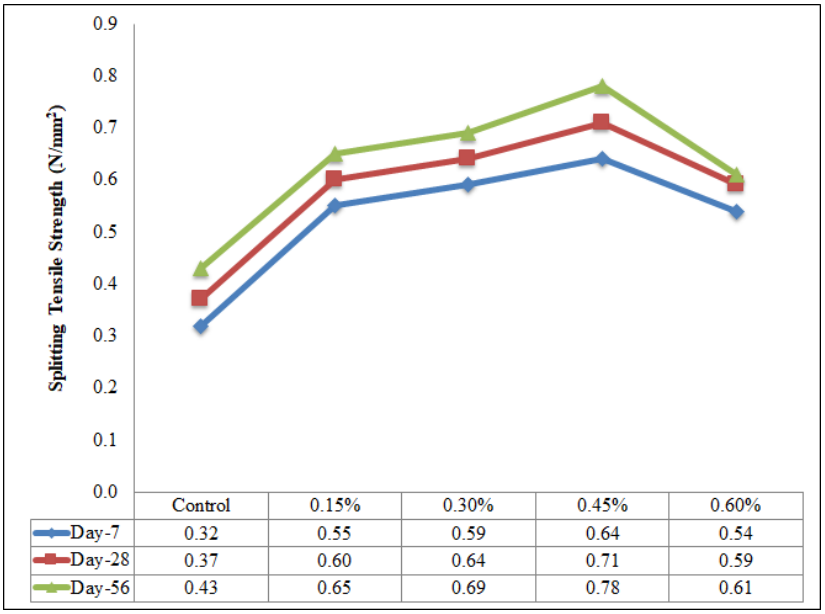

	Control	0.15%	0.30%	0.45%	0.60%
Day-7	0.32	0.55	0.59	0.64	0.54
Day-28	0.37	0.60	0.64	0.71	0.59
Day-56	0.43	0.65	0.69	0.78	0.61

Fig. 15 - Influence of different percentages of fibre on tensile strength of 1200 kg/m^3 density LFC

Figure 16 demonstrates the scanning electron microscopy result of fractured surface of LFC reinforced with OPPF under tensile load. It can be seen that fibre pull-out was little compared to fibre breakage. There was an effective transfer of tensile stress from one member to another in LFC composites for both densities considered in this research. There was also excellent interphase between the OPPF and the cementitious matrix of LFC. The inclusion of OPPF in LFC aided in bounding the LFC cementitious matrix in transverse direction, thus enhanced the internment effect and circuitously enhanced the tensile strength of LFC.

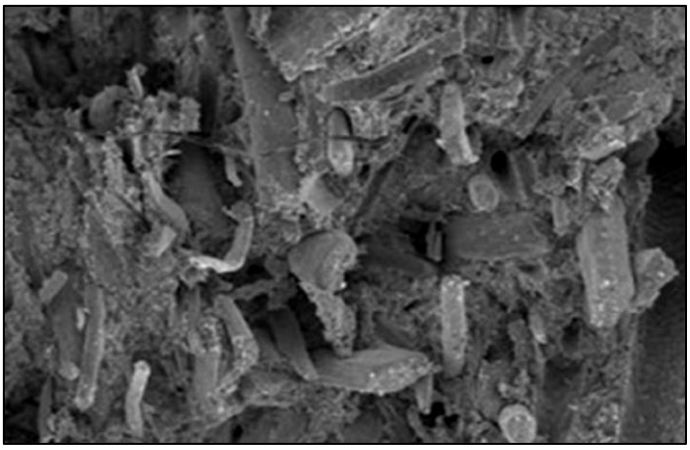

Fig. 16 - SEM image of fractured surface of 600kg/m^3 density LFC under tension

CONCLUSION

In the study, the mechanical properties with the addition of different proportions of OPPF into different densities of LFC were investigated. Two densities of LFC, 600kg/m^3 and 1200kg/m^3, were prepared and tested with five different percentages of OPPF added, which were 0%, 0.15%, 0.30%, 0.45% and 0.60%. The results show that the best outcomes, in terms of mechanical properties, were obtained with the 1200kg/m^3 density with the 0.45% addition of OPPF. This achieved the highest strength (compressive, flexural and splitting tensile), The OPPF helped to avoid the promulgation of cracks in the plastic state in the cement matrix when the load was applied.

REFERENCES

[1] Araya-Letelier G., Antico F.C., Carrasco M., Rojas P., García-Herrera C.M., 2017. Effectiveness of new natural fibres on damage-mechanical performance of mortar. Construction and Building Materials, vol. 152: 672-682.

[2] Mydin M.A.O., Phius A.F., Sani N.M., Tawil NM., 2014. Potential of Green Construction in Malaysia: Industrialised Building System (IBS) vs Traditional Construction Method. E3S Web of Conferences, vol. 3: 01009

[3] Liew K.M., Sojobi A.O., Zhang L.W., 2017. Green concrete: Prospects and challenges, Construction and Building Materials, vol. 156: 1063-1095

[4] Mydin M.A.O, Nawi, M.N.M., Munaaim M.A.C., Mohamad N., Samad, A.A.A., Johari I., 2018. Effect of steel fibre volume fraction on thermal performance of Lightweight Foamed Mortar (LFM) at ambient temperature. Journal of Advanced Research in Fluid Mechanics and Thermal Sciences, vol. 47(1): 119-126

[5] Hegyi A., Dico C., Catalan G., 2016. Construction sustainability with adobe bricks type elements. Urbanism, Architecture and Construction, vol. 7(2): 147-156

[6] Ardanuy M., Claramunt J., Toledo Filho R.D., 2015. Cellulosic fibre reinforced cement-based composites: A review of recent research. Construction and Building Materials, vol. 79: 115-128

[7] Othuman Mydin M.A., 2016. Evaluation of splitting tensile strength in plain and fibre-reinforced foamed mortar. Jurnal Teknologi, vol. 78(5): 413-419

[8] Serri E., Suleiman M.Z., Mydin M.A.O., 2014. The effects of oil palm shell aggregate shape on the thermal properties and density of concrete. Advanced Materials Research, vol. 935: 172-175

[9] Othuman Mydin M.A., Mohamed Shajahan M.F., Ganesan S., Sani N.M., 2014. Laboratory investigation on compressive strength and micro-structural features of foamed concrete with addition of wood ash and silica fume as a cement replacement. MATEC Web of Conferences, vol. 17: 01004

[10] Nechyporchuk O., Belgacem M.N., Bras J., 2016. Production of cellulose nanofibrils: A review of recent advances. Industrial Crops & Products, vol. 93: 2-25.

[11] Othuman Mydin M.A., 2015. Effect of silica fume and wood ash additions on flexural and splitting tensile strength of lightweight foamed concrete. Jurnal Teknologi, vol. 74(1): 125-129
[12] Othuman Mydin M.A., Potential of natural and synthetic fibres on flexural performance of foamcrete mortar, Jurnal Teknologi, vol. 78(5): 431-435
[13] Faruk O., Bledzki A.K., Fink H.P., Sain M., 2012. Biocomposites reinforced with natural fibres: 2000-2010. Progress in Polymer Science, vol. 37(11): 1552-1596.
[14] Jawaid M., Abdul Khalil H.P.S., 2011. Cellulosic/synthetic fibre reinforced polymer hybrid composites: A review, Carbohydrate Polymers, vol. 86(1): 1-18.
[15] Mydin M.A.O., Zamzani N.M., Ghani A.N.A., 2018. Effect of alkali-activated sodium hydroxide treatment of coconut fibre on mechanical properties of lightweight foamed concrete, in 3rd International Conference on Applied Science and Technology, vol. 5055512: 020108.
[16] Jiang D., Cui S., Xu F., Tuo T., 2015. Impact of leaf fibre modification methods on compatibility between leaf fibres and cement-based materials, Construction and Building Materials, vol. 94: 502-512.
[17] Wei J., Meyer C., 2016. Utilization of rice husk ash in green natural fibre-reinforced cement composites: Mitigating degradation of sisal fibre. Cement and Concrete Research, vol. 81: 94-111.
[18] Mydin M.A.O., 2017. Preliminary studies on the development of lime-based mortar with added egg white. International Journal of Technology, vol.8(5): 800-810
[19] Othuman Mydin, M.A., Zamzani, N.M., Ghani, A.N.A., 2019. Experimental data on compressive and flexural strengths of coir fibre reinforced foamed concrete at elevated temperatures, Data in Brief, vol. 25, 104320
[20] Mydin M.A.O., Musa M., Ghani A.N.A., 2018. Fiber glass strip laminates strengthened lightweight foamed concrete: Performance index, failure modes and microscopy analysis. AIP Conference Proceedings, vol. 2016: 020111
[21] Mohan N.H., Ammayappan L., Sarma D.K., Debnath S., Tamuli M.K., 2017. Characterization of thermal properties of pig hair fibre, Journal of Natural Fibres, vol. 14(4): 1-7.
[22] Ganesan S., Othuman Mydin M.A., Sani N.M., Che Ani A.I., 2014. Performance of polymer modified mortar with different dosage of polymeric modifier. MATEC Web of Conferences, vol. 15: 01039
[23] Bentur A., Mindess S., 2006. Fibre Reinforced Cementitious Composites. CRC Press, Second edition, New York, p. 48-51
[24] Thakrele, M. H., 2014. Experimental study on foam concrete. International Journal of Civil, Structural, Environmental and Infrastructure Engineering Research and Development, 4(1), 145-158..
[25] Othuman Mydin M.A., 2016. Experimental investigation of axial compressive strength of lightweight foamed concrete with different additives, Jurnal Teknologi, vol. 78(5): 463-469
[26] Othuman Mydin M.A., Mohamad N., Johari I., Abdul Samad A.A., 2018. Determination of bending and axial compression young's modulus of cellular mortar exposed to high temperatures, International Journal of Engineering and Technology (UAE), vol. 7(2): 99-102
[27] Suhaili S.S., Mydin M.A.O., 2020. Potential of stalk and spikelets of empty fruit bunch fibres on mechanical properties of lightweight foamed concrete, International Journal of Scientific and Technology Research, vol. (3): 3199-3204
[28] Musa M., Othuman Mydin M.A., Abdul Ghani A.N., 2019. Thermal properties of foamed concrete with addition of empty fruit bunch (EFB) fiber. International Journal of Innovative Technology and Exploring Engineering, vol. 8(10): 4662-4670
[29] Othuman Mydin M.A., 2016. Assessment of thermal conductivity, thermal diffusivity and specific heat capacity of lightweight aggregate foamed concrete. Jurnal Teknologi, vol. 78(5): 477-482
[30] Islam S.M., Hussain R.R., Morshed M.A.Z., 2012. Fibre-reinforced concrete incorporating locally available natural fibres in normal- and high-strength concrete and a performance analysis with steel fibre-reinforced composite concrete. Journal of Composite Materials, vol. 46(1): 111-122.
[31] Ali M., Liu A., Sou H., Chouw N., 2012. Mechanical and dynamic properties of coconut fibre reinforced concrete, Construction and Building Materials, vol. 30: 814-825.
[32] Othuman Mydin M.A., Mohd Zamzani N., 2018. Coconut fiber strengthen high performance concrete: Young's modulus, ultrasonic pulse velocity and ductility properties. International Journal of Engineering and Technology (UAE), vol. 7(2): 284-287

CIVIL ENGINEERING JOURNAL

Article no. 48

THE CIVIL ENGINEERING JOURNAL 3-2021

STUDY ON SPATIAL STRESS EFFECT OF PC CONTINUOUS THIN-WALLED BOX GIRDER BRIDGE

Shulin Zhou[1], Honglei Zhang[2]

1. *Highway Development Center of Guangxi Zhuang Autonomous Region, Maintenance Department, Nanning, No.3 Yunjing Road, PR of China; 317880950@qq.com*
2. *Beijing Xinqiao Technology Development Co., Ltd, Bridges and Tunnels Department, Beijing, No.8 Xitucheng, PR of China; Hongleizhang_Xq@163.com, 765310906@qq.com*

ABSTRACT

In order to study the influence of spatial stress effect and shear lag effect on the cracking of PC continuous thin-walled box girder bridge, a spatial model was established by using ANSYS finite element software to analyze the internal stress distribution of the bridge. The test results are compared with the analysis results of spatial model and plane link system model through the load test of real bridge. The results show that the longitudinal stress is evenly distributed along the width direction, which means that the spatial stress effect and the shear lag effect have little influence on the downdeflection of the bridge. The shear lag coefficient at the longitudinal axis of midspan bottom plate and the intersection of bottom plate and web are larger than other positions, which is most likely to produce cracks caused by stress concentration and should be strengthened here in practical engineering. The results of load test show that the results of spatial finite element analysis are more reliable than those of plane link system calculation, and the design and construction based on the results of spatial finite element analysis is safer.

KEYWORDS

Thin-walled box girder bridge, Spatial stress effect, Shear lag effect, Load test

INTRODUCTION

The PC continuous box girder has the advantages of strong span capacity, large structural stiffness, beautiful appearance, smooth deck and easy maintenance, and is widely used in bridge structures with large span [1]. However, the section of box girder belongs to thin-walled structure. According to the investigation, the prestressed continuous thin-walled box girder bridge has cracked in different degrees after a period of operation [2]. Therefore, it needs to be equipped with a lot of structural reinforcement. There are many reasons that affect the crack generation, such as prestress spatial distribution, shear lag effect, prestress loss, overload, etc. Therefore, appropriate space analysis theory of box girder should be adopted to analyze the crack resistance of box girder, focusing on analyzing the spatial stress effect of the structure, so as to reflect the spatial stress effect of box girde. Then we can accurately understand the crack resistance of box girder structure.

The spatial stress analysis methods of PC thin-walled box girder bridges can be divided into two categories: analytical method and numerical method. Based on the analytical method and from different perspectives, some scholars have proposed such approximate calculation methods as energy variation method, generalized coordinate method, analogy beam method and frame

analysis method for the calculation and analysis of torsion and distortion of box girder [3-5]. The calculation process of these methods is relatively complicated, and the calculation accuracy depends on the numerical solution accuracy of the differential equations. So, they are mostly applied to the research of the box-girder bridge with constant section, as the theoretical analysis results of the shear lag effect of the box girder with variable section are relatively few [6-7]. With the development of electronic computers, finite element method is very common in the analysis of box girder [8-12], such as Midas Civil, Adina, ANSYS and other structural linear and nonlinear finite element analysis software. With the help of computer finite element analysis, all the stresses on the box section, such as longitudinal bending stress, torsional warping stress, distorted warping stress, distorted transverse stress, shear lag and local load stress, can be obtained. By analyzing the data and results, researchers can accurately know the spatial stress distribution, magnitude and structural deformation of the components.

In this paper, a PC continuous thin-walled box girder bridge is selected as the research object. The finite element analysis software ANSYS is used to analyze the effect of spatial stress and shear lag on the deflection and cracking of the bridge. Through load tests, the fitting degree of spatial finite element model, plane beam analysis and test results is compared, so as to further verify the validity of spatial finite element model to analyze the spatial stress effect of PC continuous thin-walled box girder bridge. It provides reference for engineering practice.

BACKGROUND

The span of the bridge is 35 m+60 m+90 m+60 m+35 m, and the width combination is 0.75 m+10.5 m+0.75 m. The box girder is prestressed in longitudinal, horizontal and vertical directions, and the tensioning stress is 1290 MPa. Lateral view of the bridge is shown in Figure 1 and Figure

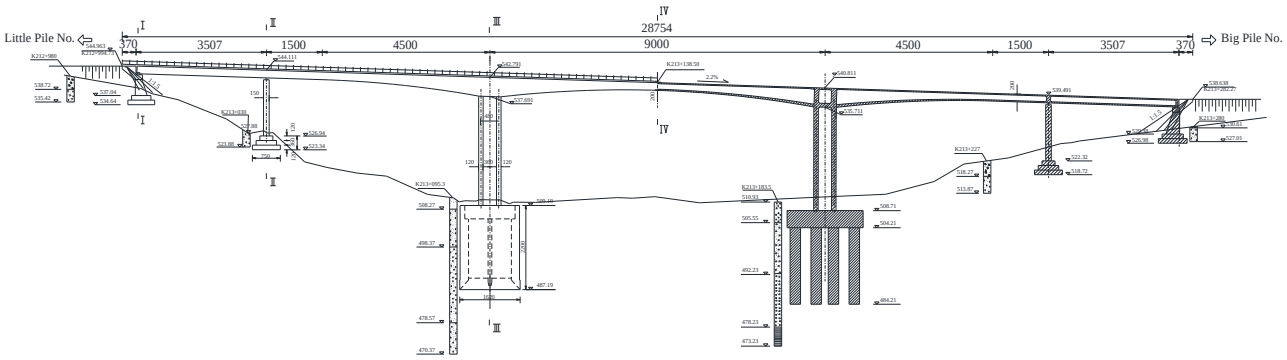

Fig. 1 – Lateral view of the bridge (unit: cm)

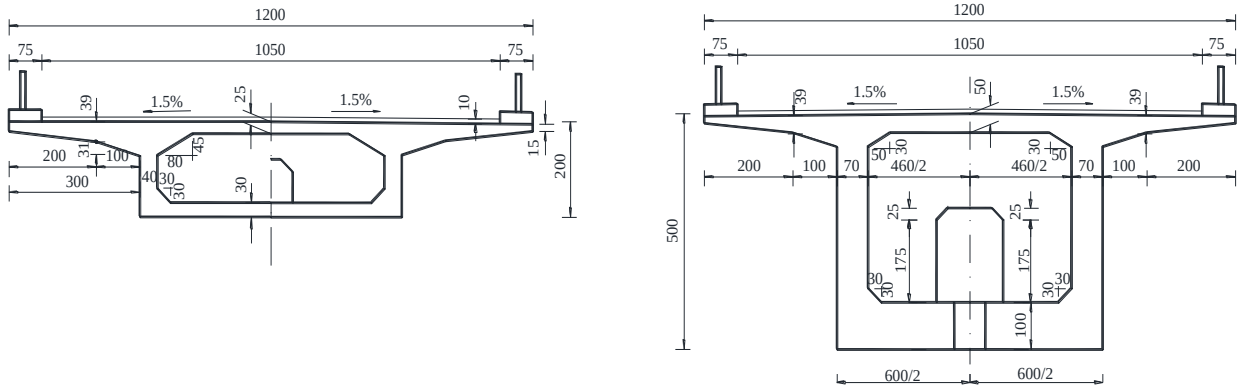

(a) Ⅰ, Ⅱ, Ⅳ *(b) Ⅲ*

Fig. 2 – Cross-section of the bridge (unit: cm)

FINITE ELEMENT MODEL ANALYSIS

Using ANSYS finite element software to establish the space solid finite element model, reinforced concrete structure using 8-node solid element SOLID 65, can well simulate the Williams-Warnke strength theory based on the concrete three- direction force of the nonlinear response. Link8 unit is selected for prestressing tendon. Separate model is used to simulate the prestress in the model, and the longitudinal, vertical and transverse prestress tendons are separately modelled. Since the linear shape of the bottom flange is a quadratic parabola and there are many control nodes, this paper adopts the bottom-up modelling method, namely K-V and K-L modes. Considering the symmetry of the structure and load of the bridge, the model of the semi-full bridge is selected, which cannot only save the number of units and nodes, but also greatly save the calculation time. The model consists of 120,490 units and 165,435 nodes. In the model, X coordinate represents the transverse bridge direction, Y coordinate represents the vertical bridge direction, and Z coordinate direction is the vertical bridge direction. The box girder concrete bulk density is calculated by 26kN/m^3, the guardrail load is calculated by 24kN/m.

According to the requirements of design specifications [13], the temperature load and the moving load were loaded according to the worst load condition of the mid-span bending moment of the main span. Working load includes deadweight, deck pavement weight, prestress, temperature gradient and moving load. The finite element model is shown in Figure 5.

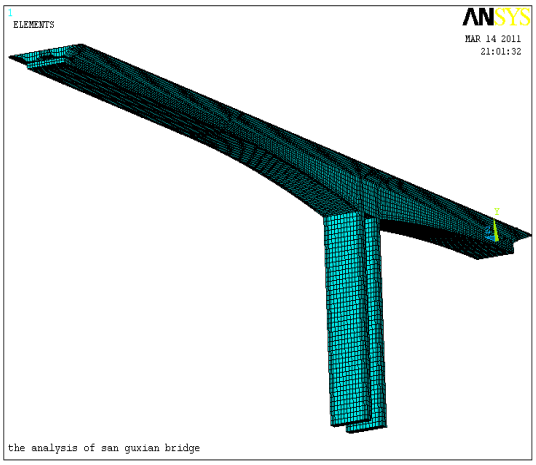

Fig. 3 – Finite element model of bridge

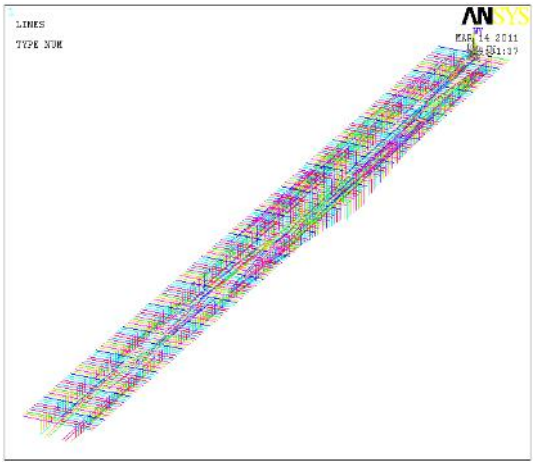

Fig. 4 – Finite element model of steel strand

ANALYSIS OF SPATIAL STRESS EFFECT

LONGITUDINAL STRESS

The calculation results of the longitudinal stress of the bridge are shown in Figure 5 – Figure 8. The top flange is under pressure as a whole, and the longitudinal stress increases from the beam end to the middle of the main span. The longitudinal stress of the top flange is distributed evenly along the width direction, and the difference is basically controlled within 0.8 MPa.

The longitudinal stress of the bottom flange is basically compressive stress, and the stress gradually increases from the pier to both sides of the longitudinal bridge. The longitudinal stress of bottom flange is evenly distributed along the width of the main span, but fluctuates greatly in the middle of the side span and the secondary side span, especially near the web. The transverse difference of other sections is basically within 1.0 MPa.

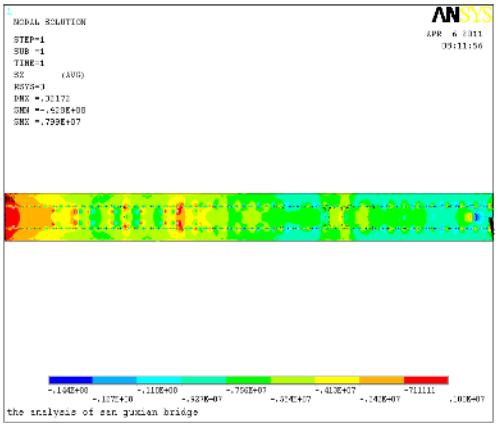

Fig. 5 – Top flange stress nephogram

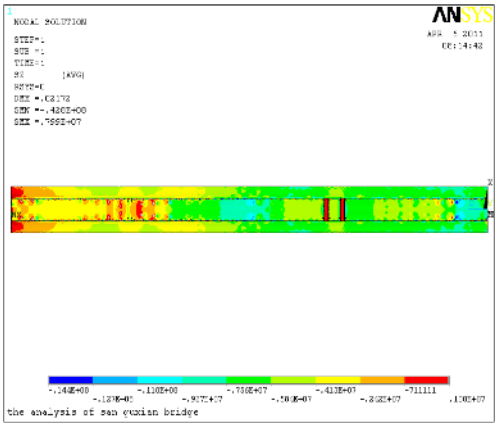

Fig. 6 – Bottom flange stress nephogram

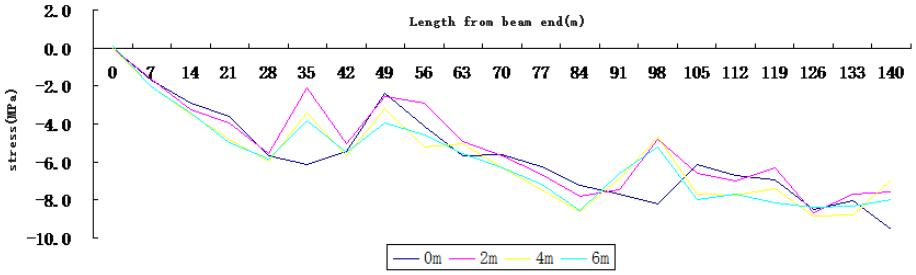

Fig. 7 – Transverse distribution of longitudinal stress along the top flange (0,2,4,6 represents the distance from the longitudinal axis)

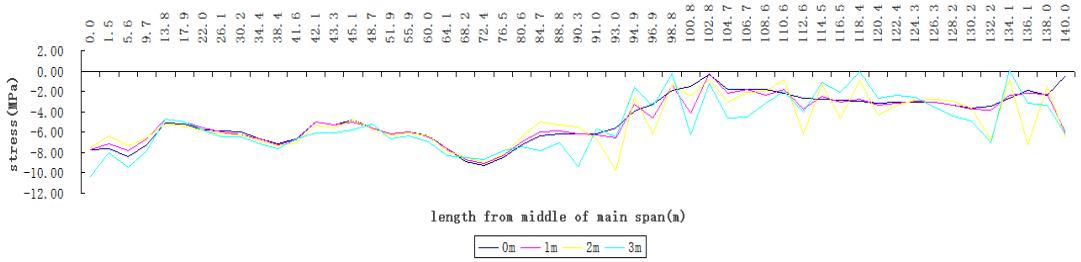

Fig. 8 - Transverse distribution of longitudinal stress along the bottom flange

PRINCIPAL STRESS

The calculation results of principal stress are shown in Figure 9 – Figure 12. The principal stress of top flange is basically between -0.3 MPa ~2.5 MPa, except for the prestressed anchorage point with stress concentration. The stress distribution along the flange slab is more uniform. At the main pier, the stress changes within the range of webs, the maximum is about 2.5 MPa. The lateral distribution of principal stress along the bridge is that the longitudinal axis increases laterally. The principal stress range of bottom flange is -1.0 MPa~6.5 MPa. Due to the influence of shear lag, the principal stress decreases gradually from the longitudinal axis of the bottom flange to the web.

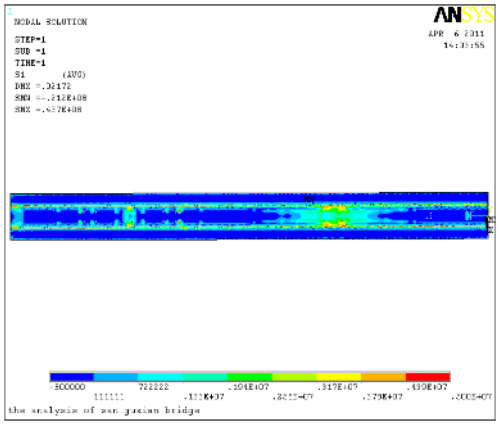

Fig. 9 – Top flange principal stress nephogram

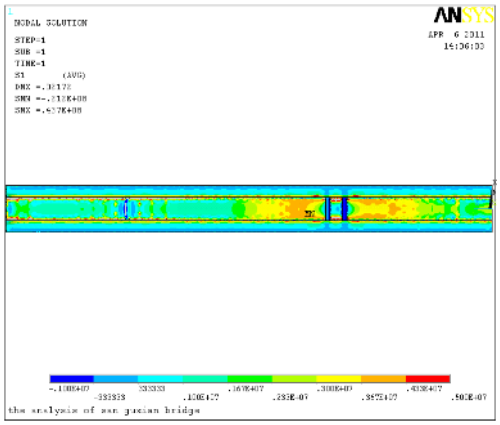

Fig. 10 – Bottom flange principal stress nephogram

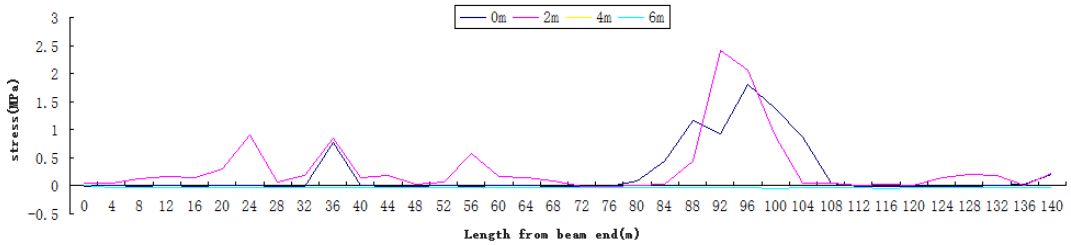

Fig. 11 – Transverse distribution of principal stress along the top flange

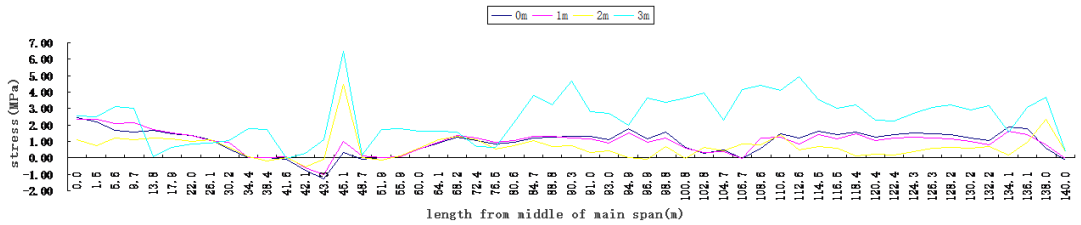

Fig. 12 – Transverse distribution of principal stress along the bottom flange

SHEAR LAG EFFECT

In order to describe the influence of shear lag effect of box girder, the concept of shear lag coefficient is introduced in the project [14-15].

$$\lambda = \frac{real\ stress}{stress\ calculated\ according\ to\ elementary\ beam\ theory}$$

Under the effect of shear lag, the shear force transmits lag from the web to the flange slab, resulting in the uneven lateral distribution of normal stress. The actual longitudinal stress of the flange slab near the web is greater than the elementary beam theory calculation, which is called "positive shear lag effect". On the contrary, it is called "negative shear lag effect".

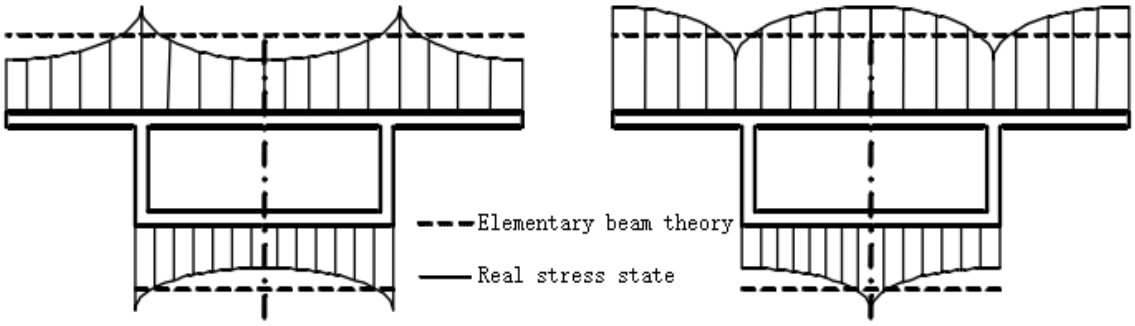

Fig.13 - Positive shear lag effect *Fig.14 - Negative shear lag effect*

Figure 15 and Figure 16 respectively show the distribution of longitudinal stress of the top and bottom flange in the middle of the main span along the transverse bridge direction. Figure 17 and Figure 18 are respectively longitudinal stress distribution diagrams of the top and bottom flange at main pier along the transverse bridge direction. It can be concluded that the top and bottom flange are in a state of compression, and the longitudinal stress distribution along the transverse is not uniform. The stress difference of the top flange at the middle of the main span is about 5.1 MPa, and that of the bottom flange is about 13.0 MPa. At the main pier, the stress difference of the top flange is 5.6 MPa, and that of the bottom flange is about 5.2 MPa.

Figure 19 and Figure 20 respectively show the shear lag coefficients of the top and bottom flange of the main span at middle. Figure 21 and Figure 22 show the top of the main pier top and bottom flange, respectively. It can be seen that the shear lag effect of these sections is positive. The shear lag coefficient of the top flange at midspan is between 0.7 and 1.7, and that of bottom flange is between 0.85 and 1.6. As the main pier, the shear lag coefficient of top flange is between 0.8 and 1.65, and that of bottom flange is between 0.8 and 1.82.

In general, under the action of deadweight and prestress, the transverse difference of the longitudinal stress of the key sections and the dispersion degree of the shear lag coefficient is larger. Compared with the top flange, the dispersion degree of the shear lag coefficient in the same section is larger than that of the bottom flange.

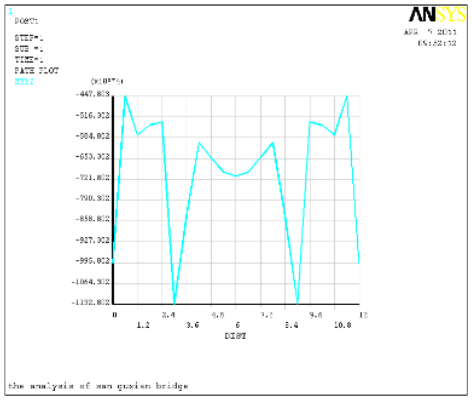

Fig. 15 - Longitudinal stress along the top flange of midspan

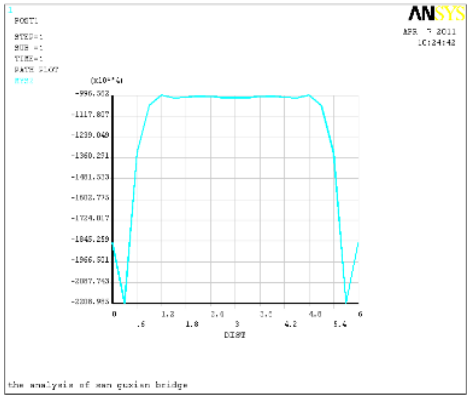

Fig. 16 - Longitudinal stress along the bottom flange of midspan

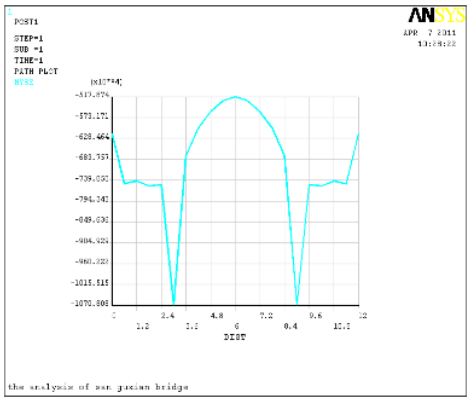

Fig. 17 - Longitudinal stress along the top flange of main pier

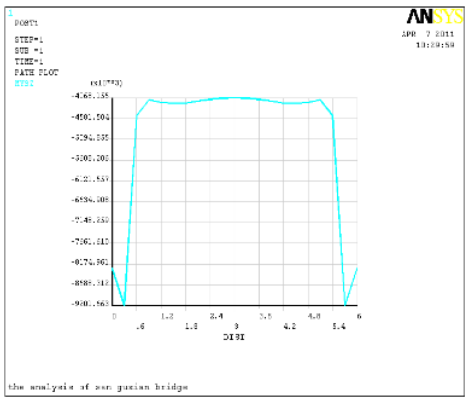

Fig. 18 - Longitudinal stress along the bottom flange of main pier

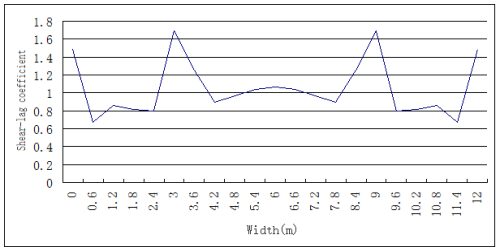

Fig. 19 - Shear-lag coefficient along the top flange of midspan

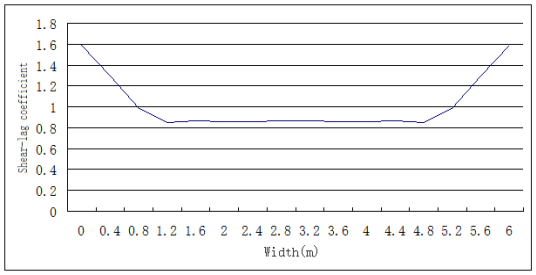

Fig. 20 - Shear-lag coefficient along the bottom flange of midspan

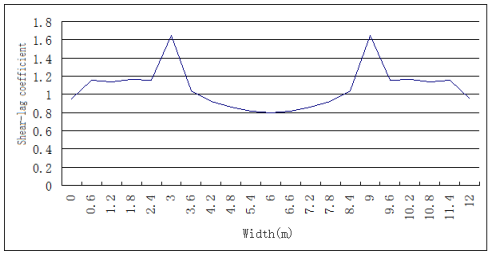

Fig. 21 - Shear-lag coefficient along the top flange of main pier

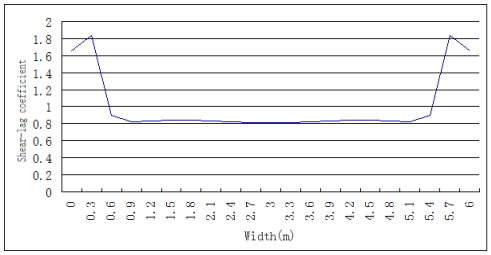

Fig. 22 - Shear-lag coefficient along the bottom flange of main pier

LOAD TEST ANALYSIS

According to the requirements of design specifications [13], the maximum effect of the combination of bending moment and shear force is considered in the test condition. The measuring points arrangement is shown in Figure 23 and Figure 24.

(a) *(b)*

Fig. 23 - Measuring points arrangement of longitudinal stress

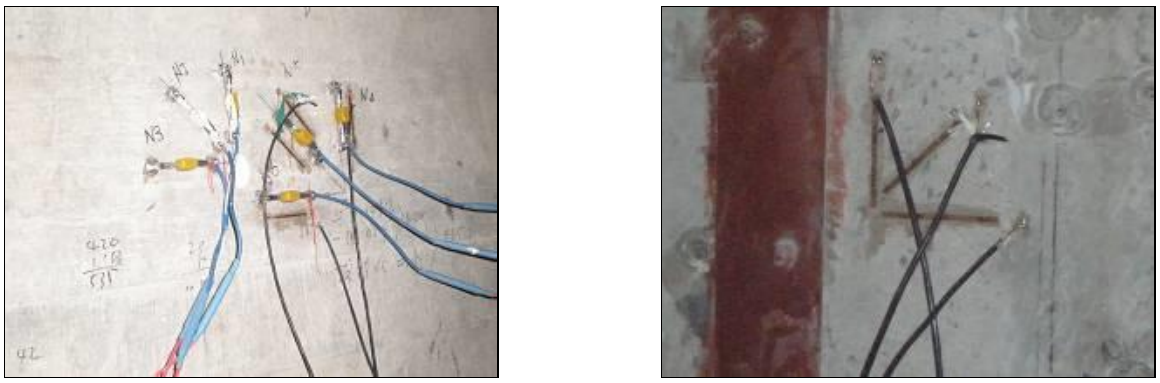

(a) (b)

Fig. 24 - Measuring points arrangement of principal stress

The test results are shown in the tables and figures below. It can be seen that the theoretical calculation of longitudinal stress and principal stress have the same law as the test results, and the results are basically consistent with less error. In general, the results of spatial calculation are smaller than those of plane calculation. The maximum longitudinal stress difference is 0.35MPa, and the principal stress is 0.34 MPa. The spatial calculation are closer to the test results, which indicates that the spatial finite element model established in this paper accords with the practice and the theoretical calculation results are reliable. At the same time, the calculation of the spatial model is slightly larger than the test results, so the calculation is somewhat safe.

Tab.1 - Test results of longitudinal stress (unit: MPa)

Test position			Test result	Plane calculation	Spatial calculation	Plane / Spatial
Negative moment for pier 1	1	Top flange	0.17	0.69	0.44	1.57
	2	Bottom flange	-0.86	-1.35	-1.12	1.21
Negative moment for pier 2	3	Top flange	0.35	0.80	0.72	1.11
	4	Bottom flange	-0.41	-0.70	-0.51	1.37
Midspan for span 2	5	Top flange	-0.63	-1.04	-0.71	1.46
	6	Bottom flange	1.27	1.74	1.39	1.25
Midspan for main span	7	Bottom flange	1.21	1.84	1.62	1.14
	8	Web	1.01	1.66	1.56	1.06

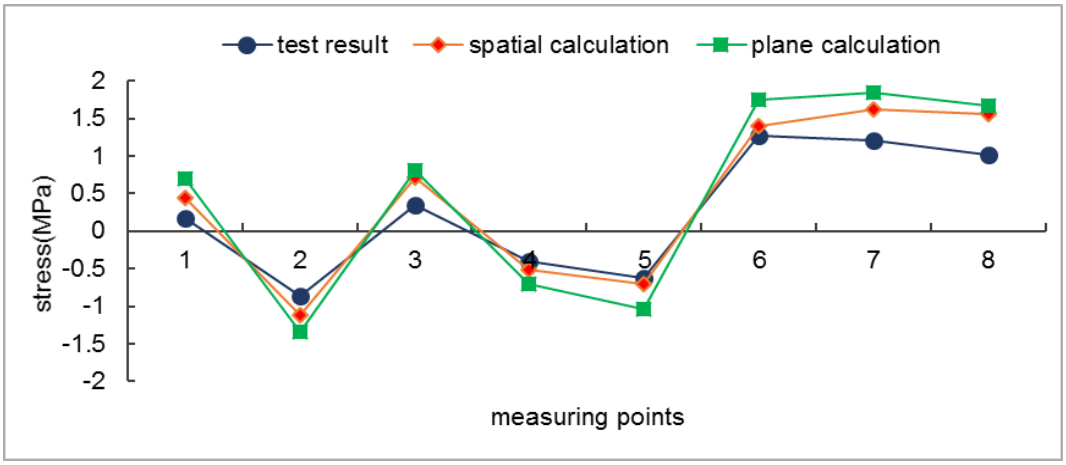

Fig. 25 - Longitudinal stress line chart

Tab. 2 - Test results of principal stress (unit: MPa)

Test position	Measuring points	Strain（με）			Test result	Plane calculation	Spatial calculation	Plane /Spatial
		0°	45°	90°				
5# segment for span 2	1	12.40	6.40	20.80	0.95	1.17	1.38	1.18
	2	30.10	17.2	-23.00	1.15	1.38	1.52	1.10
Top for pier 2	3	0.41	1.47	-5.50	0.18	0.22	0.29	1.32
	4	3.70	-1.50	-2.20	0.35	0.42	0.49	1.17
5# segment for main span	5	5.70	-49.40	-33.20	0.93	1.24	1.58	1.27
	6	-20.40	-70.90	-30.30	0.71	1.02	1.32	1.29

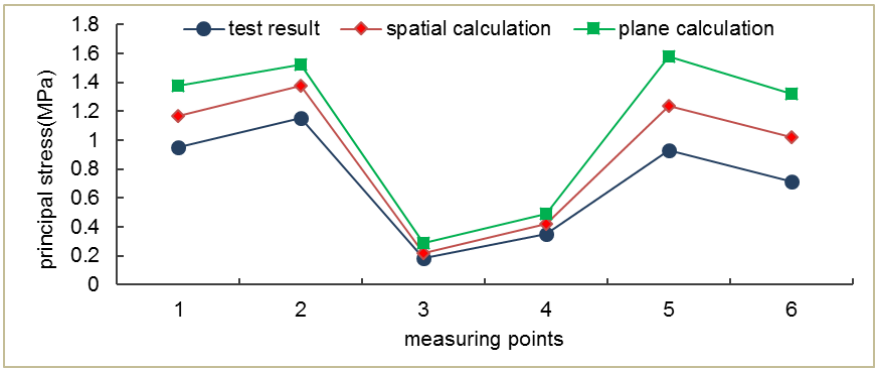

Fig.26 - Principal stress line chart

CONCLUSION

Based on the research results, the following conclusions can be drawn:

(a) The top and bottom flange are under longitudinal compression, and the longitudinal stress is evenly distributed along the width direction, which indicates that the spatial stress effect and shear lag effect have little influence on the down deflection of the bridge.

(b) The stress at the main pier within the webs is abrupt, and it is easy to crack. Due to the influence of shear lag effect, the main stress from the longitudinal axis of the bottom flange to the web gradually decreases, and the stress concentration occurs at this place, where transverse cracks are more likely to occur than both sides.

(c) The top and bottom flange of the main span and the main pier are positive shear lag effect. The shear lag coefficient of the top flange at midspan is between 0.7 and 1.7, and that of bottom flange is between 0.85 and 1.6. As the main pier, the shear lag coefficient of top flange is between 0.8 and 1.65, and that of bottom flange is between 0.8 and 1.82. Under the action of deadweight and prestress, the longitudinal stress of box girder is distributed unevenly in the transverse direction, and the dispersion degree of shear lag coefficient is larger in top flange than that in bottom flange.

(d) The spatial calculations are closer to the test results than those of plane calculations, the maximum longitudinal stress difference is 0.35MPa, it indicates that the spatial finite element analysis is more practical and reliable. Moreover, the spatial calculations analysis are generally larger than the test results, so it is safe to carry out design and construction according to the spatial finite element analysis.

(e) The shear lag coefficient reaches its maximum value at the intersection of the top and bottom flange with web, and decreases to both sides. In the design and construction stage, the cracking and bending situation of this position should be fully considered, and the strengthening treatment should be carried out here. And reasonable arrangement of prestressed and structural reinforcement to prevent cracks caused by stress concentration. For bridges that have been cracked and flexed down, external prestress or steel plate can be used to reinforce them. Cracks should be treated before reinforcement. If the number of external prestressing steel strand is numerous, the scheme of dispersed arrangement along the top and bottom flange can be adopted.

REFERENCES

[1] Guo JM. Design Theory of Box Girder[M]. Beijing: China Communications Press, 1999.
[2] Peng W, Xing HY, Ke SG. Study on Cracking Control of PC Continuous Box Girder Bridges[J]. Journal of Zhejiang Universitr of Technology, 2003, 31(1): 22-27.
[3] Li Z, Nie JG, Ji WY. Positive and Negative Shear Lag Behaviors of Composite Twin-Girder Decks with Varying Cross-Section[J]. Science China Technological Sciences, 2017, 60(1): 116-132.
[4] Lin PZ, Liu FK, Ji W, et al. Analysis on Shear Lag Effect of Concrete Box Beam by Variation Principle[J]. Journal of The China Railway Society, 2013, 35(2): 93-98.
[5] Guo ZW, Li LJ, Zhang JB. Theoretical Analysis for Shear-lag Effect of Variable Box Section Cantilever Girder Based on Bar Simulation Method[J]. China Civil Engineering Journal, 2019, 52(8): 72-80.
[6] Cambronero-Barrientos F, Díaz-Del-Valle J, Martínez-Martínez JA. Beam Element for Thin-Walled Beams with Torsion, Distortion and Shear Lag[J]. Engineering Structures, 2017, 143: 571-588.
[7] Ma C, Liu SZ, Wu MQ. Matrix Analysis of Composite Box Girder with Corrugated Steel Webs Considering Shear Deformation and Shear Lag Effect[J]. China Journal of Highway and Transport, 2018, 31(3): 80-88.
[8] Feng HY. The Analysis of Space Stress and Shear Lag Effect of Prestressed Concrete Thin-Walled Box Girder Bridge[D]. Harbin: Northeast Forestry University, 2011.
[9] Zhao H, Gou HY, Ni YS. Shear Lag Effect of Corrugated Steel-Concrete Composite Multi-Box Cable-Stayed Bridge[J]. Journal of South China University of Technology (Natural Science Edition), 2020, 48(7): 93-103.
[10] Xu D, Ni YS, Zhao Y. Analysis Corrugated Steel Web Beam Bridges Using Spatial Grid Modeling[J]. Steel and Composite Structures, 2015, 18(4): 853- 871.
[11] Zhang, Zhongwen, Li, et al. Effects of the shear lag on longitudinal strain and flexural stiffness of flanged RC structural walls[J]. Engineering Structures, 2018.
[12] Lin PZ,Sun LX,Yang ZJ, et al. Research on Shear Lag Effect of Twin-Cell Box Girders[J]. Journal of Railway Engineering Society, 2014(1): 59-60.
[13] CCCC Highway Consultants Co., Ltd, Specifications for Design of Reinforced Concrete and Prestressed Concrete Highway Bridges and Culver（JTJ 023-85）[M]. Beijing: China Communications Press, 1985.
[14] Tan D, Li X. Analysis of Wide Box Gird's Shear-lag Effect Based on Energy Method in Single-Cable-plane Cable Stayed Bridge[J]. IOP Conference Series Materials Science and Engineering, 2020, 768: 032-044.
[15] Duan HJ, Zhao RD. Segment Element of Thin-Walled Curved Box Girder by Spatial Analysis[J]. China Civil Engineering Journal, 2004, 37(12): 1-5.

CIVIL ENGINEERING JOURNAL

Article no. 49

THE CIVIL ENGINEERING JOURNAL 3-2021

EVALUATION OF EFFECTIVE POLYMER FIBRE LENGTH ON ENERGY ABSORPTION CAPACITY OF REINFORCED BEAMS BY EBR AND NSM METHODS

Komeyl Karimi-Moridani

Department of Civil Engineering, Lahijan Branch, Islamic Azad University, Lahijan, Iran; karimi.k@srbiau.ac.ir

ABSTRACT

This study presents a comparison of two methods used for retrofitting Reinforced Concrete (RC) beams, namely, the Externally Bonded Reinforcement (EBR) and the Near-Surface Mounting (NSM) methods. A parametric analysis was carried out using variables such as the retrofitted, the retrofitting method (EBR and NSM), and the thickness of the Carbon Fibre-Reinforced Polymer (CFRP) sheets. To achieve this goal, the finite element method and ABAQUS software were employed. An un-retrofitted beam was also simulated as the control specimen for comparison. Beam responses were compared through load–displacement and energy absorption capacity diagrams. Results show that the higher energy absorption capacity in all CFRP-retrofitted RC beams, which was 1.69–5.54 times higher than in un-retrofitted beams. Also, when half the length of the beam span is reinforced with a CFRP sheet, the entire beam assembly with CFRP participates in the bearing. In this situation, beam cracking occurs with a delay and leads to an increased energy absorption capacity of the beam. As a result, the energy absorption capacity of the beam, in this case, was less than that obtained in the previous one where half of the span of the beam was retrofitted.

KEYWORDS

Retrofitting, Externally Bonded Reinforcement (EBR) method, Near-urface Mounting (NSM) Method, Finite Element Method, RC beam

INTRODUCTION

Retrofitting reinforced concrete structure is essential due to the increased applied structural loads during operation, structural damage or destruction, and potential shortcomings in the design or construction of the structure [1,2]. Furthermore, because of the age of many historical buildings, monuments, and strategic buildings, and the fact that their potential collapse would inflict an enormous burden on the national economy, retrofitting has become a great interest to civil engineers today. On the other hand, the lower life expectancy of the newly-built structures in harsh climates has led engineers to substitute the incorporated materials with new ones [3].

Fig. 1 – FRP sheets bonded to the external surface of RC beams

Corrosion of the steel used inside reinforced concrete structures, the heavyweight of steel-reinforced structures, and the lower resistance of steel against acids and bases are among the disadvantages that can be enumerated for steel-reinforced concrete structures. For this reason, civil engineers in the 1980s turned to fibre-reinforced polymers (FRPs) for reinforcing concrete structures. Of the methods using FRPs, two are more prominent: (1) the EBR method which involves bonding FRP sheets to the external surface of a structure (Figure 1), and (2) the NSM method which is based on placing reinforcing materials along the grooves opened into the beam surface (Figure 2). In the NSM method, FRP straps are placed inside the grooves opened into the concrete surface, and subsequently, epoxy is used to provide a strong bonding between the FRP straps and the concrete [4]. The present study aimed to use the finite element method to study the effect of the effective FRP length on the energy absorption capacity of concrete beams reinforced through the EBR and the NSM methods. To this end, several RC beams were simulated using the finite element analysis by ABAQUS to examine the effect of FRP sheets and the role they can play in improving the flexural behaviour of these beams.

Fig. 2 – Use of FRP composites in surface grooves of a beam by the NSM method

Numerous studies have been conducted so far on retrofitting reinforced concrete buildings, a number of the most important are referred below. Abdoljalil (2014) studied the behaviour and performance of deep RC beams with openings retrofitted with CFRP linings. To this end, eight RC beams with external CFRP linings were tested. Several parameters were examined including the layout of the CFRP linings at different positioning angles inside the beam. The results of this experimental study showed that the use of externally attached CFRP straps is not only helpful in increasing the ultimate shear capacity but also in limiting the width of shear cracks, thus increasing the stiffness of deep RC beams with openings [6]. In another experimental study, Kharatmol et al. (2014) used CFRPs to retrofit RC beams. They also compared the retrofitted beams with un-retrofitted RC beams in their load-bearing capacity, as well as ductility, and evaluated the effects of

such parameters as fibre thickness and fibre layout on the beam performance. According to their results, since CFRP linings can significantly increase the tensile strength of concrete, they can be effectively added to the tensile part of RC beams to improve their load-bearing capacity [7]. In their experimental study, Mofidi et al. (2015) used the NSM method for retrofitting RC beams with polymer composites and studied the behaviour of these beams in terms of their shear strength. To this end, six full-scale T-shaped RC beams (span= 4.52m) were built and subjected to incremental loading to examine the respective effects of such parameters as FRP rebars (by the NSM method), steel stirrups, and reinforcement ratio. According to their results, the steel stirrups used alongside the FRP rebars mounted near the concrete surface did not deteriorate the performance of any of the abovementioned elements [8]. In another experimental study by Tahsiri et al. (2015), the respective behaviours of RC beams retrofitted with FRP sheets and with steel jackets were compared and the respective characteristic of both these beam groups duly explained [9]. In the experimental study conducted by Khalifa (2016), six RC beams were retrofitted with CFRP rods buried in the concrete surface and their performance under flexural loading evaluated [10]. Ceroni (2010) experimentally examined FRP-retrofitted RC beams. To this end, FRP layers were used to retrofit the RC beams by the NSM method before the beams were subjected to uniform and cyclic loadings. A full comparison in terms of beam failure was made in this study between the obtained theoretical and experimental results [11]. Chen et al. (2018) studied experimentally the flexural behaviour of RC beams retrofitted with U-shaped basalt fibre linings. To this end, they conducted the three-point flexural loading test and then compared the failure modes and the structural responses obtained for the retrofitted beams with those obtained for the un-retrofitted beam. In addition, the formula used for predicting the flexural behaviour of FRP-retrofitted beams (in two cases: CFRP-retrofitted beams and GFRP[1]-retrofitted beams) using basalt fibres was evaluated [12]. Carlos et al. (2018) studied the flexural behaviour of beams retrofitted with CFRP linings against the conditions imposed by fire. The main objective of this study was to evaluate the behaviour of retrofitted beams in response to the heat generated by a fire. Fire-resistance tests were conducted by spraying vermiculite-perlite, Portland cement, and expansive clay over the specimens. The test beams were also placed on a concrete slab so that their circumferential interactions could be correctly simulated. The results of this study showed that the beams covered with the mentioned protective materials, while maintaining their robustness, could withstand fire for a longer time. It was also found that the concrete slab placed around the beams influenced the way heat was applied to the beams as well as the mechanical response of the beams [13]. Haville et al. (2018) used the nonlinear finite element method to study the shear strength of CFRP-retrofitted RC beams under unsymmetrical loading, comparing their simulation results with experimental results. According to their results, the type of applied load has a significant influence over the response of beams retrofitted with CFRP rods [14]. In an experimental study, Reddi (2018) compared the behaviour of the beams retrofitted with CFRP rods to the behaviour required or these beams in the relevant retrofitting codes. To this end, four RC beams were duly made and exposed to the four-point loading conditions. According to the results, retrofitting an RC beam with CFRP sheets could increase the load-bearing capacity of the beam by 23% at most. The experimental results obtained in this study were also in good agreement with the theoretical results obtained in the relevant construction codes [15]. In another study, experimental results and numerical analyses performed in the past showed that the failure load in RC beams reinforced with EBR could be influenced by the effect of the loading pattern [16].

[1] Glass-reinforced plastic

THE FRAMEWORK OF THE PRESENT STUDY

As mentioned in the introduction, the use of FRP sheets using the EBR technique is applied to increase the flexural capacity of reinforced concrete beams. It assumed the EBR technique is not subject to physical damage, fire, temperature variation, and ultraviolet rays. Also, the NSM technique was introduced for increasing the flexural strength of reinforced concrete beams. Several studies have shown that the use of global externally connected CFRP sheets can increase the final shear capacity and limit the width of the shear cracks. The studied variables included: (1) method of attaching the CFRP strips to the beam (by the EBR and NSM methods); (2) thickness of CFRP sheets (t=0.165mm and 0.33mm): and (3) length of FRP strips (the full span of the beam or half of it). Nevertheless, among the variables mentioned and their limited range, the focus of the present study is on the length of the FRP strips. Thus, nine RC beams with identical dimensions, spans, and reinforcing bars were simulated under different conditions using ABAQUS [17]. The dimensions of the beams and their steel reinforcing bars were assumed to remain constant in all the simulations. In other words, a 6.00m x 0.50m x 0.0.30m beam with 4ϕ14 steel bars grade S400 was used in all the 9 simulation cases (Figure 3). The dimensions of the FRP strips were the same as those used in Khalifa (2016) [10]. Upon completion of the simulation, the energy absorption capacity values obtained for each beam in different cases were duly compared. The loading is applied incrementally in the center of the beam span and the corresponding displacement is considered in different states. The simulation outputs included the load-displacement diagram (which exhibits the ultimate capacity of the concrete beam) as well as the stresses developed in each beam. The specifications of the simulated samples are given in Table 1. Figure 4 shows different simulation samples applied to the retrofitted beams.

Tab. 1 - Different simulation cases used in the present study

Simulation Case	Characteristic Strength of Concrete (MPa) and steel bar	Retrofitting Method	FRP Sheet Thickness (t)	FRP Strip Thickness	Abbreviation
1	fc=21; 4ϕ14	---	---	---	Not Retrofitted
2		EBR	t=0.165mm	Half the beam span	EBR (t, L/2)
3			t=0.165mm	Entire beam span	EBR (t, L)
4			2t=0.33mm	Half the beam span	EBR (2t, L/2)
5			2t=0.33mm	Entire beam span	EBR (t, L/2)
6		NSM	t=0.165mm	Half the beam span	NSM (t, L/2)
7			t=0.165mm	Entire beam span	NSM (t, L)
8			2t=0.33mm	Half the beam span	NSM (2t, L/2)
9			2t=0.33mm	Entire beam span	NSM (2t, L)

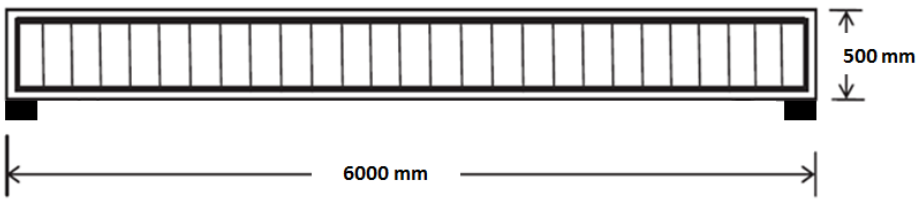

Fig. 3 – Dimensions of the retrofitted RC beam used in the study

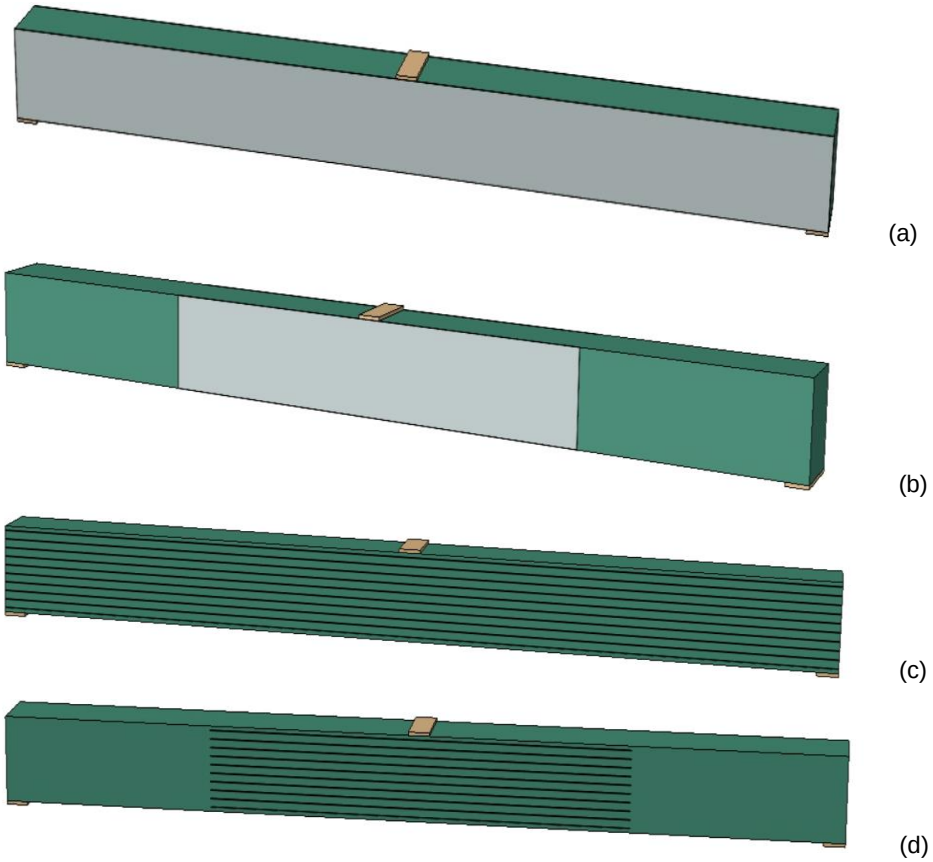

Fig. 4 – Different simulation cases applied to the retrofitted beams: (a) EBR method applied along the full span of the beam; (b) EBR method applied along half the beam span; (c) NSM method applied along the full span of the beam; and (d) NSM method applied along half the beam span

FINITE ELEMENT SIMULATION

In this section, the materials, the parameters, and the element types used in ABAQUS for simulating the RC beams are explained. The most important part of the numerical simulation of a reinforced concrete structure is to identify the nonlinear behaviour of the concrete. The nonlinear behaviour of brittle materials in ABAQUS is defined through three models: the smeared crack model, the brittle failure model, and the concrete damage plasticity model. Each model has certain advantages that can be used as required. The concrete damage plasticity model is the only model that can be used for both static and dynamic analysis of a structure. In this model, tensile cracking and compressive crushing are assumed to be the two main aspects of the concrete failure mechanism. The model was designed for simulating the failure of brittle materials and allows for stiffness recovery during loading cycles. Due to the model's lack of rupture criteria, elements cannot be removed by cracking during the analysis. However, this model can well predict the position and direction of crack formations. In the present study, the concrete damage plasticity model was used to simulate the nonlinear behaviour of concrete in tension and compression. The eight-node C3D8 and the Truss elements (with suitable sizes) were used for generating the meshes required for modelling concrete sections and reinforcing bars, respectively. Yield and ultimate strengths for longitudinal and transverse bars were assumed 400 MPa and 500MPa, and 280MPa and 380MPa, respectively. The density, Poisson's ratio, and modulus of elasticity for the CFRP sheets were assumed 1536 MPa, 0.25, and 2.4 x 10^5 MPa, respectively. Embedded region is used to define the behavior of rebar

inside concrete; Therefore, one object can be assumed to be buried inside another object. The nonlinear analysis of reinforced concrete structures as well as their components can be conducted through the behaviour models used for either concrete and reinforcing bars or concrete–rebar bonding. However, as these behaviour models are costly due to their high computation times and multiple degrees of freedom, much attention has been focused in recent years on the use of smeared cracking and the concrete damage plasticity methods. The contact element is not explicitly modelled and adhesion is indirectly introduced in calculations through average behaviour models defined for concrete and reinforcing bars in two methods. In the concrete damage plasticity model, cracked concrete is assumed to be a continuous homogeneous material. In addition, the damage in the concrete specimen is demonstrated in this model by its reduced stiffness and not by modelling its developed cracks. The characteristic compressive strength of the concrete used in the beams was assumed to be 21 MPa. The stress-strain characteristic of this concrete is shown in Figure 5.

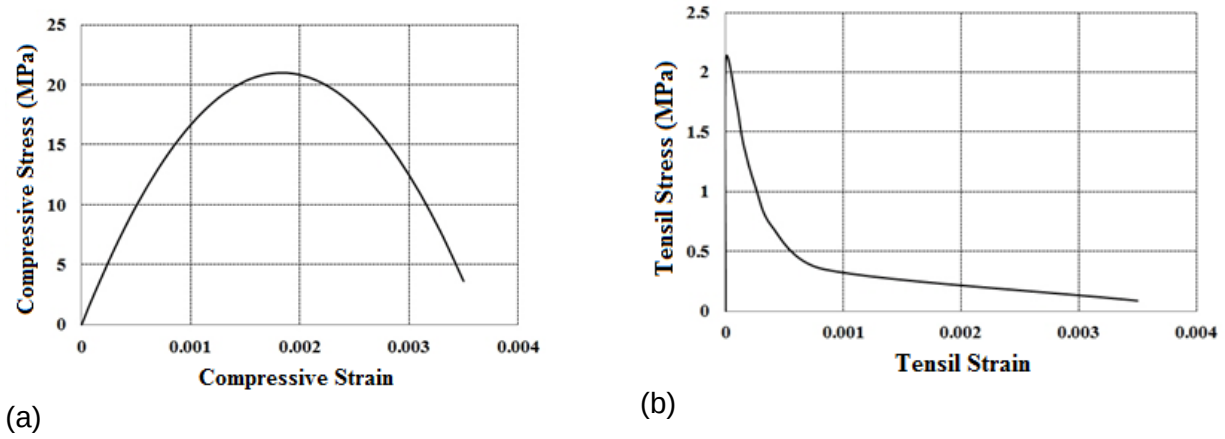

Fig. 5 – Stress–strain diagram obtained for the concrete with a compressive strength of 21MPa: (a) in compression, and (b) in tension.

Also, the accuracy of the simulation method used by modelling a CFRP-reinforced beam, which was made in the study of Kotynia and Cholostyako (2015) [18], and a good agreement was observed between the results of the finite element model and the experimental results. Figure 8 compares the load-displacement values of the finite element and experimental models of the B30-214-1T-15 beam [18]. As can be seen, the maximum load-displacement values corresponding to the experimental and numerical models have a relatively good correlation.

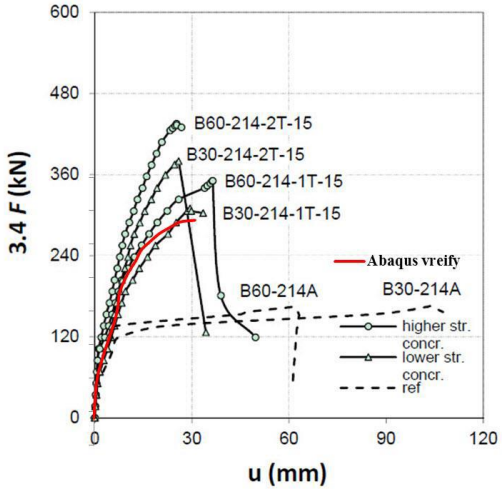

Fig. 6 – Finite element model validation and experimental results [18].

RESULTS AND DISCUSSION

Figures .7 and 8 show the stress characteristics as well as the load-displacement diagrams obtained from the present simulation and finite element analysis of the models generated for the studied beams. The diagrams express stress, displacement, and force in kPa (kN/m2), m, and kN, respectively. When CFRP sheets coat on the surface of the beam, the beam's ability to prevent cracking and crack spreading and the flexural strength of the beam increased. In this situation, the combination of normal and shear stresses makes the von Mises stress criterion more prominent, while the NSM method is not considered crack propagation. The other concept considered in this study was the energy absorbed in different cases by the studied beams.

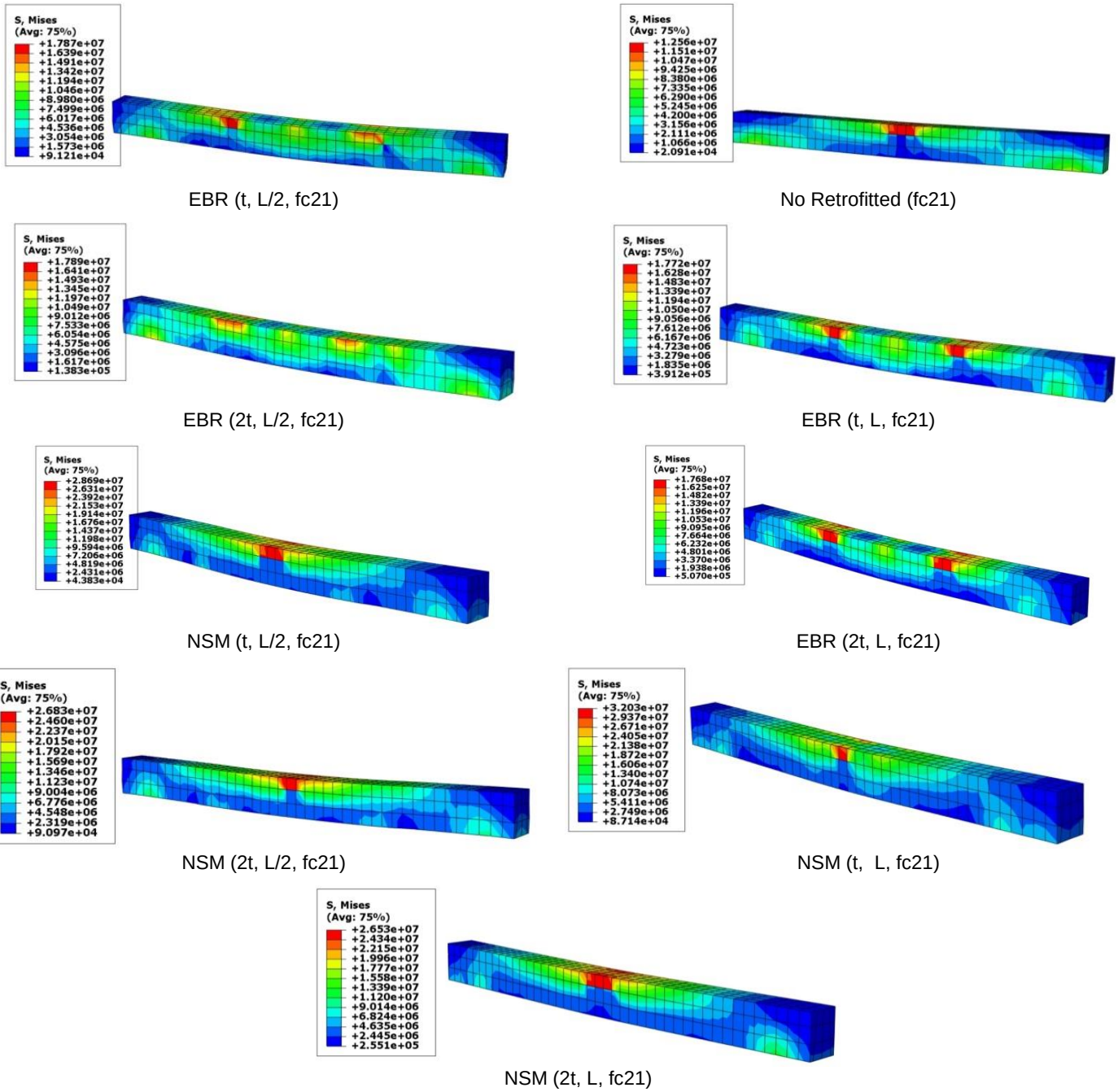

Fig. 7 – Stresses developed in the studied beams in different cases

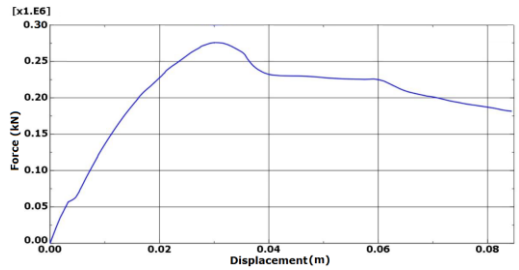

EBR (t, L/2, fc21)

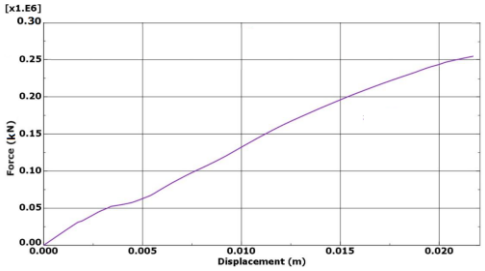

No Retrofitted (fc21)

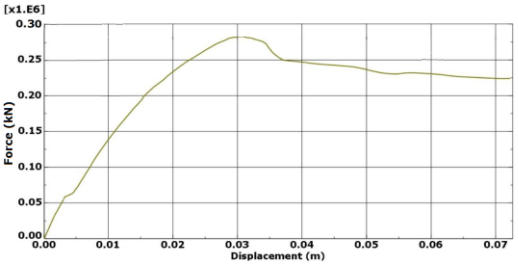

EBR (2t, L/2, fc21)

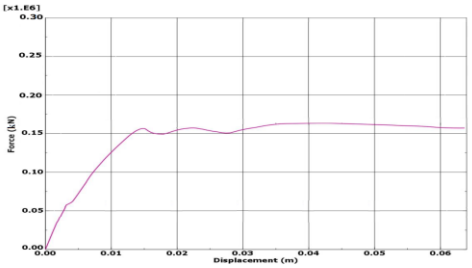

EBR (t, L, fc21)

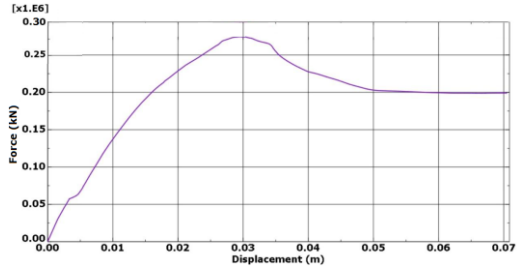

NSM (t, L/2, fc21)

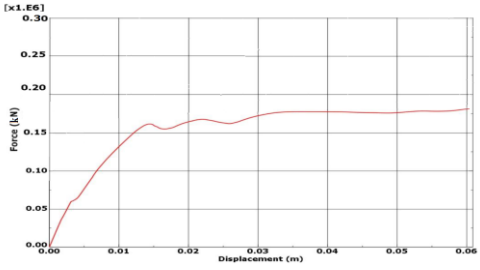

EBR (2t, L, fc21)

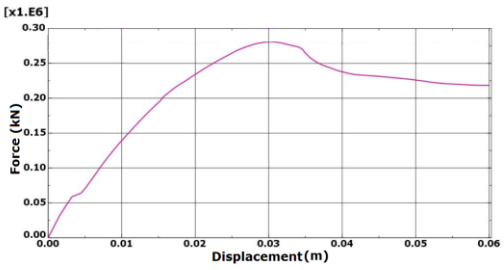

NSM (2t, L/2, fc21)

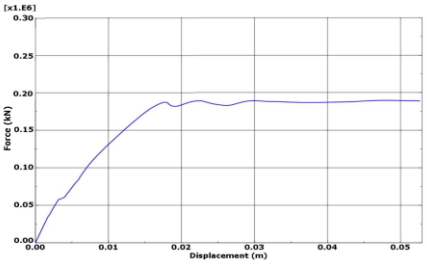

NSM (t, L, fc21)

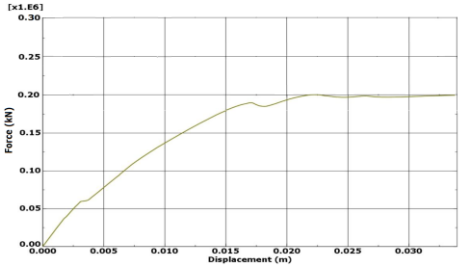

NSM 2t, L, fc21)

Fig. 8 – Load–displacement diagrams obtained for the studied beams in different cases

This energy is obtained by calculating the area under a load-displacement curve and is expressed in Figure 9. The energy absorbed and dissipated by a structure is among the most important factors in seismic retrofitting of that structure and must receive due attention. Accordingly, the area under the load-displacement diagram was calculated for each of the nine studied cases to represent the energy absorbed by the model in each case.

$$U = W = \int_0^{\delta} P_1 \, d\delta_1$$

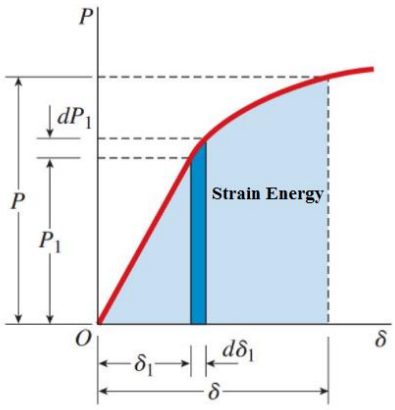

Fig. 9. - Load-Displacement curve

Figure 10 shows the energy absorption values obtained for the studied RC beams in different cases. The incorporation of CFRP sheets enhanced the energy absorption capacity of the beams in all studied cases, increasing the parameter up to 1.69-5.54 times that of the un-retrofitted beam. The energy absorption results are presented in Figure 11.

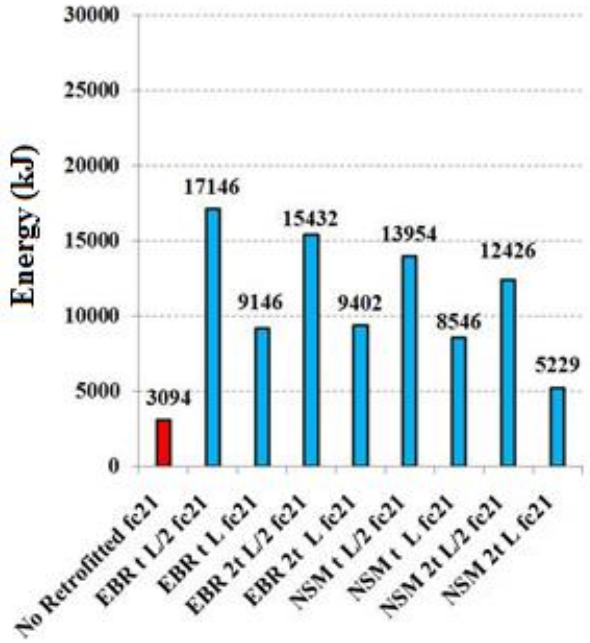

Fig. 10 – Energy absorption capacity of the simulated beams in different cases

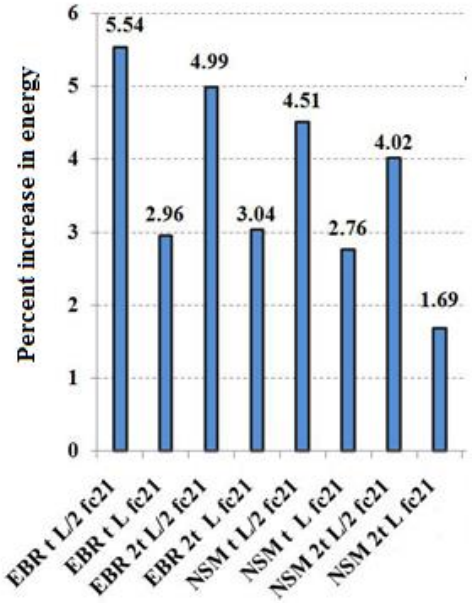

Fig. 11 – Percent increase in energy absorption ratios obtained in different cases

As already explained, the CFRP sheets used for retrofitting the studied beams were applied at two different lengths over the surface of each beam: (1) along the full span of the beam, and (2) along 50% (half) of the span of the beam, at equal distances from the middle of the beam.

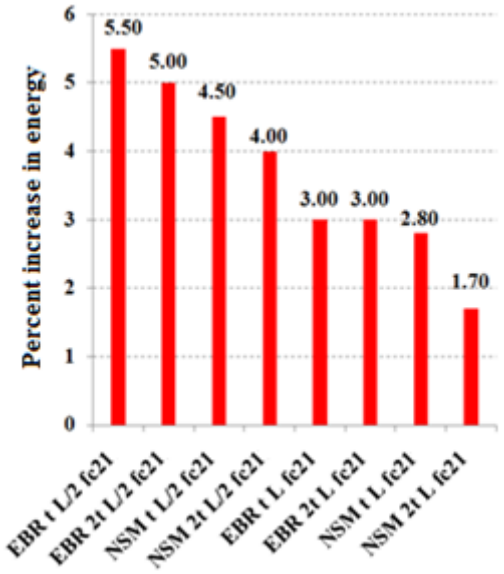

Fig. 12 – Comparison of energy absorption ratios for investigating the effect of retrofitted length in different cases

Figure 12 compares the energy absorption ratios of the beams in the eight different studied cases. The purpose of this comparison was to investigate the effect of retrofitted length on beam behaviour. As evident from the figure, in most studied cases, the percent energy absorption obtained for the 50% CFRP-retrofitted length was greater than that obtained for the 100% CFRP-retrofitted length. For example, in the case where the EBR method was applied to retrofit the RC beam (with compressive strength of 21MPa along 50% of its span with a CFRP sheet of 0.165mm thickness, the energy absorption capacity was increased 5.50 times; whereas, in the case where the same

beam was similarly retrofitted along its full span, a lower energy absorption capacity increase of 4.23 times was obtained (compared with the un-retrofitted case). Incremental loading continues in the middle of the span until the beam reaches the destruction step. The reason is that in the former case (50% retrofitted length), the entire beam assembly (concrete plus reinforcing bars) contributed to load-bearing alongside the CFRP sheet, postponing occurrence of crack and increasing the energy absorption capacity of the beams. Conversely, in the case where retrofitting was applied along the full span of the beam, the CFRP sheet carried the greater share of the load without the full engagement of the beam assembly in load-bearing. As a result, the energy absorption capacity of the beam, in this case, was less than that in the case with the entire length of the beam retrofitted. It should be noted that this process is before the failure of CFRP, after which the steel reinforcement must be engaged and increase the absorption capacity.

Figure 13 compares the increase in the energy absorption capacity in different cases to determine the impact of the retrofitting method on the results. As evident from the figure, the energy absorption capacity increase in most studied beams retrofitted by the EBR method was greater than that obtained by the NSM method, amounting to more than 76% in the case abbreviated as EBR 2t L fc21MPa. This can be attributed to the fact that, when the entire length of the beam is retrofitted with CFRP sheets, crack formation and propagation in the beam will be better prevented, further increasing the load-bearing capacity.

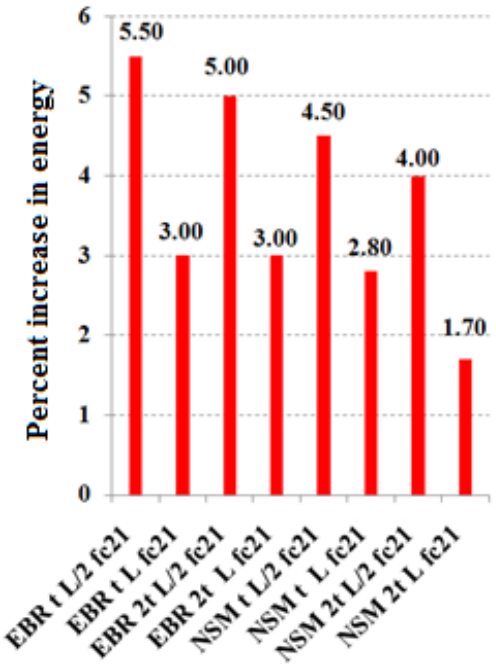

Fig. 13– Comparison of energy absorption ratios in different cases, demonstrating the respective effects of the employed retrofitting methods

CONCLUSION

A comparative study of the EBR and NSM methods used for retrofitting RC beams was created. For this purpose, the finite element method (using ABAQUS) was implemented. In the present study, variables such as the retrofitted length (equal to the entire beam span and half the beam span), the retrofitting method employed (EBR and NSM methods), and the CFRP sheet thickness (t and 2t) were investigated. An un-retrofitted beam was also simulated as the control specimen for comparison. The response of the beams was compared according to the load-displacement diagrams and energy absorption capacity. The most significant results obtained in the present study were:

1. Retrofitting RC beams with CFRP sheets increased the energy absorption capacity of the beams in all studied cases. The extent of this increase was between 1.69 and 5.59 times the corresponding value obtained for the un-retrofitted beam.
2. The energy absorption capacity of the retrofitted beam was greater when the CFRP sheet was applied to the entire length of the beam in most of the studied cases. For example, in the case of using the EBR method for retrofitting the RC beam (compressive strength=21 MPa) along 50% of its length with a 0.165 mm thick CFRP sheet, the energy absorption capacity was enhanced to 5.50 times that of the un-retrofitted control specimen. Meanwhile, in the case of the entirely-retrofitted beam (twice the retrofitted length as the previous case), the energy absorption capacity exhibited a lower increase as it rose to 4.23 times the capacity of the un-retrofitted control specimen.
3. In the case where half the span of the beam was retrofitted using CFRP sheets, the whole beam assembly (concrete plus rebars) and the CFRP sheets jointly participated in carrying the load, thus postponing cracking in the beam and increasing the beam energy absorption capacity. Conversely, when CFRP retrofitting was applied to the entire beam span, the CFRP sheets carried most of the load, thus preventing the beam assembly from realizing its load-bearing capacity in full. As a result, the energy absorption capacity of the beam, in this case, was less than that obtained in the case with to half (50%) of the length retrofitted.
4. In most of the cases studied, the EBR method proved more effective than NSM, by offering a greater beam energy absorption capacity. In some cases (the case of EBR 2t L fc21), the energy absorption capacity corresponding to the EBR method was 76% of that offered by NSM. The reason is, when the CFRP sheets cover the entire beam surface, crack formation and propagation are prevented more effectively, allowing for a further increase in the load-bearing capacity.

REFERENCES

[1] American Concrete Institute. ACI Committee 440 .(2008) “Guide for the design and construction of externally bonded FRP system for strengthening concrete structures”. Farmington Hills, MI: ACI 440.2R-08.

[2] Galecki, G. and Myers, J., (2001)," Limitation to use of waterjets in concrete substrate preparation", American Waterjet Conference, No. 53, Minneapolis, USA.

[3] Babaei, m; Laki, A.,(2014), Comparison of New Methods of Reinforcing Concrete Beams, 6th National Congress of Civil Engineering, Semnan, Iran (persian).

[4] De Lorenzis L.a, J.G. Teng, (2007). "Near-surface mounted FRP reinforcement: An emerging technique for strengthening structures. *Composites Part B: Engineering*, *38*(2), pp.119-143.

[5] Afzir Retrofit Cataloge.,(2013), https://www.afzir.com/catalogues.

[6] Abduljalil, B.S., (2014), Shear resistance of reinforced concrete deep beams with opening strengthened by CFRP strips. *Journal of Engineering and Development*, *18*(1), pp.14-32.

[7] Kharatmol, R., Sananse, P., Tambe, R. and Khare, R.J., (2014). Strengthening of Beams Using Carbon Fibre Reinforced Polymer. *International Journal of Emerging Engineering Research and Technology*, *2*(3), pp.119-125.

[8] Mofidi, A., Chaallal, O., Cheng, L. and Shao, Y., (2016). Investigation of near surface–mounted method for shear rehabilitation of reinforced concrete beams using fiber reinforced–polymer composites. *Journal of Composites for Construction*, *20*(2), p.04015048.

[9] Tahsiri, H., Sedehi, O., Khaloo, A. and Raisi, E.M., (2015). Experimental study of RC jacketed and CFRP strengthened RC beams. *Construction and Building Materials*, *95*, pp.476-485.

[10] Khalifa, A.M., (2016). Flexural performance of RC beams strengthened with near surface mounted CFRP strips. *Alexandria Engineering Journal*, *55*(2), pp.1497-1505.

[11] Ceroni, F., (2010). Experimental performances of RC beams strengthened with FRP materials. *Construction and Building materials*, *24*(9), pp.1547-1559.

[12] Chen, W., Pham, T.M., Sichembe, H., Chen, L. and Hao, H., (2018). Experimental study of flexural behaviour of RC beams strengthened by longitudinal and U-shaped basalt FRP sheet. *Composites Part B: Engineering*, *134*, pp.114-126.

[13] Carlos, T.B., Rodrigues, J.P.C., de Lima, R.C. and Dhima, D., (2018). Experimental analysis on flexural behaviour of RC beams strengthened with CFRP laminates and under fire conditions. *Composite Structures*, *189*, pp.516-528.

[14] Hawileh, R.A., Abdalla, J.A. and Naser, M.Z., (2019). Modeling the shear strength of concrete beams reinforced with CFRP bars under unsymmetrical loading. *Mechanics of Advanced Materials and Structures*, *26*(15), pp.1290-1297.

[15] Reddy, H.J., (2018). A Comparative Study on the Experimental Results of Strengthened Beams using Externally Bonded Laminate Technique with Strengthening Codes. *International Journal of Applied Engineering Research*, *13*(5), pp.2119-2124.

[16] Bilotta, A., Ceroni, F., Nigro, E. and Pecce, M., (2015). Efficiency of CFRP NSM strips and EBR plates for flexural strengthening of RC beams and loading pattern influence. *Composite Structures*, *124*, pp.163-175.

[17] ABAQUS theory manual. (2016), Pawtucket, R.I: Hibbitt, Karlsson and Sorensen.

[18] Kotynia, R. and Cholostiakow, S., (2015). New proposal for flexural strengthening of reinforced concrete beams using CFRP T-shaped profiles. *Polymers*, *7*(11), pp.2461-2477.

CIVIL ENGINEERING JOURNAL

Article no. 50

THE CIVIL ENGINEERING JOURNAL 3-2021

STUDY ON BONDING PROPERTY OF POLYURETHANE CEMENT (PUC) TO STEEL BAR

Kexin Zhang[1,2], Dachao Li[2], Xinyuan Shen[2], Tianyu Qi[2] and Xingwei Xue[2]

1. *MOE Key Lab of Disaster Forecast and Control in Engineering, Jinan University, No.601 Huangpu Dadao West, Guangzhou, Guangdong Province, China; jt_zkx@sjzu.edu.cn*
2. *School of Traffic Engineering, Shenyang Jianzhu University, No.25 Hunnan Zhong Road,Shengyang, Liaoning Province, China*

ABSTRACT

The pull-out test of the bar and PUC is carried out in this paper, the effects of protective layer thickness, reinforcement anchorage length, diameter and shape of reinforcement on bonding properties were studied. The results show that the bond strength between reinforcement and PUC material increases with the increase of the thickness of the protective layer but decreases with the increase of the anchorage length and diameter of reinforcement. The bond strength of bare round steel is significantly lower than that of ribbed steel, and the maximum bond strength is about 47.4% of ribbed steel. By analyzing the bond slip curve obtained from the pull-out test, the stress process of bond anchorage between reinforcement bar and PUC material is mainly summarized into three stages: the rising stage, the falling stage and the residual stage. The characteristics of the curve, the stress process and the failure mode of specimen at each stage are analyzed.

KEYWORDS

Polyurethane cement (PUC) material, Steel bar, Bond stress, Pull-out test, Bond-slip curve

INTRODUCTION

The bond between steel bar and concrete is a complex interaction between steel bar and peripheral concrete, and the two materials can achieve deformation coordination through the transfer of bond stress to ensure the joint work. This effect is essentially the bond stress [1-6]. The bonding force is mainly composed of the chemical bonding force, friction resistance and mechanical biting force between the steel bar and concrete and is expressed as a shear stress along the length of the steel bar macroscopic. With the action of external load, there will be relative sliding between reinforcement and concrete, and whether the strength of reinforcement can be fully exerted depends on the bond strength of the two. In recent years, the investigation on earthquake disasters shows that many reinforced concrete bridge piers are destroyed in weak bond anchorage locations under strong earthquakes, and bond degradation often leads to the loss of bond in joint areas under earthquake action, and the stiffness is significantly reduced or even the strength is lost [7-12].

Polyurethane (PU) is a kind of polymer elastic material with excellent performance. The polyurethane cement composite material (elastic concrete) formed by mixing it with cement has the advantages of chemical corrosion resistance, rapid hardening, light weight and high strength compared with traditional building materials [13-15]. It can replace traditional building materials to a certain extent. Haleem K. Hussain et al. [16-18] used polyurethane and fly ash to make polyurethane cement (PUC) material. The flexural and compressive tests of the composite material were carried out, and the stress-strain curve relationship of the material under different densities was obtained. At the same time, the elastic modulus, Poisson's ratio and bonding strength of the material to

concrete are also studied. Based on the material research, the bending reinforcement tests of seven T-section beams under different failure degrees were carried out. The results show that the ultimate bearing capacity of the beams strengthened by polyurethane cement (PUC) material can be significantly improved, and the cracks of the beams can be significantly reduced. Liu Guiwei et al. [19] prepared polyurethane cement (MPC) material to reinforce Baixi Bridge in Ningbo, Zhejiang. The results show that polyurethane concrete material can better improve the bearing capacity of the structure and can carry out construction operations without stopping traffic.

The combination of polyurethane cement (PUC) and reinforcement can give full play to the superior mechanical properties of the two, and obtain more excellent crack prevention, earthquake resistance and crack control ability. However, there is still a lack of systematic experimental study on bond anchorage between reinforcement bar and PUC. Due to the significant difference between PUC material and ordinary concrete in mechanical properties, the existing research results on the bond properties of ordinary concrete to steel bar are not applicable to the bond properties of PUC material to steel bar. In this paper, through the pull-out test of PUC material and steel bar, the bond anchorage performance of steel bars and PUC material was studied by the test parameters of steel bar type, anchorage length, protective layer thickness and so on. Meanwhile, the bond slip constitutive relationship between PUC material and steel bar is analyzed.

ADHESIVE PULL-OUT PROPERTY TEST OF PUC AND STEEL BAR

The bond anchorage tests currently used can be divided into three categories according to their purposes: The first is the center drawing test, which is used to compare the bonding and anchorage properties of different steel bars. The second is beam type test or simulated beam type test, which is used to determine the design service strength and related construction requirements of bond anchorage. The third is the local bond slip test, which mainly studies the basic law of bond stress and deformation. Pull-out test has the advantages of simple method, eliminating the interference of other factors on the test results, the results are easy to analyze and so on. For a long time, it has been used as the basis for the relative comparison of the bonding properties of materials, and it is also the widely used benchmark test in all countries. Therefore, the method of drawing test is used in this paper, in order to study the bond anchorage performance of steel bar.

Experimental material

Polyurethane cement (PUC)

Polyurethane cement is a kind of polymer concrete material, whose main component is the polymerization of polyurethane raw material and cement. Polyurethane is a polymer with excellent performance, which is mainly composed of isocyanate and polyether polyol. The main raw material components are shown in Table 1.

The hardness range of polyurethane materials is 10-100 (IRHD), where 0 (IRHD) represents an elastic modulus of 0, 100 (IRHD) represents an infinite elastic modulus. Polyurethane material has good wear resistance, chemical corrosion resistance, fluidity, bonding and molding properties.

Tab.1 - Composition of polyurethane raw material

Raw material		Percentage（%）
Polyols	polyether	49
	Silicone oil	1
	Water	0-1
Isocyanate		50-51

Polyurethane cement raw materials are mixed in accordance with the mass ratio, and the mass ratio is polyol: isocyanate: cement =1:1:2. High density polyurethane cement material is

prepared, as shown in Table 2. Polyol, isocyanate and cement were the main raw materials in the mixture ratio. The PUC material was cured in dry environment for 7 d.

Tab. 2 - Composition of PUC

PUC	Percent（%）
polyether polyol	25
isocyanate	25
cement	50

The main mechanical properties of polyurethane cement are as follows:

Tab. 3 - Main mechanical properties of PUC

Index	Density（kg/m^3）	Compress stress（MPa）	Flexural stress（MPa）	Axial tensile strength（MPa）
PUC	1500	59.3	41.5	31

Fig. 1 - PUC material mixing diagram

Fig. 2 - Pouring drawing of PUC

Steel bar

The steel bars used in this test are ribbed steel bars and round steel bars, and the steel bars basically have no corrosion. In the process of specimen making, the same batch of steel bars are selected to conduct tensile test to determine the tensile yield strength, elongation and other parameters of steel bars. During the test, the spacing of reinforcement is the diameter of reinforcement, and the test results are shown in Table 4.

Tab. 4 - Basic mechanical properties of steel bar

Diameter（mm）	Yield strength（N/mm^2）	Ultimate strength（N/mm^2）	Elasticity modulus（N/mm^2）	Extend rate（%）
12（HRB335）	373	560	2.0×10^5	32
16（HRB335）	385	552	2.0×10^5	27
20（HRB335）	375	585	2.0×10^5	30
20（HPB335）	286	410	2.1×10^5	34

SPECIMEN DESIGN AND FABRICATION

The cement was dried at 100 ℃ ~ 110 ℃ for 24 h, and then mixed with polyurethane raw materials and defoaming agent, mechanically mixed for 3 ~ 5 min, and the mixture was poured into a 150 mm × 150 mm × 150 mm cube mold. After hardening, the specimen was demoulded and cured at room temperature for 28 d, with dimensions as shown in Figure 3 and Figure 4. The dumbbell shaped sheet specimens were made of PUC material separately. The sizes were shown in Figure 5. The thickness of the specimens was 10 mm, the width in the middle was 25 mm, and the width on both sides was 40 mm. The mold test in the casting process is self-designed, as shown in Figure 6.

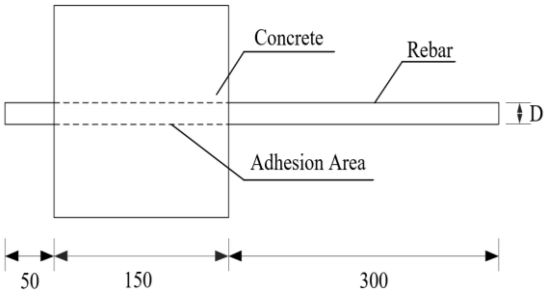

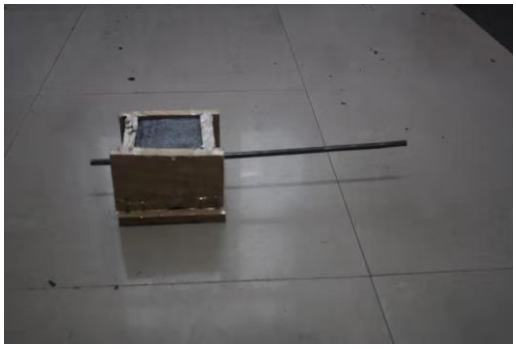

Fig. 3 - Detail of specimen (unit: mm) *Fig. 4 - Pouring diagram of specimen*

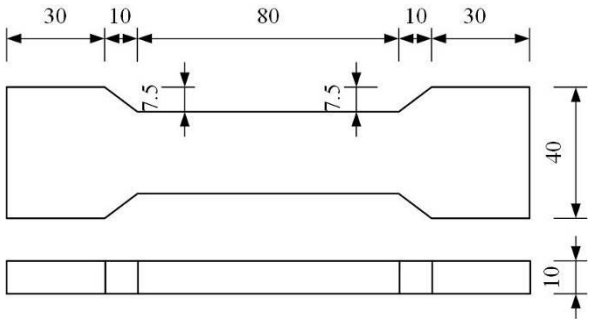

Fig. 5 - Dimensions of polyurethane cement material axial tensile specimen (unit: mm)

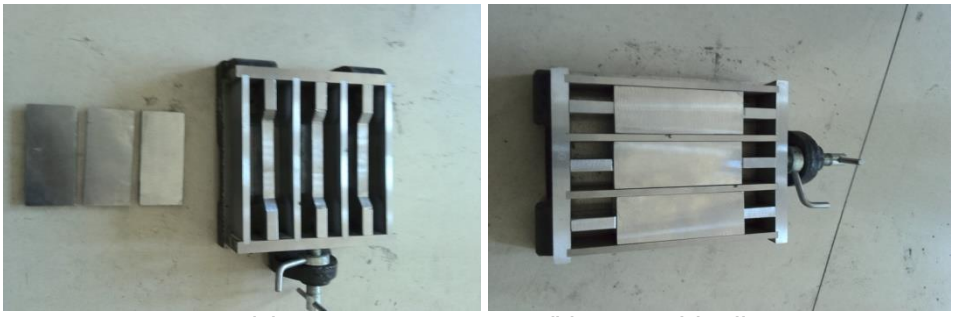

(a) apart *(b) Assembly diagram*

Fig. 6 - Steel formwork diagram of dumbbell type specimen

This test uses the center pull-out test to test the bond property of steel bar and PUC and the pull-out specimens were made according to the Chinese code (Test Rules for Cement and Cement Concrete in Highway Engineering) [20-22]. A total of 45 specimens were made in the test. Considering the influence of three parameters, including the thickness of the protective layer, the

diameter and shape of the steel bar, and the anchorage length, the number and parameters of the specimens are shown in Table 5.

Tab.5 - List of pull-out specimens

Specimen number	Thickness of protective layer c（mm）	Anchorage length la（mm）	Steel bar diameter d（mm）	Number of specimens
1	70	30	16	3
2	70	50	12	3
3	70	50	16	3
4	70	50	20	3
5	70	50	20（plain round bar）	3
6	70	80	12	3
7	70	80	16	3
8	70	80	20	3
9	70	80	20（plain round bar）	3
10	70	100	16	3
11	40	80	16	3
12	50	80	16	3
13	60	80	16	3
ZL	—	—	—	6

LOADING AND MEASURING SCHEME

The testing machine adopts the universal testing machine with the maximum range of 10 t to carry out direct pull-out test. During the test, the displacement value is directly read by the testing machine, and the strain is measured by static resistance strain gauge. The loading process is as follows :(1) Fix the test fixture to the universal testing machine, connect the strain gauge wire to the static resistance strain gauge, and debug the instrument to ensure the data stability of the acquisition system. (2) The maximum load that the steel bar can bear is taken as the ultimate pull-out load P to determine the test loading scheme. The test is divided into 20 levels of loading, and the load of each level is 0.05 P. In the first step of the test, preloading was carried out with a load of 0.05P. Displacement and strain values were recorded and then unloaded. (3) Formal loading. After the loading of each stage is completed, the anchorage end and the whole of the specimen are photographed to record the state of the specimen. After the data are stable, the strain and displacement values are recorded. (4) Loaded to the specimen failure, the failure load was recorded, displacement and strain data were recorded, and photos of the specimen failure were collected. The loading device diagram is shown in Figure 5. PUC material test was carried out on a small-range tester with a loading speed of 50 N/s. The resistance strain gauge was pasted in the middle of the specimen and pasted symmetrically on both sides along the stretching direction to measure the strain change in the stretching process. The dynamic strain acquisition instrument was used for data acquisition.

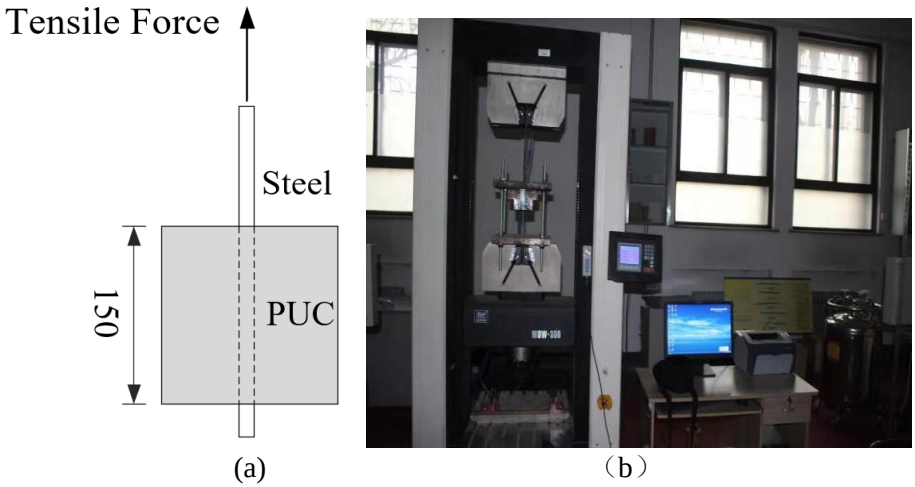

Fig. 7 - Detail of specimen arrangement

According to the measured value of the drawing force, the average bond stress can be obtained by the following formula:

$$\tau = \frac{P}{\pi d l_a} \quad (1)$$

Where P — the pulling force,

τ — the average bond stress

d — bar diameter

l_a — anchorage length

As can be seen from the formula, the bond stress is obtained by comparing the force with the surface area by simplifying the reinforcement bar in the anchorage section into a smooth cylinder macroscopic. Therefore, the bond stress at all points on the anchorage length is the same, so it is the average bond stress on the anchorage length.

INFLUENCE OF ANCHORAGE CONDITIONS ON BOND STRENGTH

Tensile strength of PUC

According to the data in Table 6, the average axial tensile strength of polyurethane cement material is 31.0 MPa, and the straight-tension elastic modulus is calculated to be 4200 Mpa - 5700 MPa according to the stress-strain curve relationship.

Tab. 6 - Table of axial tensile strength of PUC material

Number	ZL01	ZL02	ZL03	ZL04	ZL05	ZL06	Average value
Strength（MPa）	30.5	31.8	31	32.1	31.6	28.9	31.0

According to the tensile force and the corresponding strain data collected during the test, the stress-strain relationship curves of the six specimens in straight tension were drawn, as shown in Figure 8. According to the straight-tension measurement results of the test block, the average stress-strain curve of straight-tension is obtained, as shown in Figure 9.

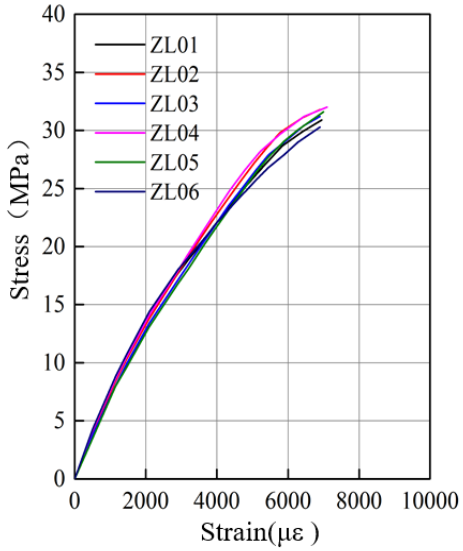

Fig. 8 - Direct tensile stress-strain curve

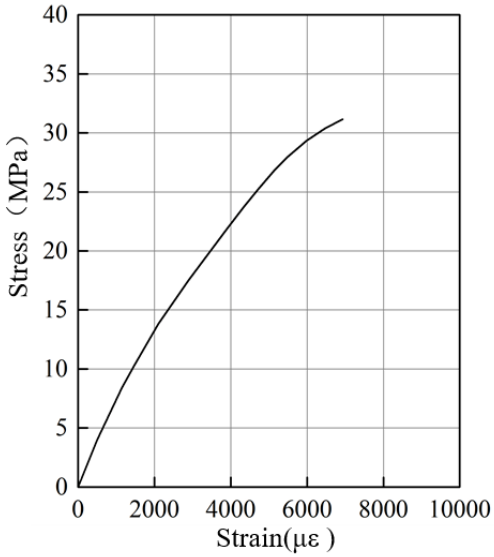

Fig. 9 - Stress-strain curve in direct tension (average)

According to the stress and strain relationship points of axial tensile specimens, the stress-strain relationship curve is fitted, as shown in Figure 10. The fitting formula is as follows:

$$\sigma=0.496+6977.3\varepsilon-365682.2\varepsilon^2 \quad R^2=0.999 \tag{2}$$

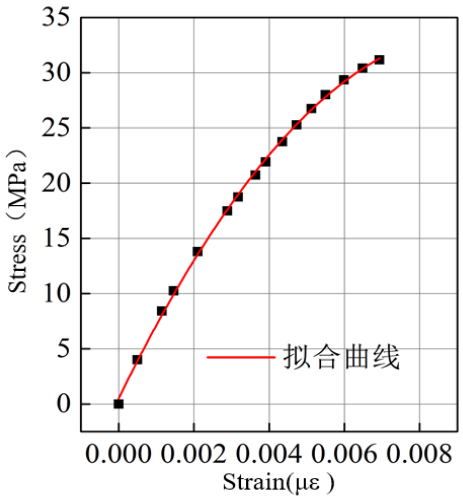

Fig. 10 - Fit curve of axial tensile stress-strain relationship

Coverage thickness

In the test, there are three groups of pullout specimens represented by Φ16mm ribbed steel bar, and the conditions in each group are the same. The thickness of the protective layer of steel bar in each group is 40 mm, 50 mm, 60 mm and 70 mm. After calculating the average value of the bond stress in each group, the influence of the thickness of the protective layer on the bond anchorage performance of steel bar and polyurethane cement is studied. Figure 11 is the comparison diagram of bond stress under each protective layer thickness, and Figure 12 is the average bond stress diagram of the three groups of specimens. It can be seen from the figure that the thickness of the protective layer has a significant effect on the bond strength of the deformed reinforcement, because the significant characteristic of the anchorage failure of the deformed reinforcement is led by splitting.

The thicker the protective layer is, the greater the constraint effect on splitting will be. For PUC specimens, the increase in the thickness of the protective layer can limit the propagation of splitting cracks, or even prevent the occurrence of cracks, but this restriction is not infinite. It can be seen from the figure that the bond strength increases with the increase of the thickness of the protective layer. When the thickness of the protective layer is 40 mm, the average bond stress is 10.53 MPa. When the thickness of the protective layer is C50, the average bond stress is 12.36 MPa, which increases by 17.38% compared with that of 40 mm. When the thickness of the protective layer is 60, the average bond stress is 14.00 MPa, which increases by 13.27% compared with that of 50mm. When the thickness of the protective layer is 70 mm, the average bond stress is 16.38 MPa, which increases by 17.00% compared with that of 60 mm.

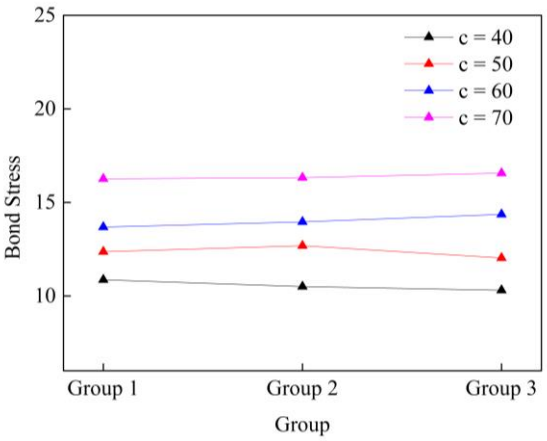

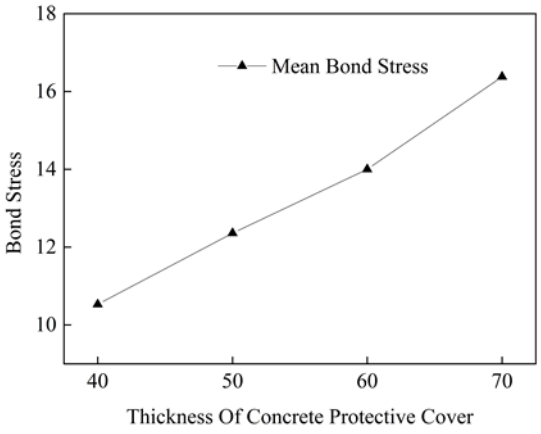

Fig. 11 - Bond stress under each protective layer thickness *Fig. 12 - Average bond stress*

Anchorage length of steel bar

This test selected Φ16 ribbed steel bar as the representative of the pull-out specimens, a total of 3 groups, each group of 4 total specimens, anchoring length of 30 mm, 50 mm, 80 mm, 100 mm. The test results show that the average bond strength decreases with the increase of the anchorage length, because the pull-out force of the specimen is closely related to the bond area, and the pull-out force increases with the increase of the anchorage length and the bond area. However, from the analysis of the bonding mechanism between ribbed reinforcement and concrete, the average bonding stress in the anchorage section decreases with the increase of the anchorage length. Since the bond stress distribution in the anchorage section is not uniform, when the ultimate bond stress is constant, the longer the anchorage section is, the lower the average bond stress will be. The results of this test accord with the above law. It can be seen from the figure that the bond strength decreases with the increase of the anchoring length. When the anchoring length l_a is 30 mm, the average bond stress is 19.55 MPa. When the anchoring length l_a is 50 mm, the average bond stress is 16.47 MPa, which is 15.75% lower than that when l_a is 30 mm. When the anchorage length La is 80 mm, the average bond stress is 13.33 MPa, which is 19.06% higher than that when l_a is 60 mm. When the anchorage length l_a is 100 mm, the average bond stress is 10.65 MPa, which increases by 20.11% compared with 70 mm.

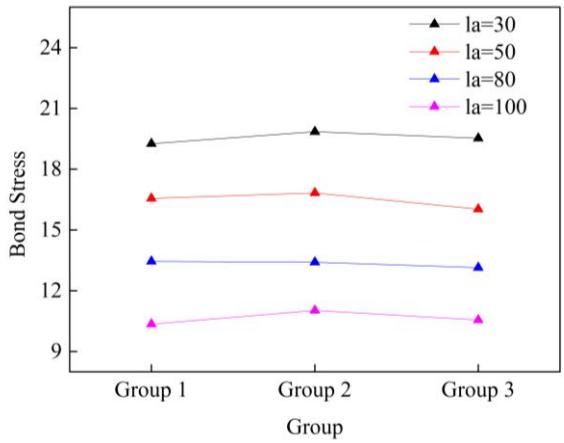

Fig. 13 - Bond stress under each anchorage length

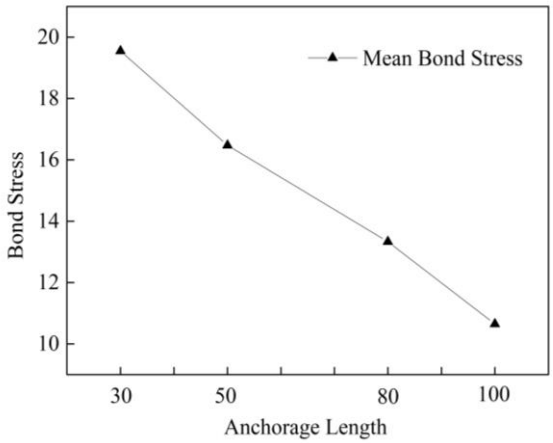

Fig. 14 - Average bond stress diagram

Diameter and shape of steel bar

The bonding properties of Φ12 ribbed bars, Φ 16 ribbed bars, Φ 20 ribbed bars and Φ 20 straight round bars under two different anchorage lengths were compared. The bond area of ribbed steel bar, circular steel bar and surrounding concrete is proportional to the perimeter length of the section, while the tensile force is proportional to the section area. The ratio of the two reflects the relative bond area of the steel bar. The relatively small bonding area of steel bars with larger diameter is not conducive to the improvement of ultimate bonding strength. In general, under the same anchoring condition, the bond strength between bars and PUC decreases with the increase of the diameter, and the bond stress between bars with the same diameter and PUC decreases with the increase of the anchoring length under different anchoring lengths, and the bond strength of ribbed bars is obviously higher than that of rounded bars. Figure 15 shows the comparison diagram of bond stress between steel bars of different diameters with anchorage length La of 50 mm and polyurethane cement, and Figure 16 shows the summary diagram of average bond stress. As shown in the figure, the bond strength decreases with the increase of diameter. When the diameter is 12 mm, the average bond stress is 17.97 MPa; when the diameter of reinforcement is 16 mm, the average bond stress is 16.47 MPa, which is 8.35% lower than that when d is 12 mm. When the diameter of steel bar is 20 mm, the average bond stress is 13.5 MPa, which is 18.03% lower than that when d is 16 mm. The bond stress of 20 mm diameter round steel bar is only 6.4MPa, which is only 47.4% of ribbed steel bar under the same condition, mainly because the bond strength of ribbed deformation steel bar is mainly determined by the mechanical bite force, while the bond strength of round steel bar is mainly determined by the friction resistance. For the concrete drawing specimens equipped with smooth circular bars, the interfacial friction resistance under load will make the microcracks in the concrete specimens develop and extend continuously, and the interface slip between the stress bars and concrete will increase, resulting in a rapid reduction of the friction resistance and a significant reduction of the corresponding interfacial bond stress.

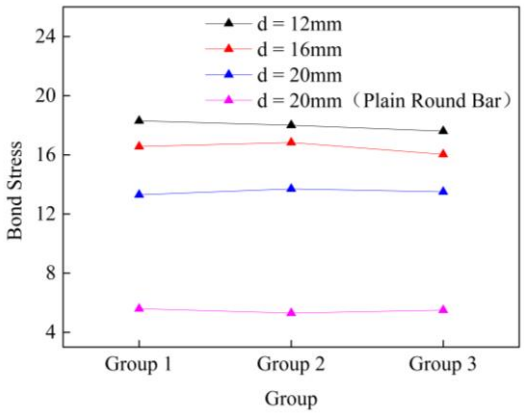

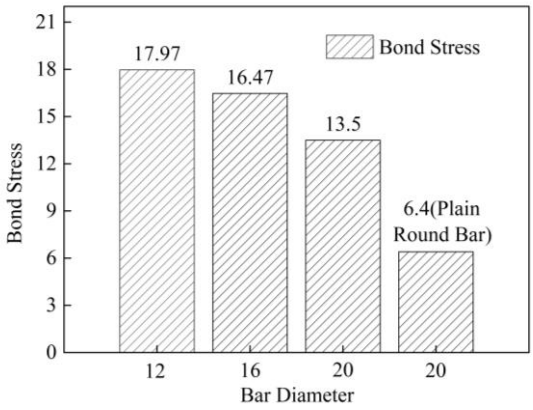

Fig. 15 - Bond stress under each steel bar diameter (l_a=50) *Fig. 16 - Average bond stress*

Figure 17 shows the comparison diagram of bond stress between steel bars with different diameters and polyurethane cement with anchorage length l_a of 80 mm, and Figure 18 shows the summary diagram of average bond stress. As shown in the figure, when the diameter is 12 mm, the average bond stress is 14.37 MPa. When the diameter of reinforcement is 16 mm, the average bond stress is 13.33 MPa, which is 7.24% lower than that when d is12 mm. When the diameter of steel bar is 20 mm, the average bond stress is 12.07 MPa, which is 9.45% lower than that when d is 16mm. The bond stress of 20 mm diameter circular steel bar is only 6.4 MPa, which is only 32.31% of ribbed steel bar under the same condition.

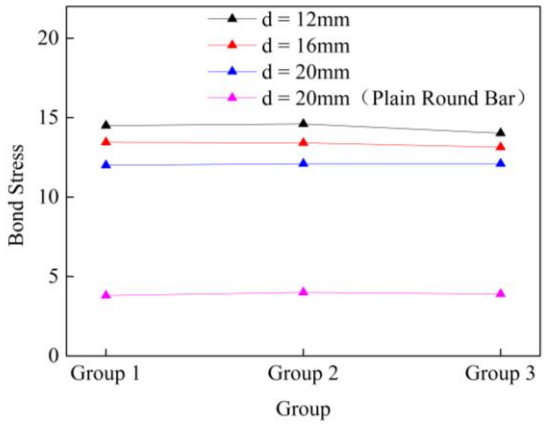

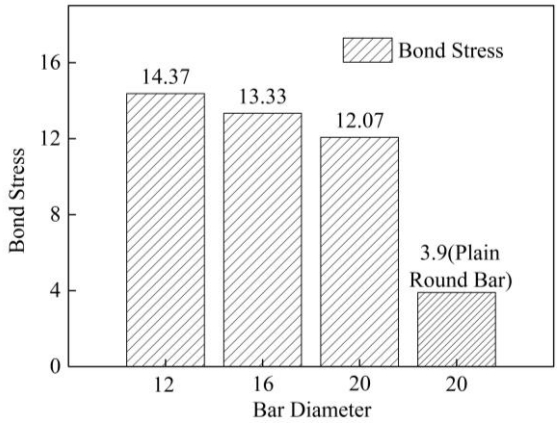

Fig. 17 - Bond stress under each anchorage length (l_a=80) *Fig. 18 - Average bond stress*

BONDING STRESS-SLIP CURVE

The bond stress and the corresponding slip under different loads are plotted in the same coordinate plot to form a bond - slip (τ-s) curve. The values of bond stress and slip are the average values. In order to compare the variation trend of the bond-slip curve of PUC of HRB335 steel bar, the typical bond-slip curve in each group of specimens was selected for comparative analysis in this test. See Figure 19 and Figure 20 for the bond-slip curve.

From the point of view of bond-slip curve, similar to the bond-slip curve of reinforced concrete, the curve is divided into three parts: rising section, falling section and residual section. According to the bond-slip curve, the stress process of the pull-out specimen can be divided into the following stages:

1) The rising stage: At the early stage of loading, the bond stress increases rapidly, the loading end slip is small, and the free end has no slip. The bond-slip (τ-s) curve shows a linear relationship

with a large slope. At this stage, the bonding stress is mainly borne by the bonding force of reinforcement and concrete. When the load increases to about 70% of the ultimate drawing force, part of the pre-ribbed concrete is crushed due to the extrusion effect of the transverse ribs on the interribbed concrete, and the interribbed concrete produces micro-cracks. As a result, the bond stiffness decreases, the slope of the bond slip curve becomes smaller, showing a nonlinear relationship, and soon reaches the ultimate bond stress. In the contrast test, the ultimate bond stress of the deformed steel bar is obviously higher than that of the circular steel bar.

2) Descending section: when the bond stress reaches the limit value, the concrete in front of each rib in the anchor length is basically destroyed, and the bond stress begins to decline. With the increase of the slip amount, the broken zone of intercostal concrete also expands continuously, the mechanical bite force gradually loses, and the bond slip curve decreases rapidly and ends at the point where the curvature of the underconcave curve reaches the maximum.

3) Residual stage: when the load drops to a certain degree, the bond slip curve enters the residual stress section, and the bond force will not disappear at this time. For the circular steel bar, the load is basically unchanged, and the binding force is mainly provided by the friction force between the steel bar and the PUC material. For the deformed ribbed steel bar, the curve shows that the load tends to rise and then to fall, and so on, until the steel bar is completely pulled out. This phenomenon indicates that the mechanical bite force of reinforcement and steel still exists at this stage. Therefore, in this stage, the bonding force of ribbed reinforcement is still composed of mechanical bite force and friction force.

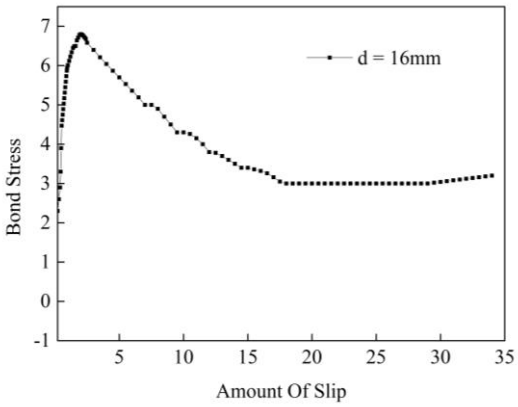

Fig. 19 - Bond-slip curve of deformed steel bar

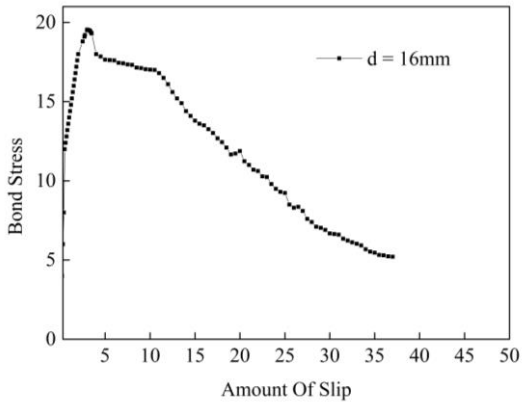

Fig. 20 - Bonding slip curve of circular steel bar

CONLUSION

In this paper, the test results of pull-out specimens are analyzed. The effects of the thickness of the protective layer, the anchoring length, the diameter of the steel bar and the surface shape of the steel bar on the bond anchoring performance were studied. The conclusions are as follows:

The average axial tensile strength of PUC material is 31 MPa, and the Poisson's ratio of the material is 0.27. The bending tensile stress-strain curve and the axial tensile stress-strain curve are obtained through fitting.

Contrastive analysis of pull-out specimens with different thickness of protective layer shows that the bond strength between steel bar and PUC material increases with the increase of thickness of protective layer. When coverage thickness is 70 mm, the average bond stress is 16.38 MPa, and when coverage thickness is 40 mm, the average bond stress is 10.53 MPa, which is only 76.50% of that when coverage thickness is 70 mm.

The average bond strength of pull-out specimens with different anchoring lengths decreases with the increase of anchoring length. When anchoring length (la) is 30 mm, the average bond stress

is 19.55 MPa, and when anchoring length (l_a) is 100 mm, the average bond stress is 10.65 MPa, which is only 54.48% of the average bond stress when anchoring length (l_a) is 30mm.

By comparing and analyzing the pull-out specimens with different steel bar diameters, it is found that the bond strength between steel bar and PUC decreases with the increase of diameter under the same anchoring condition, and the average bond stress decreases with the increase of anchoring length under different anchoring lengths. The bond strength of the round steel bar is significantly lower than that of the deformed steel bar, and the maximum bond strength is about 47.4% of that of the deformed steel bar under the same condition.

The bond slip curve of PUC material is similar to the bond slip curve of reinforced concrete, and the bond anchorage stress process can be divided into three stages: rising stage, falling stage and residual stage.

ACKNOWLEDGEMENTS

Thank You for the Open Fund project of key Laboratory of Ministry of Education for Disaster and Control of Major Engineering, Jinan University (20200904012)

REFERENCES

[1] Yalciner H, Eren O, Sensoy S, 2012. An experimental study on the bond strength between reinforcement bars and concrete as a function of concrete cover, strength and corrosion level. Cement and Concrete Research, 42(5):643–655.

[2] MB Muñoz, 2010. Study of bond behaviour between FRP reinforcement and concrete. universitat de girona.

[3] He S, Gong J, Jin F, et al, 2009. Deterioration characteristics of the bond between reinforcement and concrete subjected to freezing-thawing cycles and steel corrosion. Journal of Hydroelectric Engineering.

[4] Khalaf J, Huang Z, Fan M. 2018. A Study About the Effect of Bond between Steel Reinforcement and Concrete Under Fire Conditions// 2018 11th International Conference on Developments in eSystems Engineering (DeSE).

[5] Al-Dulaijan S U, 1996. Effect of environmental and mechanical conditioning on bond between FRP reinforcement and concrete.. The Pennsylvania State University.

[6] Al-Safy, R., Al-Mahaidi, R., Simon, G. P. 2013. A study of the use of high functionality-based resin for bonding between cfrp and concrete under harsh environmental conditions. Composite Structures, 95: 295-306.

[7] Hu, Y., Yuan, B., Cheng, F., Hu, X. 2019. Naoh etching and resin pre-coating treatments for stronger adhesive bonding between cfrp and aluminium alloy. Composites, 178: 107478.1-107478.11.

[8] Fernandes D, Azevedo R, Carvalho E P, et al, 2017. A Review on the Study of Bond Behavior between Reinforcement Thin Bars and Concrete.

[9] Henkhaus R E, 2009. Effect of epoxy thickness on bond between concrete and coated reinforcement. Purdue University.

[10] Ai T C, Gang X, Wang Q, 2009. experimental study on the bond behavior between corroded bar and concrete // International symposium on lifetime engineering of civil infrastructure;ISLECI 2009. College of Civil＆Hydropower Engineering,China Three Gorges University,Yichang 443002,P. R.China.

[11] UM Mahran. 2013. Theoretical Study for Bond Between Reinforcement Steel and Concrete.

[12] Zhang J F, Zhuang B Z, Zhang K X, 2016. EXPERIMENTAL STUDY TO INVESTIGATE MECHANICAL PROPERTIES OF POLYURETHANE-CEMENT COMPOSITE. Low Temperature Architecture Technology.

[13] Hussain H K, Liu G W, Yong Y W, 2014. Experimental study to investigate mechanical properties of new material polyurethane–cement composite (PUC). Construction & Building Materials, 50(jan.):200-208.

[14] Zhang K, Sun Q, University N F, 2018. Research on mechanical properties of the high-toughness polyurethane-cement composite(PUC) materials. New Building Materials.

[15] Haleem K. Hussain, Lianzhen Zhang, Guiwei Liu, 2013. An experimental study on strengthening reinforced concrete T-beams using new material poly-urethane-cement (PUC). Construction and Building Materails, 40: 104-117.
[16] Haleem K. Hussain, Guiwei Liu, Yuwen Yong, 2014. Experimental study to investigate mechanical properties of new material polyurethane-cement composite (PUC). Construction and Building materials, 50: 200-208.
[17] G Liu, H Otsuka, Y Mizuta, A shimitsu, 2006. A Foundational Study on Static Mechanical Characteristics of the Super Lightweight and High Strength Material Using Fly-ash. Journal of the Society of Material Science Japan, 55(8):738-745.
[18] Wang J, Liu G W, Y LH, 2013.Research on the application technology of strengthening hollow slab bridge with MPC composite material. Highway, 8: 39-43.
[19] Jing L, Yin S P , Duan K , 2019. Analysis of the interface bond property between the concrete and steel bar under textile reinforced concrete confinement. Construction and Building Materials, 224:447-454.
[20] Zhao Y , Jin W , 2002. Test Study on Bond Stress-Slip Relationship of Concrete and Steel Bar. Journal of Building Structures.
[21] Cao F, Li J, Wang C, et al, 2016. Experimental study on bond-slip property between corroded rebar and recycled concrete. Journal of Building Structures.

CIVIL ENGINEERING JOURNAL

Article no. 51

THE CIVIL ENGINEERING JOURNAL 3-2021

BACK ANALYSIS OF OSTERBERG-CELL PILE LOAD TEST BY MEANS OF THREE-DIMENSIONAL GEOTECHNICAL MODELING

Szilárd Kanizsár

Multidisciplinary Doctoral School of Engineering Sciences, Széchenyi István University, Győr, Egyetem tér 1., H-9026, Hungary; kanizsar@t-online.hu

ABSTRACT

In 3D geotechnical modelling it is essential for the realistic simulation of soil behavior that the parameters of the hardening soil with small strain constitutive model are specified appropriately. The possibility of deriving these parameters for very stiff cohesive soils similar to the so called Kiscell clay that has a significant role in deep construction projects in Budapest, from laboratory and field tests is rather limited. The results of the pile load test completed for the MOL Campus high-rise building project proved to be useful data source. The article presents the circumstances of the quoted Osterberg-cell pile load tests and the modelling of the pile performed by the above-mentioned soil model. The parameters specified on the basis of laboratory tests - and in absence of those based on literature - data can be fine-tuned by approaching the load test results.

KEYWORDS

Geotechnical modeling, Kiscell clay, Plaxis 3D, Soil material model, Pile load test

INTRODUCTION

The landscaping regulations that are currently in force indicate two areas for tower buildings of 120 m height. One of them is on the northern edge of Csepel Island (Budapest XXI. district), while the other is near Kopaszi Dam (Budapest, XI. district), where the first high-rise building is currently under construction. The office complex named “MOL-Campus” will consist of a 120 m high, 28-storey tower and the adjoining 6-storey “podium” building, with a 4-level underground parking lot underneath. The foundation of the tower building was constructed as a CPRF (combined pile raft foundation) structure, the loads of the building are transferred to the subsoil partially by the typically 2.2 m thick reinforced concrete foundation slab and the 135 pcs of 1.20 m diameter bored piles. The foundation is confined in a watertight manner by means of a diaphragm wall, the temporary dewatering during construction was ensured by the Kiscell clay constituting the bedrock of the area and temporary drainage wells. The final drainage of the building is provided by the seepage system constructed under the foundation slab. The podium building was constructed on reinforced concrete raft foundation.

For the design of the CPRF structure a test pile had previously been bored. This – differently from the traditional reaction beam layout – was carried out by implementing the so-called O-cell (Osterberg-cell) technique. The aim of the load test was so that its results would provide values for the shaft friction and base resistance of the piles of the foundation structure. 3D modeling was performed related to the CPRF structure and the test pile by means of PLAXIS 3D geotechnical software, the results of which were published [1]. In this finite element model the Kiscell clay with its stiff, rock-like behavior was described by the Mohr-Coulomb soil model selected on the basis of more considerations. As an enhancement to the modeling, the newer model of the pile load test was also prepared in relation to the Kiscell clay, using the more advanced HSS (hardening soil with small strain stiffness) soil model. This possibility among all enables to take into consideration over-

consolidation, deformation moduli depending on stress level and greater stiffness acknowledged in the range of initial and small deformations.

Certain parameters related to the Kiscell clay could not be determined either from field or laboratory tests. The determination of these was among the aims of the research. Once the building is structurally complete and the settlement data is available, the validation and – if required – the correction of the parameters of the HSS soil model of the Kiscell clay and of the entire geotechnical model of the building will be enabled.

METHOD OF THE MODELING

Soil environments

On the basis of the borings in the vicinity of the test pile, soil stratification outlined in Figure 1. is to be considered. Due to quantity restrictions, there is no possibility for the detailed outlining of the layers located above the Kiscell clay, their parameters are included in Table 1.

The Kiscell clay appears in the depth of 18.5 m under the surface. It must be noted, however, that this depth is only valid in the vicinity of the borehole near the test pile, the clay surface related to the entire area shows an inclination moving away from the Danube. On the basis of the plasticity index (I_p = 15 - 25%) the clay can be regarded as low-medium plasticity clay. Resulting from its low water content (w < 10%) and high consistency index (I_c = 1.4 - 1.5), it can be classified as hard. According to tests related to permeability (k = (3÷5)·10^{-12} m/s), it can be regarded as watertight. Figure 2. presents the soil samples of the Kiscell clay taken at depth of ~20 m.

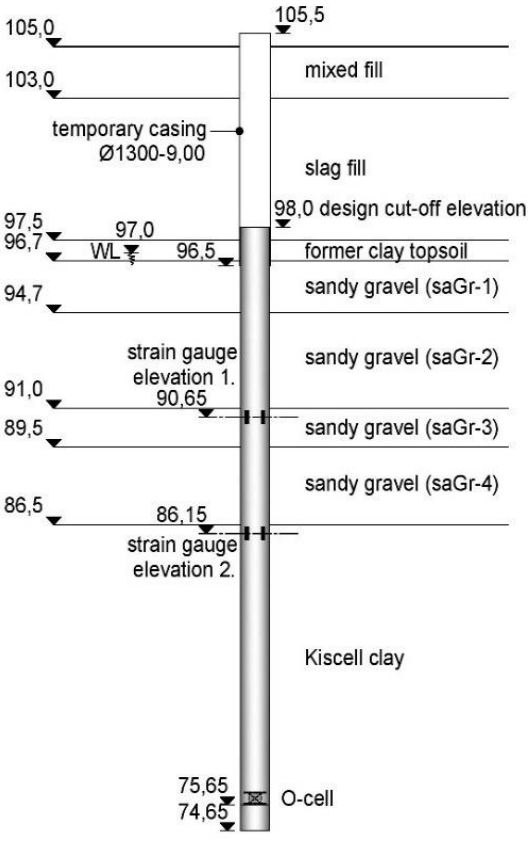

Fig. 1 – Stratification

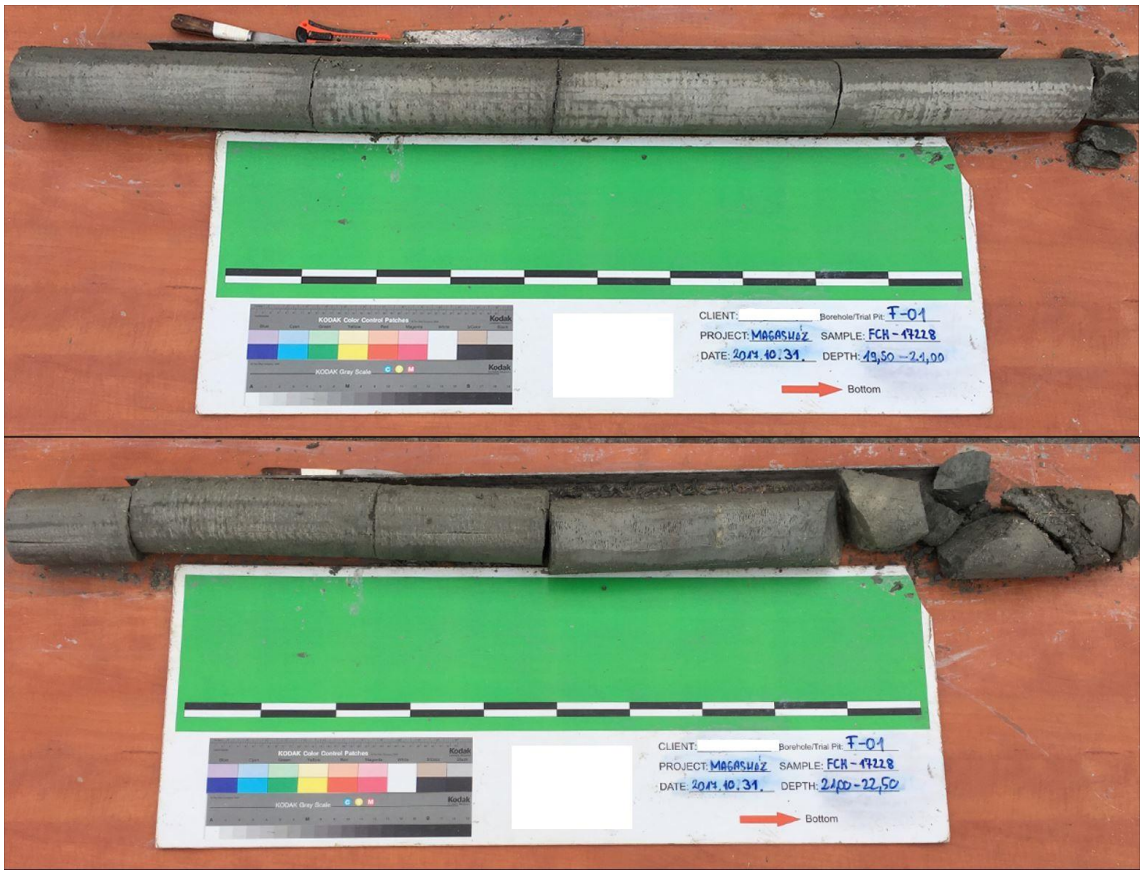

Fig. 2 – Core samples from the top zone of the Kiscell clay layer

Tab. 1: Model parameters of soil layers

model parameter	unit	coarse grained fill	slag fill	sandy silt fill	sandy gravel saGr-1	sandy gravel saGr-2	sandy gravel saGr-3	sandy gravel saGr-4	Kiscell clay
natural unit weight (γ_n)	kN/m^3	17,0	17,0	18,0	20,0	21,0	20,0	21,5	23,0
saturated unit weight (γ_t)	kN/m^3	18,0	18,0	19,0	20,0	21,1	20,0	21,5	23,0
initial void ratio (e_{init})	-	0,80	0,80	0,70	0,65	0,50	0,65	0,4	0,3
internal friction angle (ϕ')	°	28	24	22	31	31	31	31	28
cohesion (c)	kPa	1	1	5	1	1	1	1	var
dilatation angle (ψ)	°	0	0	0	10	10	10	10	-
undrained shear strength (s_u)	kPa	-	-	-	-	-	-	-	951
oedometric modulus (E_{oed}^{ref})	MPa	33,0	9,5	5,1	16,9	26,9	14,3	26,9	var
Poisson-ratio (ν)	-	-	-	-	-	-	-	-	0,2
reload modulus (E_{ur}^{ref})	MPa	99,0	28,5	15,3	50,0	90,0	50,0	80,0	var
dev. elastic modulus (E_{50}^{ref})	MPa	33,0	9,5	5,1	16,9	26,9	14,3	26,9	var
exp. of hardening function (m)	-	0,6	0,8	0,8	0,5	0,5	0,5	0,5	1,0
initial shear modulus (G_0^{ref})	MPa	95,6	61,9	53,0	108,7	153,7	101,9	211,6	var
shear strain ($\gamma_{0,7}$) [$\cdot 10^{-4}$]	-	1,0	1,0	1,0	2,3	2,6	2,4	2,9	var
permeability (k)	m/s	10^{-3}	10^{-3}	10^{-5}	10^{-6}	10^{-6}	10^{-6}	10^{-6}	$4 \cdot 10^{-12}$
over-consolidation ratio (OCR)	-	-	-	-	-	-	-	-	var

The groundwater typically saturates in the sandy gravel layers, its level is controlled by the actual water level of the Danube, which is located nearby. The groundwater level observed at the time of the construction of the test pile was in the depth of 8 m below the construction platform. The model parameters deriving from the results of the laboratory tests performed on the soil layers and those estimated are included in Table 1.

The non-measured parameters and those that were measured but clearly had greater uncertainties had not previously been set, their determination was the task of the modeling. These parameters are included in the table with the indication *var* (variable).

Layout and loading of the test pile

Description of the O-cell pile load test

In comparison to the traditional, reaction beam pile load test, the O-cell technology does not require anchoring piles to provide the reaction forces. One or more single-use hydraulic loading unit, the O-cell is installed in the pile to be loaded at a certain depth or even in more than one depth levels. The position of O-cell/cells shall be determined so that the characteristics of the toe resistance and skin resistance of the pile and the curves of the specific skin frictions mobilized in typical layers shall be determined from the displacements originating from the loads. Rationally, it must also be observed that for the exhaustion of the resistances arising on single pile sections those arising on other parts of the pile shall provide sufficient resistance. In the simplest case, the toe resistance and the skin friction of the pile can be separated by means of the cell located in the immediate vicinity of the toe presuming that they are essentially of the same magnitude.

Due to the hydraulic pressure in the O-cell, the cell starts to open along the pile axis and forces of opposite directions transferred on its bottom and top plains to displace the pile section under the cell downwards and the pile section above the cell upwards. If the cell is immediately above the toe, the displacement of the bottom part is practically determined by the toe resistance, whereas the top part is determined by the skin friction and the elastic compression of the pile. Since the toe resistance of the bottom part and the skin resistance of the top part balance each other, the loading can only be carried on until the ultimate value of either bearing capacity component is reached. Consequently, no direct information is available on the ultimate value of failure resistance of the stronger part.

Construction and instrumentation of the test pile

The test pile at MOL Campus was constructed with a 1200 mm nominal diameter in a location outside but in the vicinity of the diaphragm wall enclosed area. The pile was bored from the original 105.00 maBSl (meter above Baltic Sea level) terrain level following the installation of a Ø1300 mm, 8.65 m long guide tube casing, by means of auger and drum tools using fluid support protection. The borehole following the cleaning of the toe, the change of the slurry and the installation of the reinforcement cage was concreted between the 74.65 maBSl toe level and the 98.00 maBSl designed trim back level.

The pile was loaded using a 540 mm diameter, 12.9 MN O-cell unit, which had previously been positioned and installed into the reinforcement cage 1.00 m above the pile toe. Thus the 23.35 m long pile was divided by the O-cell into a 22.35 m long top part and a 1.00 m long bottom toe section. The displacements of the O-cell were measured by four installed displacement gauges. Two pairs of strain gauges were installed at two levels in the top pile section, which when measuring deformation as a result of the normal force provide data for the determination of the change of specific shaft resistances. The elastic compression of the pile was measured by means of the installed indication rods. For the measurements a reference holder set up on the terrain level and

displacement gauges installed on it were used. The displacements of the pile were corrected by the movement of the reference holder.

Measurement results of the test pile

Resistance of the top part

The resistance of the top part is provided by the skin friction. For the determination of the net load acting upon the pile from the load operated by the cell for the top section the counterforce shall be deducted, the value of which is 0.36 MN. Ignoring the last three load steps due to the above-mentioned reasons, the displacement of the top section was 55.97 mm due to the 12.34 MN force (11.98 MN net load). It is worth taking into consideration the measurement data describing the relationship between the force and the displacement for the modeling up to this point as the unconsolidated displacements measured in the last three steps are probably smaller than the actual ones.

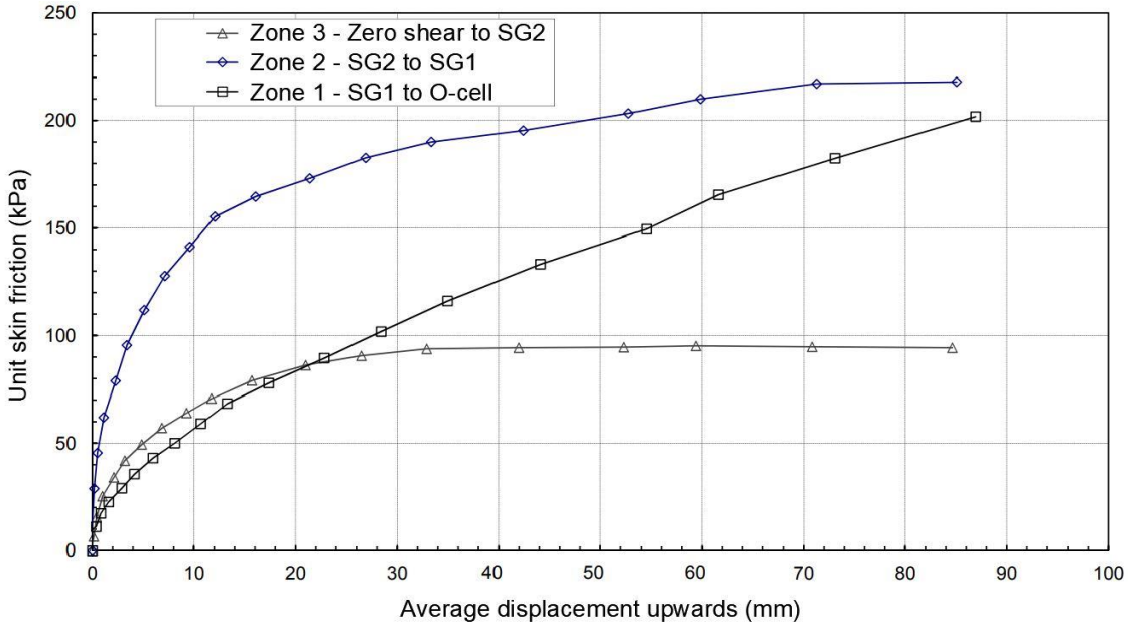

Fig. 3 – Mobilized specific shaft resistances

The strain gauges set up on two levels divided the shaft along its length into three zones. The increase of specific shaft resistance values could be determined for each zone and it was striking that their characteristics significantly differ. The curves related to individual zones are indicated in Figure 3.

The resistance of the top part is constituted by two values. One is the rigid body displacement of the pile, the other is its elastic compression. It results from the curves of Figure 3. that the characteristics of the load-displacement are determined by the behavior typical of zones 2 and 3. In accordance with the above, the load-displacement curve of the top section (Fig. 4.) does not follow the classic shape of Zone 1, but similar to curves characterizing zones 2 and 3, it demonstrates that increasing forces are related to the increasing displacements in the range under investigation.

Resistance of the bottom part

The displacement of the bottom section is fundamentally a rigid body displacement as in relation to it the amount of the elastic compression can be ignored due to the small length. Ignoring the last three load steps, the displacement of the top section was 51.54 mm due to the 12.34 MN force, which is similar to that of the top section. The characteristics of the toe resistance, which is entirely determined by the Kiscell clay, cannot be regarded as typical (Figure 4). The curve includes

an inflexion point at the load that belongs to it a certain degree of stiffening might be experienced for greater forces. The displacements do increase due to the increasing load but at a slightly smaller rate than before. This is a contrary behavior to what is common. No direct explanation can be traced in the measurement data, however, the displacement gauges of the O-cell and the strain gauges both indicated some anomaly, which might refer to uneven force transfer and eccentricity. (It might also arise that the initial greater displacements derive from the compression of the soil that was slightly loosened at the base of the boring and of the settled slurry.) Certainly, the modeling of the inflexion curve could not have been the aim, only the approximation of the curve with the least deviation.

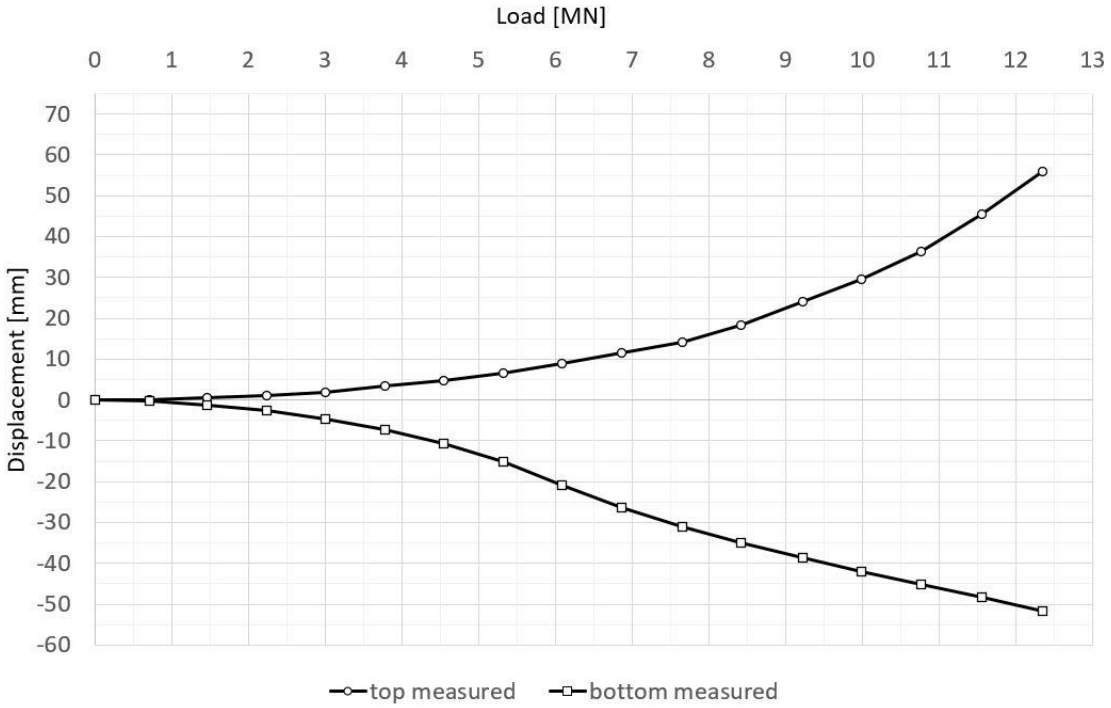

Fig. 4 – Load test curves of top and bottom parts

Modeling of the pile load test

Model formation

The 3D finite element model of the test pile was constructed in the Plaxis 3D software (Figure 5.). By taking into consideration the dimensions of the pile, a layered soil-block of 20x20 m layout and 40 m depth modelled the bedding medium, which was ensured by the distance from its limit surfaces from the pile so that the model boundaries could not influence the results.

The model of a 1.20 m nominal diameter 23.35 m long pile was constituted by tetrahedron volume elements with 10 nodes.

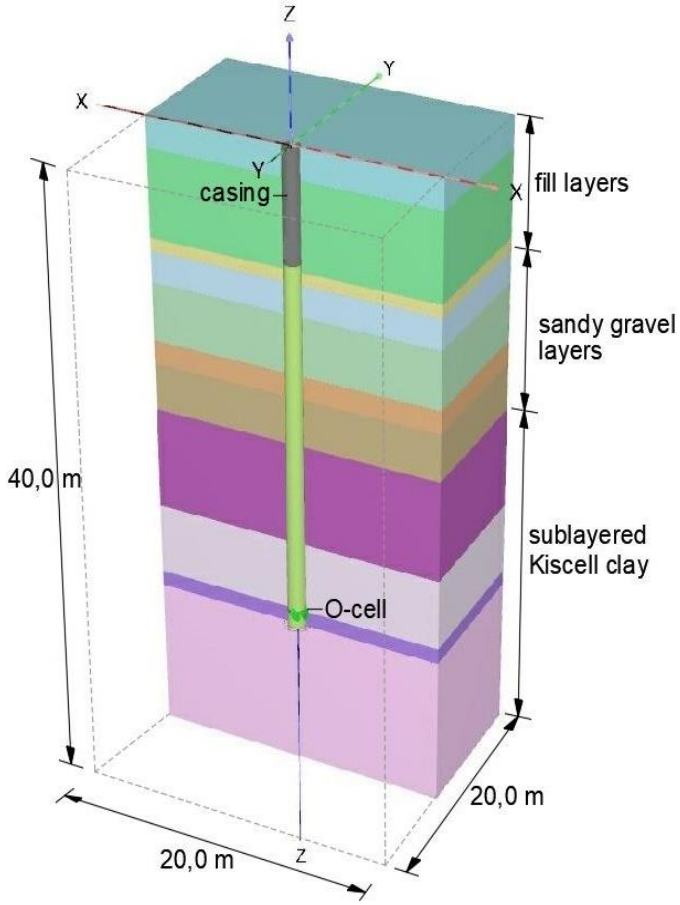

Fig. 5 – Model of O-cell pile load test

The special details of the test pile got unique attention, therefore, the realistic description of these is very important in the behavior of the entire model. These details are the casing, the O-cell, the interface elements simulating the relationship between the soil and the structure, the characteristics of the fresh concrete and the modeling technological aspects of the over-consolidation of the Kiscell clay.

The installation of the casing is a preliminary step that must be modelled as it also has a role in supporting the soil above the trim back level plain and the simulation of the stress state preceding the load. Its material and geometry can directly be modelled.

The modeling of the O-cell is a cardinal issue (Figure 6.) since this structure divides the pile in two and loads them immediately. The results that had been stated and published in Tschuchnigg's [2] PhD dissertation were taken into account at the modeling. The extension of the O-cell and thus the contrary movements of the two pile sections must be modelled in a way that the cell located between the pile sections shall represent materialistic continuity just like in reality but the volume elements of the neighboring soil could not "enter" the hole expanding due to the loading as a result of horizontal soil stresses. This for example might be achieved by means of the modeling of the steel membrane with orthotropic characteristics, which is located between the loading plates of the O-cell. In order to eliminate any load uptake by the membrane, its vertical stiffness was selected to be practically zero. Also, the prescribed displacement required for vertical elements shall be operated along the membrane surface, the value of which is also zero. It ensures that the steel "collar" is able

to follow the opening-closing axial movement of the O-cell. However, for radial forces on the pile axis it behaves stiffly, supporting the neighboring soil elements.

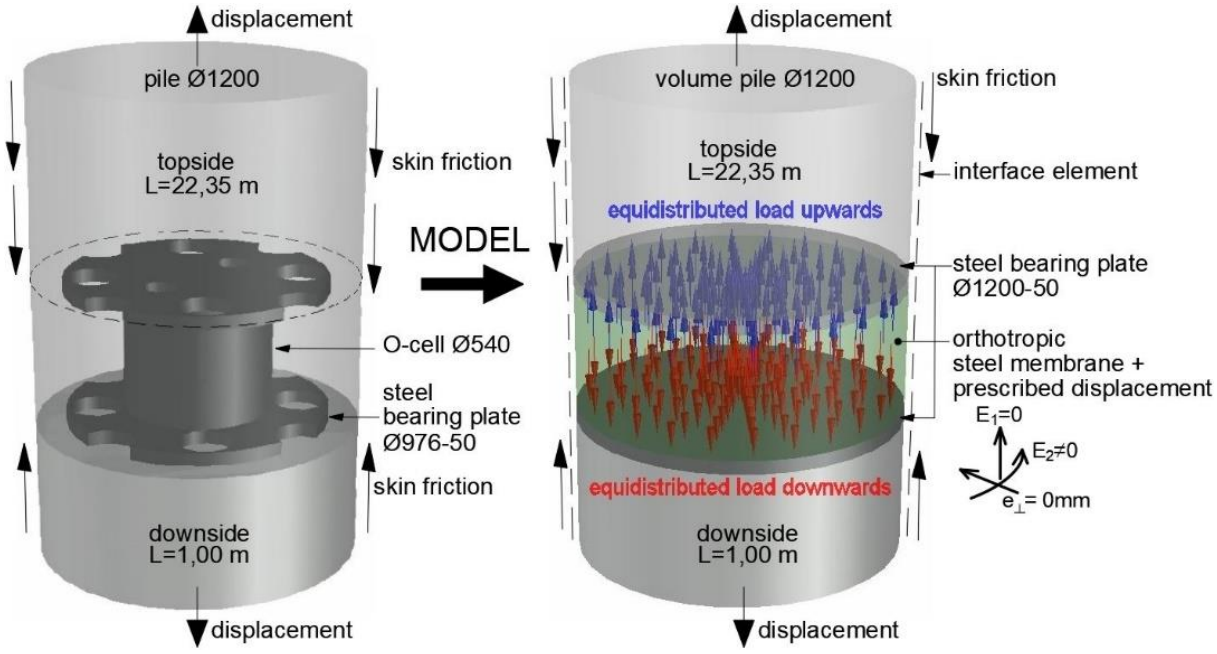

Fig. 6 – Model of O-cell

The relative displacement of the soil and the pile might be ensured by the use of interface elements. The ratio (R_{inter}) serving for the quantification of the interaction can be set to be proportional to the shear strength of the soil being in contact with the pile. This also means that for the explored layers along the shaft different R_{inter} values shall be provided. Besides the shaft surface the relative displacement must also be allowed along the toe surface. Since the shaft surface and the toe level of the bottom section are in the same Kiscell clay, the interactions under the toe and along the shaft cannot be modelled with the same R_{inter} set value. There are two different mechanisms in which the rate of displacements significantly differs. The cm magnitude relative vertical displacement forming along the shaft and the mm magnitude horizontal displacement of the soil moving out of the loaded zone laterally under the toe shall be handled separately from modeling aspects. A part of the shaft of the top section is located in the Kiscell clay just like the shaft of the bottom section. As their displacements are nearly identical due to the identical loads, the specific shear strength is mobilized on the shaft surfaces in a similar scale. On the basis of the above, it is reasonable to relate the same R_{inter} value for the shaft sections. Since the shaft surface of the pile boreholes deepened in the very stiff ($I_c \approx 1.5$) Kiscell clay – in accordance with information gained on the excavated pile walls – is characterized by a texture that is very smooth (near glass), which in this case also had a bentonite „lubrication", the value $R_{inter} \approx 0.15$ applied during the modeling shall be regarded as realistic. In order that different R_{inter} values could be provided for the toe surface and shaft surface of the bottom section, the Kiscell clay had to divided in two sublayers in the plain of the toe. Their parameters are all identical, apart from the R_{inter} values. With this technique, different R_{inter} values might be set for the pile toe and pile shaft operating in the same soil.

At the concreting of the pile bore it is reasonable to take the liquid state of the concrete into account as until it sets it only acts as a loading medium for the soil zone around the borehole to reach its stress state prior to the loading. Therefore, during the modeling, in the piling phase,

regarding its material the application of the elastoplastic concrete soil model was justified, with time dependent strength, stiffness and plasticity characteristics.

Another essential question is the consideration of over-consolidation of the Kiscell clay. In the HSS soil model this might be realized by providing the OCR (over-consolidation ratio) or POP (pre-overburden pressure) stress, the latter of which is also known as OCD (over-consolidation difference). The modeling of the load test was completed by providing the OCR values, which were available from the laboratory test results published by Józsa [3] regarding the over-consolidation. The soil samples were taken of the boreholes deepened for metro line M4. For the estimation of the pre-consolidation stress Józsa set up some connections regarding the Kiscell clay located on the Buda side (Kelenföld, Lágymányos) by using the results of the oedometric and triaxial tests (E_{oed} and E_{ur}). According to this publication, the OCR values that are hyperbolically connected to depth, fall between 1.5 and 4.5 from the connection set up by means of the oedometric modulus, whereas on the basis of the connection determined from the unloading-reloading modulus, the values range between 2.0 and 4.6. During the modeling the OCR ratio changing by depth might be taken into consideration with division to sublayers. The bottom of the sublayers is -25, -30 and -40 m counting from terrain level regarded as zero. The average OCR values determined for the three sublayers are 3.5, 3.0 and 2.5, respectively.

The modeling follows the entire process of the pile load test, from the preparation of the boring until the last load step. For this the following phases had to be defined in the finite element software:

Step 1: initial conditions and stress state
Step 2: boring of the casing
Step 3: pile boring, concreting, setting of the concrete
Step 4: activation of O-cell with 1.51 MN force
Step 5: unloading of O-cell, zeroing the displacements
Step 6-21: O-cell loading in 16 steps up to the force of 12.34 MN.

Initial parameters

The values of modeling parameters that are required for the application of the HSS soil model are included in Table 1. No fixed values are included in the table for certain parameters of the Kiscell clay that bear uncertainty greater than usual. Concerning the above, it is worth starting from the value ranges derived from the statistic processing of previous laboratory tests and their precision, their values considered the most favorable are provided by the modeling output calibrated on the basis of the pile load test results. The values of the parameters will be outlined in the following:

- compression modulus: E_{oed_init} = 150 ÷ 250 MPa, which signifies fairly vast value ranges. However, after the comparison of the values of associated moduli related to different locations and various depth (see [4]), the examination of such a value range seemed reasonable for the different Kiscell clay samples,
- deformation modulus related to 50% of the final value of the deviatoric stress: $E_{50\_init} = E_{oed\_init}$ = 150÷250 MPa and $E_{50}^{ref}{}_{\_init} = E_{oed}^{ref}{}_{\_init}$ on the basis of the Plaxis 3D software and bibliographical references [5], as no laboratory test was performed for this modulus,
- unloading-reloading modulus: $E_{ur}^{ref}{}_{\_init} = 3 \div 5 \cdot E_{oed}^{ref}{}_{\_init}$, also on the basis of biographical recommendations [6] replacing the missing actual test results,
- cohesion: c = 750 ÷ 1000 kPa the range of values determined on the basis of the current triaxial tests,
- reference value of the initial shear modulus: $G_0^{ref}{}_{\_init}$ = 200 MPa, which resulted from the comparison of the results of the 2 x *downhole* measurements and the laboratory tests, which showed a significant deviation and also of the values that can be calculated by the formula recommended by Hardin and Black [7],

- amount of the shear deformation for the modulus of $0.722 \cdot G_0 \rightarrow \gamma_{0.7\_init} = 7.5 \cdot 10^{-3}$ is the value estimated on the basis of the biography due to the uncertain results of the resonant column tests and the torsional shear tests,
- over-consolidation ratio: OCR = 1.5 ÷ 4.5 in the lack of direct laboratory measurements in accordance with related description in the previous section,
- interface parameter for the shaft: R^s_{inter} = 0.15 ÷ 0.30 estimated range of values,
- interface parameter for the toe: R^t_{inter} = 0.80 ÷ 1.00 estimated range of values.

The calculation of various modulus values for the 100 kPa reference stress level used in Plaxis 3D was completed by the following formula:

$$\mathrm{M}^{\mathrm{ref}} = \frac{\mathrm{M}}{\left(\frac{\mathrm{c} \cdot \cos\varphi + \sigma' \cdot \sin\varphi}{\mathrm{c} \cdot \cos\varphi + \mathrm{p}^{\mathrm{ref}} \cdot \sin\varphi}\right)^{\mathrm{m}}} \qquad (1)$$

, where

- M is the oedometric modulus (E_{oed}, E_{50}, E_{ur}) or the initial shear modulus (G_0) in kPa,
- c and φ according to *Tab 1*,
- σ is the σ'_1 (effective vertical stress) for E_{oed} *or* σ'_3 *(confining stress in triaxial test)* for E_{50}, E_{ur}, G_0 in kPa
- p^{ref} = 100 kPa is the reference confining pressure.

RESULTS

The final results of the modeling were represented by the curves produced for the bottom and top parts that were obtained by the systematic fine tuning of the model parameters of the Kiscell clay and their deviation in relation to the load test curves was the least. The deviation was measured by the method of the least squares. The minimization of the error function was realized on the basis of the following expression:

$$min[\sum_{i=1}^{16}(s^b_{mo_i} - s^b_{me_i})^2 + \sum_{i=1}^{16}(s^s_{mo_i} - s^s_{me_i})^2] \qquad (2)$$

, where

- $s^b_{mo_i}$ the modelled displacement of the bottom section in the ith load step,
- $s^b_{me_i}$ the measured displacement of the bottom section in the ith load step,
- $s^s_{mo_i}$ the modelled displacement of the top section in the ith load step,
- $s^s_{me_i}$ the measured displacement of the top section in the ith load step.
- i the number of load steps (1-16).

During the modeling the values of the model parameters of the layers located above the Kiscell clay that had been assumed on the basis of the Soil Investigation Report were kept unchanged. It must be mentioned that the specific shaft resistances simulated by the above demonstrated a good match with the values of the load test. Although approximately half of the entire pile resistance was provided by the pile section that is in the grained layer, the parametrization is primarily focused on the Kiscell clay due to related research aspects of the CPRF structures designed to be installed in this layer. Apart from the fixed parameters of the Kiscell clay, by the fine

tuning of the factors regarded as sensitive on the basis of the parameter test that cannot be outlined in detail due to lack of space, their values optimal from the aspect of the curve fitting were determined. These were the following: E_{oed}^{ref}, E_{50}^{ref}, E_{ur}^{ref}, c'_{ref}, R^{s}_{inter}, R^{t}_{inter}. When fitting the curve, the parameters of the numerical simulation were selected that provided the similarities in the nature and values of the model curves and pile load test curves with the least deviation. In this simulation the parameters of the Kiscell clay were provided with the values included in Table 2, this shall thus be regarded as the most appropriate group of HSS parameters on the basis of the simulation of the pile load test. In the Table, sublayers *a, b* and *c* of the clay layer divided due to the above-mentioned modeling technical reasons are included. The curves measured and obtained by the HSS model are represented in Figure 7. in which a curve achieved by the so-called Cemsolve calculation procedure is also demonstrated. This latter method was developed by a professional company specializing in O-cell pile load tests. Although the curve fit can be regarded as very good, the mobilization procedure of the specific shaft resistance of the Kiscell clay could not be modelled correspondently. A good correspondence in this aspect only resulted from the reproduction of the values obtained at the end of the load test with almost no deviation, by means of numeric simulation.

Tab. 2: Calibrated model parameters of Kiscell clay

sub-layer	E_{oed}^{ref}	E_{ur}^{ref}	m	c'_{ref}	ϕ'	ψ'	$\gamma_{0,7}$	G_0^{ref}	R_{inter}	OCR
	kPa	kPa		kPa	°	°	-	kPa	-	-
a	125.500	502.500	1,00	850	28	0	$7{,}5 \cdot 10^{-3}$	215.000	0,1400	3,5
b	118.000	472.000							0,1400	3,0
c	109.000	437.000							0,8500	2,5

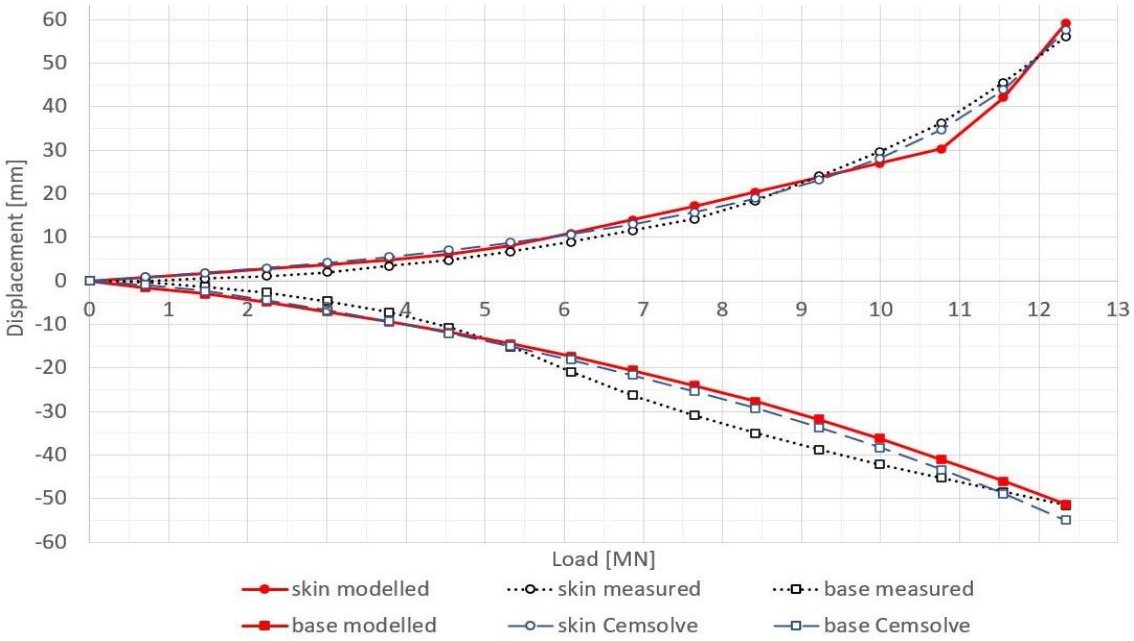

Fig. 7 – Modeled and measured load-displacement curves

It shall be mentioned that the simulation of the up to down loading was also realized using the model parameters included in Table 2, which cannot be published in the present article due to lack of space. It must also be noted that the self-anchoring, split pile so-called VUIS-pile load test can also be processed in a similar manner, a simpler attempt at which had previously been demonstrated by Szepesházi [8].

CONCLUSION

It results evident from the paper that by applying the HSS soil model with the Plaxis 3D software, if the model parameters are selected appropriately a real O-cell pile load test can be simulated correctly. It is also justified by the good correspondence of the load/displacement curves obtained for the bottom and top pile sections and the curves of measured values.

The article describes the HSS soil model parameters of the Kiscell clay settled as the deep soil environment of the test pile that are regarded as the most authentic on the basis of simulation, which in case of Kiscell clay soils of similar characteristics (typically located in Lágymányos and Kelenföld) might be used for their future modeling.

Although the Mohr-Coulomb soil model might also be suitable for the modeling of the stiff Kiscell clay that has rock-like characteristics, the HSS soil model promises to provide more precise results. One of its important advantages is the possibility of consideration of over-consolidation. On the basis of the parameter sensitivity test it might be stated that the OCR has a significant influence on the toe resistance. The issue of unloading-reloading modulus is related to over-consolidation, which has an essential role in all displacement calculations. On the basis of the simulation, it can be suggested that its value shall be 4 times the modulus related to the primary loading.

The article also demonstrates that for the modeling the Kiscell clay shall be divided into zones, especially due to the significant dependence of the OCR value on depth. It is also demanded by the fact that for the good modeling various R_{inter} values shall be provided regarding the different structures and the interface elements of the pile shaft and toe.

The modeling techniques of the O-cell loading equipment that were presented and the processing based on the comparison of data measured and gained by simulation might – presumably – be applied for modeling other O-cell pile load tests. Besides the above, the results of the outlined pile load test can also be used in the modeling of the structural piles for the design of a traditional pile foundation or a CPRF structure.

ACKNOWLEDGEMENTS

The author would like to thank Dr. Szepesházi Róbert and Dr. Wolf Ákos for providing help and proof reading.

REFERENCES

[1] Hudacsek P., Kanizsár Sz., Koch E., Szepesházi R., Szilvágyi Zs., Wolf Á., 2020. A MOL Campus alapozásának vizsgálata (Analysis of Foundation of MOL Campus), In: Proceedings of the Geotechnika 2020 Conference, Herceghalom, Hungary, 12–14 October 2020, pp. 62–74.

[2] Tschuchnigg, F., 2012. 3D Finite Element Modeling of Deep Foundations Employing an Embedded Pile Formulation – Dissertation, Graz, pp. 162-168.

[3] Józsa V., 2016. Estimation and Separation of Pre-consolidation Stress Using Triaxial- and Oedometer Test in Kiscelli Clay, Periodica Polytechnica Civil Engineering, Vol. 60, No. 2, pp. 297–304. (DOI: 10.3311/PPci.9068)

[4] Görög P., 2007. Engineering geologic properties of the Oligocene Kiscell Clay, Central European Geology, Vol. 50, No. 4, pp. 313–329. (DOI:10.1556/CEuGeol.50.2007.4.2)

[5] Schanz, T., Vermeer, P.A., Bonnier, P.G., 1999. The hardening-soil model: Formulation and verification. In R.B.J. Brinkgreve, Beyond 2000 in Computational Geotechnics, Balkema, Rotterdam, pp. 281-290. (DOI:10.1201/9781315138206-27)

[6] R.B.J. Brinkgreve, W. Broere, 2004. Plaxis 3D Foundation Version 1., Part 3: Material Model Manual, Balkema, Rotterdam, pp. 1-1.

[7] Hardin, B.O., Black W.L., 1969. Vibration Modulus of Normally Consolidated Clay, Journal of the Soil Mechanics and Foundation Division, ASCE, Vol. 95, No. 6, pp. 1531–1537.

[8] Szepesházi R., Németh Gy., 2005. Az osztott cölöpös próbaterhelés feldolgozásának fejlesztése, Kutatási jelentés (Developing of the processing of split pile load test, Research Report), Széchenyi István Egyetem, Győr

CIVIL ENGINEERING JOURNAL

Article no. 52

THE CIVIL ENGINEERING JOURNAL 3-2021

RESEARCH ON FORCE AND MODAL ANALYSIS OF THE CANTILEVER ROOF MODEL OF A STADIUM

Qian Zhang, and Bairu Lu and Bei Jia

Xi 'an Eurasia university, School of Architecture And Engineering, xi 'an, shaanxi, 710065, China; zhangqian1@eurasia.edu

ABSTRACT

The large-span roof structure is favored by architects and structural engineers all over the world for its novel architectural shape and reasonable structural characteristics. It has been widely used in large public buildings such as sports buildings, memorial buildings and cultural buildings. Based on the structure design of the fourth national college students' competition winning entries for the model, this paper introduces the stadium upper cantilever roof structure model selection, process design, interface, etc. Using the finite element software ANSYS to analyze the model structure under different load conditions of the static performance, we acquire its natural frequency. The results show that the model meets both the strength and stiffness requirement.

KEYWORDS

Roof structure, Static analysis, Modal analysis, Strength

INTRODUCTION

The large-span roof structure is favored by architects and structural engineers all over the world for its novel architectural shape and reasonable structural characteristics. It has been widely used in large public buildings such as sports buildings, memorial buildings and cultural buildings [1,2]. The national college student structural design competition aims to cultivate students' innovation consciousness, team work and engineering practice ability. The students will organically combine the learning and the need together which will effectively raise the quality of innovative talent training. The competition of the titled is upper stadium cantilever roof structure design. We use the method of combining the theoretical analysis and experimental research together to conduct the structure model selection and determine the component section. With the finite element design software to analysis the force and modal, we can optimize the production process according to the analysis results so as to ensure the overall stability of the structure.

MODEL DESIGN

Model overview

According to the requirements of the structural design competition, we designed the cantilevered roof model of the stadium, with the column height of 200mm. The base of which is triangular and the top of which is quadrilateral. Cantilever girder is triangular with a cantilever length of 600mm, as shown in Figure 1. The model structure is made of wood, and the surrounding material is made of cloth paper. The mechanical properties are shown in Table 1.

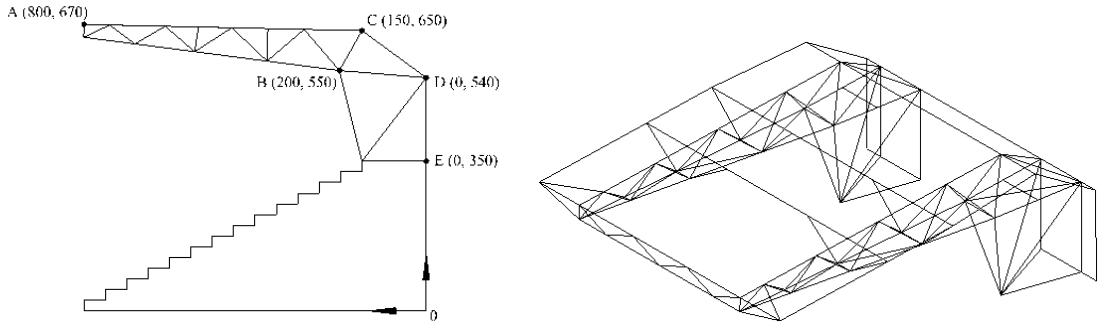

Fig. 1 - Schematic diagram of the model:

Tab. 1: Mechanical properties of wood

Name of the material	Elastic modulus （MPa）	Poisson's ratio	Density (kg/m^3)	Tensile strength (MPa)	Compressive stress (MPa)
wood	1.0×10^4	0.3	283	30	19

By analyzing the mechanical characteristics, the advantages and disadvantages of various stadium roof systems, and referring to a large number of classic stadiums around the world, the model design scheme was finally determined after repeated theoretical analysis, optimization and comparison. In other words, the cantilever roof structure of truss stadium was adopted as shown in Figure 2.

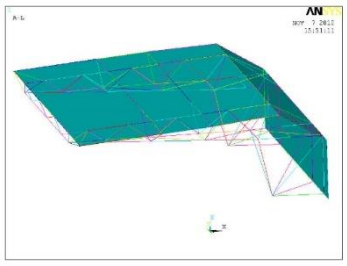

Fig. 2 - Truss type of the stadium roof structure

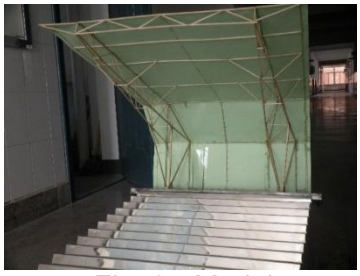

Fig. 3 - Model

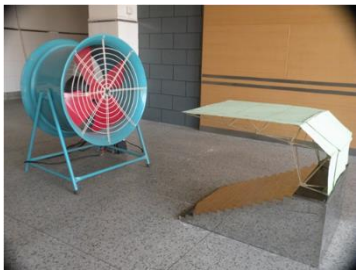

Fig. 4 - Model test

Selection of the section

In the process of model making, we adhere to the design idea of "clear concept, reasonable innovation, clear force, reliable structure", and comprehensively consider the mechanical properties of wood, the feasibility of model making, the appearance of model facade as well as the overall effect and other factors.

By combining theoretical analysis and experimental study together, we compared the mechanical and deformation properties of hollow section column and solid section column, and then finally determined the form of cantilever section. The model is shown in Figure 3, and the model test is shown in Figure 4. The vertical column adopts the combination of two spatial quadrangles, each limb adopting the wooden rod with rectangular section. The upper chord of the cantilever girder adopts the “T” shape wood, the lower chord adopts the “L” shape angle wood and the abdomen pole adopts the square wood and rectangular rod. The detailed section is shown in Table 2.

Tab. 2 - Section size details

Cross Section type	Wooden pole with rectangular section	"T" type of wood	"L" type Angle of wood	Square wood	Rectangular wood
Section size （mm）	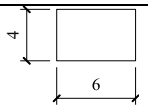	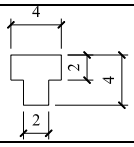	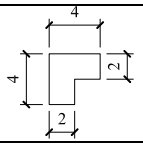	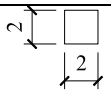	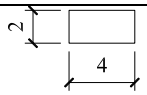

Model structure diagram

See Figure 5 for the plan and elevation of the model, and Figure 6 for the 3D effect of the model. See Table3 for the model materials and details.

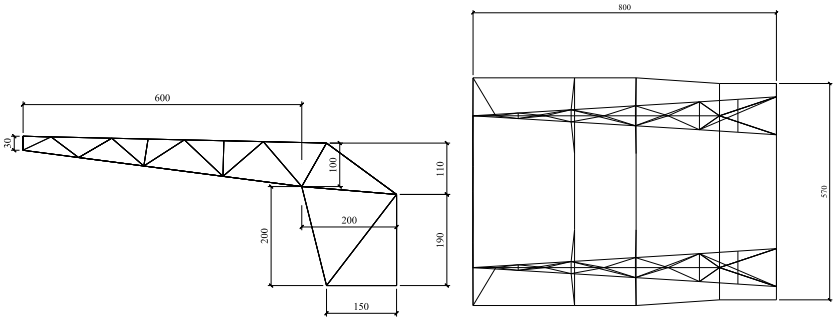

Fig. 5 - Front elevation and top view of the model (unit in the Figure: mm)

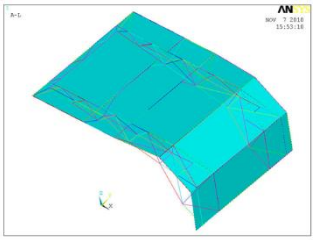

Fig. 6 - 3D rendering of the model

FORCE ANALYSIS OF THE MODEL

Load analysis

The model is mainly subjected to two kinds of loads, namely, gravity load and variable wind load.

Gravity load

The gravity load of the model includes the dead weight of component and the dead weight of cloth paper.

Wind load

Wind load is the main variable load of the cantilever roof structure for the main stadium, which is the important parameter for the structural design and the architectural dressing design. However, the domestic research on the wind pressure distribution and wind load prediction of this kind of structure is not sufficient. Therefore, it is necessary to put forward a simple and reasonable wind load calculation method for the structure design and the covering design of this structure [3].

In the study of dynamic wind loads on roofs, one of the purposes is to study the possible critical frequency range of fluctuating wind. Near the critical frequency, the dynamic load is very large, and the roof stiffness should not be too low in the design, so as to avoid the design wind at the roof height reaching the critical wind [4,5]. The critical wind speed is calculated by the following formula.

$$\overline{v}_{hcr} = \frac{n_1 h}{s_t} \quad (1)$$

Tab. 3 - Model material and detail dimension Table

Component name	Serial number	Section size	Number	Component name	Serial number	Section size	Number
Vertical and horizontal bars at the top of the roof	①	2×2×650	3	Lower compression bar	25	2×2×36	2
	②	2×4×650	2		26	2×2×58	2
	③	2×2×600	1		27	2×2×79	2
	④	2×2×580	4		28	2×2×9.6	2
Diagonal tie bar	⑤	2×4×30	2		29	2×2×156	2
	⑥	2×2×7.8	6		30	2×2×179	2
	⑦	2×2×10.3	2		31	2×2×183	2
	⑧	2×2×410	1		32	2×4×218	2
	⑨	2×2×6.8	2	Column	33	4×6×218	4
	⑩	2×2×7.7	4		34	4×6×227	4
	11	2×2×8.6	4		35	2×2×195	8
	12	2×2×9.5	4	Base	36	2×6×162	4
	13	2×2×10.9	4		37	2×6×100	2
	14	2×2×11.5	4		38	2×4×30	4
	15	2×2×12.6	4		39	2×6×86	2
	16	2×2×12.3	4	Tail	40	2×2×403	1
	17	2×2×13.4	4		41	2×2×320	3
	18	2×2×14.3	4		42	2×2×300	1
	19	2×4×12.8	4		43	2×2×230	1
	20	2×4×19.1	4		44	2×2×239	2
	21	2×4×15.2	2		45	2×2×185	1
lower compression bar	22	2×4×810	4		46	2×2×192	2
	23	2×2×565	4	Purlin	47	1×2×1050	2
	24	2×2×15	2		48	2×2×35	4

Where n_1 is the first natural vibration frequency (Hz) of the roof, h is the ground clearance height (m) of the leading edge of the roof, and s_t is the Strouhal number.

Wind load on the cantilever roof of the grandstand comes from a very high negative pressure applied on the upper surface of the roof lip. The negative pressure is caused by the fluctuating pressure of the reattached shear layer. Under the action of the wind the response of cantilever roof is the combination of the random low frequency responses, which comprises a fluctuating pressure distribution due to shedding of the reattached shear layer at the roof tip, and a resonant response. The resonance response is induced by the first vibration mode of the roof. The load of resonance response is determined by the distribution of inertial load [6-8], and the pressure distribution of the low-frequency response can be derived by the quasi-steady method. For the mass per unit length and linear mode, the distribution is shown in Figure 7.

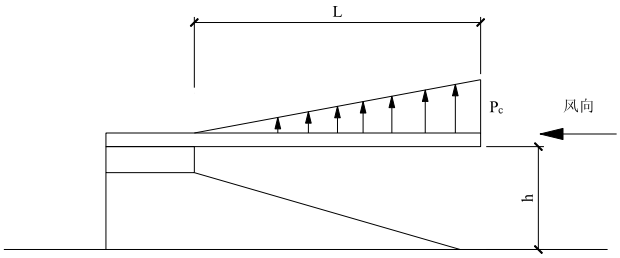

Fig. 7 - Schematic diagram of calculated wind pressure distribution of roof

The equivalent design wind load with triangular distribution is adopted to calculate the common load in China.

$$w_{he} = \xi \mu_h w_0$$
$$\xi = 1.45 + 0.40\left[\frac{\overline{v}_h T_1}{L} - 0.73\right] \quad (2)$$

Where, w_{he} is the maximum value of triangular load on the leading edge of roof surface (kN/m^2); ξ is the dynamic discharge corresponding to the first frequency of roof; μ_h is the variation coefficient of wind load at the height of roof; w_0 is the basic wind pressure (kN/m^2). The symbol $\overline{v}_h$ and L represent the average wind speed at the height of the roof, the cantilever length of the roof respectively. T_1 represents the first natural vibration period of the roof structure.

Force analysis of stadium roof structure

When designing the stadium roof, it is necessary to consider whether the load strength of the structure meets the requirement of static strength under various working conditions. The stress distribution and displacement distribution of roof structure can be obtained through analyzing under various loading conditions, which provides reliable analysis basis for roof design.

The finite element model was established based on the data of the designed model as shown in Figure 8. The bearing capacity and displacement of stadium roof under three load conditions were checked as follows:

(1) load condition 1: roof dead weight +1.88kg heavy load steel bar

The displacement diagram, axial stress diagram, bending stress diagram and other effect diagram of the structure under this working condition are shown in Figures 9-13.

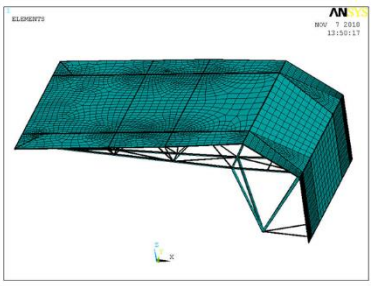

Fig. 8 - Finite element model of roof structure

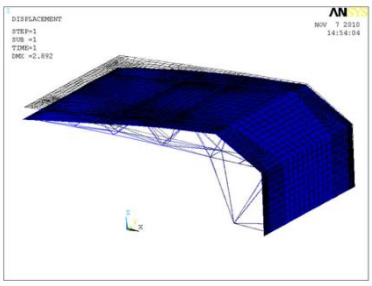

Fig.9 - Deformation diagram in Z direction

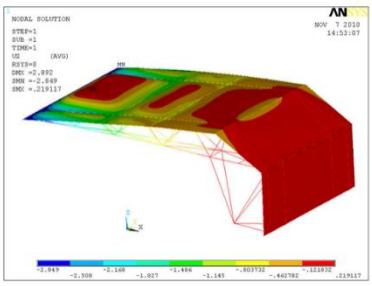

Fig. 10 - Displacement diagram in Z direction

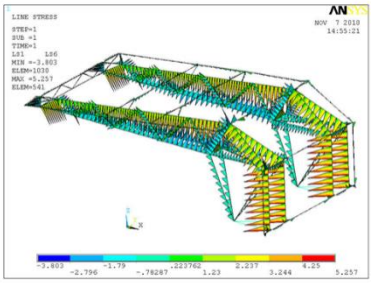

Fig. 11 - Axial stress distribution diagram

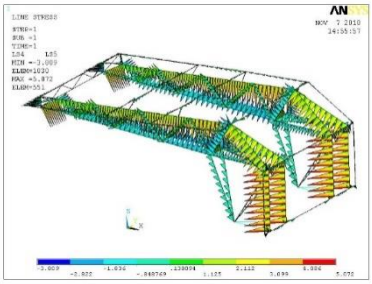

Fig. 12 - Distribution of bending stress

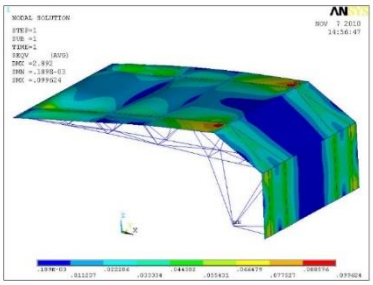

Fig. 13 - Equivalent stress distribution diagram

(2) load condition 2: roof dead weight + wind pressure generated by aerodynamic load of first gear wind speed

1) wind load calculation of the cantilevered roof of the stadium

According to equation (2) $w_{he}=\xi\mu_h w_0, \xi=1.45+0.40\left[\frac{\bar{v}_h T_1}{L}-0.73\right]$ can calculate the maximum value of the triangular load on the leading edge of roof surface.

Here

$$\mu_h=1.0$$

$$w_0=\frac{\bar{v}_h^{\,2}}{1630}=\frac{9^2}{1630}=0.05\,\mathrm{kN/m^2}$$

$$T_1=\frac{1}{8.1496}=0.123\mathrm{s}$$

According to modal analysis,

$$\xi=1.45+0.40\left[\frac{\bar{v}_h T_1}{L}-0.73\right]=1.45+0.40\left[\frac{9\times0.123}{0.6}-0.73\right]=1.896$$

$$\therefore w_{he}=\xi\mu_h w_0=1.896\times1.0\times0.05=0.095\,\mathrm{kN/m^2}$$

2) wind load calculation of column enclosure structure

According to the code for load of building structures GB50009-2012, when calculating the envelope, the standard value of wind load can be calculated according to the following formula

$$w_k=\beta_{gz}\mu_s\mu_z w_0 \tag{3}$$

Where, μ_s is the wind load carrier shape coefficient; μ_z is the change coefficient of wind pressure height; β_{gz} is the gust coefficient at height z ,and w_0 is the basic wind pressure.

According to the code for load of building structures, $\mu_s=1.8, \mu_z=1.0, \beta_{gz}=1.0$

$$\therefore w_k=1.0\times1.8\times1.0\times0.05=0.09\,\mathrm{kN/m^2}$$

The displacement diagram, axial stress diagram, bending stress diagram and other effect diagram of the structure under this working condition are shown in Fig. 14 and Fig. 18.

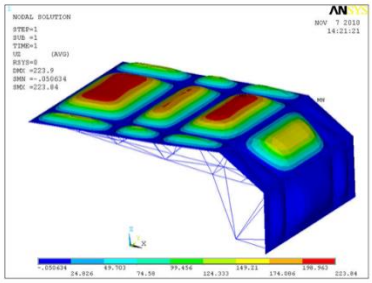

Fig. 14 - Displacement diagram in Z direction

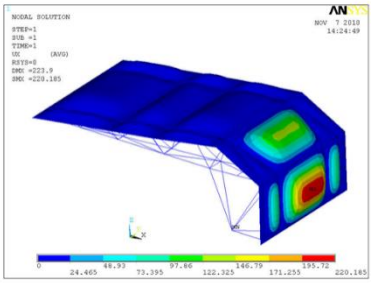

Fig. 15 - Displacement diagram in X direction

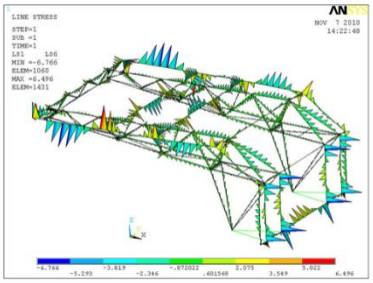

Fig. 16 - Axial stress distribution diagram

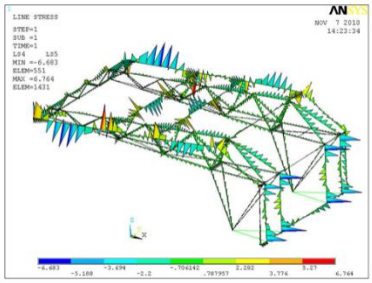

Fig. 17 - Distribution of bending stress

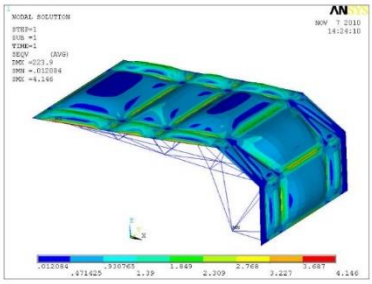

Fig. 18 - Equivalent stress distribution diagram

(3) load condition 3: roof dead weight + wind pressure generated by aerodynamic load of second gear wind speed

According to equations (2) and (3),

$$w_{he} = 0.189\,\mathrm{kN/m^2}$$

$$w_k = 0.158\,\mathrm{kN/m^2}$$

The displacement diagram, axial stress diagram and bending stress diagram of the structure under this working condition are shown in Figures 19-23.

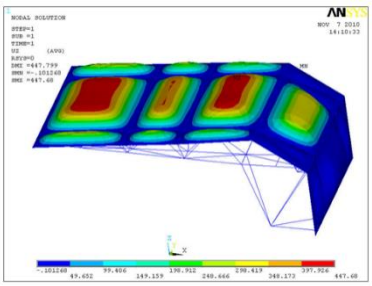

Fig. 19 - Displacement diagram in Z direction

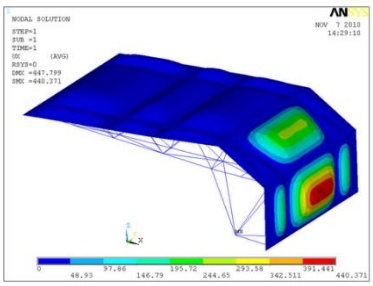

Fig. 20 - Displacement diagram in X direction

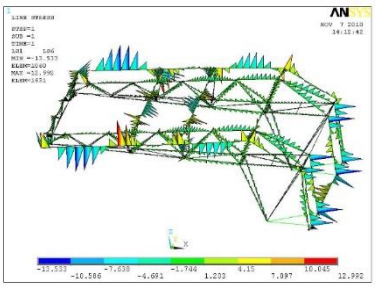

Fig. 21 - Axial stress distribution diagram

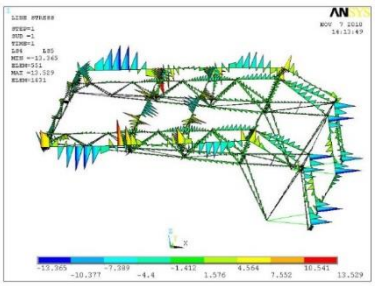

Fig. 22 - Distribution of bending stress

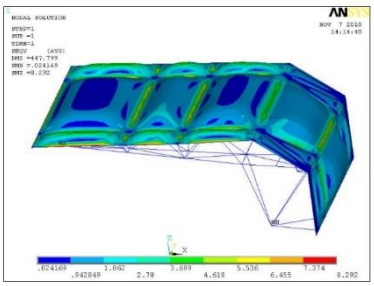

Fig. 23 - Equivalent stress distribution diagram

The analysis results of load conditions 1, 2 and 3 are shown in Table 4:

Tab. 4: Analysis results of load conditions 1, 2 and 3

Stress or displacement	Load condition		
	1	2	3
Maximum axial stress(MPa)	5.257	6.496	12.992
minimum axial stress(MPa)	-3.803	-6.766	-13.533
maximum bending stress (MPa)	5.082	6.764	13.519
minimum bending stress (MPa)	-3.809	-6.683	-13.365
maximum displacement (mm)	2.892	223.9	447.799

As can be seen from Table 4, when working under condition 1, the maximum displacement of the cantilevered roof is 2.892mm, indicating that the roof structure has a relatively high stiffness and the section selection is reasonable. The overall stiffness of the structure is greatly improved by the diaphragm effect of the cloth paper, but the displacement is different from that measured by the test. When working under conditions 2 and 3, the maximum displacement is up to 223.6mm and 447.799mm, which is quite different from the test results. The main reason is that the flexural stiffness outside the cloth paper plane is not considered, and the finite element model itself is different from the actual one to some extent. It can also be seen from the Tab that the internal forces of the bar meet the requirements.

MODAL ANALYSIS OF THE MODEL

The frequencies of each order of the structure are shown in Table 5. The modes of the first five orders, seventh order, tenth order, fourteenth order and the twentieth order are shown in Figures 24-32.

Tab. 5 - Natural frequencies of each order

Order number	1	2	3	4	5	6	7	8	9	10
Frequency	8.149	8.292	8.432	8.587	8.633	8.670	9.028	9.101	9.124	9.207

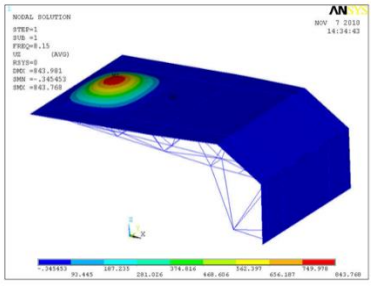

Fig. 24 - Mode 1

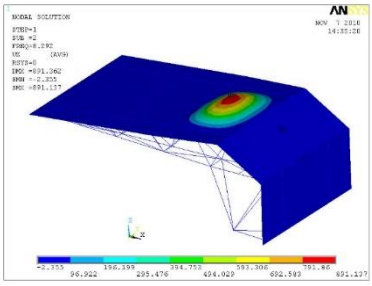

Fig. 25 - Mode 2

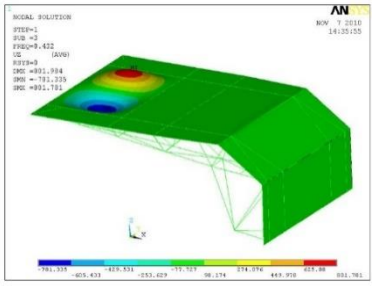

Fig. 26 - Mode 3

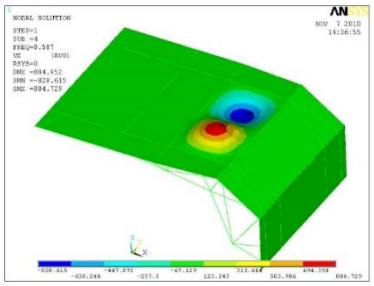

Fig. 27- Mode 4

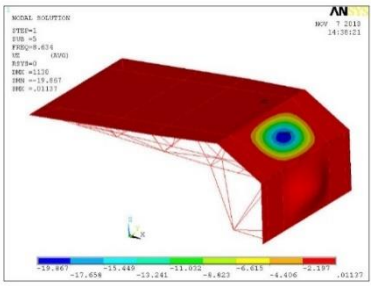

Fig. 28 - Mode 5

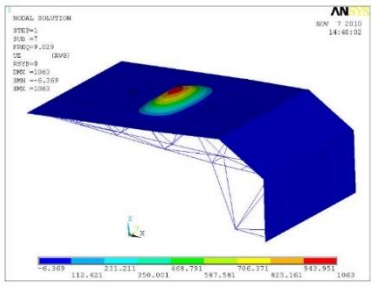

Fig. 29 - Mode 7

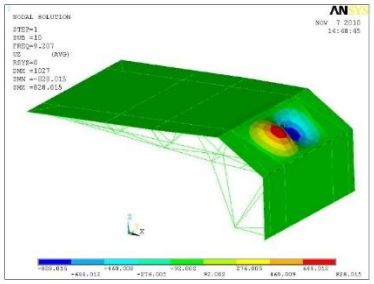

Fig. 30 - Mode 10

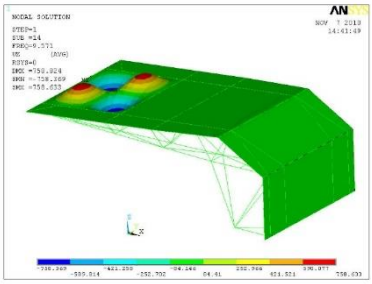

Fig. 31 - Mode 14

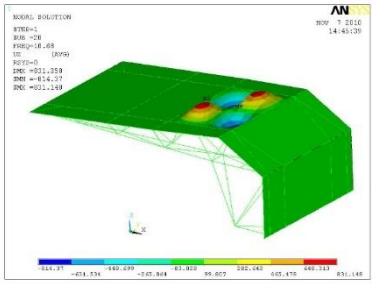

Fig. 32 - Mode 20

CONCLUSION

Through the analysis of the cantilever roof structure in the upper part of the stadium stand, the following conclusions can be drawn:

(1) There are still some differences in the force analysis and test results of the structure under different load conditions, mainly because the bending stiffness outside the cloth paper plane and the difference between the finite element model and the actual structure are not considered.

(2) It can be seen from Table 5 and the modal analysis of the vibration pattern diagram that the cantilever roof model of the stadium has a dense distribution of vibration modes of all orders, which is mainly local vibration of the structure, indicating that the model does not play a good role in spatial integrity. This is mainly because the bending stiffness outside the cloth paper plane is not considered. During the model design and production, the local enhancement of the low-order mode should be carried out to ensure the overall stability of the structure.

ACKNOWLEDGEMENTS

This work described in this paper was supported by the Natural Science Basic Research Plan in Shaanxi Province of China (Grant Nos. 2020JQ-917), and Key Curriculum Construction Project of Xi'an Eurasia University (Grant no. 2019KC007).

REFERENCES

[1] Zhou Yu, research on the selection and application of roof structure of large-space architecture-a swimming pool in Hefei as an example [D]. Huai Nai: Anhui University of Science and Technology,2018.

[2] Hu jing, research on the damping effect of restrained buckling support in floor spherical reticulated shell [D]. Zhou: Lanzhou university of technology, 2008.

[3] Zhang Xue-an Shui-fu Chen. wind load calculation of the stadium stands cantilever roof [J]. Low temperature of architectural technology, 2006, 3:48-50.

[4] Chen Fubin, large-span structure wind effect of in-situ test and wind tunnel test and theoretical analysis research [D]. Changsha: hunan university, 2011.

[5] Shen Qinghua, Dong-ming Zheng, the wind-induced vibration of roof structure analysis [J]. Journal of foreign building materials science and technology, 2008, 29(3): 57-59.

[6] Zhang Xue-an, structure wind load research on the stadium stands cantilever roof [D]. Hangzhou: Zhejiang University, 2006.

[7] Wang Ying, wind load numerical simulation study on large-span space structure [D]. Tianjin: Tianjin University, 2012.

[8] Xiao-kang Li, Zhuang-ning Xie, wind vibration response of long-span roof structures and the fast algorithm and the application of equivalent calm wind load [J]. Journal of civil engineering, 2010, 43 (7) 29-36.

CIVIL ENGINEERING JOURNAL

Article No. 53

THE CIVIL ENGINEERING JOURNAL 3-2021

DAMAGE ASSESSMENT OF CONSTRUCTION COMPONENTS OF THE JAKARTA SION CHURCH BUILDING

James Rilatupa[1], Grace Putri Dianty[2], Sally Napitupulu[2] and Gloria Z. Rilatupa[2]

1. *Christian University of Indonesia, Postgraduate Programme, Magister of Architecture, Jakarta, Jl. Mayjen Sutoyo No. 2, Indonesia; jedrilatupa@gmail.com*
2. *Christian University of Indonesia, Faculty of Engineering, Department of Architecture, Jakarta, Jl. Mayjen Sutoyo No. 2, Indonesia; gdianty@gmail.com, salnapitt.3@gmail.com, gloryabigail@gmail.com*

ABSTRACT

The Sion Church is one of the cultural heritage buildings that still needs to be maintained, given its condition to deteriorate. It is fitting that a cultural heritage building needs to be preserved, especially as a heritage asset in the capital that is more than three centuries old in dire need of conservation action. Meanwhile, routine monitoring and evaluation activities are one of the tools in preserving cultural heritage buildings. This activity aims to discover and collect data on maintaining a cultural heritage building so that any damage found in the cultural heritage building can be followed up. It is intended that cultural heritage buildings can be maintained and their existence is preserved because there are things that are valuable to human civilization, including religion, science, and culture. The conditions of ability and upkeep of the Sion Church Building were assessed based on weighting assessments, namely in design and upkeep work suitable, adjusted for Indonesia (humid tropical climate, based on BRE Digest 268). Based on the examination results, the ability quality of the Sion Church building was 33.90, which is categorized as the moderate damaged maintenance condition category.

KEYWORDS

Damage assessment, Building maintenance and ability, Jakarta Sion Church building

INTRODUCTION

Routine monitoring and evaluation activities are one of the tools in preserving cultural heritage buildings. This activity aims to discover and collect data on maintaining a cultural heritage building so that any damage found in the cultural heritage building can be followed up. It is done to intend that cultural heritage buildings be maintained and preserved because things are valuable to human civilization, including religion, science, and culture. [1][2][3]. The Indonesian government has regulated cultural heritage, which explains that objects, buildings, or structures can be declared as cultural conservation objects or cultural conservation buildings by fulfilling the requirements [4]:

a) Have been aged 50 years or more;
b) Shows a certain period of at least 50 years;
c) There is a particular purpose in history, science, education, religion and culture;
d) There are cultural values to strengthen national identity.

DOI 10.14311/CEJ.2021.03.0053

The Republic of Indonesia regulated cultural heritage as outlined in the form of a law in 2010. Community involvement in the management of cultural heritage must be increased. The cultural heritage management paradigm is no longer intended only for academic interests but must include ideological and economic interests. Therefore, synergy is needed to achieve these three interests between the government, academia, society, and the private sector [4]. Through the Ministry of Public Works and Public Housing of the Indonesian government regulated the preserved cultural heritage buildings in 2015 and explained that it is necessary to maintain, prevent and overcome cultural heritage buildings from failure and vandalism employing redemption, safekeeping, preservation, and restitution [5]. Besides, in the second part, article 8 explains that the reliability requirements of cultural heritage buildings consist of safety, health, convenience, and easiness [5][6].

Safeguarding the building can be interpreted as convenience with which a result can be maintained to ease next upkeep or cope with a changing surrounding environment. Maintenance of buildings is a part of the design characteristics (in architecture). Thus, the elements of building maintenance become design parameters (in architecture) related to the ease of maintenance of the building [7][8]. Thus, when designing a building, we must pay attention to a method to elongate a building's service time (save costs) by framing the structure adaptable. The service life depends on several elements, starting from how often the maintenance element is included in its design (architecture), the degree to which the owner/occupants perform caring obligations during the service life of the building, and estimated costs.

Building pathology is a systematic knowledge in building "disease" by understanding the causes, symptoms, and remedial treatment needed to overcome it. Building pathology both conceptually and as a whole requires a holistic approach from the anatomical conditions. Some of the detailed elements needed in this approach are building design, material selection, building, using, existing changes, and other mechanisms related to local environmental conditions [9][10]. The use of building pathology was known in the past few decades, but in the present, it seems unnecessary, as is the case with the current building. If there is a building with hundreds of service life years, it is considered good maintenance, robust construction, or good management. Buildings can have a long service time because someone works to solve all the problems in the building by caring for, loving, and paying attention to stay in top condition. From the design period until after the building was built, building pathology is still needed to be used for a long time [11]. The purpose of an environmentally sound building is to maximize its utilization and minimize damage [12]. Meanwhile, it was also explained that its service time could exceed 50 years [13].

The Sion Church in Jakarta, which became the research material, is one of the cultural heritage sites with the stipulation of the Governor's Decree No. 475 of 1993 [1] and DKI Jakarta Regulation No. 9 of 199 [14], as well as Ministerial Decree No.193/M/2017 [15]. The Sion Church consists of two buildings close to each other or is united, namely the main building (prayer room) and the consistory building. The architectural style of this church building is heavily influenced by ancient Roman architecture, with the architect H. Bruyn. A distinctive feature of the Romanesque style seen in the Church of Sion is the arch at the entrance to the church. Similar to the Romanesque style building, this church looks very big and sturdy, with very thick and solid walls to strengthen the structure [15]. Meanwhile, research on the Sion Church aims to obtain and collect data on the maintenance and condition of the construction components by identifying their maintenance.

MATERIALS AND METHOD

General conditions

The Sion Church Cultural Heritage Site in Jakarta is located at Jalan Pangeran Jayakarta, RT 009 RW 04, Pinangsia Village, Tamansari District West Jakarta. This church

DOI 10.14311/CEJ.2021.03.0053

building faces north, surrounded by a wall, but the eastern part has been demolished due to road widening. This church consists of the main building and additional buildings, with 6,750 m2 and 768 m2. The main building is rectangular. This church building has a Baroque-style interior. This church has Romanesque architectural features erected using 10,000 wooden posts from Ewout Verhagen from the Netherlands, with the architect, H. Bruyn [17]. Even when the eruption of Krakatoa caused the earthquake, this church was still strong. The Sion Church is divided into a worship room, balcony, pulpit, and church offices.

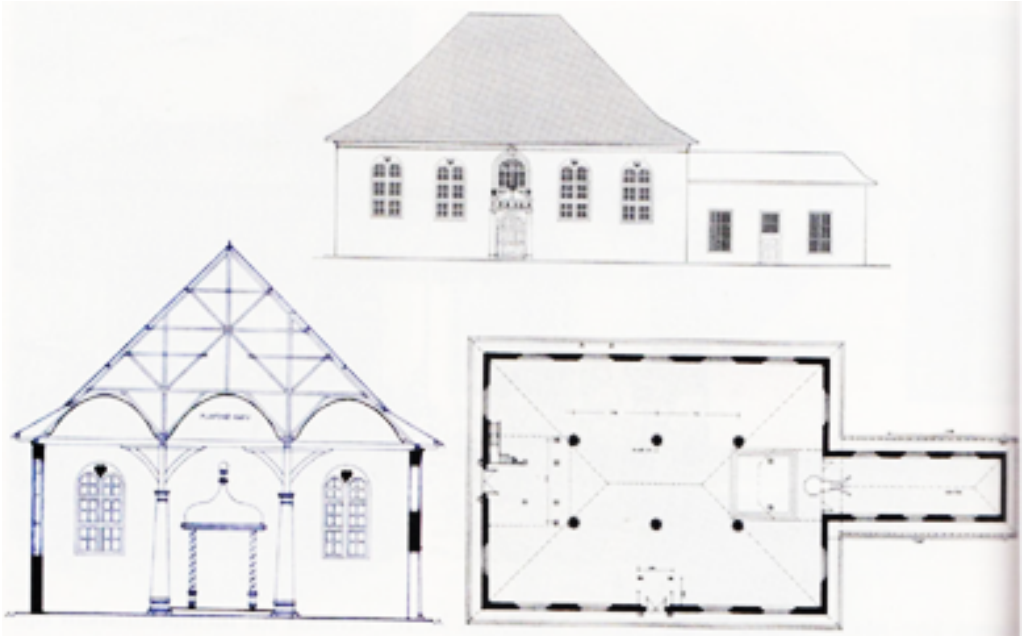

Fig. 1 - Sketch, facade, and a cross-sectional the Jakarta Sion Church (source: Heuken,2009)

In Sion Church, there are 2 entrances, the north and west, with a width of 2.6 m, semi-circular doorway with a height of 3.2 m. The door is made of 5 cm thick wooden planks. The northern entrance is still the original door, while the western entrance is an additional door. The church's interior is equipped with glass windows as many as 15 windows measuring 2.6 m and 5 m high, whose lintel is also semi-circular. This window is made of stained-glass panels. In the northern front yard of the church, there is a cast iron bell. This bell was made in 1675. The bell is hung on the wall to the left of the church door.

On the courtyard to the west side of the church door, several large gravestones typical of the Dutch era. The tombstones are made of stone materials imported from India (the Coromandel Coast area). They are ancient tombs of several important figures such as government officials and other prominent people (17th century to 18th century). Some of these graves are the tombs of the husband and wife of the Bengali Mardijkers (slaves), namely: Ragel Titis (died 1701) and Tities Anthonijse (died 1720). Besides, there is also the tomb of Governor-General Hendrik Zwaardecroon (died 1728) and others. Only 11 ancient tombs are left in Sion Church at the church's west entrance.

The drawing plan of the Sion Church building is the material in this research. In this research, some of the tools used are water level gauges, digital meters, digital cameras, drones to record the roof images of the Sion Church, laptops/computers, stationery, and forms to record damage or other data.

DOI 10.14311/CEJ.2021.03.0053

Research Method

The procedure of the research stages in the main building by:

- Noting the state of the building structure (upper structure), both indoors and outdoors area;
- Determining damaged area by recognizing the type of damage, in terms of both design and maintenance organizations; and
- Investigation of repairs that have been made of the repaired construction components.

Data Analysis and Instruments

a) The first stage performs ratings for each construction element of the building. It is to specify the degree of the primacy of the building elements of the Sion Church building based on BRE Digest 268 [9]. The method used in BRE Digest 268 is for general building construction damage in traditional low-rise housing. The instruments used can be seen in Table 1.

Tab. 1: Architectural rating estimation for construction elements [9]

Construction Elements	Estimation of Connections with * 1 2 3 4 10	Total	Rate (%)
Outside wall			
Roof			
Doors and windows			
.....			
Etc.			
			100

* rate 3: tight connection, 2: moderate connection, 1: deficient connection
Estimation elements relate to (1) durability-reliability, (2) permanence toleration, (3) the influence meteorological conditions, (4) keeping, (5) fire avoidance, (6) deterrence against noise, (7) building construction method, (8) circulating air conditioning, (9) earth tremor endurance, (10) other causes

b) The second phase is to verify the ability of the building with a scoring and rating system to achieve the ability of construction and building elements based on BRE Digest 268 [9].The score of the condition of the construction is (1) heavily damaged, (2) moderate damaged, (3) minor damaged, (4) moderate, (5) suitable.

The building ability rate is achieved based on the equation:

$$\text{Building ability} = \frac{\text{Total Rate x Value}}{500} \text{ x } 100 \quad (1)$$

Meantime, the upkeep circumstances of the building are acquired to the advanced calculated ability value. The category of building upkeep circumstances is estimated to the effect of building ability estimation [16], as shown in Table 2.

DOI 10.14311/CEJ.2021.03.0053

Tab. 2: Building ability values and keeping conditions [16].

Ability Value	Keeping Condition
81 – 100	good
61 – 80	moderate
41 – 60	lightly damaged
21 – 40	moderate damage
0 – 20	heavily damaged

RESULT AND DISCUSSION

Components Condition

The outer wall of the Sion Church building is painted white, but it looks peeling and dirty. There is a slightly yellowish stain in certain areas, which may be due to mold. In construction, the outer walls still look solid, so they need to be repaired and repainted. Some of the damage to the outer walls of the building was caused by weather (natural) and biological factors. It can be said that the construction of the walls of the Sion Church is excellent, but with a long age (325 years), of course, it requires continuous maintenance. The condition of the outer walls of Sion Church is in the category of medium damage.

Fig. 2 - Damage to the roof frame of the Jakarta Sion Church.

The roof covering of the Sion Church building is in the form of a trapezoid (shield), while the roof of the conservatory building (church court) is rectangular. The roof frame covering the Sion Church is made of clay tile, as shown in Figure 1. This clay tile was only used in the 20th century, so tile was only used when the Sion Church was restored in 1978. The roof supporting pillars of the Sion Church looks big and sturdy. Overall, the condition of the roof of the Sion Church building is in the medium damaged category. It can be seen from the shifting of the roof tiles because the roof truss has also begun to break down and there is weathering, causing leaks in the prayer room (church pulpit). The damage is caused by natural factors (weather and climate) and biological damage.

The wooden door's paint is faded, like the paint color on the windows and walls (visible from the outside). The bottom ends of the doors and windows were torn off. It is not definite that the door and window materials of this Sion Church are made of certain types of wood. Perhaps because it was restored in 1920 and 1978, material that was used was possibly traded wood, for example, camphor wood. In general, the conditions of damage to the doors and windows of the Sion Church are categorized as severely damaged. This damage occurred because the doors and windows in the Sion Church were without a canopy or gurgling to shelter rainwater

DOI 10.14311/CEJ.2021.03.0053

and sunshine. It indicates that the doors and windows of the Sion Church should be replaced with better wood materials and make a canopy to protect them from rain and sunshine.

Fig. 3 - Door and window of the Jakarta Sion Church

The floors in this building are from marble and natural stone materials. Meanwhile, the material on the balcony floor is made of teak wood. The damages of the floor of the prayer room and balcony are due to the life and age of the floor coverings used. It also resulted in the floor surface not having a water pass. The condition of the damage to the floor is included in the category of minor damage. The utility element observed in this building is the air conditioner (AC) device. The outdoor AC unit (compressor) is located on the outside of this building. This air conditioning device is an addition to modern equipment to support the comfort of worshipping the congregation. Generally, the damage to these utility elements is caused by service life and the joints in the gutter plate and pipelines. The condition of the damage experienced by the utility element component is a medium damage.

Fig. 4 - Cracked wall pairs (left) and damaged ceiling (right).

The foundation uses 10,000 wooden posts (round wooden blocks), Ewout Verhagen, from the Netherlands. When checking the damage to the foundation, it cannot be seen directly,

DOI 10.14311/CEJ.2021.03.0053

but there is a distance between a wall and a door/window, indicating a settlement in the foundation. The decrease in the foundation was caused by land subsidence [18]. From the lowering of the wall, the damage to the Sion Church foundation categorizes as medium damage. Wall pairs in the Sion Church were found to be quite cracked. It is due to the condition of the foundation subsidence that occurs during the life of the building. The cracks that occur significantly affect the condition of the building. From the examination results on the wall pairs, the damage condition has reached the medium damaged category.

The ceiling material for this building is made of white plasterboard and supported by six dark brown teak wood poles. Meanwhile, many damaged ceilings were found. The damage occurred due to the ceiling damp condition due to rainwater seepage on the roof. Damage to the ceiling is included in the medium damage category. The interior walls are still visible in their original state, in shape, material, and size. The maintenance carried out was inadequate, so the quality of walls in the Sion Church building looked quite apprehensive. Damage conditions to the inner walls and upholstery are in the heavy category. The Sion Church stairs condition is quite alarming, as well as the staircase railing. Stairway and stair railings at Sion Church are made of good quality wood. However, with long service life, weathering has occurred, mainly due to biological factors (termites). The condition of the damage to the stairs and railings is in the medium damaged category. The building facilities referred to in this case are a consistory building and a church bell. The condition of the Sion Church's consistory building is in the category of moderate damage. The church bell is currently on the wooden tower beside the church's north entrance. The condition of the damage to the Sion Church bell is included in the medium damaged category.

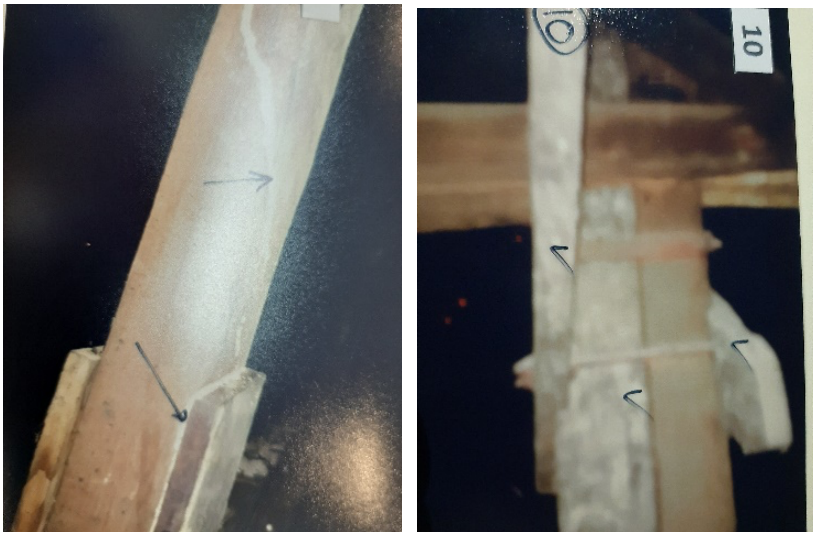

Fig. 5 - Condition of roof truss of the Jakarta Sion Church

In the structural frame system, there has been damage (weathering) to the roof truss. To maintain the roof frame of the Sion Church, people make wooden supports to hold the weight of the roof. Seeing the condition of the roof truss, of course, it needs immediate repairs, but until now, no repair work has been carried out. Meanwhile, with the occurrence of land subsidence, it is easier for rainwater to penetrate the slot surface of the building, which results in a decrease in the condition of the column (cracks). The damage that occurred in the framework system of the Sion Church structure was included in the medium damage category. Overstek in this building seems to have started to rot and dirty, caused by weather and biological factors. Besides, the roof cover (tile) can be seen without wooden battens on the overstek and only

DOI 10.14311/CEJ.2021.03.0053

visible wooden rafters. In this case, it is necessary to replace rotten rafters in the overstock to support the load of the roof tiles above. The condition of the supporting components of the Sion Church building is in the category of heavy damage and is in dire need of immediate repair.

The Ability of the Sion Church

The ability and keeping conditions of the Sion Church Building are elaborated based on a rating estimation of the architecture and upkeep work declared as a percentage. Architectural rating goals to achieve the connection among the building construction elements and the showing shown in the plan (design). The rating implementation indicated BRE Digest 268 [9], adjusted for Indonesia (wet/humid tropical climate). Meantime, the rating of upkeep work goals to achieve a connection among construction elements and the showing of the building since it was established 325 years ago (1695 - 2020).

Tab. 3: Rating assessment of elements of the Jakarta Sion Church building construction (based on design and upkeep condition)

No.	Construction Element	Rating (%)	
		Design	Upkeep
1	Outer wall	8.0	10,07
2	Roof	8.1	8.9
3	Doors and windows	7.4	6.9
4	Floor	7.3	6.3
5	Utility element	7.1	5.9
6	Foundation	6.8	6.9
7	Wall pairs	9.5	10.07
8	Ceiling	6.4	4.5
9	Inner wall (interior)	7.4	6.5
10	Inner wall cladding	6.1	6.9
11	Stairs	5.1	4.9
12	Placement of building facilities	6.7	6.9
13	Structural frame system (roof and column trusses)	8.2	8.9
14	Building construction elements (overstek)	5.9	6.3
		100	100

A study in the investigation at the Sion Church Building was implemented to achieve arrangements and modifications in the continuity of interest of construction elements undertake. An analysis of the connection matrix among the classifying of construction element work and its influence on its showing is building upkeep perform. Attempts or alterations are made to avoid contraction and failure to construction elements, degrade/depress substitution/ correction of construction elements, and indeed depress the upkeep of all construction elements [19][20]. It is necessary to check the condition of the building by the maintenance and repair department to obtain information about the condition of the main building and public zone: water pipes, electricity, structural systems, roofs, and windows. Establishing an inspection shall be shortly found out which refinement should be implemented soon to eliminate failure or accidents (danger), such as fixing bad electrical connections or damaged fixtures, or finding out what repairs can be delayed [21]. Due to changing building conditions, the maintenance and repair department must survey the condition of the building every three months [22].

DOI 10.14311/CEJ.2021.03.0053

In Table 3, it shall be visible that there is an alteration in the quality percentage of every construction element from an architectural perspective to the upkeep performance of the Sion Church building. Then, for assessing the condition of the construction components, it will be carried out in terms of architecture and upkeep performed by the Sion Church building. Meanwhile, the reliability of the construction components in the Sion Church building was obtained based on the results of examinations on the maintenance work of the construction components. It aims to see the condition of the Sion Church building based on its maintenance work. The maintenance conditions acquired will be supposed to be accomplished based on the architectural work. The examination of each construction component is obtained based on a scoring system magnified by the quality of every construction element [9]. Meanwhile, all construction components are in good condition (multiplied by a score of 5).

Tab. 4: The results of the inspection of upkeep work at the Jakarta Sion Church building

No.	Construction Component	Ability (%)		(Decrease)/ Increase (%)
		D*	U**	
1	Outer wall	40.00	20.14	(19.86)
2	Rooftop	40.50	17.80	(22.70)
3	Doors and windows	37.00	6.90	(30.10)
4	Floor	36.50	18.90	(18.10)
5	Utility element	35.50	11.80	(23.70)
6	Foundation	34.00	13.80	(20.20)
7	Wall pairs	47.50	10.07	(37.43)
8	Ceiling	32.00	9.00	(23.00)
9	Inner wall (interior)	37.00	6.50	(30.50)
10	Inner wall cladding	30.50	6.90	(23.60)
11	Stairs	25.50	9.80	(15.70)
12	Placement of building facilities	33.50	13.80	(19.70)
13	Structural frame system (roof and column trusses)	41.00	17.80	(23.20)
14	Building construction elements (overstek)	29.50	6.30	(23.20)
	Total	500.00	169.51	-

D*: Architecture U**: Upkeep

The results of ability checks of the Sion Church building construction components indicated an alleviation in the grade of every construction component, as in Table 4. The most significant decrease was found in wall pairs (37.43%), inner walls (30.50%), and doors and windows (30.10%). There was a decrease in the wall pairs quality due to a decrease in the Sion Church building foundation. As one of the oldest buildings in Southeast Asia, of course, the Sion Church, which is 325 years old, has experienced a deep decline in its foundation due to land subsidence. The settlement of this foundation resulted in the walls crack, both the outer walls and the inner walls of the Sion Church.

Meanwhile, generally, for doors and windows, the damage that occurs is due to weathering and the wood materials' age. The quality of the wood also used dramatically affects the service life of the wood material. The doors and windows components must be replaced periodically to overcome the problem.

Based on the results of the upkeep work in Table 4, it proved that the care work at Sion Church is very lacking. All construction components in the Sion Church building were damaged

DOI 10.14311/CEJ.2021.03.0053

(Table 5), and only the floor components were slightly damaged. Construction components of the outer walls, roofs, utility elements, foundations, ceilings, stairs, building facilities, and structural frame systems were medium damaged. Meanwhile, components of doors and windows, ceilings, inner walls, inner wall cladding, and building supports (overstek) were severely damaged. Based on the examination results, it was found that the reliability value of the Sion Church Building was 33.90, which was included in the moderate damaged maintenance condition category (see Table 2).

Forensic Factors Affecting Construction Components

Forensic factors that influenced the outer walls of the building, rooftop, floors, wall pairs, and placement of building facilities are sunlight and radiance, temperature, wind, aerial movement, rainfall, grit and ash, intense winds, and hurricane, earth tremor, and biological disturbers. Meanwhile, forensic factors that influence doors and windows are sunlight and radiance, temperature, wind and aerial movement, rainfall, grit and ash, intense winds and hurricane, and biological disturber. Forensic factors that influence the elements of utilities and stairs are grit and ash and a biological disturber.

Tab. 5: Forensic factors influence the Jakarta Sion Church building

No.	Construction Component	Condition	Forensic Factors
1	Outer wall	medium damage	a,b,c,d,e,f,g
2	Rooftop	medium damage	a,b,c,d,e,f,g
3	Doors and windows	heavily damage	a,b,c,d,e,g
4	Floor	minor damage	a,b,c,d,e,f,g
5	Utility element	medium damage	d,g
6	Foundation	medium damage	a,b,d,f,g
7	Wall pairs	medium damage	a,b,c,d,e,f,g
8	Ceiling	heavily damage	a,b,c,d,g
9	Inner wall (interior)	heavily damage	a,b,d,f
10	Inner wall cladding	heavily damage	a,b,d,f,g
11	Stairs	medium damage	d,g
12	Placement of building facilities	medium damage	a,b,c,d,e,f,g
13	Structural frame system (roof and column trusses)	medium damage	a,b,c,d,e,f,g
14	Building construction elements (overstek)	heavily damage	a,b,c,d,g

The inspected forensic factors are: (a) sunlight and radiance, (b) temperature, wind, and aerial movement, (c) rainfall, (d) grit and ash, (e) intense winds and hurricane, (f) earth tremor, (g) biological disturber

A biological disturber consists of fungi, termites, and beetles. Mold can cause stains on concrete walls, wood, floors, and others construction components. In addition, termites and beetles can cause weathering/porousness in wood materials. Generally, the damage to wood material is mainly caused by the availability of media for the development of termites, for example, damp wood due to frequent exposure to rainwater. Moist wood conditions are very popular with termites, especially subterranean termites. For more details, the forensic factors that influence every construction element can be seen in Table 5.

DOI 10.14311/CEJ.2021.03.0053

The Cost of Maintenance and Cleaning of the Sion Church

Although the Government of Indonesia has established the status as a national cultural heritage building, the management of the church is under the Sion authority. Daily management is carried out at the expense of the Sion's congregation. For example, donations and tithes during worship. This maintenance management includes cleanliness and building maintenance. It can be said that the costs for the maintenance of the Sion Church are only incidental, which of course, amount does not match the needs of the Sion Church maintenance.

The Sion Church is a cultural heritage building that still needs to be maintained. In 2001 and 2002, church walls and doorframes were painted. However, lately, this kind of treatment is rarely carried out, even though it requires ongoing costs to maintain cultural heritage buildings. Meanwhile, to get special treatment, the operational costs must be based on submitting funds needed to the Jakarta Provincial Government's Cultural Heritage Conservation Center, considering the large number of costs required.

Apart from the government, of course, the preservation of cultural heritage must include togetherness with the community. From the results of observations to the Sion Church, the condition is indeed very costly for its conservation. Uniquely, the maintenance or conservation measures taken should not use ordinary building materials. Furthermore, they must adjust to the existing building materials in the Zion Church. It is fitting that a cultural heritage building needs to be preserved, especially as a heritage asset in the capital city that is more than three centuries old and requires consistent conservation action.

CONCLUSION

The examination of the building construction components observed was in the category of minor to severe damage. The construction component, which is included in the minor damage category, is the floor. Damage to this floor can be caused by lowering the foundation, which results in a cracked part of the floor. Meanwhile, the construction components of the outer walls, roofs of buildings, utility elements, foundations, ceilings, stairs, placement of building facilities, and structural frame systems were moderately damaged.

Construction components of doors and windows, ceilings, inner walls, inner wall cladding, and building supports (overstek) were severely damaged. Damage to door and window components was caused by wood shrinkage by solar radiation, rainwater humidity, and biological destroyers (especially termites). Generally, the damage to the construction components in the Sion Church is caused by the age factor. Based on the examination of the condition of the Sion Church, it was found that the reliability value was 33.90 with moderate damaged maintenance conditions.

The most significant decrease was found in wall pairs (37.43%), inner walls (30.50%), and doors and windows (30.10%). It decreased the wall pairs quality due to a profound decrease in the foundation due to land subsidence. The settlement of this foundation also resulted in the cracks of the walls, the outer walls, and the Sion Church's inner walls. The quality of wood used in the doors and windows is greatly influenced by the lifetime of the wood material. As a problem solving, the components of doors and windows must be replaced periodically.

Currently, the care management at Sion Church only relies on the costs from the congregation of Sion Church. This maintenance management only includes cleanliness and building maintenance. It can be said that the costs for the maintenance of the Sion Church are only incidental, which of course, amount does not match the needs of the Sion Church maintenance. As a particular treatment, the operational costs must be based on submitting funds needed to the Jakarta Provincial Government's Cultural Heritage Conservation Center,

DOI 10.14311/CEJ.2021.03.0053

considering that the costs required are pretty significant. Besides, further research is needed on the Jakarta Sion Church, especially conserving this cultural heritage building.

ACKNOWLEDGMENT

We would like to thank the Jakarta Sion Church Council for allowing us to research that building. We also express our gratitude to the Christian University of Indonesia for providing funding for the implementation of this research.

REFERENCES

[1] Ministry of State Secretariat of the Republic of Indonesia, 2017. Law of the Republic of Indonesia Number 5 of 2017 concerning the advancement of culture. Jakarta: Ministry of State Secretariat of the Republic of Indonesia, Accessed on: Sept. 13, 2020, [Online] Available: https://jdih.bsn.go.id/produk/detail/?id=733&jns=2.

[2] Sonkoly, G. and T. Vahtikari, 2018. Innovation in cultural heritage research: for an integrated European research policy. Luxembourg: Directorate-General for Research and Innovation European Commission, Accessed on: Sept. 13, 2020, [Online] Available: https://op.europa.eu/en/publication-detail/-/publication/1dd62bd1-2216-11e8-ac73-01aa75ed71a1/language-en.

[3] L. Petti *et al.*, 2019. Towards a shared understanding of the concept of heritage in the European context. Heritage 2019, 2(3), 2531-2544; https://doi.org/10.3390/heritage2030155, Accessed on: Nov. 06, 2020, [Online] Available: https://www.mdpi.com/2571-9408/2/3/155/htm.

[4] Ministry of Law and Human Rights, 2010. Law of the Republic of Indonesia No. 11 of 2010 concerning cultural heritage. Jakarta: Ministry of Law and Human Rights, Accessed on: Sept. 13, 2020, [Online] Available: https://jdih.kemdikbud.go.id/arsip/UU_Tahun2010_Nomor11.pdf.

[5] Ministry of Public Works and Housing of the Republic of Indonesia, 2015. Regulation of the Minister of Public Works and Public Housing of the Republic of Indonesia Number 01/PRT/M/2015. Jakarta: Ministry of Public Works and Housing of the Republic of Indonesia RI, Accessed on: Sept. 14, 2020, [Online] Available: https://legalitas.org/peraturan-menteri-kementerian-negara-perumahan-rakyat-no-01-prt-m-2015-tahun-2015-tentang-bangunan-gedung-cagar-budaya-yang-dilestarikan.

[6] T. M. Ferreira *et al.*, 2020. Risk and resilience in practice: cultural heritage buildings. International Journal of Architectural Heritage, pp. 1-3, May 12 2020, DOI: 10.1080/15583058.2020.1759007, Accessed on: Oct. 23, 2020, [Online] Available: https://www.researchgate.net/publication/341345833_Risk_and_Resilience_in_Practice_Cultural_Heritage_Buildings.

[7] S.J.L. Chua *et al.*, 2018. Building maintenance practices towards the common defects and resident's satisfaction of elderly homes. Journal of Design and Built Environment, Special Issue(1), pp:62-71, June 2018, DOI:10.22452/jdbe.sp2018no1.6, Accessed on: Jan. 08, 2021, [Online] Available: https://www.researchgate.net/publication/326199452_Building_Maintenance_Practices_towards_the_Common_Defects_and_Resident's_Satisfaction_of_Elderly_Homes.

[8] G. Wicaksono *et al.*, 2017. Implementation of sustainable architecture to support the efforts to achieve a green city. Journal of Architectural Research and Design Studies, vol. 1, no.1, Oct. 2017, pp. 1-10, DOI: https://doi.org/10.20885/jars.vol1.iss1.art1, Accessed on: Jan. 10, 2021, [Online] Available: https://journal.uii.ac.id/jards/article/view/7752/7609.

[9] D. Watt, 2009. Building pathology: principles and practice. Oxford: Blackwell Science Ltd.

[10] L. Kruszka and P. Muzolf, 2019. Diagnostics of the structural failure of Sports Hall external wall layers. (Presented at the 29th International Conference on Structural Failures, Miedzyzdroje, Poland, May 20-24, 2019), DOI: https://doi.org/10.1051/matecconf/201928402005, Accessed on: Dec. 17, 2020, [Online] Available: https://www.matec-conferences.org/articles/matecconf/pdf/2019/33/matecconf_icsf2019_02005.pdf.

[11] P. S. Gahlot and S. Sharma, 2019. Building repair and maintenance management. London: CBS Publishers & Distributors.

[12] M. Randall, 2017. Environmental science in building, 8th Edition. New York: Palgrave.

[13] I. Puķītea and I. Geipele,2017. Different approaches to building management and maintenance meaning explanation. Procedia Engineering 172 (2017) 905 – 912, pp. 905-912, 2017, DOI:10.1016/j.proeng.2017.02.099, Accessed on: Jan. 08, 2021, [Online] Available: https://www.researchgate.net/publication/313884168_Different_Approaches_to_Building_Management_and_Maintenance_Meaning_Explanation.
[14] DKI Jakarta Provincial Government,1999. DKI Jakarta Regional Regulation No. 9 of 1999, Jakarta: Provincial Government of DKI Jakarta. Accessed on: Nov. 06, 2020, [Online] Available: https://jdih.jakarta.go.id/himpunan/produkhukum_detail/7767.
[15] Ministry of Education and Culture, 2017. Decree of the Minister of Education and Culture of the Republic of Indonesia Number: 193/M/2017. Jakarta: Ministry of Education and Culture.
[16] S. Linggar *et a*l., 2018. Analysis of building and its components condition assessment case study of dormitory buildings. (Presented at the International Conference on Sustainable Civil Engineering Structures and Construction Materials, Yogyakarta, Indonesia, Sept. 5-7, 2018), DOI: https://doi.org/10.1051/matecconf/20192580303, Accessed on: Jan. 08, 2021, [Online] Available: https://www.matec-conferences.org/articles/matecconf/pdf/2019/07/matecconf_scescm2019_03003.pdf.
[17] Heuken, 2009. Historical Churches of Jakarta. Jakarta: Erlangga.
[18] E.A. Ariefa *et a*l., 2019. Correlation analysis of changes in pattern of building area on soil advance using the method index-based built-up index (ibi) and dinsar (case study: North Jakarta city). Jounal of Geodesy Diponegoro University, vol. 8, no. 4, pp. 215-224, Oct. 2019, Accessed on: Feb. 02, 2021, [Online] Available: https://ejournal3.undip.ac.id/index.php/geodesi/article/view/25161/22370.
[19] B. Chanter and P. Swallow, 2017. Building maintenance management, 2nd Edition. New York: Wiley Publishing Company.
[20] C. Rutherford, 2018. Building Maintenance & Construction: Tools and Maintenance Tasks, Kahului. Hawai: University of Hawai'i Maui College and the Construction Technology Program.
[21] C. Talamo and M. Bonanomi, 2017. Knowledge management and information tools for building maintenance and facility management. New York: Springer International Publishing.
[22] J. Klemisch, 2011. Maintenance of Historic Buildings: A Practical Handbook. New York: Routledge.

DOI 10.14311/CEJ.2021.03.0053

CIVIL ENGINEERING JOURNAL

Article no. 54

THE CIVIL ENGINEERING JOURNAL 3-2021

COMPARATIVE ANALYSIS OF SPATIAL STRESS IN THE JOINT ZONE OF TOWER PIER UNDER DIFFERENT SYSTEMS OF CABLE-STAYED BRIDGE

Long Liu[1], Yingying Bi[2]

1. *Anyang Institute of Technology, the west end of Huanghe Avenue, Anyang 455000, China;20160913@ayit.edu.cn*
2. *Anyang Institute, 599 Zhonghua Road, South Section, Anyang 455000,China; 1586743384@qq.com*

ABSTRACT

To explore the stress of the tower-beam-pier joint zone of a cable-stayed bridge under different systems, the submodel method in the finite element software ABAQUS was used to establish the local model of the tower-beam-pier joint zone of the bridge. At the same time, Midas/Civil was used to establish the rod system finite element model of the whole bridge. The correctness of the local model was verified by comparing the results of the finite element model and the local model. Then, by changing the combination mode of tower beam pier, the stress comparison analysis of the joint zone of the tower-beam-pier under different systems was carried out. The results showed the stress distribution of the semi-floating system which had no tensile stress at the pier top was more reasonable than that of the rigid frame system and the consolidation system. In the use of three different systems, there was concentrated tensile stress at the chamfer of the web and the bottom plate, where the steel bars should be added. In the rigid frame system, deflection of the main beam under load was the smallest, and the maximum displacement occurred at the boundary section, with the value of only 2.668mm.

KEYWORDS

Cable-stayed bridge, Joint zone of tower-beam-pier, Stress analysis, Semi-floating system, Rigid frame system, Tower-beam consolidation system

INTRODUCTION

The joint zone of tower-beam-pier is an important node of cable-stayed bridge, presenting a complex three-dimensional force state, which is a blind zone for stress calculation by the finite element method of rod system. The spatial stress analysis by solid finite element method can provide a basis for the improvement of the stress state of this position.

According to the combination mode of tower-beam-pier, cable-stayed bridge can be divided into floating system, semi-floating system, tower-beam consolidated system and rigid frame system. Scholars have carried out research on the stress condition of the tower-beam-pier joint zone of various systems of cable-stayed bridges. Yu Yanxia [1] made a comparative study on the parameters of the bridge system, and the results showed the consolidation system of tower-beam-pier was suitable for the connection form of cable-stayed bridges because of its large stiffness and small shrinkage. Wen Wangqing [2] compared and analyzed the influence of four systems on stiffness, temperature effect and structural force of three-span cable-stayed bridge. Pan Xiangwen [3] compared the mechanical properties of cable-stayed bridge under load by changing the system and different structural parameters, and found the combined system of tower-beam consolidation

and rigid frame had a larger stiffness. Deng Jiangtao [4] and Long Peiheng [5] established the tower-beam-pier joint zone model of rigid-frame cable-stayed bridge by using finite element software to analyze its spatial stress. Yu Lusong [6] studied the stress effect of prestressed beams of semi-floating cable-stayed bridges on the consolidated parts. Song Jun [7] made a study on stress state of the consolidation position of tower-pier of rigid frame system under four different working conditions with the submodel method. Through literature investigation, it is found that scholars had carried out research on spatial stress analysis of the tower girder pier joint zone in structural systems, but there is no report on the comparative stress analysis of tower-beam-pier joint zone under different systems of cable-stayed bridges.

To explore spatial stress of tower-beam-pier in the joint zone of cable-stayed bridge, several methods are commonly used, such as scale model test, photoelastic test, analytical calculation and finite element analysis. Hu Yuliu [8] used method of scaled model test to study parameters such as stress and displacement in the consolidation zone of tower-beam-pier in the using stage. Wang Ziwen [9] studied static performance of the tower-girder joint zone of single-tower cable-stayed bridge with consolidation of tower-girder piers with method of scale model test and finite element method. Shang Guanping [10] analyzed the stress of cable-stayed bridge with beam-pier consolidation system with method of finite element and photoelastic test comparison. Dai Gonglian [11] studied the stress of the consolidation model of tower-beam-pier of a trussing-section cable-stayed bridge by combining model test with numerical simulation. Among these methods, the test cost of scale model is higher; the calculation accuracy of analytical method is poor; the calculation result of finite element is accurate and the cost is low.

Zhou Min [12] established the overall and local models of cable-stayed bridges respectively by adopting Midas/Civil and ANSYS finite element software, who also simulated and analysed the stress of the tower-pier consolidation zone. Li Bo [13] established the integral finite element model of cable-stayed bridge and the solid model of 0# block respectively, and made a study on the spatial stress of 0# block under the most unfavourable load.

In this paper, the overall finite element model of cable-stayed bridge was established with the Midas/Civil software, and the local solid model of the tower-beam-pier joint zone of the cable-stayed bridge was established by using ABAQUS software. The accuracy of the local solid model was verified by comparison of the results, and on this basis, the stress comparison analysis of the tower-beam-pier joint zone with different anchorage forms was carried out. The influence of anchoring on the force of cable-stayed bridge was discussed.

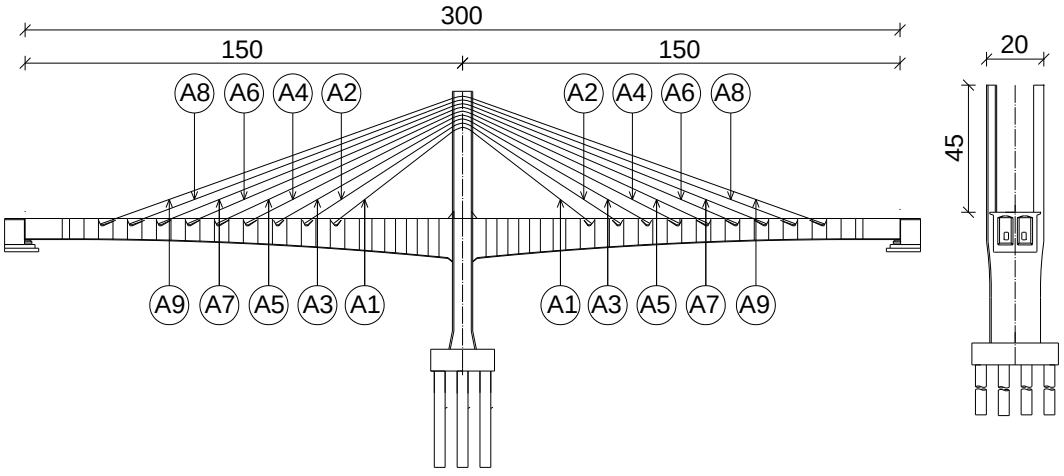

(a) Elevation *(b) Cross-section*

Fig. 1 – Schematic diagram of cable-stayed bridge layout (unit: m)

NUMERICAL SIMULATION MODEL OF TOWER-BEAM-PIER JOINT ZONE

(1) Project overview

A cable-stayed bridge with a span arrangement of (150+150) m adopted rigid frame system, which means the tower, beam and piers are consolidated. The main beam adopted the single-box double-chamber reinforced concrete box, with a total width of 20m at top of the beam and a quadratic parabolic change in beam height. The stay cables adopted symmetrical space with double cable planes, with 18 cables. The cable tower adopted rectangular section and height of the tower was 45 m. The overall layout of the bridge is shown in Figure 1.

(2) The establishment of calculation model

The finite element software ABAQUS was used to establish the local model of the tower-beam-pier joint zone of the cable-stayed bridge, as shown in Figure 2. The submodel method was adopted [14], and the whole model provided boundary conditions for the local model. To avoid the influence of boundary conditions on force of the joint zone, enough length of the main girder should be cut off. In the local model, the transverse bridge direction was the full width of the main beam, which was symmetrical along the bridge direction to the middle line of the bridge. The local corner of the chamfering section of the box girder at the end of the beam was C3D10 element, and the rest section was C3D8R element. There were 76007 elements in the model. Midas/Civil was used to establish finite element rod system model of the full bridge, and length of the intercepted main beam in tower beam pier joint zone was 31 m, as shown in Figure 3. There were 228 nodes and 188 cells in the model.

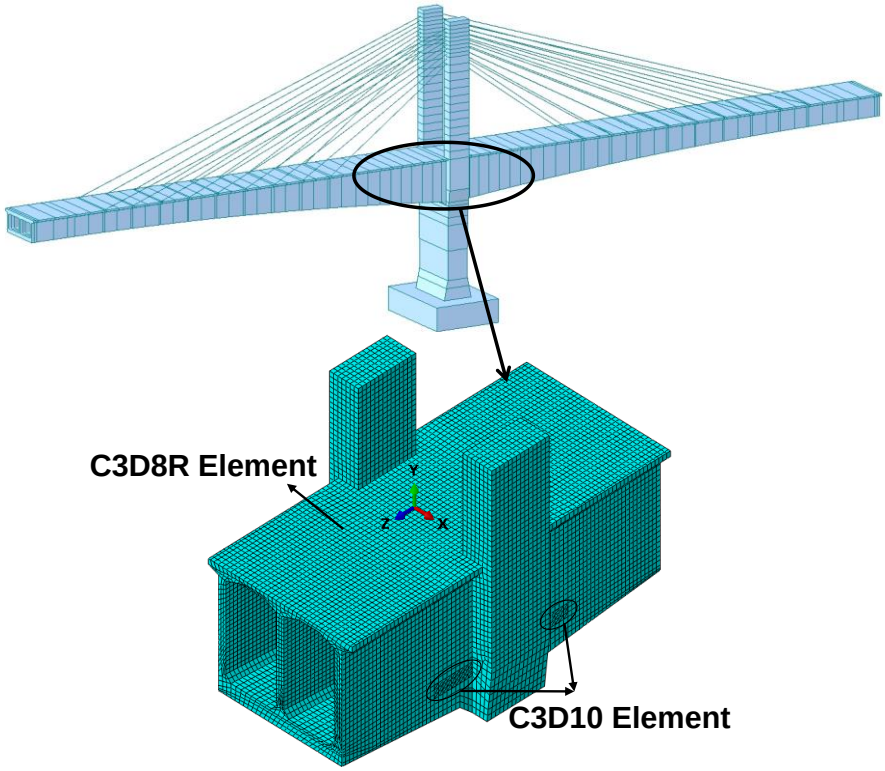

Fig. 2 – Finite element model

(3) Calculation Parameters

In the local model of the tower-beam-pier joint zone, ABAQUS internal constraints were used to couple the steel bundle node with the nearby concrete node, to consider internaction of the

prestressed steel bundles and concrete, and the prestress was simulated by using cooling method [14]. There were 12 web bundles and 6 roof bundles in the consolidation zone, and both ends of the remaining steel bundles were all truncated at the boundary of the model. The prestress effect of truncated prestressed steel bundles was considered in the boundary force. There were 8 tendons of prestressed steel anchored to roof of the beam and 6 tendons of prestressed steel anchored to bottom of the beam. The specifications of tendons were 19-15.2 steel strands. The elastic modulus of prestressed steel bundle was 1.95×10^5MPa, the bulk density was 78.5kN/m^3, and linear expansion coefficient was 1.2×10^{-5}. The stress of steel bundle was the effective prestress after considering prestress loss. The box girder and bridge tower were made of C60 concrete with an elastic modulus of 3.6×10^4MPa.

(4) Constitutive model of concrete

In ABAQUS, the commonly used constitutive relations of concrete are wired elastic model, elastoplastic model and nonlinear elastic model. The purpose of this paper is to study the spatial stress distribution in joint zone of tower girder pier. Considering that no cracks occurred in the concrete members in this paper, the linear elastic constitutive model was adopted for concrete, that meaned, concrete was regarded as an elastoplastic material. The linear elastic stress-strain curve of concrete can be expressed by different material constants, and the stress-strain relationship is shown in Formula (1) and Formula (2):

$$\sigma_{ij} = \frac{E}{1+\nu}\varepsilon_{ij} + \frac{\nu E}{(1+\nu)(1-2\nu)}\varepsilon_{kk}\delta_{ij} \tag{1}$$

$$\varepsilon_{ij} = \frac{1+\nu}{E}\sigma_{ij} - \frac{\nu}{E}\sigma_{kk}\delta_{ij} \tag{2}$$

Where, E is elastic modulus of the material, and ν is Poisson's ratio of the material. ε_{kk} is the first invariant of volumetric strain or strain tensor; When $i = j$, $\sigma_{ij} = 0$; $i \neq j$, $\sigma_{ij} = 1$.

The elastic constant relationship is shown in Formula (3):

$$\lambda_{\mu} = \frac{E\mu}{(1+\mu)(1-2\mu)} \tag{3}$$

For C60 concrete, E is 3.6×10^4MPa, then λ_{μ} is 1.0×10^4MPa.

According to reference [15], the principal tensile stress and principal compressive stress of concrete generated by preloading are shown in Formula (4) and Formula (5) :

$$\sigma_{tp} = \frac{\sigma_x + \sigma_y}{2} - \sqrt{(\frac{\sigma_x - \sigma_y}{2})^2 + \tau^2} \tag{4}$$

$$\sigma_{cp} = \frac{\sigma_x + \sigma_y}{2} + \sqrt{(\frac{\sigma_x - \sigma_y}{2})^2 + \tau^2} \tag{5}$$

In this paper, according to theory of maximum tensile stress, the failure of concrete was judged, that is, when the tensile stress of a concrete member exceeds the ultimate tensile stress of concrete, brittle failure of concrete will occur.

(5) Boundary conditions

Whether the simulation of boundary conditions is accurate or not affects stress analysis results of the joint zone of tower-beam-pier directly. To simulate the boundary conditions, local analysis model was provided with five boundaries on which displacement constraints and force actions were applied as boundary conditions. Consolidation constraints were adopted at bottom of the local model, and internal force loads were applied on left and right boundary surfaces of the main girder and the bridge tower. To facilitate load application, a master node was established at the centroid of each boundary section. Other points on section were coupled with master node, and boundary conditions were applied through master node.

In the actual situation, various working conditions need to be considered about the stress of the bridge. In this paper, internal force combination under maximum cantilever during construction stage was analyzed, and stress distribution and transfer law in the joint zone were studied. The internal forces applied to the boundary were shown in Tab. 1.

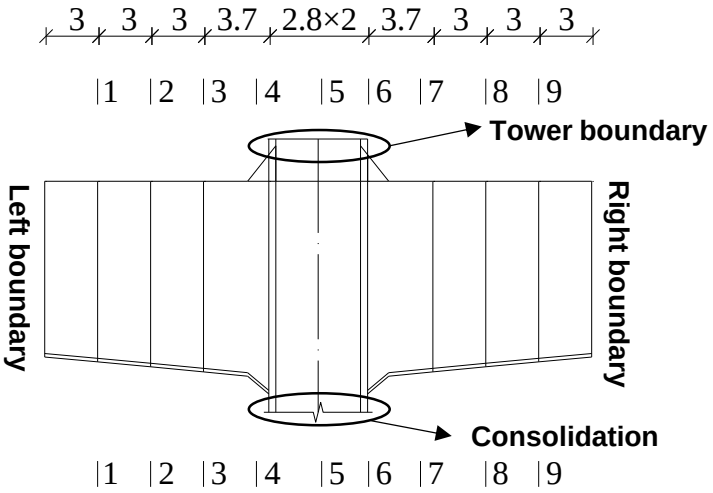

Fig. 3 – Schematic Diagram of Control Section (Unit: m)

Tab. 1: Internal forces of boundary section extracted from the maximum cantilever state in the construction stage

Position	Axial force (kN)	Shear force (kN)	Moment (kN·m)
Left boundary	-384987.35	4479.11	135028.96
Right boundary	-384987.32	-4479.11	135029.16
Tower boundary	-37027.68	0	0

(6) Model checking

To study the stress distribution rule of the model, sections at the joints of different beam parts, variable section of the main beam and middle span were taken as the control sections, as shown in Fig. 4, to analyze stress distribution of the control section under maximum cantilever load in the construction stage.

The internal force on boundary section of the local model was extracted, and compared with the internal force of the section extracted by rod system finite element models, the relative error was within 10%, which showed the calculation results of local model were reliable. Internal force checking is shown in Tab. 2.

Tab. 2: Comparison of internal forces of control section

Cross section	Axial force (kN)			Shear force (kN)			Moment (kN·m)		
	Overall model	Local model	Ratio	Overall model	Local model	Ratio	Overall model	Local model	Ratio
1-1	395071	383564	1.03	10123	10.769	0.94	110473	109379	1.01
5-5	445794	464368	0.96	-71626	-75396	0.97	90229.7	-86758	1.04
7-7	430645	448588	0.96	-42097	-40477	1.04	22119	23531	0.94

Comparative analysis of stress in the joint zone of tower-beam-pier with different systems

Because of low stiffness of all-floating system, it is not chosen for cable-stayed bridges [14]. This paper mainly studied the tower-pier consolidation system ("TBCS" for short), rigid frame system ("RFS" for short) and semi-floating system ("SFS" for short). Midas/Civil models of TBCS, RFS and SFS were obtained by modifying restraint mode of tower girder piers. The combination mode of tower girder piers is shown in Table 3. Table 4 shows the boundary internal forces extracted from finite element model of the link system at the bridge completion stage. The finite element analysis of the joint zone of tower-beam-pier of each system in completed bridge state was carried out.

Tab. 3: Boundary conditions of different systems

Cable-stayed bridge system	Rigid frame system(RFS)	Tower beam consolidation system(TBCS)	Semi-floating system(SFS)
Combination mode of tower-beam-pier	Consolidation of tower, beam and pier	Consolidation of tower and beam, elastic connection between tower and pier	Consolidation of tower and pier, elastic connection of pier and beam

Tab. 4: Internal forces of boundary section extracted under bridge condition

Cable-stayed bridge system	Position	Axial force (kN)	Shear force (kN)	Moment (kN·m)
RFS	Left of girder	-416564.5	4049.1	205621.6
	Right of girder	-416564.4	-4048.3	206005.4
	Tower	-57109.6	-0.5	12.0
TBCS	Left of girder	-359207.9	5822.6	305078.4
	Right of girder	-35207.9	-5824.8	305158.8
	Tower	-53207.2	0	27.2
SFS	Left of girder	-381097.5	-3551.3	427470.4
	Right of girder	-381097.0	3549.4	427496.8
	Tower	-66778.4	-0.1	19.8

To show stress distribution in the joint zone of tower-beam-pier, stress nephogram of the joint zone was given. According to symmetry of the structure, 1/2 model is selected for analysis, and the results are shown in Figure 4 to Figure 7.

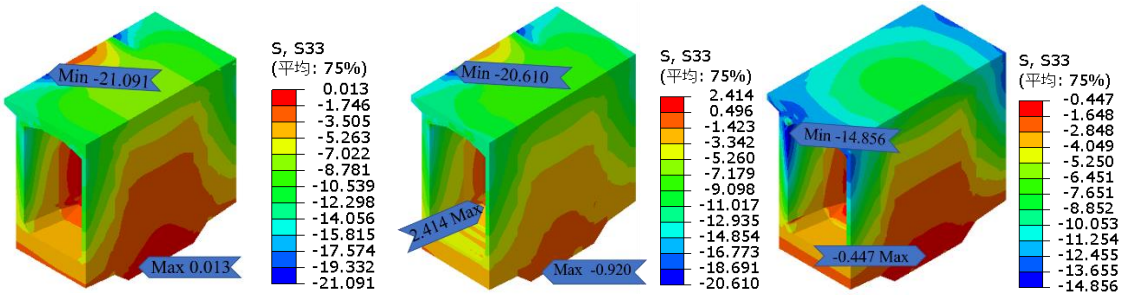

(a) RFS *(b) TBCS* *(c) SFS*

Fig. 4 – Cloud diagram of principal stress along the bridge

(1) Analysis of normal stress along the bridge

As shown in Figure 4, in RFS, the maximum tensile stress along the bridge in joint zone of tower girder pier is 0.013MPa. Except for a small amount of tensile stress at top of pier, the whole is dominated by compression. The maximum compressive stress is -21.091MPa at tower-beam junction. For TBCS, the concentrated tensile stress of 2.414MPa occurred at variable section of the beam bottom, and the reinforcement should be strengthened here. A tensile stress of 1.465MPa appeared at boundary constraint at bottom of the beam. The joint zone of tower-beam-pier was mainly under compression, and the maximum compressive stress of -20.610MPa appeared at the junction of tower-beam-pier. In SFS, the maximum normal stress along the bridge was compressive stress, which was -14.856MPa, and the whole section was under compression. The distribution of normal stress in the three kinds of systems along the bridge was similar, and stress distribution was in the shape of "∏". From the bottom to the top of the beam, the tensile stress decreased to 0 at first, and then compressive stress gradually increased. According to analysis, the normal stress of the tower-beam-pier joint zone along the bridge direction in both RFS and SFS is full-section compression, and the maximum compressive stress in SFS is less than that in RFS. Therefore, from the perspective of stress analysis, stress in the joint zone in SFS is more reasonable than that in the other two systems. The normal stress of tower-beam-pier joint zone along bridge direction in RFS is less than that in TBCS.

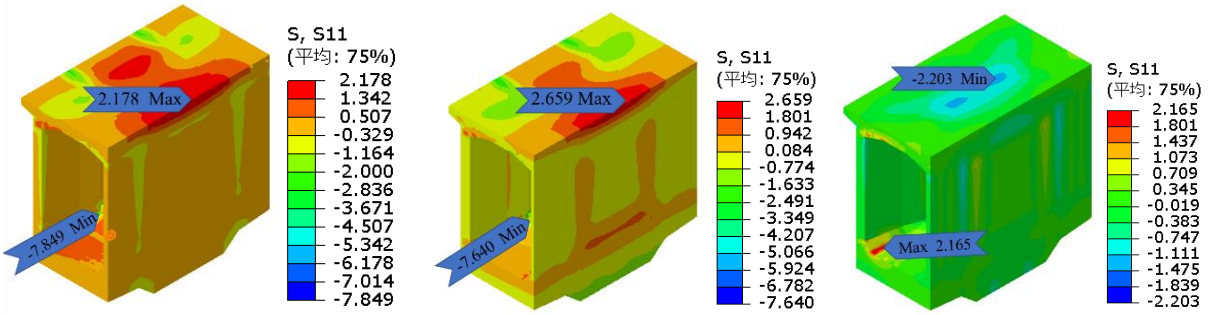

(a) RFS *(b) TBCS* *(c) SFS*

Fig. 5 – Cloud diagram of transverse principal stress

(2) Analysis of normal stress in transverse direction

As shown in Figure 5, in RFS, there was a large tensile stress at top plate of the tower-beam-pier joint zone, with value of 2.178MPa, which was mainly distributed at inner edge of the tower-beam contact and center of the top of the midspan beam, which degenerated from the center outward. The maximum compressive stress was -7.849MPa. In TBCS, distribution of normal stress in the joint zone was similar to that in RFS. The maximum tensile stress in the roof was 2.202 MPa, and the concentrated tensile stress at the intersection point of the box girder was 2.659MPa. In SFS, there was a concentrated tensile stress at the chamfering angle between web and bottom plate in tower-beam-pier joint zone, and the value was 2.160MPa. There was concentrated compressive stress at boundary constraint at bottom of the box girder and top plate of box chamber, whose maximum value was -2.200MPa, which decreased and diverged around. The transverse normal stress in joint zone of the three systems was less than the allowable value of C60 ultimate compressive stress. According to analysis, in SFS, normal stress in joint zone of tower-beam-pier is the least, and stress in the joint zone is more reasonable than the other two systems.

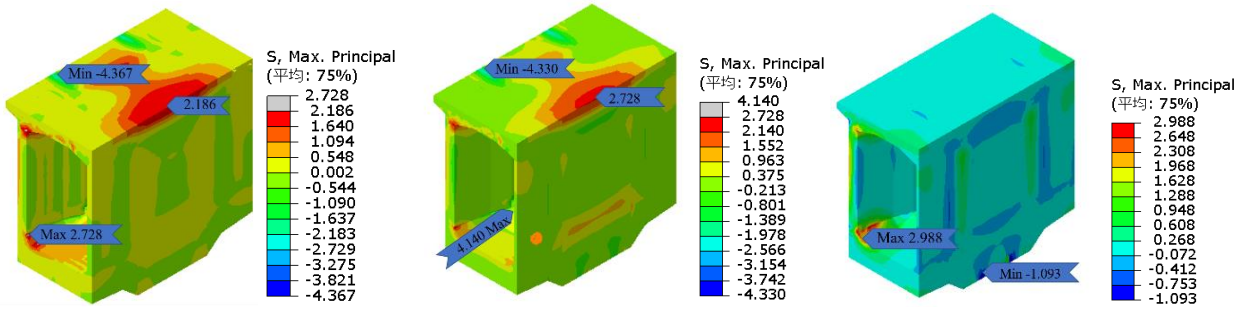

(a) RFS *(b) TBCS* *(c) SFS*

Fig. 6 – Cloud diagram of the first principal stress

(3) Analysis of Principal stress

As shown in Figure 6, in RFS, the first principal stress in joint zone of the tower-beam-pier was mainly compressive stress, and the maximum compressive stress occurred at the junction between the lower edge of the box girder roof and the tower, with a value of -4.367MPa. Tensile stress was mainly distributed in center of the beam roof and the inner edge of the junction between the tower and the top surface of the beam. The maximum tensile stress was 2.186MPa, and the compressive stress was 2.728MPa at the chamfering between the web and the bottom plate. The distribution of the first principal stress of RFS was similar to that of TBCS. The maximum compressive stress was -4.33MPa, the maximum tensile stress of the roof was 2.200MPa, and the concentrated compressive stress in the chamfering of the web and the bottom plate was -4.140MPa. In SFS, the first principal stress in the bonding zone was mainly compressive stress. In addition to the concentrated tensile stress of 2.988MPa at the chamber of the web and the bottom plate, the stress distribution of the roof, bottom plate and the web was uniform. The maximum compressive stress appeared at the boundary constraint was at bottom of the box beam, and the maximum compressive stress was -4.18MPa, which didn't exceed the strength limit of C60 concrete.

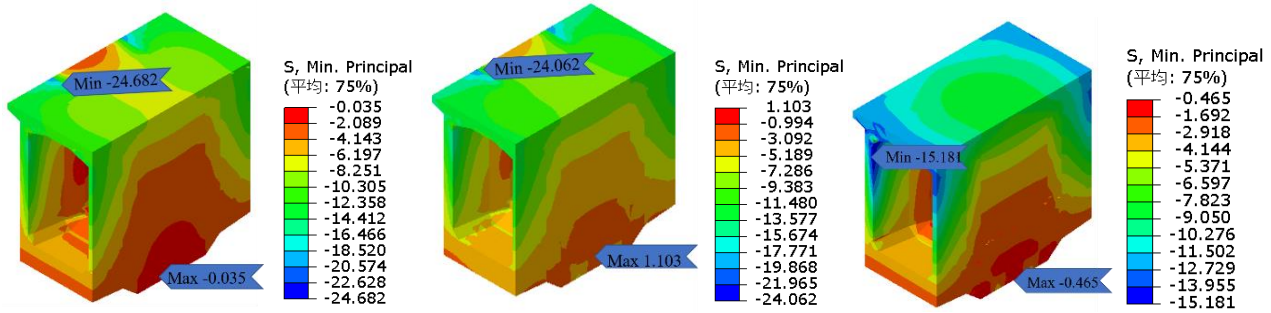

(a) RFS *(b) TBCS* *(c) SFS*

Fig. 7 – Cloud diagram of the third principal stress

As can be seen from Figure 7, the third principal stress in bonding zone of the three systems was dominated by compression. The maximum compressive stress in RFS was -24.682MPa, 24.062 MPa in tower and beam consolidation system, and -15.181MPa in SFS. The distribution of the first principal stress nephogram of RFS and TBCS was similar to that of the transverse bridge normal stress nephogram. There was a concentrated tensile stress of 1.103MPa at boundary constraint at bottom of the box girder in consolidation system. According to analysis, in case of the SFS, the transverse normal stress in junction zone of the tower beam pier is the smallest, and the force in the junction zone is more reasonable than the other two systems.

Figure 8 showed the vertical displacement of the local model. The variation range of the deflection in RFS was 0 to 2.67mm. The deflection varied between -0.19mm and -2.93 mm in the consolidation system of tower beam girder. The deflection range of SFS was -0.13mm to -2.89mm. Compared with the other two systems, the displacement generated by RFS under the action of boundary load was the smallest, and the maximum displacement occurred at the boundary section, with a value of 2.67mm.

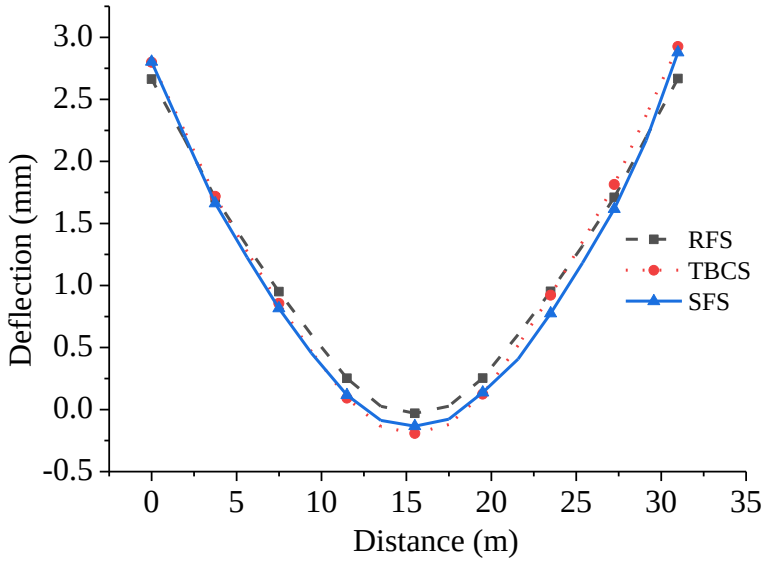

Fig. 8 – Deflection curve of main girder roof

CONCLUSION

Through the local calculation and analysis of the consolidation zone of tower-beam-pier of a cable-stayed bridge, comparison of stress state of the joint zone of tower-beam of a cable-stayed bridge under different systems, the following conclusions can be drawn.

(1) In SFS and RFS, joint zone of tower-beam-pier is subjected to compression along the full section of the bridge. The maximum compressive stress in the joint zone was -14.856MPa in SFS, -21.091MPa in RFS, and -20.610MPa in TBCS.

(2) In SFS, the maximum transverse tensile stress in bonding zone was 2.165MPa; when RFS was used, the maximum transverse tensile stress in the joint zone was 2.178MPa. The maximum tensile stress in the cross-bridge direction of the junction zone was 2.659MPa when TBCS was used. Compared with RFS and TBCS, stress distribution in bonding zone of SFS is more reasonable.

(3) The first principal stress in bonding zone of the three systems is small, and the concentrated tensile stress appears at the chamfer of the web and the bottom plate, where steel bars should be added. Compared with RFS and TBCS, SFS has no tensile stress at the pier top, and the stress distribution is more reasonable.

(4) In SFS and RFS, the third principal stress in joint zone is compressive stress. In TBCS, there was a concentrated tensile stress of 1.103MPa at boundary constraint at the bottom of the box girder. The maximum compressive stress in joint zone along the bridge was -15.181MPa in SFS, -24.682MPa in RFS and -24.062MPa in TBCS.

(5) In RFS, deflection of the main beam under action of load was the smallest, and the maximum displacement occurs at the boundary section, and the value was only 2.668mm.

ACKNOWLEDGEMENTS

This paper is supported by the Anyang Science and Technology Plan Project (2020) (grant number: 251) and Anyang Institute of Technology Research and Cultivation Fund (grant number: YPY2020021).

REFERENCES

[1] Yu Yanxia, Wang Dezhi. Design of the 95+125 m Asymmetric Single Tower Part Cable-Stayed Bridge of Fuzhou-Xiamen High-speed Railway [J]. Railway Standard Design,2020,64(S1):147-151.

[2] Wen Wangqing, Li Diping, Yan Aiguo, Huang Naxin. Study on Structural System of 3×340m Multi-tower Cable-Stayed Bridge [J]. Railway Standard Design,2020,64(03):86-90.

[3] Pan Xiangwen. Study on Mechanical Properties of High-speed Railway Cable-stayed Bridges with Short Tower [J/OL]. Railway standard design :1-6[2021-03-16]

[4] DENG Jiangtao. Analysis and Verification of Local Stress in Consolidation Section of Low Tower Cable-stayed Bridge Pier and Tower Beam of High-speed Railway [J]. Railway Standard Design,2016,60(06):43-48.

[5] Peiheng Long, Zechao Lu, Suwei Hou, Chiyu Jiao, Guangda Zhang. Research on Stress Analysis of Consolidation Area of Tower Pier of Steel-composite Composite Cable-stayed Bridge [J]. Chinese and Foreign Highway,2018,38(01):80-83.

[6] Yu Lusong, Zhu Dongsheng. Local Stress Analysis of Consolidation Point of Pier of Partly Cable-Stayed Bridge [J]. Bridge Construction, 2008(01):54-57.

[7] Song Jun, Zhou Jianting, Chen Zengshun. Local Analysis of Consolidation Section of Pier of Cable-stayed Bridge Based on Submodel Method [J]. Journal of Chongqing Jiaotong University (Natural Science),2013,32(03):379-384.

[8] HU Yuliu. Model Test Study on Consolidation Zone of Main Bridge Pier of Changmen Bridge [J]. Bridge Construction,2018,48(02):72-76.
[9] Wang Ziwen, Xu Shiwen, Deng Lu, Liu Binghui, Guo Jinlong. Model test on tower-beam bonding zone of variable cross-section elliptic single-tower cable-stayed bridge [J]. Chinese and foreign highway,2019,39(04):83-88.
[10] Shangguan Ping, Fang Zhenzheng, Zhuo Weidong. Journal of Fuzhou University (Natural Science Edition),1999(03):21-24. (in Chinese)
[11] Dai Gonglian, Su Miao. Experimental Research and Numerical Analysis on the Structure of Tower Girder of High-speed Railway Trough-beam Cable-stayed Bridge [J]. Journal of the China Railway Society,2015,37(03):85-92.
[12] ZHOU Min, DAI Gonglian, SU Miao. Numerical Simulation of Stress in Consolidation Zone of Tower Pier of Trough-section Cable-Stayed Bridge [J]. Journal of Railway Science and Engineering,2013,10(04):35-40.
[13] Li Bo, Wang Lifeng, Chen Xinpei, Wang Erqiang. Spatial Stress Analysis of 0~# Block of Short Tower Cable-Stayed Bridge [J]. China Highway and Wai Highway,2014,34(03):127-130.
[14] Jiang Rongfeng. Stress Analysis of Consolidation Zone of Single Tower Cable-stayed Bridge with Channel Section [D]. Central South University, 2013.
[15] Zhongjiao Highway Planning and Design Institute. Code for Design of Highway Reinforced Concrete Prestressed Concrete Bridges and Culverts (JTG D62-2018). People's Communications Publishing House, Beijing, China, 2018.

CIVIL ENGINEERING JOURNAL

Article no. 55

THE CIVIL ENGINEERING JOURNAL 3-2021

PRESSED NON-FIRED BRICKS FROM PHOSPHOGYPSUM WASTE FOR NON-LOAD BEARING WALL

Lassaad Ajam[1,2] and Zied Kammoun[2]

1. *University Université de Tunis El Manar, Ecole Nationale d'Ingénieurs de Tunis, LR-03-ES05 Laboratoire de Génie Civil,1002, Tunis, Tunisia; lassaadajam@yahoo.fr*
2. *Université de Carthage, Institut Supérieur des Technologies de l'Environnement de l'Urbanisme et du Bâtiment, Tunisia; kammounzied@yahoo.fr*

ABSTRACT

In several countries of the world, phosphogypsum represents a large quantity of waste that poses serious problems of environmental and groundwater pollution. This study aims at recovering phosphogypsum, in its raw state without treatment, in the manufacture of non-load-bearing non-fired bricks. The study starts with the analysis of the radionuclide activity of the materials constituting the bricks, in particular phosphogypsum, in order to avoid any human health problems after the manufacture and use of the bricks. Then, several compositions are tested with several preservation methods in order to optimize the composition. The physical, chemical and mechanical resistance is determined. The results show the possibility to produce non-load-bearing bricks based on untreated phosphogypsum which comply with the standards requirements, using low energy. Indeed, among the considered mixtures, two compositions (60% of PG and of 75% of PG) perfectly verify the physical and mechanical tests. Also, storage of the mixtures for two days in the laboratory and then three days in an oven at 70°C, allows to obtain the best resistance to compression. Thus, the obtained resistance is much higher than the minimum value required for non-load-bearing bricks.

KEYWORDS

Non-fired bricks, Phosphogypsum, Mechanical properties, Radionuclide activity

INTRODUCTION

The industrial production of phosphoric acid generates, following the treatment of phosphate rock, a large quantity of a waste called phosphogypsum (PG). In fact, to produce one tonne of phosphoric acid, around 5 tonnes of PG are generated [1]. Thus, world production of PG, mainly composed of calcium sulphate dehydrate ($CaSO_4.2H_2O$), is enormous. It exceeds 280 million tonnes per year [2] of which 22 million tonnes in China [3], 10 million tonnes per year in Tunisia [4] and more than 6 million tonnes in India [5].

The majority of PG is nowadays deposited, without treatment, in large stocks near factories in coastal regions [6]. The problems caused by the enormous amount of PG stored is not limited by the large surface areas occupied, but also extends to environmental problems. Indeed, the presence of heavy metals and radioactive nuclides in PG increases the risk of pollution of the soil, water and atmosphere around the storage areas [1, 3].

In order to reduce stored quantities, several attempts have been made to valorise the PG, mainly in agriculture [6] and in construction sectors. Thus, the use of PG in road structures has been studied. But the results were not encouraging, and the attempts were quickly abandoned in

France as in the USA (Florida) because of the heavy rains [7]. On the other hand, its use in regions with low rainfall, such as southern Tunisia, remains possible [8]. A recent work [9] has examined the use of phosphogypsum for the production of bituminous materials and has shown that PG can improve the mechanical properties of the asphalt binder as well as its performance against rutting.

The use of PG in soil stabilization [10], [11] and in embankment [12] has also been studied. Also, since PG has qualities and properties like natural gypsum, several researchers have studied its use in the manufacture of gypsum [13-15]. Other attempts to valorise PG have considered its use in cement manufacturing [16-18]. Kuryatnyk et al [19] used it as a hydraulic binder but the formation of ettringite led to a loss of strength. In Tunisia, PG has been studied for the manufacture of cement under the name of ultimax cement [20].

One of the most studied uses for PG is the manufacture of bricks, whether non-fired or fired bricks [1, 21-23]. Ajam et al. [7,24] used PG for the manufacture of fired bricks and studied its radioactivity. Their work has shown that the radioactivity measured is acceptable and below the limits prohibited by standards. Zhou et al. [23] mention that, for non-fired bricks, some studies use the autoclaving curing process where green bricks are formed at pressures between 20 and 40 MPa then autoclaved at 100-180°C for 4-8 hours at pressures of 0.8-1.2 MPa. In other studies, the green bricks are formed under high pressure of around 80 MPa. Another process used by Zhou et al. [23] consists of the pre-treatment of Chinese phosphogypsum using two-step hydration process, one before the formation of bricks under a pressure of 20 bars, and the other after. Although these approaches provide excellent mechanical performance, they lead to a considerable consumption of energy in the manufacturing process, which causes a significant amount of greenhouse gases to be released into the environment.

Within this framework, the present work envisages the introduction of untreated PG as a raw material in the manufacture of unfired bricks made of pressed sand for use in non-load-bearing walls. The advantage of the manufacture of unfired bricks is the limitation of the energy consumption during the manufacturing process, which preserves the environment by limiting the amount of the released CO_2. In a first part, and to avoid human health problems after the use of the manufactured bricks, a study of the radioactivity of the bricks materials is presented, the results encourage the use of the PG in bricks. In a second part, several formulations with PG contents that vary between 33 and 85 % are considered with several preservation methods. Characteristics such as appearance, water absorption and compressive strength are determined to find the formulations that meet the requirements of the standards.

MATERIALS

Sand

In this study, the used sand is a 0/5 silica sand from the Khelidia quarry (northern Tunisia). The particle size analysis is carried out by wet sieving. Figure 1 shows the granulometric distribution of the sand.

The uniformity coefficient (C_u) and the curvature coefficient (C_c) are evaluated at 1.54 and 3.62 respectively. The obtained value by the sand equivalent test is 51.81, that of the methylene blue test is 0.76. Thus, it is deduced that the sand contains non-clay fines.

The chemical composition of the sand (Table 1) is determined using the X-ray fluorescence spectrometer. According to table 1, it is noticed that the used sand is relatively low in alumina which acts directly on the plasticity of the mixture, with a high silica content of more than 86% which serves to constitute the skeleton of the mixture, and with some elements which play the role of fluxing agents (K_2O, Na_2O,…).

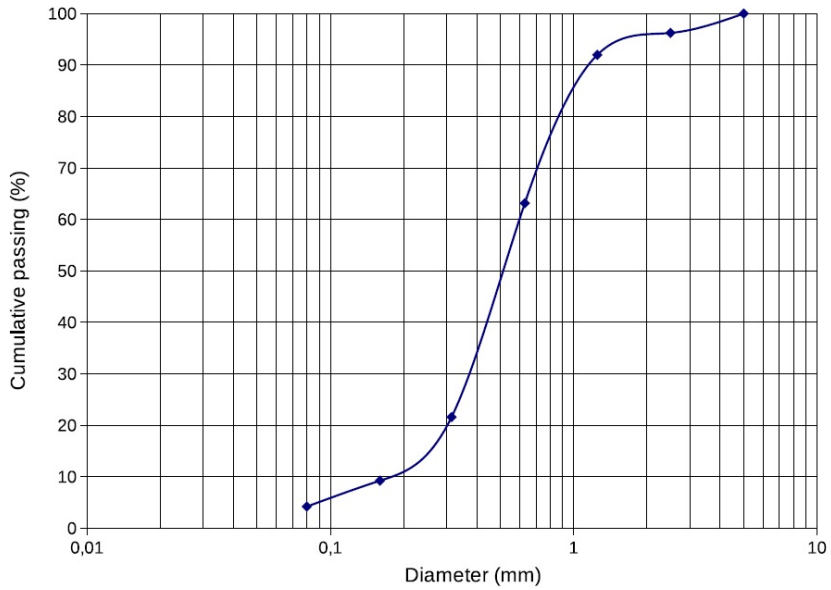

Fig. 1 – Granulometric curve of sand

The real grain density is determined by the pycnometer method. The studied sand has a density of about 2420 kg/m^3.

Tab. 1: Chemical composition of the used sand

Designation	SiO_2	Al_2O_3	Fe_2O_3	MgO	CaO	Na_2O	K_2O	Loss Ignition
Content(%)	86.15	3.22	1.27	0.86	1.32	0.76	1.13	5.42

Phosphogypsum

The used phosphogypsum comes from the Sfax region in Tunisia. Two tons of phosphogypsum are taken from one of the two slag heaps (Figure 2), which is 12 m high.

Fig. 2 – Phosphogypsum waste heap

In order to have a sample that represents as much as possible the characteristics of the heap, three locations are chosen for the sampling of the PG: the left and right sides of the bottom and at

an altitude of about 10 m. The PG is then homogenized by means of shovels, before being placed in 50 kg bags for laboratory tests.

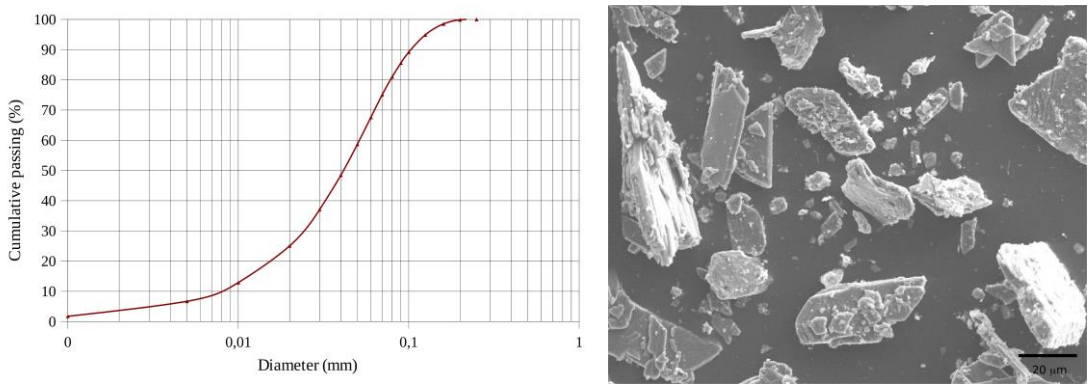

Fig. 3 – Granulometric curve and SEM photo of the studied Tunisian PG

Phosphogypsum is characterised by a grey colour. The granular distribution of PG (Figure 3) is obtained by laser diffraction (laser granulometry) and shows that PG looks like fine sand (<250 µm and about 80 % fine), with a uniform granulometry and a permeability equal to 2.6 10^{-6} m/s. Figure 3 shows also a SEM photograph of phosphogypsum. This figure shows a tabular form of crystals and that shows their length is between 20 and 200 µm, with a median length of 50 µm.

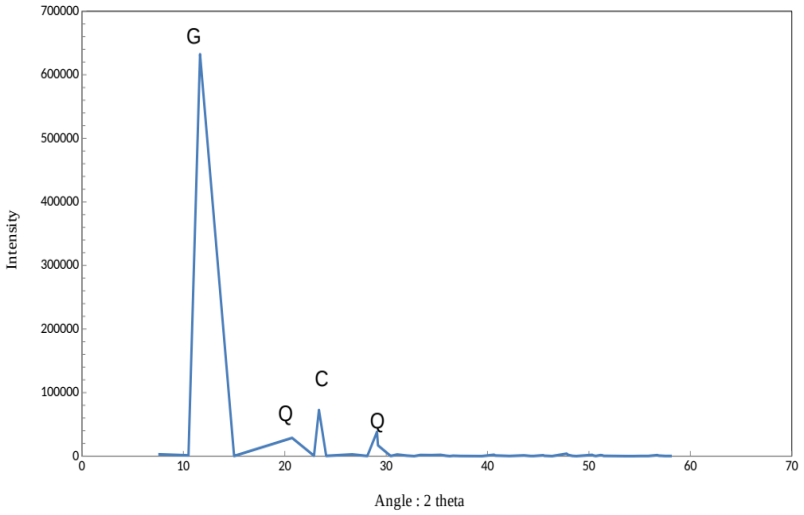

Fig. 4 –XRD patterns for the studied PG

Figure 4 shows the mineralogical phases determined using X-ray diffraction (XRD). It shows the presence of gypsum (86.15 %), calcite (10.76 %) and quartz (3.07 %). Table 2 presents the chemical analyses of the PG, which consists mainly of calcium sulphate (77 % of $CaSO_4$). Table 2 also reveals that the amount of silica present in PG is very low (1.37 % of SiO_2).

Tab 2: Chemical composition of PG

CaO	SO_3	P_2O_5	F	SiO_2 _x005F_x005F_x005F_x005F_x0001_	Fe_2O_3	Al_2O_3	MgO	Ignition loss at 1000°C
32.8	44.4	1. 69	0.55	1.37	0.33	0.11	0.007	22.3

Pycnometer method is used to determine the real density of PG. The density measured for the PG studied is 2.31 g/cm^3. This value is very close to the 2.32 g/cm^3 of natural gypsum.

METHODS

Elaboration of the composite

In their work, Felfoul et al. [25] show that the acidity of PG is an unfavourable parameter for the mechanical properties and water resistance. The study of Yang and al. [22] shows that hydrated lime, by neutralising the acidity of PG, eliminates the negative effect of acids and organic impurities on mechanical resistance of bricks.

In the present work, a percentage of hydrated lime with a $Ca(OH)_2$ content of 97.1 % is used to neutralise the PG. Thus, the optimization of the mixtures is based on the results of the evolution of the pH of the PG with the addition of the lime presented in Table 3.

Tab 3: Effect of lime on phosphogypsum pH

% of added lime	0	5	10
pH measurement	3.8	6.7	7.5

It is noticed that the variation of the lime content between 5 and 10 % has little influence on the neutralization. So, 6 % of lime may be sufficient to neutralize the PG. In addition to PG. and lime, a percentage of sand is added as aggregate and a binder is used to help the hardening of the bricks. The binder is a Portland limestone cement II/A.L32.5 used in small percentages varying between 5 and 10%. Table 4 shows the composition (percentage by weight) of the different mixtures of the studied blocks.

Tab 4: Composition of the different mixes (% weight)

Mixture	PG	Sand	Cement	Lime
M_0	33	67	0	0
M_1	45	45	10	0
M_2	60	25	9	6
M_3	75	10	5	10
M_4	65	20	0	15
M_5	85	0	0	15

Manufacturing process

In this study, miniature phosphogypsum-based pressed sand bricks (prismatic samples 10 cm × 5 cm × 1.7 cm in size) are made. Before mixing the materials, the optimum moisture content for the maximum dry density for each type of mixture must be determined. For this purpose, the Proctor test is carried out (Table 5).

The dry phosphogypsum is sieved through a 0.25 mm sieve. The weighed quantity of phosphogypsum, sand, lime and cement are first carefully mixed for a period of 10 minutes in order to obtain a uniform mixture. Then the quantity of water is added, and the mixing continues for 1 min at slow speed and 2 min at fast speed. All pressed phosphogypsum bricks are manufactured with a

semi-automatic hydraulic press under static pressure of 25 MPa (Figures 5 and 6) under laboratory conditions (humidity ≈ 70 % and temperature t ≈ 22°C).

Tab 5: Optimal water content of mixtures

	M_0	M_1	M_2	M_3	M_4	M_5
γ_d (g/cm^3)_x005F_x005F_x0001_	2.18	1.9	1.85	1.78	1.6	1.55
W_{op}(%)	11	17	17.7	18.2	24.1	29

Fig. 5 – Hydraulic press

Fig. 6 – Manufacture of pressed bricks

Finally, cylindrical specimens with a diameter of 5 cm and a height of 10 cm are made for the compressive strength measurement. These specimens are statically pressed at 25 MPa and then stored under different conditions in order to seek the best characteristics. It is noted that for each composition, three samples are developed for each test. This allows the determination of the average measurement and the standard deviation.

Experimental techniques

Radio-element contents

The radio-element content measurements are carried out by gamma spectrometry using a high-purity germanium detector. This method allows to estimate the activities of the studied samples by identifying the different gamma emitting radioelements and calculating their activities. Thus, the phosphogypsum sample is crushed and placed in a Marinelli Beaker type container (Figure 7). The container is then hermetically sealed with paraffin to prevent the escape of radon gas.

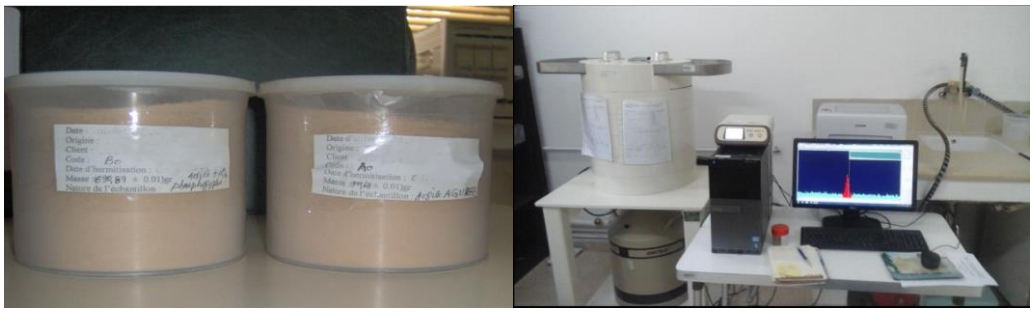

Fig. 7 – Samples to be analysed and the Germanium detector

Physical characteristics

The determination of the optimum water content required for each type of mixture is carried out with the Proctor test. The water absorption, appearance and spalling tests are carried out according to NF EN 772 [26] and to Tunisian standards NT 21-287 [27].

Compression tests

Compression tests are carried out, in accordance with standard NF EN 772 [26], on cylindrical specimens using a 3000 kN "C70-Matest" mechanical press.

RESULTS

Radioactivity

Any extract from the earth, including PG, contains some radioactivity. The determination of this radioactivity is essential for any use of construction materials. Indeed, this radioactivity must not exceed the tolerated limit set at Ra_{eq}=370 Bq/kg ([28]) in order to avoid posing radiological risks to human health.

The radionuclide content of materials used in the manufacture of non-load-bearing bricks is measured by gamma spectrometry; the results are an important factor in the human health risk analysis for the use of this type of brick after manufacture. The results of the radionuclide activity analysis are given in Table 6.

Tab 6: Radionuclide activities (Bq/kg) for different materials

	^{238}U	^{214}Pb	^{214}Bi	^{226}Ra	^{40}K	^{232}Th	^{228}Ac	^{212}Pb
Sand Khelidia	19.75	7.01	6.18	6.6	65.95	6.82	7.85	5.78
PG	39	191	209	200	15	18	17	18
Cement	25.57	11.54	10.84	11.19	265.09	11.75	13.42	10.09

The gamma-radionuclides present in soil are mainly ^{40}K, ^{238}U and ^{232}Th [29]. The obtained results for these radionuclides are close to the results obtained by Reguigui et al. [30] in Tunisian soil. Indeed Reguigui et al. show that radioactivity values for the natural radionuclides vary from 10 to 25 Bq/kg for ^{238}U, from 11 to 30 Bq/kg for ^{232}Th and from 30 to 520 Bq/kg for ^{40}K.

Several parameters can be calculated to estimate whether the use of construction materials is safe for human health, among these parameters radium-equivalent activity, absorbed dose rate, external and internal hazard indices, indoor and outdoor annual effective dose and radioactivity level index.

Radium-Equivalent Activity (Ra_{eq})

Let consider A_{Ra}, A_{th} and A_k, respectively the specific activities of ^{226}Ra, ^{232}Th, and ^{40}K. To be able to estimate the total gamma activity of a building material, the Radium-Equivalent Activity (Bq/kg) can be estimated by the Equation 1 [28].

$$\mathrm{Ra_{eq}(Bq/Kg)}=\mathrm{A_{Ra}}+\mathrm{A_{Th}}\times 1.43+\mathrm{A}_K\times 0.077 \quad (1)$$

Absorbed Dose Rate (D_γ)

Building materials at a height of 1 m above the earth's surface provides a gamma dose rate that can be estimated using the same conversion factors as in [28] (Equation 2).

$$D_\gamma(\mathrm{nGy}/h) = 0.462\times A_{\mathrm{Ra}} + 0.604\times A_{\mathrm{Th}} + 0.0417\times A_K \quad (2)$$

D_γ must be less than the maximum limit of 55 *nGy/h.*

External and Internal Hazard Indices (H_{ex} and H_{in})

The external and internal hazard indices of building materials [28], defined in Equations 3 and 4.

$$H_{\mathrm{ex}} = \frac{A_{\mathrm{Ra}}}{370} + \frac{A_{\mathrm{Th}}}{259} + \frac{A_K}{4810} \le 1 \quad (3)$$

$$H_{\mathrm{in}} = \frac{A_{\mathrm{Ra}}}{185} + \frac{A_{\mathrm{Th}}}{259} + \frac{A_K}{4810} \le 1 \quad (4)$$

A permissible risk of irradiation is characterised with an index value less than one (≤1).

Indoor and Outdoor Annual Effective Dose (E_{in} and E_{out})

The annual effective dose rates to the general public is estimated using the following expression ([28]):

$$E_{\mathrm{in}}(\mathrm{mSv/year})=\mathrm{D}_\gamma(\mathrm{nGy}/h)\times 10^{-6}\times 8760\times 0.8\times 0.7\le 1 \quad (5)$$

$$E_{\mathrm{out}}(\mathrm{mSv/year})=\mathrm{D}_\gamma(\mathrm{nGy}/h)\times 10^{-6}\times 8760\times 0.2\times 0.7\le 1 \quad (6)$$

Radioactivity Level Index (I_γ)

The radioactivity level index (I_γ) ([28]) of a building material is expressed by :

$$I_\gamma = \frac{A_{\mathrm{Ra}}}{150} + \frac{A_{\mathrm{Th}}}{100} + \frac{A_K}{1500} \le 1 \quad (7)$$

Table 7 gives the different parameter values. For all used materials, the calculated Ra_{eq} = 226.895 *Bq/kg* is less than the maximum value 370 *Bq/kg*. The gamma dose rate D_γ obtained for the PG are higher than the suggested limit value. However, Tunisian Phosphogypsum registers a much lower level of absorbed gamma dose rate than Indian PG characterised by 198.5 *nGy/h* ([28]).

Tab 7: Radionuclide activities (Bq/kg) for different materials

	Ra_{eq} (*Bq/kg*)	D_{γ}(*nGy/h*)	H_{ex}	H_{in}	E_{in}	E_{out}	I_{γ}
Sand	21.43	9.92	0.06	0.08	0.05	0.01	0.16
PG	226.9	103.9	0.61	1.15	0.51	0.13	1.52
Cement	48.4	23.32	0.13	0.16	0.11	0.03	0.37
Limit	≤ 370	≤ 55	≤1	≤1	≤1	≤1	≤1

The external hazard index, the indoor effective dose and outdoor effective dose of all materials were well within the safety limit (<1).

The internal hazard index and the radioactivity level index calculated for the PG were superior to the permissible level. Therefore, the building materials used have a tolerable radiation level for external use in buildings. For internal use, the percentage of PG must be limited to limit the level of radioactivity.

Physical Characterization of Bricks

The bricks should be free of visible defects such as cracks, fractures, deformations. Some cracks may be tolerated at a percentage of the product and if their number does not exceed the limits defined by the standards. All the formulations, except M_0 and M_1, have a good appearance. The poor appearance of the M_0 formulation is due to the presence of a large quantity of sand which is a pulverizing material in addition to the quantity of PG (50 % of the sand) which has a character of a fine sand.

Spalling

The specimens of the bricks obtained with the different mixtures (except M_0 as it presents a bad aspect), are carefully examined in order to detect any spalling. Next, these specimens are immersed in water at 80°C, then they are kept for 3 hours at boiling temperature. In order to be considered as not scaled, the external surface of the specimen must satisfy two conditions: no pop outs with an average diameter greater than 10 mm/dm^2, and no more than 3 pop outs with an average diameter between 5 and 10 mm. The test has shown that the different mixtures M_1, M_2 and M_3 are stable chemically and mechanically on bursting (Table 8).

Tab 8: Appearance test results

M_0	M_1	M_2	M_3	M_4	M_5
-	Stable	Stable	Stable	Instable	Instable

Water absorption

Water absorption is a main factor for the durability of the product and its behaviour in the natural environment. High water absorption contributes to the rapid deterioration of this type of material.

Table 9 gives the value of the water absorption of the different mixtures except that of the M_0 mixture which deteriorates rapidly in the presence of water. This deterioration is due to the large amount of sand in the formulation (67 %) and to the absence of the binder.

For M_2 and M_3 mixtures, the absorption coefficient is less than the tolerated limit value. Although the value of mixture M_3 is close to the required limit by the standard (15 %) [27, 31]. The increase in the absorption coefficient for mixtures M_4 and M_5 is due to the fineness of the PG and associated sand (around 85 %). For the mixture M_1, it shows a lower absorption coefficient than that of M_4 and M_5 although the percentage of sand and PG is higher (90 %). This is due to the presence of cement (10 %).

Tab 9: Water absorption for different mixtures (%)

Mixtures	M_1	M_2	M_3	M_4	M_5
Water absorption	25.53	6.36	14.49	33.82	32.77

Storage methods and compressive strength

In order to optimize the mechanical resistance, several storage methods are considered. The modes are chosen in order to improve the mechanical resistance on the one hand and to seek a method of economic conservation on the other. Table 10 represents the considered five modes of conservation.

Tab 10: Storage method

Mode	Storage method
Mode 0	water conservation
Mode 1	5 days in the laboratory
Mode 2	3 days in the laboratory + 2 days in an oven at 70°C _x005F_x0001_
Mode 3	2 days in the laboratory + 3 days in an oven at 70°C _x005F_x0001_
Mode 4	2 days in the laboratory + 5 days in an oven at 70°C

Tables 11, 12, 13 give the compressive strength for different mixtures and storage method on the 7th, 14th and 28th days.

Tab. 11: Compressive strength (MPa) at 7 days

	Mode 0		Mode 1		Mode 2		Mode 3		Mode 4	
	Average	S.D.	Average	S.D.	Average	S.D.	Average	S.D.	Average	S.D.
M_0	-	-	0.350	0.009	0.398	0.019	0.480	0.035	0.276	0.007
M_1	0.703	0.034	0.703	0.034	0.735	0.048	0.763	0.019	0.764	0.024
M_2	0.479	0.047	1.113	0.228	0.534	0.113	1.266	0.217	0.969	0.066
M_3	0.754	0.016	0.905	0.064	1.493	0.225	0.621	0.059	0.504	0.244
M_4	0.205	0.006	1.013	0.171	2.135	0.150	1.691	0.299	1.597	0.173
M_5	0.243	0.005	0.745	0.132	3.217	0.296	1.727	0.644	2.174	0.200

Tab. 12: Compressive strength (MPa) at 14 days

	Mode 0		Mode 1		Mode 2		Mode 3		Mode 4	
	Average	S.D.	Average	S.D.	Average	S.D.	Average	S.D.	Average	S.D.
M_0	-	-	0.522	0.104	0.593	0.016	0.652	0.026	0.427	0.055
M_1	0.860	0.075	0.860	0.075	0.906	0.032	0.930	0.038	0.892	0.019
M_2	0.851	0.013	1.292	0.239	1.709	0.207	1.913	0.441	1.608	0.249
M_3	0.669	0.011	1.025	0.092	2.588	0.073	1.080	0.134	1.608	0.249
M_4	0.232	0.011	1.402	0.062	2.013	0.116	1.638	0.380	1.129	0.306
M_5	0.315	0.004	1.311	0.038	2.967	0.575	1.715	0.589	1.593	0.434

Tab. 13: Compressive strength (MPa) at 28 days

	Mode 0		Mode 1		Mode 2		Mode 3		Mode 4	
	Average	S.D.	Average	S.D.	Average	S.D.	Average	S.D.	Average	S.D.
M_0	-	-	0.715	0.067	0.663	0.050	0.710	0.026	0.516	0.086
M_1	0.800	0.030	0.800	0.030	0.932	0.012	0.974	0.017	0.932	0.010
M_2	2.389	0.210	1.550	0.209	2.400	0.157	3.490	0.341	2.671	0.097
M_3	0.643	0.07	1.281	0.117	3.860	0.141	4.120	0.278	2.510	0.098
M_4	*	*	1.452	0.115	1.953	0.142	1.427	0.145	1.060	0.078
M_5	*	*	1.227	0.105	2.787	0.172	1.600	0.144	1.573	0.180

The mixture M_0, consisting only of sand and PG and considered as a reference mixture, cannot be stored in water. Indeed, the sample loses its shape during the conservation. Moreover, the obtained strength for the M_0 mixture (without binder) is almost insensitive to the storage mode. In addition, when using the mode 0 and beyond the 14th day, the M_4 and M_5 mixes burst and only the M_2 mix retains a good appearance and good mechanical resistance.

At 14th day, the conservation mode 2 provides the best mechanical resistance, with more than 2 MPa. At 28th day, only the M_2 and M_3 mixtures have a mechanical strength greater than 2 MPa for the 2, 3 and 4 storage methods. This is expected since the physical, appearance, bursting and water absorption tests are fully verified only for M_2 and M_3 mixtures.

By comparing M_2 and M_3 mixtures at 28th day, it is clear that the mechanical strength of M_2 is higher than that of M_3 for storage modes 1 and 4, while the strength of M_3 is higher for storage modes 2 and 3. Moreover, it is noticed that Mode 3 gives a better resistance compared to the other modes and that in Mode 4 the resistance of all mixtures decreases. This clearly shows that the storage time in the oven at 70°C has a significant effect on the mechanical resistance.

Mode 1 is a laboratory storage mode, while in mode 2 and 3 the sample is placed in the oven at 70°C for 2 and 3 days respectively. Thus, the improvement in mechanical strength can only be attributed to the longer storage time in the oven. Exposure to 70°C for up to 3 days, although it positively affects the mechanical strength of all samples, the extent of the improvement differs from one sample to another since the composition of the samples in phosphogypsum, lime and sand varies.

The experimental values obtained for the M_2 and M_3 mixtures in modes 2, 3 and 4 are mechanically comparable to most non-load-bearing bricks on the market. Indeed, the Tunisian standard imposes a minimum value of 2.3 MPa for non-load-bearing bricks [27, 31], and consequently, solid pressed phosphogypsum-based bricks can replace fired clay-based bricks.

CONCLUSION

As an economic and environmental solution for the PG deposited in heaps near the factories, this study considers the valorisation of PG in the manufacture of unfired bricks as a substitute for clay. Thus, a study of the radioactivity of the used materials was carried out and the results show that all the materials have radionuclide activities below the standard for outdoor use. For indoor use, the amount of phosphogypsum must be limited.

Several mixtures have been tested in several preservation methods. Among these mixtures, the compositions M_2 (composed of 60 % PG) and M_3 (composed of 75 % PG) fully verify the physical and appearance tests in addition to a good mechanical resistance. Therefore, the third mode of conservation (2 days in the laboratory + 3 days in an oven at 70°C) has allowed to have the best resistance to compression, which is much higher than the minimum value required for non-load-bearing bricks.

In conclusion, this study resulted in a formulation of phosphogypsum-based unfired bricks. The use of this type of non-load-bearing brick requires a low amount of energy and consumes a large amount of waste, which largely reduces environmental pollution, in addition to the high economic and social benefits. In addition, this study shows that the radioactive emission of the components of this brick is below the limit values recommended by the standards, and therefore its use is safe.

REFERENCES

[1] Yang, L., Yan, Y., & Hu, Z. H. (2012). Utilization of Phosphogypsum as raw Material for manufacturing of non-fired load-bearing wall bricks. In Advanced Materials Research (Vol. 374, pp. 787-791). Trans Tech Publications Ltd.

[2] Zhou, J., Sheng, Z., Li, T., Shu, Z., Chen, Y., & Wang, Y. (2016). Preparation of hardened tiles from waste phosphogypsum by a new intermittent pressing hydration. Ceramics International, 42(6), 7237-7245.

[3] Yang, L., Zhang, Y., & Yan, Y. (2016). Utilization of original phosphogypsum as raw material for the preparation of self-leveling mortar. Journal of Cleaner Production, 127, 204-213.

[4] Mechi, N., Ammar, M., Loungou, M., & Elaloui, E. (2016). Thermal study of Tunisian phosphogypsum for use in reinforced plaster. Current Journal of Applied Science and Technology, 1-10.

[5] Naresha, R., Laxminarayana, P., & Sailaja, K. S. D. V. (2016). Yield and Moisture Studies of Rabi Groundnut as Influenced by Moisture Regimes and Phosphogypsum Levels. Research Journal of Agricultural Sciences, 7(3), 487-491.

[6] Saadaoui, E., Ghazel, N., Ben Romdhane, C., & Massoudi, N. (2017). Phosphogypsum: potential uses and problems–a review. International Journal of Environmental Studies, 74(4), 558-567.

[7] Ajam, L., Hassen, A. B. E. H., & Reguigui, N. (2019). Phosphogypsum utilization in fired bricks: Radioactivity assessment and durability. Journal of Building Engineering, 26, 100928.

[8] Felfoul, H. S., Clastres, P., Carles, G. A., & Ouezdou, M. B. (2002). Amélioration des caractéristiques du phosphogypse en vue de son utilisation en technique routière. Waste Sci Tech, 28, 21.

[9] Amrani, M., El Haloui, Y., Hajikarimi, P., Sehaqui, H., Hakkou, R., Barbachi, M., & Taha, Y. (2020). Feasibility of using phosphate wastes for enhancing high-temperature rheological characteristics of asphalt binder. Journal of Material Cycles and Waste Management, 1-11.

[10] Degirmenci, N., Okucu, A., & Turabi, A. (2007). Application of phosphogypsum in soil stabilization. Building and environment, 42(9), 3393-3398.

[11] Krishnan, K. D., Deepika, M., Ravichandran, P. T., Sudha, C., & Kottuppillil, A. K. (2016). Study on Behaviour of Soil with Phosphogypsum as Stabiliser. Indian Journal of Science and Technology, 9(23).

[12] Amrani, M., Taha, Y., Kchikach, A., Benzaazoua, M., & Hakkou, R. (2020). Phosphogypsum recycling: New horizons for a more sustainable road material application. Journal of Building Engineering, 30, 101267.
[13] Ennaciri, Y., Zdah, I., El Alaoui-Belghiti, H., & Bettach, M. (2020). Characterization and purification of waste phosphogypsum to make it suitable for use in the plaster and the cement industry. Chemical Engineering Communications, 207(3), 382-392.
[14] Singh, M. (2002). Treating waste phosphogypsum for cement and plaster manufacture. Cement and Concrete Research, 32(7), 1033-1038.
[15] Singh, M. (2005). Role of phosphogypsum impurities on strength and microstructure of selenite plaster. Construction and building materials, 19(6), 480-486.
[16] Altun, İ. A., & Sert, Y. (2004). Utilization of weathered phosphogypsum as set retarder in Portland cement. Cement and Concrete Research, 34(4), 677-680.
[17] Islam, G. S., Chowdhury, F. H., Raihan, M. T., Amit, S. K. S., & Islam, M. R. (2017). Effect of phosphogypsum on the properties of Portland cement. Procedia engineering, 171, 744-751.
[18] Kacimi, L., Simon-Masseron, A., Ghomari, A., & Derriche, Z. (2006). Reduction of clinkerization temperature by using phosphogypsum. Journal of hazardous materials, 137(1), 129-137.
[19] Kuryatnyk, T., da Luz, C. A., Ambroise, J., & Pera, J. (2008). Valorization of phosphogypsum as hydraulic binder. Journal of Hazardous Materials, 160(2-3), 681-687.
[20] Karray, M. A., & Mensi, R. (2000, April). Etude de la deformabilite des poutrelles en beton arme a base de ciment Ultimax. In ANNALES DU BATIMENT ET DES TRAVAUX PUBLICS (No. 2).
[21] Kumar, S. (2002). A perspective study on fly ash–lime–gypsum bricks and hollow blocks for low cost housing development. Construction and Building Materials, 16(8), 519-525.
[22] Yang, J., Liu, W., Zhang, L., & Xiao, B. (2009). Preparation of load-bearing building materials from autoclaved phosphogypsum. Construction and Building Materials, 23(2), 687-693.
[23] Zhou, J., Yu, D., Shu, Z., Li, T., Chen, Y., & Wang, Y. (2014). A novel two-step hydration process of preparing cement-free non-fired bricks from waste phosphogypsum. Construction and Building Materials, 73, 222-228.
[24] Ajam, L., Ouezdou, M. B., Felfoul, H. S., & El Mensi, R. (2009). Characterization of the Tunisian phosphogypsum and its valorization in clay bricks. *Construction and Building Materials*, *23*(10), 3240-3247.
[25] Felfoul, H. S., Clastres, P., & Benouezdou, M. (2005). Gestion des sous-produits industriels et developpement durable: cas du phosphogypse de sfax (tunisie). Sciences & Technologie. B, Sciences de l'ingénieur, 66-81.
[26] EN, B.: 772. Methods of test for masonry units (2011)
[27] Inorpi: Nt 21-287. Specification des elements en maconnerie (2004)
[28] Sankaran Pillai, G., Shahul Hameed, P., & Mazhar Nazeeb Khan, S. M. (2016). Radioactivity in building materials and assessment of risk of human exposure in the Tiruchirappalli District of Tamil Nadu, India. Journal of Hazardous, Toxic, and Radioactive Waste, 20(3), 04016004.
[29] United Nations Scientific Committee on the Effects of Atomic Radiation. (1994). Sources and effects of ionizing radiation. UNSCEAR 1994 report to the General Assembly, with scientific annexes.
[30] Reguigui, N., Ben Kraiem, H., & Latrous, H. (1999). Monitoring and measurements of radioactivity around the valley of Madjerdah river in Tunisia (No. IAEA-TECDOC--1094).
[31] AFNOR: Nf en 771-1. Specification des elements en maconnerie (2003)

CIVIL ENGINEERING JOURNAL

Article no. 56

THE CIVIL ENGINEERING JOURNAL 3-2021

STUDY ON THE INFLUENCE OF SUDDEN CHANGE OF WATER LEVEL ON HIGH FILL CANAL SEGMENT

Chenyang Yuan[,1,2], Xinyong Xu[1,2], Xiangtian Nie[1,2,3] and Weifeng Bai[1,2]*

1. *North China University of Water Resources and Electric Power, School of Water Resources, No.36, Beihuan Road, Zhengzhou, Henan, China; chenyang_yuan@yeah.net; xuxinyong@ncwu.edu.cn; xtnie@126.com; yf9906@163.com*
2. *North China University of Water Resources and Electric Power, Collaborative Innovation Center of Water Resources Efficient Utilization and Support Engineering, No.36, Beihuan Road, Zhengzhou, Henan, China; chenyang_yuan@yeah.net; xuxinyong@ncwu.edu.cn; xtnie@126.com; yf9906@163.com*
3. *North China University of Water Resources and Electric Power, Henan Key Laboratory of Water Environment Simulation and Treatment, No.36, Beihuan Road, Zhengzhou, Henan, China; xtnie@126.com*

ABSTRACT

Extreme conditions will cause the water level of high fill canal segment to change suddenly, which will affect the velocity and pore pressure of the slope. In this paper, numerical method is used to study the influence of water level sudden change on seepage characteristics of high fill canal segment. HyperMesh software is used to establish the finite element model of typical high fill canal segment under complex foundation conditions. Through the combination of secondary development program and fluid-structure coupling calculation method, the fluid structure coupling effect of canal under sudden change of water level is analyzed in ABAQUS. The results show that when the water level changes suddenly, the pore pressure below the free water surface and the velocity near the free surface will be greatly affected.

KEYWORDS

High fill canal segment, Sudden change of water level, Water conveyance project, Rainfall infiltration, Fluid-structure coupling

INTRODUCTION

Water resources are an important guarantee for production and life in modern society. Water transfer project is a major strategic infrastructure to realize the optimal allocation of water resources, promote the sustainable development of economy and society, and ensure and improve people's livelihood. In China, The Eastern and Central Routes of the South-to-North Water Transfer Project (SNWTP) consist of a long open canal, inverted siphon, aqueduct and complex hydraulic structures [1] (Figure 1), and they divert water from the Yangtze River to China's arid northern regions. The construction work of the Central Route started on 30 December 2003 and began to supply water on 12 December 2014 [2], in which the concrete construction technology of water box culvert is used in the construction process. The SNWTP mostly adopts the open channel water conveyance mode, and the channel adopts the trapezoidal cross section. In order to prevent seepage and reduce roughness, the whole section is lined. The Central Route of SNWTP is 1431.95km, and the topography along the main canal is complex. With the comprehensive influence of the project in the

construction and operation period, its reliability, stability and durability are related to seepage, especially when the extreme conditions occur, for example water level suddenly change, the influence on the high fill canal segment needs to be further studied.

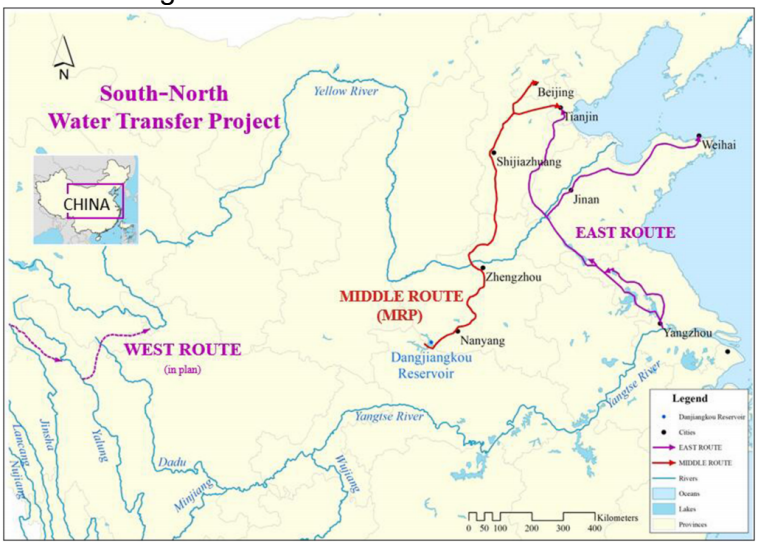

Fig. 1 – Sketch of Central Route of the SNWTP [1]

The soil is composed of more complex porous media. In the soil structure of channel slope, the change of water level causes the continuous change of underground seepage field; at the same time, due to the effect of gravity, the settlement of the channel continuously changes in a long period of time, resulting in the continuous change of structural stress, thus forming the interaction of seepage field and stress field. The seepage field and stress field in soil interact with each other [3]. When there is water head difference in soil, the water in the pore will flow and produce hydrodynamic pressure, namely seepage volume force. The seepage volume force acts on the soil for a long time in the form of external load, which makes the stress field of rock and soil change greatly [4], and the change of stress field will cause the change of displacement field of soil particles, and the spatial position between soil particles will change. After a series of changes mentioned above, the porosity of the soil changes [5], which affects the coefficient of hydraulic conductivity of the soil, and finally changes the seepage field in the soil. CAI and Ugai [6] evaluated the slope stability under rainfall infiltration based on shear strength reduction technology and considering the non-coupling condition of seepage and deformation, combined with statistical and observation methods. Rahardjo et al. [7] studied the influencing factors of slope stability under the condition of rainfall infiltration, and found that slope instability mainly depends on rainfall intensity and soil properties, and other influencing factors are slope type and groundwater level. Baum et al. [8] established the saturated and unsaturated transient rainfall infiltration model, which connected the groundwater transient, unsaturated hydraulic conductivity analysis and groundwater pressure diffusion, and predicted the time and main source area of landslide caused by rainfall. Rahardjo et al. [9] analyzed the stability of residual soil slope under the condition of rainfall infiltration considering different groundwater level, rainfall intensity and soil properties, and the results showed that they were in good agreement with the trend in the parameter study. Based on the Green-Ampt infiltration model and infinite slope stability model, muntohar et al. [10] analyzed the failure law of shallow slope under rainfall infiltration. The proposed model can be used as the first-order approximation to estimate the occurrence time and sliding depth of shallow landslide caused by rainfall. Tsai et al. [11] compared the design scheme with the actual case data, and investigated the influence of unit weight and unsaturated shear strength as a function of saturation on shallow landslide triggered by rainfall infiltration. Borja et al. [12] established a finite element model coupling solid deformation with fluid pressure in unsaturated soil to evaluate slope stability. Rahimi et al. [13] applied three rainfall modes to analyze the transient seepage of soil slope, and applied the calculation results of pore water pressure to the stability

analysis to study the influence factors of rainfall induced slope failure. Zhang et al. [14] analyzed the slope stability under the condition of rainfall infiltration, summarized the variation law of rainfall infiltration, and discussed the main causes of landslide, so as to provide a certain guarantee for the slope stability. Zhang et al. [15] used the numerical method to analyze the delay phenomenon and influencing factors of slope caused by rainfall infiltration, and determined that the possibility of delay phenomenon is higher when the slope is smaller or slower.

In recent years, many scholars have done a lot of research on fluid-structure coupling calculation method and models. Based on the three-dimensional elastic-plastic finite element theory, Bian et al. [16] proposed a seepage stress coupling method for lining structure. Deng et al. [17] combined the finite element method and the adaptive genetic algorithm, established a model based on the stress seepage coupling model and applied to the highway tunnel, and determined the initial hydraulic conductivity coefficient of the formation and the lateral pressure coefficient of the initial insitu stress through the back analysis method. Yang et al. [18] described and considered the coupling effect of seepage and stress, established a seepage stress cross coupling anisotropic numerical model, and used it to analyze the influence of joint principal direction on rock mass anisotropy. The results show that the anisotropy of rock mass has great influence on stress distribution, hydraulic conductivity and failure area. Godt et al. [19] provided a transient hydraulic conductivity analysis method to analyze a series of soil texture and landslide prone hillsides, and to predict the location and time of shallow landslide caused by rainfall. Garcia et al. [20] described the process of one-dimensional soil column rainfall infiltration based on the multi-phase coupling elastic viscoplastic finite element analysis formula of porous media theory, and numerically analyzed the generation and deformation of pore water pressure when rainfall was applied to soil. Mallari et al. [21] compared and analyzed the applicability of Horton and green amp infiltration models in overland flow, and considered that compared with Horton equation, Green-Ampt equation can more accurately describe the antecedent water content condition and flow process in soil. Wang et al. [22] combined the Green-Ampt model with the law of mass conservation to establish a rainfall infiltration model considering vertical and parallel slope seepage. Based on the Saint Venant continuity and momentum equation of surface runoff, the Green-Ampt model and explicit finite difference method were used to calculate the rainfall runoff of embankment slope [23]. Yao et al. [24] proposed SGA model to evaluate the rainfall infiltration process of slope based on the concept of layered soil moisture above the wetting front. Gavin et al. [25] improved the Green-Ampt model by assuming that the matric suction of soil increases linearly with depth after rainfall. Tsai et al. [26] established an MAGM infiltration model considering the dynamic effect of capillary pressure based on the traditional Green-Ampt model. Zeng et al. [27] investigated the macro-mesoscopic characteristics of seepage flow in porous media. Zhai et al. [28] derived a modified Shields number considering the two-dimensional seepage. Hou et al. [29] studied the effects of seepage on the long-term stability of cemented gangue fly ash backfill.

Based on the aforementioned introduction, this study explores the influence of sudden change of water level on the high fill canal segment through the combination of secondary development program and fluid-structure coupling calculation method, the fluid structure coupling effect of canal under sudden change of water level is analyzed in ABAQUS. The saturation, velocity and pore pressure of the high fill canal segment were performed.

THE THEORY OF SEEPAGE AND STRESS COUPLING

Basic model of seepage field

Generally, the actual engineering materials are porous media in seepage analysis. Under the action of hydraulic gradient, water flows between the pores. Assuming that water and soil are incompressible, the continuity equation of saturated seepage can be written in tensor form, which can be expressed as follows:

$$-\frac{\partial}{\partial x_i}\left(\rho v_t\right)+S=\frac{\partial}{\partial t}\left(\rho n\right),\ i=1,2,3 \tag{1}$$

where, ρ is fluid density; v_t is velocity; n is porosity; S is sink source term. For unsaturated seepage, $\theta=nS_w$, S_w is saturation, $0\le S_w\le 1$, the continuity equation of saturated unsaturated seepage problem is obtained:

$$-\frac{\partial}{\partial x_i}\left(\rho v_t\right)+S=\frac{\partial}{\partial t}\left(\rho nS_w\right),\ i=1,2,3 \tag{2}$$

$$-\frac{\partial}{\partial x_i}\left(\rho v_x\right)+\frac{\partial}{\partial y_i}\left(\rho v_y\right)+\frac{\partial}{\partial z_i}\left(\rho v_z\right)=-\frac{\partial}{\partial t}\left(\rho nS_w\right)+S \tag{3}$$

Darcy's law for unsaturated soils:

$$v_i=-k_{ij}k_r\left(\theta\right)\frac{\partial H}{\partial x_j},\ i,j=1,2,3 \tag{4}$$

In the continuity equation:

$$\frac{\partial}{\partial x_i}\left(\rho k_{ij}k_r\left(\theta\right)\frac{\partial H}{\partial x_j}\right)+S=\frac{\partial}{\partial t}\left(\rho nS_w\right),\ i,j=1,2,3 \tag{5}$$

where, k_{ij} is the saturated hydraulic conductivity tensor; $k_r\left(\theta\right)$ is the ratio of the hydraulic conductivity coefficient of unsaturated zone to that of saturated zone. Considering that there is a functional relationship between θ, h and k_r, $k_r\left(\theta\right)=k_r\left(\theta\left(h\right)\right)$, h is the pressure head, z is the position head:

$$\frac{\partial\theta}{\partial t}=\frac{\partial\theta}{\partial h}\frac{\partial h}{\partial t} \tag{6}$$

The following differential equation of saturated and unsaturated seepage flow can be obtained by taking the water capacity $C=\frac{\partial\theta}{\partial h}$ into formula (6) with water content instead of saturation, where the water capacity C is equal to zero in the saturated area and S_s is the unit storage capacity.

$$\frac{\partial}{\partial x_i}\left(k_{ij}k_r\left(h\right)\frac{\partial h}{\partial x_j}+k_{i3}k_r\left(h\right)\right)+S=\left(C\left(h\right)+\beta S_s\right)\frac{\partial h}{\partial t} \tag{7}$$

When the time factor is not considered, the saturated unsaturated differential equation of steady seepage can be expressed:

$$\frac{\partial}{\partial x_i}\left(k_{ij}k_r\left(h\right)\frac{\partial h}{\partial x_j}+k_{i3}k_r\left(h\right)\right)+S=0 \tag{8}$$

For the saturated unsaturated seepage field, the whole seepage region can be divided into saturated region and unsaturated region; the boundary conditions include the head boundary, known flow boundary, free surface boundary and overflow surface boundary. Where q is the normal flow,

outward is positive; n is the cosine of the external normal direction; t_0 is the initial time; Γ_1 is the known head boundary; Γ_2 is the known flow boundary; Γ_3 is the free surface boundary; Γ_4 is the over-flow surface boundary.

Initial conditions:

$$h\left(x,y,z,t_0\right)=h_0\left(x,y,z,t_0\right) \tag{9}$$

Water head boundary conditions:

$$h\left(x,y,z,t\right)\big|_{\Gamma_1}=h_1\left(x,y,z,t\right) \tag{10}$$

Flow boundary conditions:

$$-k\frac{\partial h\left(x,y,z,t\right)}{\partial n}\bigg|_{\Gamma_2}=q\left(x,y,z,t\right) \tag{11}$$

Free surface boundary conditions:

$$-k\frac{\partial h\left(x,y,z,t\right)}{\partial n}\bigg|_{\Gamma_3}=0,\ \ p\big|_{\Gamma_3}=0 \tag{12}$$

Overflow surface boundary condition:

$$-k\frac{\partial h\left(x,y,z,t\right)}{\partial n}\bigg|_{\Gamma_4}\geq 0,\ \ p\big|_{\Gamma_4}<0 \tag{13}$$

Calculation theory of seepage field

When the space domain is assumed to be discretized, the following coupling equations of seepage and stress can be obtained, which $\left[K_m\right]$ is the structural stiffness matrix, $\left(u\right)$ is the column vector of node displacement, and $\left(F\right)$ is the node load of the structure:

$$\left[K_m\right]\left(u\right)=\left(F\right)+\left(F_s\right) \tag{14}$$

Fluid-structure coupling analysis

The main difference between the saturated and unsaturated regions is the coefficient of hydraulic conductivity. In the saturated region, the coefficient of hydraulic conductivity is generally regarded as a constant, while in the unsaturated region, the coefficient of hydraulic conductivity is a relation between the saturation and the matric suction. In the unsaturated region, the pore water pressure is negative, while in the saturated region, the pore water pressure is positive. Even with these differences, the local differential equations of flow are the same. According to the principle of conservation of mass, the governing differential equation of saturated unsaturated seepage is

$$\frac{\partial}{\partial x_i}\left(k_{ij}k_r\left(y\right)\frac{\partial h}{\partial x_j}+k_{i3}k_r\left(h\right)\right)+S=\left(C\left(h\right)+\beta S_s\right)\frac{\partial h}{\partial t} \tag{15}$$

where, $k_r\left(h\right)$ is the relative coefficient of hydraulic conductivity, in the saturated area $k_r\left(h\right)=1$, in the unsaturated area $k_r\left(h\right)\in\left[0,1\right]$; k_{ij} is the saturated hydraulic conductivity tensor; S_s is the unit

water storage coefficient; $C(h)$ is the water capacity, positive pressure area, negative pressure area, $C(h)=\frac{\partial\theta}{\partial h}$; θ is the water content; β is the parameter to determine the saturated and unsaturated state, $\beta=0$in the unsaturated area, $\beta=1$ in the saturated area; t is the time; S is the source sink term.

The relationship between matric suction and saturation was obtained by Van Genuchten model

$$S_e=\left[1+(\alpha P_c)^n\right]^{-m} \tag{16}$$

where, P_c is the matric suction; m, n and α are the fitting parameters.

The relationship between parameters m and n can be used by $n=\left[-m\right]^{-1}$, then equation (16) can be expressed as:

$$P_c=P_0\left[S_e^{-1/m}-1\right]^{1/n} \tag{17}$$

where, $P_0=1/\alpha$; S_e is the effective saturation, $S_e=(\theta_w-\theta_r)/(\theta_s-\theta_r)$; θ_s is the saturated volumetric water content; θ_r is the residual volumetric water content; and θ_w is the volumetric water content of the corresponding matrix suction.

SECONDARY DEVELOPMENT PROGRAM

In order to study the influence of sudden change of water level, an ideal slope model is used to verify the effectiveness of the secondary development program.

Ideal slope model

The mathematical model established in this section is an ideal slope. The slope angle is 45° and the slope height is 5 m. The initial groundwater level is 2 m above the foot of the slope, and the foundation size is 10 m. Based on the above theoretical analysis, the finite element model was established in ABAQUS and shown in Figure 2.

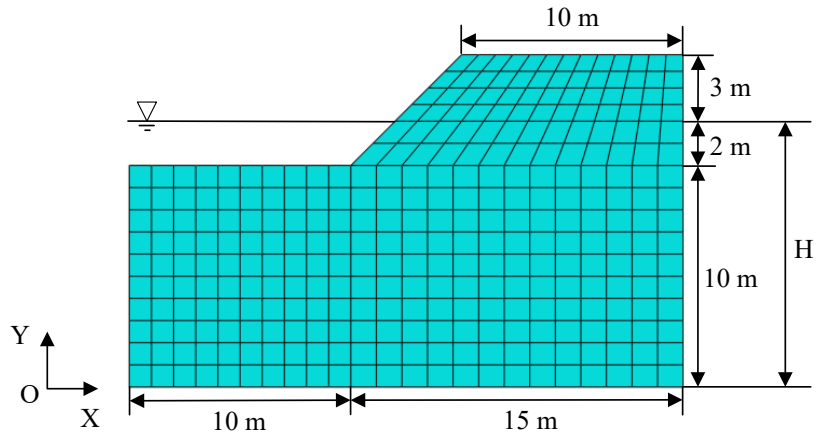

Fig. 2 – Finite element mesh model

Program code

When there is a rainstorm or other special circumstances, the water level of the channel will change suddenly in a short time. In ABAQUS, there is no function to directly set the sudden change of water level. In order to further analyse and study the canal segment performance in the case of sudden change of water level, it needs to be realized through secondary development. This research is implemented by FORTRAN program. The calculation flow chart is shown in Figure 3, where Y is the height value of node on the boundary below water level, ρ is the density of water, γ_{water} is the bulk density of water, t1 is the time of Step 1, t2 is the time of Step 2, s1 is the water level that decreases in time t0. It is assumed that the water level will drop by 2 m within 24 hours as an example.

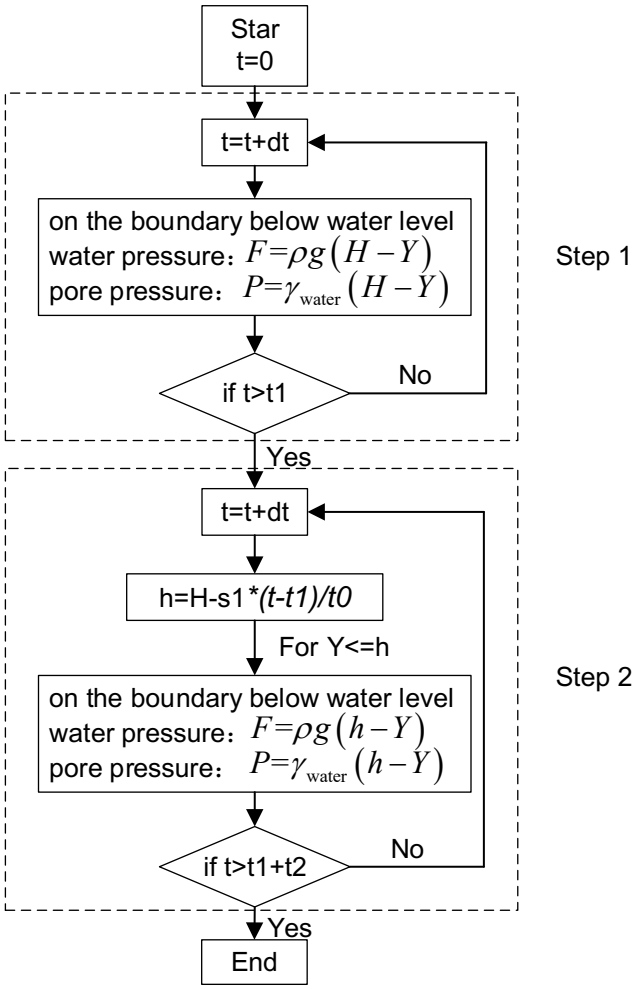

Fig. 3 –Calculation flow chart

Analysis of sudden change of water level

The seepage analysis of ideal model before and after the sudden change of water level is carried out in ABAQUS. Figure 4 shows the distribution of pore pressure before and after the sudden change of water level. The pore pressure distribution after the sudden change of water level is significantly different from the initial state. With the decrease of water level, the phreatic line

decreases at the slope position. However, due to the change of water level in a short time, the seepage of internal soil changes little, so the position of internal phreatic line changes little.

Figure 5 shows the vertical displacement distribution before and after the sudden change of water level. It can be seen from the figure that due to the influence of seepage, the vertical displacement at the foot of the slope changes from -2.57 mm to -1.85 mm (positive upward), and the vertical displacement at the middle of the bottom plane of the slope changes from 0 mm to 1.64 mm.

Through the analysis of ideal model, the rationality of secondary development program is verified, which is helpful to apply to high fill canal segment.

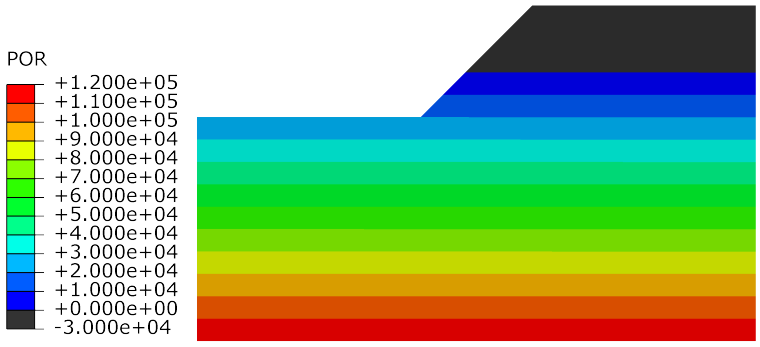

(a)

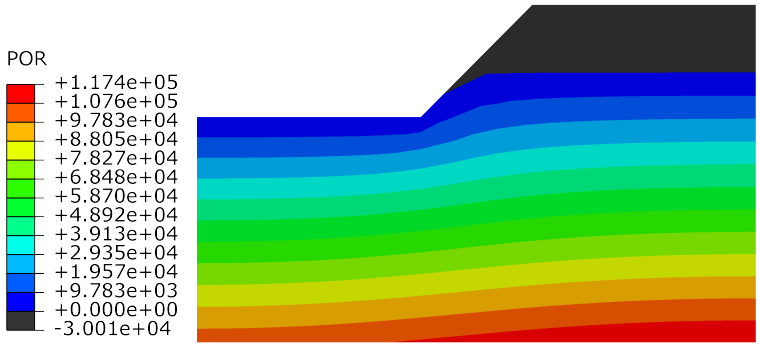

(b)

Fig. 4– The pore pressure nephogram: (a) before sudden change of water level; (b) after sudden change of water level

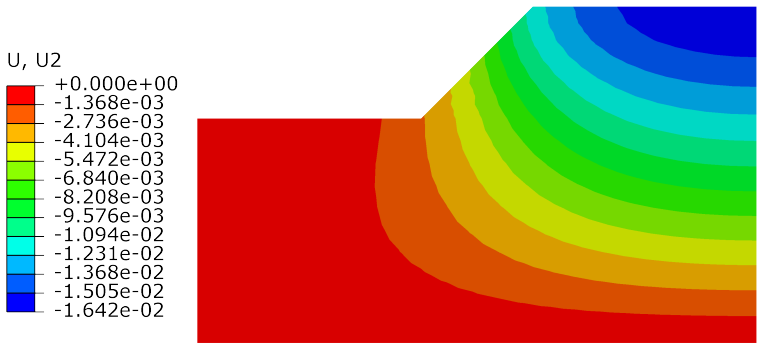

(a)

Fig. 5 – Vertical displacement nephogram: (a) before sudden change of water level; (b) after sudden change of water level

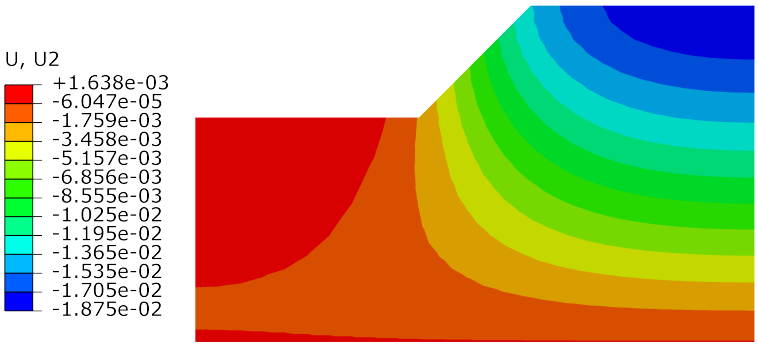

(b)

Fig. 5 – Vertical displacement nephogram: (a) before sudden change of water level; (b) after sudden change of water level

SIMULATION AND DISCUSSION

The model of high fill canal segment

The typical high fill canal segment is selected for seepage stress coupling numerical simulation analysis. Because the thickness of lining plate is smaller than that of soil, the element transition is used in HyperMesh to realize the connection between meshes of different sizes, as shown in Figure 6. The model includes: concrete lining slab, asphalt pavement, foundation and fill. In the calculation, CPE4P coupling element with high accuracy is selected as the material element of the model, and the calculated mechanical parameters of the material model are shown in Table 1. It should be pointed out that the positions of silty clay and compacted silty clay are foundation and filling respectively.

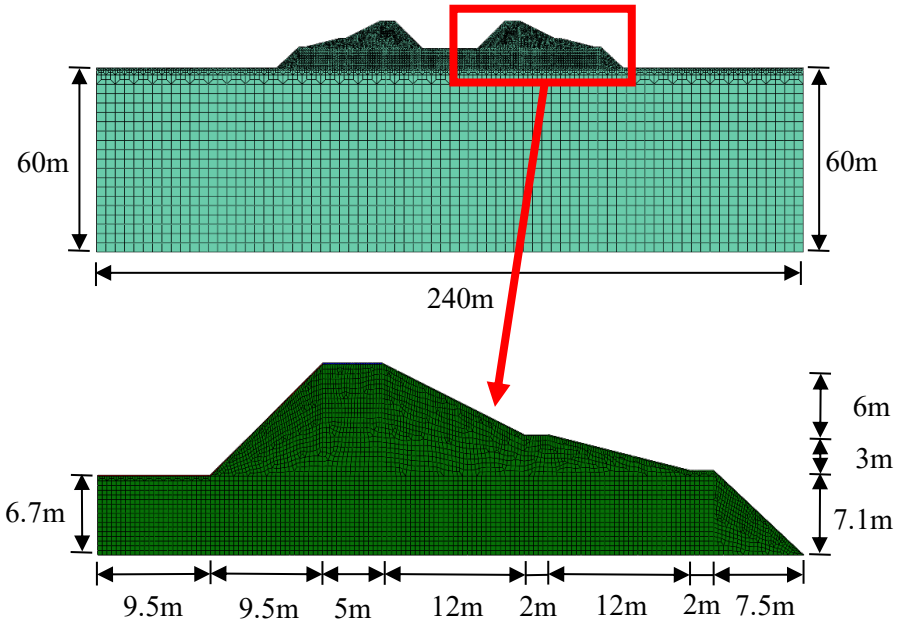

Fig. 6 – The finite element model of high fill canal segment

Tab. 1: Calculation mechanical parameters of material

material type	compression modulus（MPa）	density（kg.m^{-3}）	cohesion（kPa）	friction angle (°)	porosity	hydraulic conductivity (m/s)	grain size (mm)
silty clay	23	2020	42.0	25.0	0.48	3.5e-8	0.005
compacted silty clay	22	2010	36.6	17.6	0.50	7.3e-7	0.005

Seepage analysis of sudden change of water level

The lining plate has the function of anti-seepage and reducing roughness under normal conditions. During the operation of SNWTP, due to various factors such as uneven settlement and rainfall, the lining plate will crack, swell and collapse, which will make the lining plate lose its anti-seepage function. ABAQUS provides special "displacement pore pressure coupling elements" for solving seepage stress coupling problems. The pore pressure of these elements is linear distribution, and the displacement can be taken as the first-order or second-order distribution function, which can be used to solve porous media seepage problems of plane strain, axisymmetric and H dimensional problems.

In order to better analyse the calculation results, the top A, middle B and bottom C of the canal slope are selected as the characteristic points to analyse the seepage characteristics of the canal slope (Figure 7).

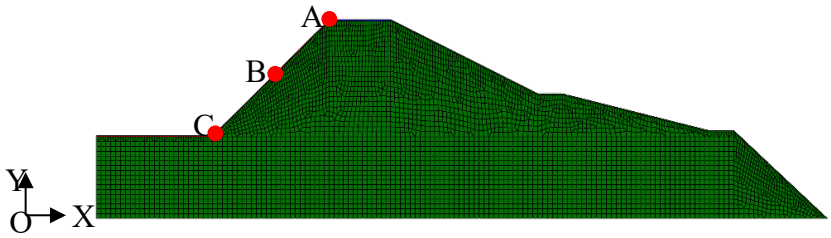

Fig. 7 – Distribution map of characteristic points

When there is rainstorm, leakage or other extreme conditions, the water level of the channel will rise or fall in a short time. In order to further analyze and study the seepage characteristics of the sudden rise and fall of water level, it needs to be realized through the secondary development in ABAQUS. In this study, according to the dynamics of actual changes in the channel, FORTRAN program is used to realize the situation of water level sudden drop of 0.5 m (case 1) and sudden rise of 0.5 m (case 2) within 3 hours, and two analysis steps are set: Step 1 is seepage steady analysis, Step 2 is seepage transient analysis, and subroutine plays a role in Step 2.

Figure 8 shows the distribution of pore pressure before and after the sudden change of water level with two cases. And the Table 2 shows the results of pore pressure for A, B, and C. For the normal case, the Figure 8(a) shows that pore pressure nephogram under design water level when lining plate and composite geomembrane fail at the same time, which indicates that when the anti-seepage effect of lining plate fails, the water in the channel will seep into the soil, which may lead to the outward leakage of river water. It can be seen from the Figure 8 that the sudden drop or rise of water level will lead to the drop or rise of the pore water pressure at B and C, and the change of pore water pressure at A point is not obvious, because a point is above the free water surface, the pore water pressure is negative, and there is no significant change.

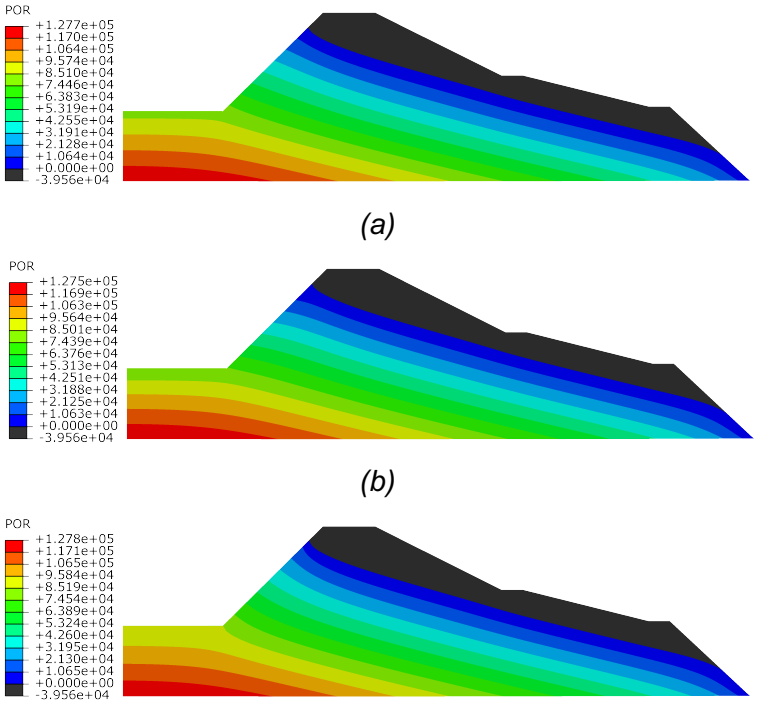

Fig. 8 – The pore pressure nephogram of high fill canal segment: (a) normal; (b) case 1; (c) case 2

Tab. 2: Pore pressure of seepage analysis (kPa)

Type	normal	case1	case 2
A	-25.63	-25.63	-25.63
B	32.30	27.30	37.23
C	80.00	75.00	85.00

Figure 9 shows the velocity vector diagram of grid integration point before and after the sudden change of water level with two cases. It can be seen form the figure that the sudden change of water level leads to obvious change of velocity near the free water surface, but not obvious change inside the fill. This is because the time of sudden change of water level is short, and it has not caused too much impact on the inside of the fill.

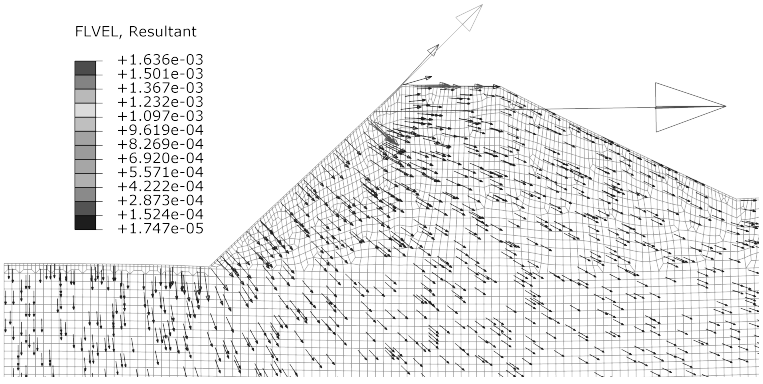

Fig. 9 – The velocity vector diagram of grid integration point of high fill canal segment: (a) normal

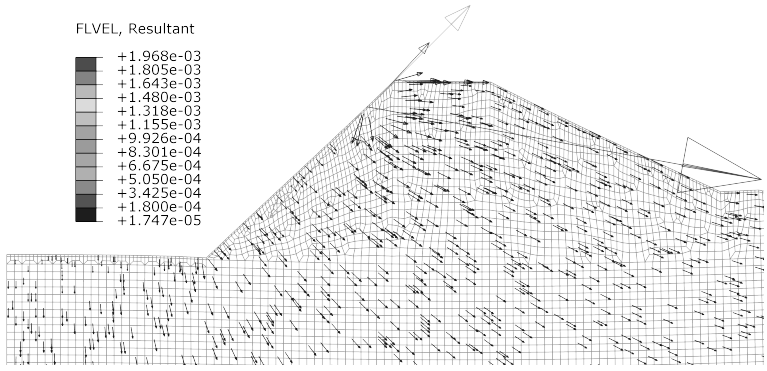

(b)

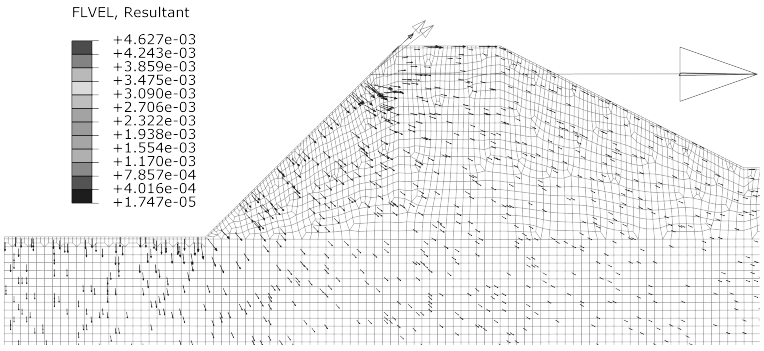

(c)

Fig. 9 – The velocity vector diagram of grid integration point of high fill canal segment: (a) normal; (b) case 1; (c) case 2

CONCLUSION

This study has focused on the influence of water level sudden change on seepage characteristics of high fill canal segment. FORTRAN program was used to realize the situation of water level sudden change. One ideal slope model was used to verify the rationality of secondary development program. For high fill canal segment, the two cases with sudden drop of 0.5 m and sudden rise of 0.5 m in 3 hours were studied. Considering the fluid-structure interaction, the change of seepage performance under the condition of sudden change of water level is analyzed. The conclusions is as follows:

1. The FORTRAN program given in this paper can effectively simulate the sudden change of water level. Under the action of sudden change of water level, it will lead to the change of pore pressure below the free water surface, but the change of pore pressure above the free water surface is not obvious; the velocity near the free water surface has a great influence, but it has little influence on the velocity inside the fill due to the short time.

2. When the anti-seepage effect of lining plate fails, the water in the channel will seep into the soil, which may lead to the outward leakage of river water, which will result in the structural failure.

3. The safety for earthquake action, the uneven settlement of the joint parts of different buildings and the influence of different site conditions on seepage can be studied in the near future.

4. For high fill canal segment, it is suggested to increase the anti-seepage measures at the external slope toe in the design process.

ACKNOWLEDGEMENTS

This research was funded by the National Key Research and Development Project (grant no. 2018YFC0406901), National Natural Science Foundation of China (grant nos. 51979109 and 51679092), and Scientific Research Project of North China University of Water Resources and Electric Power (grant no. 201811007).

REFERENCES

[1] Yang Y., Lei X., Long Y., et al., 2019. A novel comprehensive risk assessment method for sudden water accidents in the Middle Route of the South–North Water Transfer Project (China). Science of The Total Environment. 698, 134167.

[2] Dong J , Lai S , Wang N , et al., 2021. Multi-scale deformation monitoring with Sentinel-1 InSAR analyses along the Middle Route of the South-North Water Diversion Project in China. International Journal of Applied Earth Observation and Geoinformation, 100:102324.

[3] Yang T. H., Jia P., Shi W. H., et al., 2014. Seepage–stress coupled analysis on anisotropic characteristics of the fractured rock mass around roadway. Tunnelling and Underground Space Technology incorporating Trenchless Technology Research. 43, 11-19.

[4] Zhang M., Dong Y., Sun P., 2012. Impact of reservoir impoundment-caused groundwater level changes on regional slope stability: a case study in the Loess Plateau of Western China. Environmental Earth Sciences. 66(6), 1715-1725.

[5] Leong E. C., Rahardjo H., 2012. Two and three-dimensional slope stability reanalyses of Bukit Batok slope. Computers and Ge-otechnics. 42(3), 81-88.

[6] Ugai C., 2004. Numerical analysis of rainfall effects on slope stability. International journal of geomechanics. 69-78.

[7] Rahardjo H., Ong T. H., Rezaur R. B., Leong E. C., 2007. Factors controlling instability of homogeneous soil slopes under rainfall. Journal of Geotechnical & Geoenvironmental Engineering. 1532-1543.

[8] Baum R. L., Godt J. W., Savage W. Z., 2010. Estimating the timing and location of shallow rainfall-induced landslides using a model for transient unsaturated infiltration. Journal of Geophysical Research-Earth Surface. 115, 26.

[9] Rahardjo H., Nio A. S., Leong E. C., Song N. Y., 2010. Effects of Groundwater Table Position and Soil Properties on Stability of Slope during Rainfall. Journal of Geotechnical and Geoenvironmental Engineering. 136, 1555-64.

[10] Muntohar A. S., Liao H. J., 2010. Rainfall infiltration: infinite slope model for landslides triggering by rainstorm. Natural Hazards. 54, 967-84.

[11] Tsai T. L., Chen H. F., 2010. Effects of degree of saturation on shallow landslides triggered by rainfall. Environmental Earth Sciences. 59, 1285-95.

[12] Borja R. I., White J. A., 2010. Continuum deformation and stability analyses of a steep hillside slope under rainfall infiltration. Acta Geotechnica. 5, 1-14.

[13] Rahimi A., Rahardjo H., Leong E. C., 2011. Effect of Antecedent Rainfall Patterns on Rainfall-Induced Slope Failure. Journal of Geotechnical and Geoenvironmental Engineering. 137, 483-91.

[14] Zhang L. L., Zhang J., Zhang L. M., Tang W. H., 2011. Stability analysis of rainfall-induced slope failure: a review. Proceedings of the Institution of Civil Engineers-Geotechnical Engineering. 164, 299-316.

[15] Zhang J., Li J. T., Lin H., 2018. Models and influencing factors of the delay phenomenon for rainfall on slope stability. European Journal of Environmental and Civil Engineering. 22, 122-36.

[16] Bian K., Xiao M., Chen J., 2009. Study on coupled seepage and stress fields in the concrete lining of the underground pipe with high water pressure. Tunnelling and Underground Space Technology. 24, 287-295 .

[17] Deng X. H., Yuan D. Y., Yang D. S., Zhang C. S., 2017. Back Analysis of Geomechanical Parameters of Rock Masses Based on Seepage-Stress Coupled Analysis. Mathematical Problems in Engineering. 13.

[18] Yang T. H., Jia P., Shi W. H., Wang P., Liu H. L., Yu Q. L., 2014. Seepage-stress coupled analysis on anisotropic characteristics of the fractured rock mass around roadway. Tunnelling and Underground Space Technology. 43, 11-19.

[19] Godt J. W., Sener-Kaya B., Lu N., Baum R. L., 2012. Stability of infinite slopes under transient partially saturated seepage conditions. Water Resources Research. 48, 14.
[20] Garcia E., Oka F., Kimoto S., 2011. Numerical analysis of a one-dimensional infiltration problem in unsaturated soil by a seepage-deformation coupled method. International Journal for Numerical and Analytical Methods in Geomechanics. 35, 544-68.
[21] Mallari K. J. B., Arguelles A. C. C., Kim H., et al., 2015. Comparative analysis of two infiltration models for application in a physically based overland flow model. Environmental Earth Sciences. 74(2), 1579-1587.
[22] Wang D. J., Tang H. M., Zhang Y. H., et al., 2017. An improved approach for evaluating the time dependent stability of colluvial landslides during intense rainfall. Environmental Earth Sciences. 76(8), 321.
[23] Asim, Krishna, Sajjan, et al., 2013. Rainfall–runoff modelling of railway embankment steep slopes. Hydrological Sciences Journal. 58(5), 1162-1176.
[24] Yao W., Li C., Zhan H., et al., 2019. Time dependent slope stability during intense rainfall with stratified soil water content. Bulletin of Engineering Geology and the Environment. 78(7), 4805-4819.
[25] Gavin K., Xue J., 2008. A simple method to analyze infiltration into unsaturated soil slopes. Computers and Geotechnics. 35(2), 223-230.
[26] Tsai Y. Z., Liu Y. T., Wang Y. L., et al., 2018. Effects of the Grain Size on Dynamic Capillary Pressure and the Modified Green-Ampt Model for Infiltration. Geofluids. 2018, 1-11.
[27] Zeng F., Guo Z., Wang L., et al., 2020. Experimental investigation on macro-mesoscopic characteristics of seepage flow in transparent porous media. Applied Ocean Research. 105, 102424.
[28] Zhai H., Jeng D. S., Guo Z., et al., 2021. Impact of two-dimensional seepage flow on sediment incipient motion under waves. Applied Ocean Research. 108, 102510.
[29] Hou J., Guo Z., Li J., et al., 2020. Study on triaxial creep test and theoretical model of cemented ganguefly ash backfill under seepage-stress coupling. Construction and Building Materials.

CIVIL ENGINEERING JOURNAL

Article no. 57

THE CIVIL ENGINEERING JOURNAL 3-2021

FREE STATION TASK WITH DRONE

David Zahradník

Czech Technical University in Prague, Faculty of Civil Engineering, Department of Geomatics, Thákurova 7, Praha 6, Czech Republic; david.zahradnik@fsv.cvut.cz

ABSTRACT

The main purpose of drones is to take pictures, but different developers are inventing new possibilities of use. Drones are used mainly for reconnaissance. During survey they can be also used in other ways than taking pictures. A drone containing GNSS RTK and a prism can be used as an orientation point for a total station. The idea of this use is based on the need to establish a boundary of ownership in the forest. Forests with tall trees are bad for GNSS receivers, the signal will not go through the treetops and the GNSS receiver cannot pinpoint its location. When the GNSS receiver reaches above the trees, it is possible to receive the GNSS signal and determine the position of the GNSS receiver. Position projection in terrain is problematic. The first method is to project the position of the GNSS receiver along the vertical axis by some measurement equipment. The second method involves using a total station and prism. The free station method is used with a connection to orientation points on a drone. This article discusses the accuracy of the free station task with the connection to orientation points on a drone.

KEYWORDS

Free station task, Drone, Precision analysis

INTRODUCTION

Drones are an important part of surveys. Land surveying is much faster and allows analyzing larger areas with similar accuracy [1] [2]. Use of dronesgrows with various devices deployed on the drone like LIDAR, etc.

3D models of buildings and structures can be created using drones, but sometimes it is difficult to fly with drones in a limited space. A combination of total station and drone solves this problem [3] [4] [5] [6] [7] [8]. Total station measures the position of the drone and it sends this information to the drone program. This helps to fly it more precisely than drones equipped with GNSS RTK.

Other works show that drones can place construction points in the field. Drone flies to the approximate position of the construction points. Drone lands on the plane and it starts measuring the observation by RTK method. Difference between drone position and construction point is set by mechanical tools on the drone. After setting the right position of the mechanical tool, drone drills nail into the ground and construction point is stabilized. [9]

The drone is equipped with a pri sm and a GNSS receiver. GNSS receivers must allow centimeter position accuracy. Drone serves as orientation points, total station measure on them and it calculates the coordinates of its position. This method applies to locations without permanent points and without a GNSS signal. Traditionally permanent points are created by polygon method via total station. Primary permanent points are measured by GNSS receiver in an environment with good GNSS signal and secondary permanent points are measured by total station in forest. This method is time consuming and expensive. Combination of total station and drone will help accelerate this type of measurement.

METHODS

A free station task is used for combination measuring of a total station and a drone. Drone with GNSS RTK receiver and prism serves as orientation points. Total station measures on drone and calculates its coordinates. Precision of this method must be known for its credibility.

Orientation points have a main effect on resulting precision. Precision of orientation points depends on precision of GNSS receiver, horizontal offset between prism and GNSS antenna and drone movements in specific air conditions.

Ublox F9P with ANN-BN antenna is used as a GNSS receiver. Horizontal and vertical position accuracy of the module in RTK method is 1 cm + 1ppm given by the datasheet. Position accuracy from manufacture is confirmed by testing this module [10]. Some studies also confirmed this claim in open space without multipath [11] [12].

Horizontal offset is minimized in design solutions, and it causes the smallest errors of all three aspects.

Drone movement must be considered. The drone is constantly moving. Drone holds position via GNSS, IMU, and visual sensors. If a drone flies in the wind, the system reacts after changing position. This causes time gaps in the holding position process, so the drone moves. Drone movements in the holding position function are determined in this article.

A process of a free station task with drone depends on a total station and a drone. At least two permanent points must be created by this method to allow subsequent measurement. Two places must be found with visibility to the sky for permanent points. Total station is prepared for measurement and the drone flies above trees. GNSS receiver on drone starts to measure coordinates. Distance, horizontal and vertical angle are measured by total station to prism on the drone. When two orientation points are measured, total station calculates its coordinates.

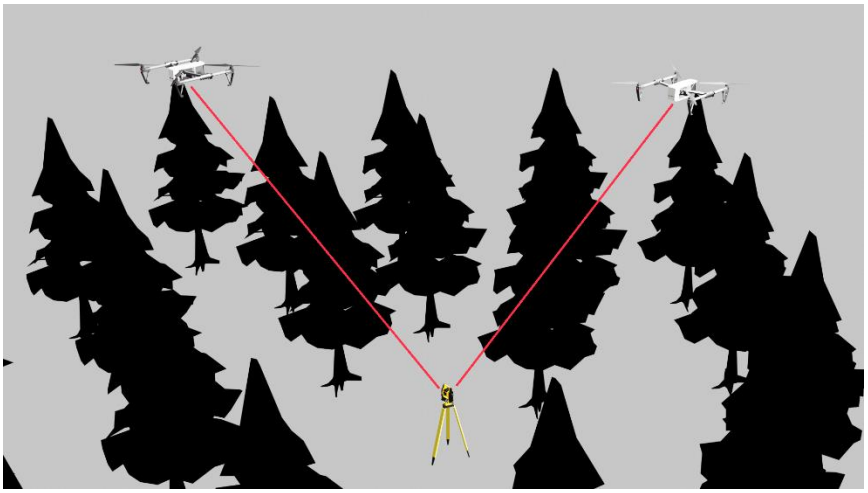

Fig. 1 – Free station task scheme

The configuration of orientation points and total station have also an effect on position accuracy.

There is limited visibility in the forest, so it is important to know limitations of free station task. The article deals with free station tasks with two orientation points. High visibility is not expected in the forest, so only two orientation points are planned.

Free station task is done by the least squares method. It is the most common calculation method used in total station software.

Drone construction

DJI Mavic 2 has been selected for this experiment. Ublox F9P with ANN-BN antenna are installed on top of the drone. GNSS receiver is independent, and it does not control drone movement. GNSS receiver is connected via NTRIP client to receive data of reference stations from CZEPOS network. [13]

Fig. 2 – DJI Mavic 2 PRO + Ublox F9P

Drone movements

Precision of orientation points affects drone movement in different wind conditions. The test of drone movements reveals how much the wind affects drone movement.

The test was performed twice, in windy (15 m/s) conditions and windless (5m/s) and the test has been verified by two methods. First method was done by installing an independent GNSS receiver and GNSS receiver measures drone positions. In the second method prism was installed on the drone, and it was measured by total station. Drone was holding position 30 m above ground in open space, where it was exposed to the wind.

First method is done by a GNSS receiver with RTK method, position data was recorded for 5 minutes in each wind condition and was analyzed for finding standard deviation of drone movements. Results are presented in Table1.

In the second test, the position of the drone was measured by total station with automatic targeting. Position was measured in the same conditions as the first test, in wind (15 m/s) and windless (5m/s). Drone was flying 30 m above the ground and the distance between the total station and drone was 50 m. Position was measured every 15 seconds for 5 minutes, 20 positions were captured. Results are in Table 2.

Data from the second method was analyzed and compared to the first method. The second method verifies the results of the first method.

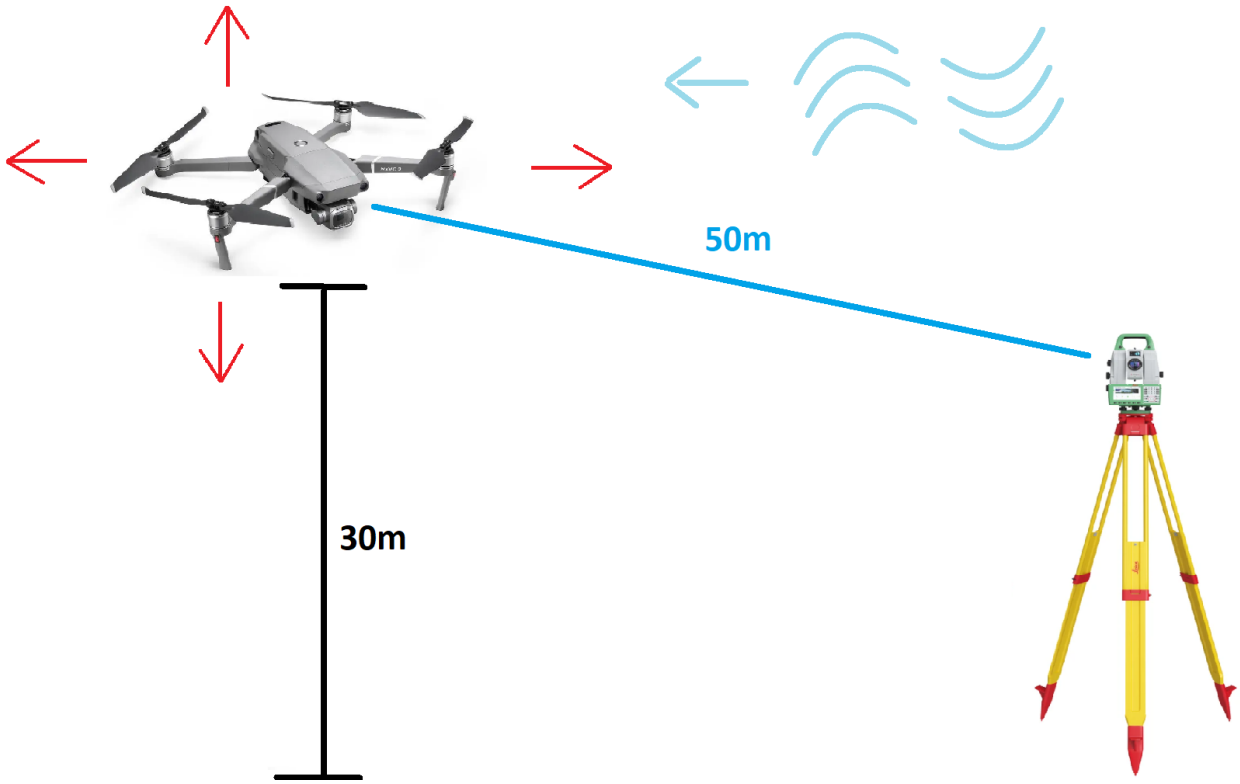

Fig. 3 – Drone movement test scheme

Theoretical precision analysis

Free station task is calculated by measured angles and distances at known points. If the measurement contains redundant values that are subject to normal distribution, errors are adjusted by least squares.

The approximate coordinates must be known for the calculation, and it is calculated by different method like distance intersection [14] [15] [16].

In our example results of least squares are free station coordinates and orientation shift.

$$X = (X_c Y_c Z_c o_p)^T \quad (1)$$

Measured values on orientation points are horizontal direction, zenith angle, and distance.

$$l = (\varphi_1 \varphi_2 \zeta_1 \ \zeta_2 sd_1 sd_2) \quad (2)$$

Each measured value is equation for unknown results.

$$t = f(X) \quad (3)$$

Equation of horizontal direction of orientation point:

$$\varphi_{ij} = \arctan\left(\frac{Y_j - Y_i}{X_j - Y_i}\right) + o_p \quad (4)$$

Equation of distance between orientation point and free station:

$$sd_{ij} = \sqrt{(X_j - X_i)^2 + (Y_j - Y_i)^2 + (Z_j - Z_i)^2} \quad (5)$$

Equation of zenith angle of orientation point:

$$\zeta_{ij} = \arccos\left(\frac{(Z_j - Z_i)}{\sqrt{(X_j - X_i)^2 + (Y_j - Y_i)^2 + (Z_j - Z_i)^2}}\right) \quad (6)$$

Derivation matrix of equation of measured values:

$$A = \begin{pmatrix} \frac{\partial \varphi_{cj}}{\partial X_c} & \frac{\partial \varphi_{cj}}{\partial Y_c} & \frac{\partial \varphi_{cj}}{\partial Z_c} & \frac{\partial \varphi_{cj}}{\partial o_p} \\ \frac{\partial \varphi_{ci}}{\partial X_c} & \frac{\partial \varphi_{ci}}{\partial Y_c} & \frac{\partial \varphi_{ci}}{\partial Z_c} & \frac{\partial \varphi_{ci}}{\partial o_p} \\ \frac{\partial sd_{cj}}{\partial X_c} & \frac{\partial sd_{cj}}{\partial Y_c} & \frac{\partial sd_{cj}}{\partial Z_c} & \frac{\partial sd_{cj}}{\partial o_p} \\ \frac{\partial sd_{ci}}{\partial X_c} & \frac{\partial sd_{ci}}{\partial Y_c} & \frac{\partial sd_{ci}}{\partial Z_c} & \frac{\partial sd_{ci}}{\partial o_p} \\ \frac{\partial \zeta_{cj}}{\partial X_c} & \frac{\partial \zeta_{cj}}{\partial Y_c} & \frac{\partial \zeta_{cj}}{\partial Z_c} & \frac{\partial \zeta_{cj}}{\partial o_p} \\ \frac{\partial \zeta_{ci}}{\partial X_c} & \frac{\partial \zeta_{ci}}{\partial Y_c} & \frac{\partial \zeta_{ci}}{\partial Z_c} & \frac{\partial \zeta_{ci}}{\partial o_p} \end{pmatrix} \quad (7)$$

Derivation matrix of equation of measured values after inserting derived derivatives:

$$A = \begin{pmatrix} \frac{\Delta Y_{cj}}{d_{cj}^2} & -\frac{\Delta X_{cj}}{d_{cj}^2} & 0 & 1 \\ \frac{\Delta Y_{ci}}{d_{ci}^2} & -\frac{\Delta X_{ci}}{d_{ci}^2} & 0 & 1 \\ -\frac{\Delta X_{cj}}{sd_{cj}} & -\frac{\Delta Y_{cj}}{sd_{cj}} & -\frac{\Delta Z_{cj}}{sd_{cj}} & 0 \\ -\frac{\Delta X_{ci}}{sd_{ci}} & -\frac{\Delta Y_{ci}}{sd_{ci}} & -\frac{\Delta Z_{ci}}{sd_{ci}} & 0 \\ -\frac{\Delta X_{cj} \cdot \Delta Z_{cj}}{d_{cj} \cdot sd_{cj}^2} & -\frac{\Delta Y_{cj} \cdot \Delta Z_{cj}}{d_{cj} \cdot sd_{cj}^2} & \frac{d_{cj}}{sd_{cj}^2} & 0 \\ -\frac{\Delta X_{ci} \cdot \Delta Z_{ci}}{d_{ci} \cdot sd_{ci}^2} & -\frac{\Delta Y_{ci} \cdot \Delta Z_{ci}}{d_{ci} \cdot sd_{ci}^2} & \frac{d_{ci}}{sd_{ci}^2} & 0 \end{pmatrix} \quad (8)$$

Scale matrix:

$$P = diag(\, p_1\, p_2\, p_3\, p_4\, p_5\, p_6\,) \quad (9)$$

Individual's scale is given by a priori standard deviation and standard deviation of measured value:

$$p_i = \frac{\sigma_0^2}{\sigma_i^2} \quad (10)$$

Standard deviation of horizontal direction given by angle standard deviation, standard deviation of orientation point in horizontal plane and centration standard deviation:

$$\sigma_\varphi = = \sqrt{\sigma_{\overline{\varphi}}{}^2 + \left(\frac{\sigma_{XY}}{sd}\right)^2 + \left(\frac{\sigma_c}{sd}\right)^2} \quad (11)$$

Standard deviation of zenith angle given by angle standard deviation, standard deviation of orientation point in vertical axis and centration standard deviation:

$$\sigma_\zeta = \sqrt{\sigma_{\overline{\zeta}}{}^2 + \left(\frac{\sigma_Z}{sd}\right)^2 + \left(\frac{\sigma_c}{sd}\right)^2} \quad (12)$$

Standard deviation of distance given by angle standard deviation, standard deviation of orientation point and centration standard deviation:

$$\sigma_{sd} = \sqrt{\sigma_{\overline{sd}}{}^2 + \sigma_{XYZ}^2 + \sigma_c^2} \quad (13)$$

Covariance matrix:

$$\Sigma = \sigma_0^2 \cdot (A^T \cdot P \cdot A)^{-1} \quad (14)$$

Standard deviation of free station in X axis:

$$\sigma_x = \sqrt{\Sigma_{1,1}} \quad (15)$$

Standard deviation of free station in Y axis:

$$\sigma_y = \sqrt{\Sigma_{2,2}} \quad (16)$$

Standard deviation of free station in Z axis:

$$\sigma_z = \sqrt{\Sigma_{3,3}} \quad (17)$$

Standard deviation of orientation shift:

$$\sigma_{O_p} = \sqrt{\Sigma_{4,4}} \cdot 200/pi \quad (18)$$

Standard deviation of free station in horizontal plane:

$$\sigma_{xy} = \sqrt{\frac{\Sigma_{1,1} + \Sigma_{2,2}}{2}} \quad (19)$$

Orientation of standard deviation is not identical to coordinates system. The largest value will take effect depending on configuration of orientation points. Error ellipse solves this problem.

Twist angle of error ellipse:

$$tg(2\omega) = \frac{2\sigma_{xy}}{\sigma_x^2 - \sigma_y^2} \quad (20)$$

Standard deviation main half axis of error ellipse:

$$\sigma_\xi^2 = \sigma_x^2 \cdot \cos^2(\omega) + \sigma_{xy} \cdot \sin(2\omega) + \sigma_y^2 \cdot \sin^2(\omega) \quad (21)$$

Standard deviation second half axis of error ellipse:

$$\sigma_\eta^2 = \sigma_x^2 \cdot \sin^2(\omega) - \sigma_{xy} \cdot \sin(2\omega) + \sigma_y^2 \cdot \cos^2(\omega) \quad (22)$$

Precision analysis

Free station task analysis was divided into two sections. Both analyses deal with position accuracy of free station. Inputs are two points with coordinates (X, Y, Z) and free station in the centre of the coordinate system. The position of the two points changes depending on analysis. Standard deviation of orientation shift and main half axis of error ellipse are monitored in both analyses. Standard deviation of orientation shift is monitored because it directly affects the following measurement from a free station.

Horizontal and vertical angles

Inputs are two point coordinates (X, Y, Z) and free station in the centre of the coordinate system. Two points lay on a sphere with a 50m radius. Horizontal angle between orientation points is changing in span 0 to 200 gon. The zenith angle is changing for each orientation point the same in span 0 - 100 gon. The standard deviation of orientation shift and main half axis of error ellipse are monitored depending on changing angles. The results can be found in Figures 4 and 5.

Horizontal angle and distance

Inputs are two point with coordinates (X, Y, Z) and free station in centre of the coordinate system. Two points lie in plain. Horizontal angle between two points is changing interval from 0 to

200 gon. At the same time distance between free station and points is changing in interval 1 - 50m. The standard deviation of orientation shift and main half axis of error ellipse are monitored depending on changing horizontal angle and distance. The results can be seen in the Figures 6 and 7.

RESULTS

Drone position experiment

Vertical movements are smaller than horizontal movements. This is due to the wind direction, which affects the drone more in a horizontal direction.

Tab. 1 - Results 1 Drone movements

	No Wind (5m/s)	*Wind (15 m/s)*
Horizontal position accuracy	*0.049 [m]*	*0.098 [m]*
Vertical position accuracy	*0.018 [m]*	*0.036 [m]*
Max difference	*0.081 [m]*	*0.143 [m]*

Tab. 2 - Results 2 Drone movements

	No Wind (5m/s)	*Wind (15m/s)*
Horizontal position accuracy	*0.065 [m]*	*0.095 [m]*
Vertical position accuracy	*0.026 [m]*	*0.038 [m]*
Max difference	*0.075 [m]*	*0.163 [m]*

Free station task analysis

Tab. 3 - Standard deviation of measurement values

	standard deviation	*Used value*
σ_{φ}	*Horizontal direction*	*1 mgon*
σ_{ζ}	*Vertical direction*	*1 mgon*
σ_{XY}	*orientation point*	*5 cm*
σ_{Z}	*orientation point*	*3 cm*
σ_{c}	*centration*	*7 mm*
σ_{sd}	*distance*	*2mm + 2ppm*

Precision of orientation points increases with greater distance and with greater horizontal angle between orientation points as shown in the results. Ideology can be imagined in drawing the intersection of two lines. When two lines are perpendicular on each other, the intersection can be clearly seen. When the angle of intersection is too small, the intersection is not precisely defined and appears as a small line. It is the same as in a case of free station task, when the horizontal angle is too small precision is worse.

Horizontal and vertical angles

These results show length main half axis of error ellipse, standard deviation of orientation shift and standard deviation of vertical position acquire from changing horizontal and vertical angles. The results are showed on 3D graph and its contour on Figure 3 and 4. Multiple graphs on Figure 3 shows standard deviation of orientation shift and main half axis of error ellipse. Main half axis of error ellipse was selected, because it is the best indicator of horizontal precision of two values (coordinates X and Y) and takes configuration of orientation points into consideration. Standard deviation of orientation shift is indicator of bad measurement of horizontal angles. The greater its value the greater the uncertainty in measuring horizontal angles. Graphs on Figure 4 shows standard deviation of vertical position. It indicates precision in vertical axis.

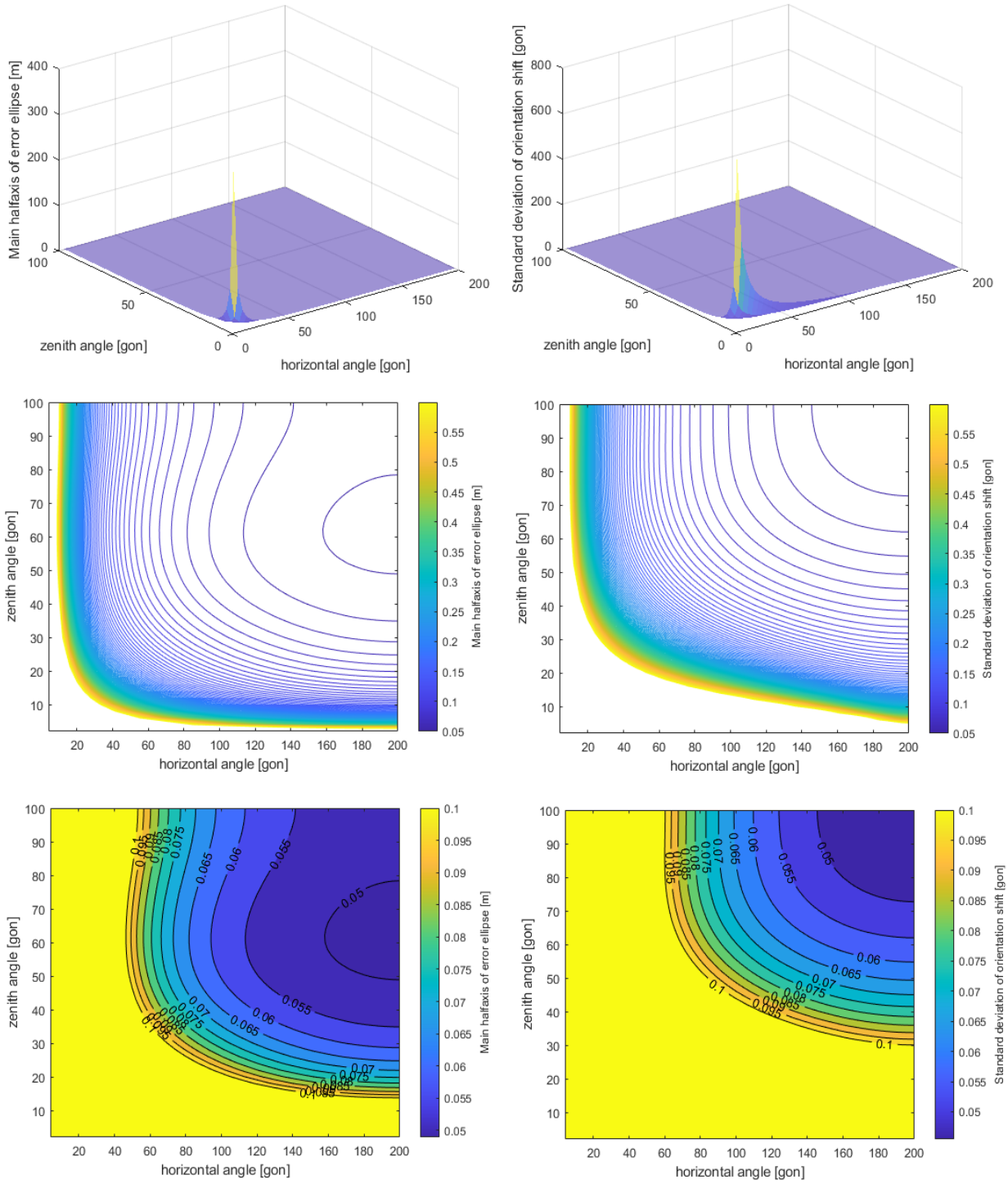

Fig. 4 – Precision analysis - main half axis of error ellipse (left column), orientation shift (right column)

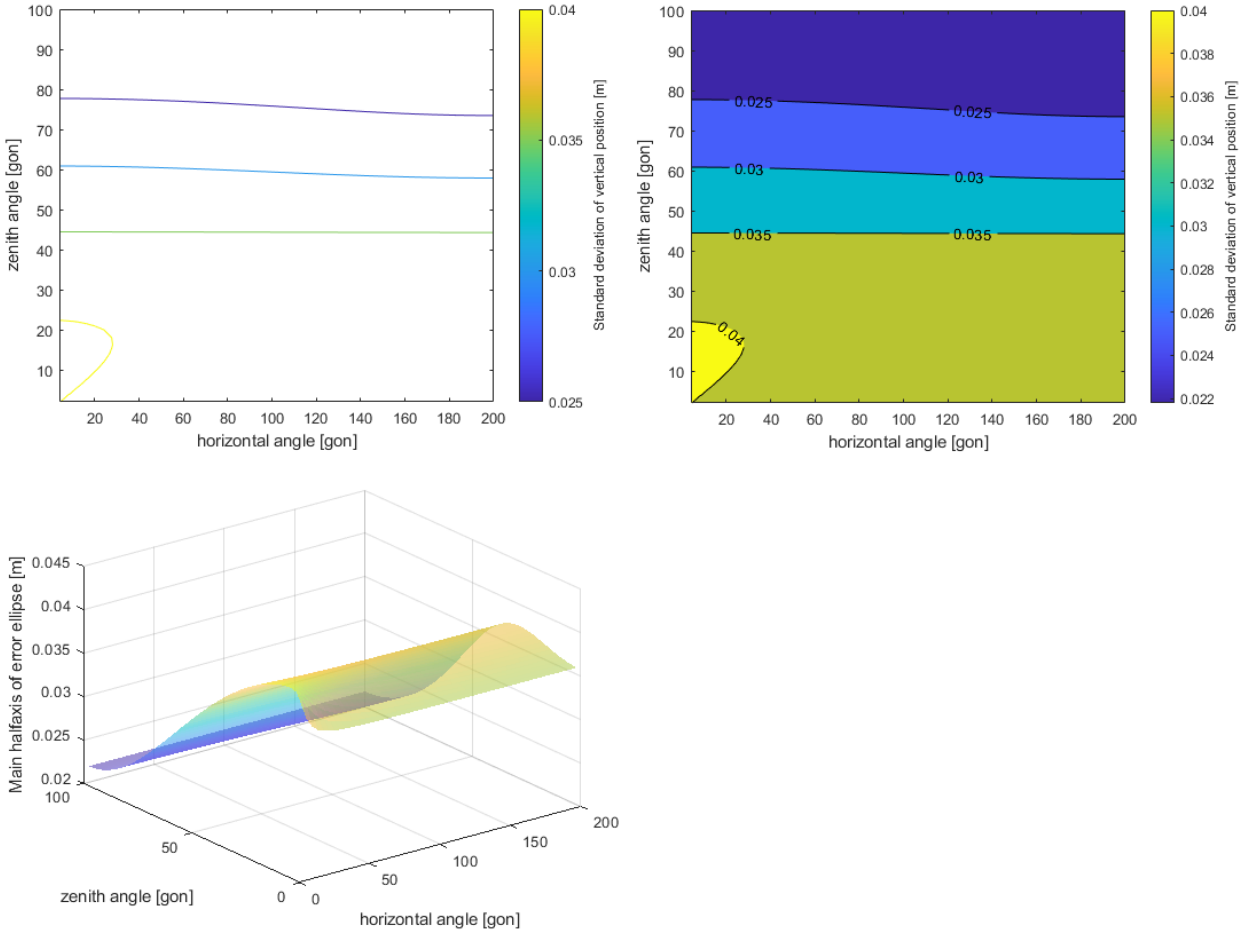

Fig. 5 – Precision analysis - vertical position

Horizontal angle and distance

These results show length main half axis of error ellipse, standard deviation of orientation shift and standard deviation of vertical position acquire from changing horizontal angle and distance. The results are showed on 3D graph and its contour in Figures 5 and 6. Multiple graphs in Figure 5 shows standard deviation of orientation shift and main half axis of error ellipse. Graphs in Figure 6 shows standard deviation of vertical position. It indicates precision in vertical axis.

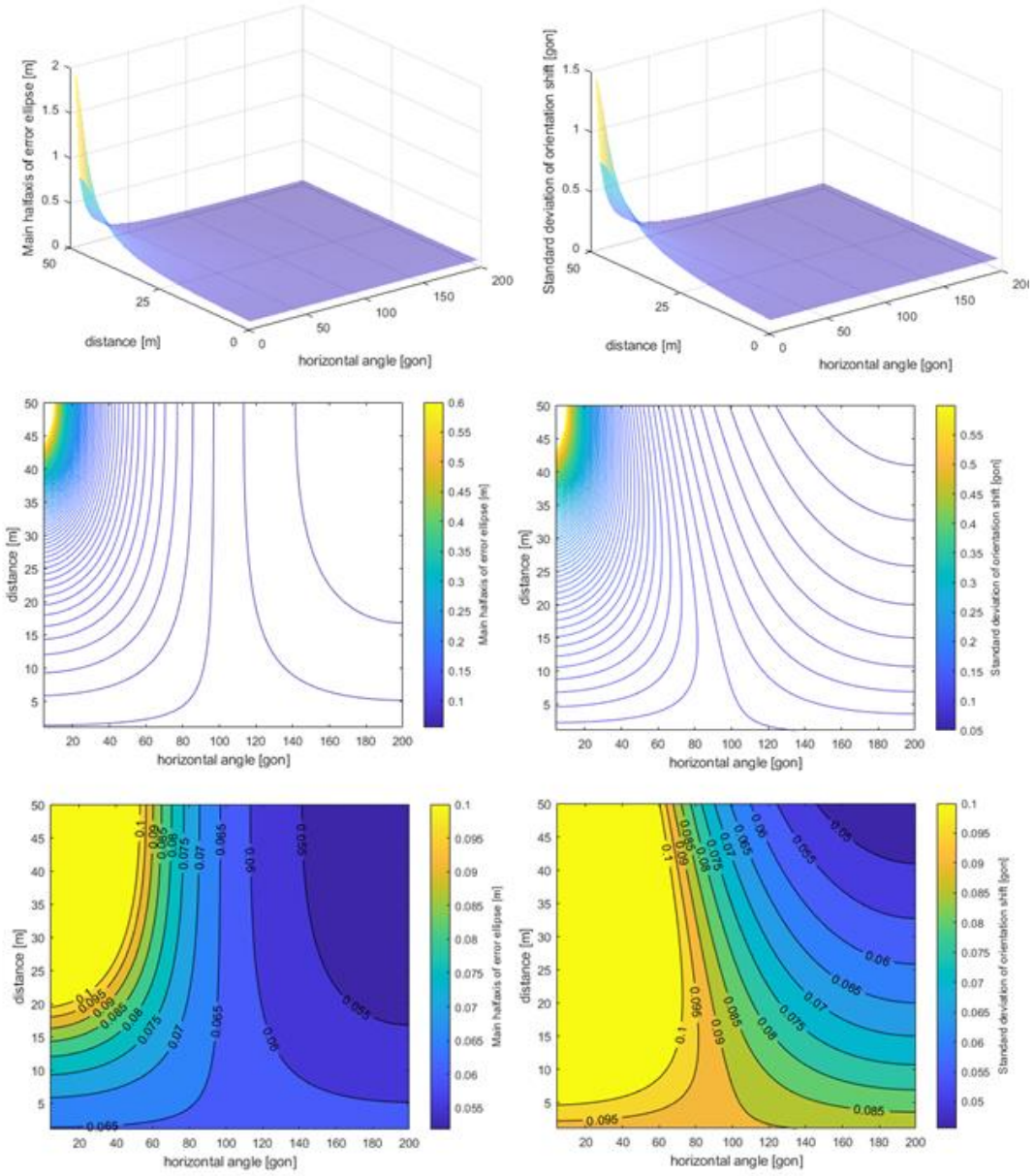

Fig. 6 – Precision analysis - main half axis of error ellipse (left column), orientation shift (right column)

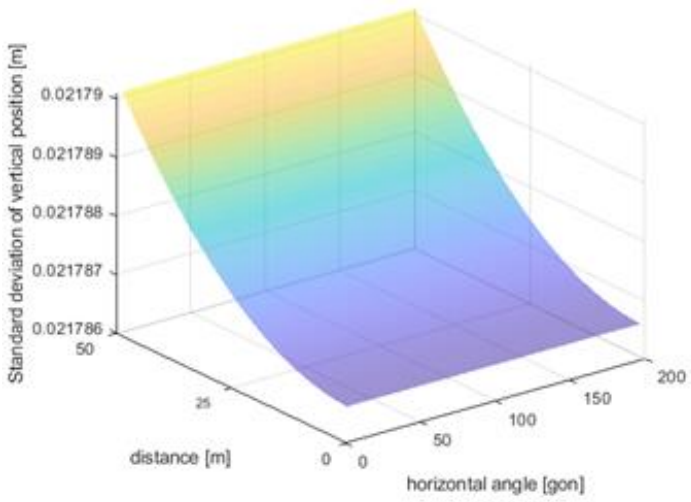

Fig. 7 – Precision analysis - vertical position

CONCLUSION

A drone equipped with GNSS RTK and prism can be used as orientation points. The conditions must be noticed, and high position accuracy of the free station must not be required. Position accuracy free station coordinates mainly depend on position accuracy of orientation points. Position accuracy of orientation points also depends on GNSS measurement and weather conditions. Drone can be used as an orientation point when it is not windy (e.g. up to 5 m/s). Standard deviation of orientation points was determined by drone movements test. Horizontal value is 5cm and vertical is 3cm. The accuracy of the GNSS receiver is better (1cm + 1ppm) than the drone movements standard deviation from results. Drone movements standard deviation is used for precision analysis as standard deviation of orientation points.

Horizontal position precision of a free station is mainly dependent on precision of orientation points. Configuration of orientation points has some considerable effect especially in extreme cases. Results show that with longer distance between orientation points and total station, position and orientation shift accuracy is better. Horizontal distance has the greatest effect on the accuracy of the orientation shift. Horizontal angle between control points is recommended to keep above 80 gon as can be seen in the results. Zenith angle of orientation points has minimal effect on position precision of free station. Short horizontal distance between free station and orientation points has a bad effect on orientation shift accuracy. Horizontal distance must be longer than 30m.

Configuration of orientation points does not have much effect on vertical position precision. The result was expected. Vertical position is calculated independently from both orientation points by trigonometry. Vertical position precision mainly depends on position accuracy of orientation points.

Two surveyors are needed in this method. First surveyor uses a total station and the second surveyor flies with a drone. Drone movements are expected e.g. up 10cm. This value comes from the drone movements test, and it is the maximum horizontal change in position. Total station with automatic targeting handles drone movement. Angles change from slightly moving drone is 0.1gon. In the future it would be appropriate to test the method directly in the field. Free station would be calculated from orientation points on the ground. In the next step free station would be calculated from orientation points done by drone. Differences will confirm theoretical precision analysis in this article.

ACKNOWLEDGEMENTS

This work was supported by the Grant Agency of the Czech Technical University in Prague, grant No. SGS21/054/OHK1/1T/11

REFERENCES

[1] Gupta, Sharad Kumar; Shukla, Dericks P. Application of drone for landslide mapping, dimension estimation and its 3D reconstruction. Journal of the Indian Society of Remote Sensing, 2018, 46.6: 903-914.

[2] Tiwari, Nidhi P., et al. Advanced techniques used in surveying: total station, GPS, GIS, DRONE Arial survey. International Journal for Research in Applied Science and Engineering Technology, 2018, 6.3: 896-902.

[3] Jimenez-Cano, A.E.; Sanchez-Cuevas, P.J.; Grau, P.; Ollero, A.; Heredia, G. Contact-Based Bridge Inspection Multirotors: Design, Modeling, and Control Considering the Ceiling Effect. IEEE Robot. Autom. Lett. 2019, 4, 3561–3568. [Google Scholar] [CrossRef]

[4] Suzuki, Takayuki; Kumagai, Taichi; Yoshida, Hiroshi. Accuracy evaluation of drone control system using total station. IEICE Technical Report; IEICE Tech. Rep., 2020, 119.461: 67-72.

[5] Delgado, Javier Prada, et al. Bridge mapping for inspection using an UAV assisted by a total station. In: Iberian Robotics conference. Springer, Cham, 2017. p. 309-319.

[6] Maxim, Artyom, et al. UAV Guidance with Robotic Total Station for Architectural Fabrication Processes. Unmanned Aerial Vehicles; Wißner-Verlag: Augsburg, Germany, 2017, 145-161.

[7] ISHII, A., et al. Autonomous UAV flight using the Total Station Navigation System in Non-GNSS Environments. In: ISARC. Proceedings of the International Symposium on Automation and Robotics in Construction. IAARC Publications, 2020. p. 685-692.

[8] Hankus-Kubica, Agnieszka, et al. Verification tests of total station usability for UAV position measurements. In: 2020 IEEE 7th International Workshop on Metrology for AeroSpace (MetroAeroSpace). IEEE, 2020. p. 331-335.

[9] CivDot, https://www.civrobotics.com/

[10] Jan, Šikola. Testování GNSS modulu Ublox 9. generace. 2020. Master's Thesis. České vysoké učení technické v Praze. Vypočetní a informační centrum.

[11] Wielgocka, N.; Hadas, T.; Kaczmarek, A.; Marut, G. Feasibility of Using Low-Cost Dual-Frequency GNSS Receivers for Land Surveying. Sensors 2021, 21, 1956. https://doi.org/10.3390/s21061956

[12] Hamza, V.; Stopar, B.; Sterle, O. Testing the Performance of Multi-Frequency Low-Cost GNSS Receivers and Antennas. Sensors 2021, 21, 2029. https://doi.org/10.3390/s21062029

[13] Zahradník, D. Hodík, Š. Vyskočil, Z. Ublox F9P for geodetic measurment Stavební obzor-Civil Engineering Journal 30.3 (2021).

[14] Štroner, M. - Hampacher, M.: Process and analyses surveying measurment (Zpracování a analýza měření v inženýrské geodézii). 1. vyd. Praha: CTU Publishing House, 2011. 313 s. ISBN 978-80-01-04900-6.

[15] Štroner, M.: Free station task precision (K přesnosti volného stanoviska). Geodetický a kartografický obzor. 2012, roč. 58, č. 8, s. 170-176. ISSN 0016-7096

[16] Andrew Marshall, Analysis of free station errors, Surv431 Engineering Surveying at the National School of Surveying in 2007

CIVIL ENGINEERING JOURNAL

Article no. 58

THE CIVIL ENGINEERING JOURNAL 3-2021

EFFECT OF RISK ANALYSIS ON PERFORMANCE OF LARGE CONSTRUCTION PROJECTS IN KUWAIT

Rashid Aldaiyat

MPW, Maintenance of road and networks department, Riqqa, Ahmadi, Kuwait; aldaiyat1988@gmail.com

ABSTRACT

Since construction projects are usually associated with high range of risks, risk analysis is an essential part within the decision-making processes in this industry. This study aims at finding the effect of appropriate risk analysis on enhancing the performance of the large construction projects in Kuwait. Through this correlational descriptive and qualitative study; firstly, a questionnaire was used to collect the main data where it was distributed on a sample of (150) engineers working in the large construction projects in Kuwait. Moreover, an interview was conducted with (15) project managers in the large construction projects in Kuwait. The results of the questionnaire showed that risks analysis aspects are highly implemented in Kuwait and that the performance indices for the construction projects are high. Moreover, it was found that there is a statistically significant positive effect of risk analysis on the performance of the large construction projects in Kuwait. The results showed that there were statistically significant differences in the effect of risk analysis on the performance of the construction projects attributed to the project type in favor of the private projects. Finally, the results of the interview showed that client satisfaction and maintain resources are the main effects of appropriate risk analysis tools, where project managers assured that re-allocating risks and changing roles are the main mechanisms to lessen the risks within the large construction projects in Kuwait.

KEYWORDS

Risk analysis, Construction projects, Project performance, Kuwait

JEL CLASSIFICATION

L740, D810, H430

INTRODUCTION

Construction projects are usually complex and full of uncertainties [1]. Such uncertainties are risks that can have possibly harmful consequences on the project [1, 2]. Risks can affect the accomplishment of the project objectives, which in turn will result in poor project performance [3]. That is why risk analysis is considered now as a fundamental project management feature, especially in the construction industry, that aims to effectively deal with unexpected events and uncertainties for achieving the project success [4, 5].

Risk analysis procedure includes the prospective risks critical evaluation, risks classification based on their significance, and the capability of the management to choose the main ones [6, 7]. Risk analysis is a multi-tasking process in the risk management since it includes assessing the likelihood of the risks and their impacts on the objectives of the project [8, 9]. The objective of risk analysis within construction projects is evaluating the possible risks by classifying the risk events according to their importance, chances of happening, and the size of each risk [10]. In other words, risk analysis is the intermediate process between risk identifying and risk management [11].

The importance of risk analysis in mitigating the possible risks within construction projects have been discussed widely [4, 12-15]. However, its effects on the construction project performance are still under discussion according to the indicators that have been adopted to determine the performance [16].

Kerzner (2017) argued that risks presence within the project development can affect the project objectives, which might result in a difficult decision-making associated processes [17]. Musta (2019) confirmed that effect as he found that the risk weight affect the risk probability, which in turn affect the project objectives including quality, time and costs [18]. In this study, the effect of risk analysis on the comprehensive framework of construction project performance as proposed by Nassar (2009) with eight indicators was investigated.

METHODS

In this study, the correlational descriptive and qualitative method was followed, as it is the most appropriate approach for the subject of the study. Both the questionnaire and interview were used as the data collection tools.

Population and sample

The population of this study consisted of all the working engineers in the large construction projects in Kuwait in the time of conducting this study, besides the project managers in the same projects. As the study population number could not be attained precisely, where the statistics[1] inform that (7.5%) of the total working force in Kuwait are in the construction sector and that (10%) of them are engineers and (1%) are project managers. Therefore, the study sample was determined to be (150) engineers for the questionnaire part and (15) project managers for the interview part with a level of confidence of (85%) and an error margin of (0.05). The convenient sampling method was adopted until the representative study sample was achieved.

Instrumentation

Firstly, the questionnaire was adopted where the author designed it based on the review of the previous studies mainly [19, 20]. The first draft of the questionnaire was presented to a panel of attributers specialized in project and risk management especially in the construction projects. The panel gave their comments and after making the required modifications, the second draft was prepared. In order to validate the questionnaire, it was distributed to a pilot study of (5) engineers from outside the study sample and after calculating the Cronbach Alpha coefficient, the final copy of the questionnaire was distributed on the study sample. The value of Cronbach Alpha coefficient was (0.90), indicating a good consistency of the questionnaire.

The final copy of the questionnaire consisted of two parts; the first part consisted of the sample demographics, while the second part consisted of two fields (risk analysis aspects and project performance indicators). The first field consisted of (14) items, while the second consisted of (8) items.

The interview part consisted of the main questions the questionnaire without the choices to select from to take a better perspective for the casual relationship that might exist between the main two variables of the study.

[1] https://www.csb.gov.kw/Pages/Statistics?ID=13&ParentCatID=1

Statistical analysis

The statistical analysis was conducted using the (SPSS) program where the descriptive variables including (frequencies, percentages means and standard deviation) were calculated to descriptive the study variables. Moreover, Pearson Correlation Coefficient was calculated to test the correlation between the study variables. In order to find the differences in the sample answers that might be attributed to the working setting, t-test was used. For the interview part, MAXQDA Analytics Pro 2018 software was used to analyse and code the answers of the sample under two themes; the risk analysis aspects and the indicators of the construction project performance.

RESULTS

The following sections represent the results of this study. The demographics of the study sample are listed in Table (1) below represented by frequencies and percentages, where it can be seen that the majority of the sample are males (89%). Nearly half of the respondents (46.6%) have an experience less than five years and most of them (76.7%) have a bachelor degree. Most of the respondents (74%) are working in the public sector with different job titles as showed in the table below.

Tab. 1 - Demographics of the study sample

Variable		N (%)
Gender	Male	134 (89%)
	Female	16 (11%)
	Total	150 (100%)
Experience	Less than 5 years	70 (46.6%)
	5 to 10 years	36 (24%)
	More than 10 years	44 (29.4%)
	Total	150 (100%)
Educational level	Bachelor	115 (76.7%)
	Masters	26 (17.3%)
	PhD	9 (6%)
	Total	150 (100%)
Working setting	Public sector	39 (26%)
	Private sector	111 (74%)
	Total	150 (100%)
Job title	Project Manager	7 (4.7%)
	Assistant Project Manager	19 (12.6%)
	Civil Engineer	45 (30%)
	Building Inspector	3 (2%)
	Surveyor	2 (1.3%)
	Field Engineer	31 (20.7%)
	Construction Engineer	25 (16.7%)
	Planner	18 (12%)
	Total	150 (100%)

The results of Table (2) below shows that the level of practicing the risk analysis aspects within the large construction projects in Kuwait was high with a mean of (3.71) and a standard deviation of (1.26). The item "Risk allocation analysis was performed" came first with a mean of (4.30) and a standard deviation of (1.70) in a high level. On the other hand, the item "The communication processes were e-evaluated and enhanced" came last with a mean of (2.70) and a standard deviation of (1.40) in a medium level.

Tab. 2 - Study sample answers for the items of the risk analysis aspects

No.	Item	Mean	SD	Rank	Level
1	Computer simulations and software were used	3.75	1.50	9	High
2	The financial impacts of the different risks were identified and compared	3.20	1.55	12	Medium
3	The organizational impacts of the different risks were identified and compared	4.00	1.04	6	High
4	The gaps in the current safety procedures were identified	4.23	1.22	2	High
5	The decision-making processes were e-evaluated and enhanced	3.90	1.06	8	High
6	The communication processes were e-evaluated and enhanced	2.70	1.40	14	Medium
7	The employee awareness toward possible risks was evaluated and tested	2.91	1.35	13	Medium
8	Risk assessment survey was conducted	3.33	0.99	11	Medium
9	The word classifications for risks were used for risk consequences and likelihood description	4.05	1.01	5	High
10	Likelihood analysis was conducted	4.15	1.55	3	High
11	Consequences analysis was conduced	4.10	1.20	4	High
12	Risk allocation analysis was performed	4.30	1.70	1	High
13	Alternatives for risk mitigation were investigated	3.97	1.05	7	High
14	All the involved parties of the project participated in the risk analysis processes	3.40	0.98	10	Medium
Risk analysis aspects as a whole		3.71	1.26	-	High

The results of Table (3) below shows that the project performance within the large construction projects in Kuwait came in a high level with a mean of (4.03) and a standard deviation of (1.06). The item "The construction operations were carried out with minimum financing costs" came first with a mean of (4.35) and a standard deviation of (1.13) in a high level. On the other hand, the item "The project cost efficiency" came last with a mean of (3.80) and a standard deviation of (0.95) in a high level.

Tab. 3: Study sample answers for the items of the indicators of the construction project performance

No.	Item	Mean	SD	Rank	Level
1	The project cost efficiency	3.80	0.95	8	High
2	The project schedule efficiency	3.81	1.00	7	High
3	The construction operations were carried out with minimum financing costs	4.35	1.13	1	High
4	The project was profitable to date	4.10	1.30	3	High
5	The site activities were safely carried out with minimal time incidents	4.20	1.02	2	High
6	The project was delivered with a high quality	4.00	1.09	5	High
7	Team satisfaction	3.95	1.10	6	High
8	Client satisfaction	4.05	0.90	4	High
Project performance indicators as a whole		4.03	1.06	-	High

In order to find if there is an effect of the risk analysis on the performance of the construction project, Pearson correlation coefficient was calculated as in Table (4) below. It can be seen that there is a statistically significant relationship between the risk analysis aspects and the indicators of the construction project performance.

Tab. 4: the correlation coefficient between the risk analysis aspects and the indicators of the construction project performance

Variable	Mean	correlation coefficient	Statistical significance
Risk analysis	3.71	0.843	0.000*
Construction project performance	4.03		

*** indicates statistically significant value**

Such relationship was approved by the related literature, as in table (5) below that lists the results of examining the relationship between risk analysis and the construction project performance in three of the developing countries.

Tab. 5: Examples on examining the relationship between risk analysis and construction project performance in the developing countries

Study	Country	Setting	Results
[21]	Kenya	Road construction project	Risk analysis affect risk management practices and performance.
[22]	Egypt	Roadways construction projects	Risk analysis affects the execution of the road construction project including influencing the project objectives, time and quality.
[23]	Kenya	Construction projects	The finding showed that there was positive relationship between Quantitative Risk Analysis and Risk Response, which led to the conclusion that quantitative risk analysis and Risk Response had a significance influence on performance of construction Projects.
[18]	Albania	Construction projects	risk analysis has an impact on the construction projects performance related to time, quality and cost

In order to find if there are statistically significant differences in the sample answers attributed to the working setting, t-test was conducted, as in Table (6).

Tab. 6: t-test results for testing the differences between the sample answers attributed to the working setting variable

Variable		Mean	SD	t-value	Statistical significance
Working setting	Public sector	3.2	0.92	1.20	0.00*
	Private sector	4.0	0.88		

*** indicates statistically significant value**

Finally, When the projects managers were asked about the main risk analysis tools that are common in large construction project in Kuwait, the tools included Risk matrix, Expert judgment, Value Analysis, Expected Monetary, FMEA, Fuzzy logic assessment, AHP and Monte Carlo simulation.

The projects managers also argued that the main effects of using the appropriate risk analysis tools on the performance of large construction projects in Kuwait include client satisfaction; maintaining the main resources, align with the budget, workers satisfaction, less conflict of interests among others.

Finally, the projects managers focused on the importance of communication, re-allocating risks and changing roles to reduce the risks within the large construction projects in Kuwait.

.

CONCLUSION

Construction projects have different associated risks and this can be attributed to the multiple involved parties in the project, the required funds, technical and legal restrictions among others. The presence of risks in projects was proved to have a significant influence on the construction project performance. In this study, the risk analysis aspects effect on the construction project performance was investigated. The results showed that risk analysis do have an effect on the performance of construction projects, which is consistent with the related literature [24-28].

This study involved many limitations; the first was the study sample where more multi-disciplinary sample is recommended to get a more comprehensive view of the problem since risk analysis is a mutual responsibility. The other limitation is that the results of this study cannot be generalized on the other countries and contexts; therefore, a comparative study should be conducted.

RECOMMENDATIONS

With the considerable effect of risk analysis has proved to have on the construction project performance, its associated operations should be established under both proactive and reactive ways. The effects of risk analysis should be also investigated from the perspective of project success or failure especially in the Middle East countries as most of the investigated studies in this subject were on developed economies. Risk analysis should be conducted using reliable validated methods in order to attain more reliable and practical results. With the gap found in this relationship in the public sector, more attention should be given to the risk analysis operations and the assessment methods within public large construction projects in Kuwait.

Priorities should be defined for each of the performance indicators in order to focus the risk analysis operations toward enhancing the performance. On the other hand, risk analysis operations should be directed toward sustainable risk management solutions in order to work on reducing risks with construction projects. Constant and continuous quality assurance is one of the major strategies that could be followed to decrease risks within construction projects with one integrated comprehensive platform that combine all the applications of risk analysis and management. Moreover, working systematically and taking care of documents can be a great of help to mitigate risks that could be reported earlier. Such systematic work argues that need also for good and solid communication between the project members and parties.

Risks can be reduced also by proper identification of risks and prioritize them to deal with them as they needed and by training the workers and all the parties of the construction project on how to deal with risks. Finally, there must be a guideline or standards that determine the risks and success of the construction projects in Kuwait.

REFERENCES

[1] N. Banaitiene and A. Banaitis, "Risk management in construction projects," *Risk Management–Current Issues and Challenges. In N. Banaitiene (Ed.), Risk Management–Current Issues and Challenges,* pp. 429-448, 2012.

[2] K. Chatterjee, E. K. Zavadskas, J. Tamošaitienė, K. Adhikary, and S. Kar, "A hybrid MCDM technique for risk management in construction projects," *Symmetry,* vol. 10, no. 2, p. 46, 2018.

[3] M. Loosemore, J. Raftery, C. Reilly, and D. Higgon, "Risk and Uncertainty in Projects," ed: New York, NY, USA: Taylor and Francis, 2006.

[4] S. K. Viswanathan, K. K. Tripathi, and K. N. Jha, "Influence of risk mitigation measures on international construction project success criteria–a survey of Indian experiences," *Construction Management and Economics,* vol. 38, no. 3, pp. 207-222, 2020.

[5] M. Gunduz and A. M. A. Yahya, "Analysis of project success factors in construction industry," *Technological and Economic Development of Economy,* vol. 24, no. 1, pp. 67–80-67–80, 2018.

[6] S. M. El-Sayegh and M. H. Mansour, "Risk assessment and allocation in highway construction projects in the UAE," *Journal of Management in Engineering,* vol. 31, no. 6, p. 04015004, 2015.

[7] S. M. El-Sayegh, S. Manjikian, A. Ibrahim, A. Abouelyousr, and R. Jabbour, "Risk identification and assessment in sustainable construction projects in the UAE," *International Journal of Construction Management,* pp. 1-10, 2018.
[8] S. Tan and K. Moinuddin, "Systematic review of human and organizational risks for probabilistic risk analysis in high-rise buildings," *Reliability Engineering & System Safety,* vol. 188, pp. 233-250, 2019.
[9] C. Feng and S. Lu, "Using BIM to automate scaffolding planning for risk analysis at construction sites," in *ISARC. Proceedings of the International Symposium on Automation and Robotics in Construction*, 2017, vol. 34: IAARC Publications.
[10] A. KarimiAzari, N. Mousavi, S. F. Mousavi, and S. Hosseini, "Risk assessment model selection in construction industry," *Expert Systems with Applications,* vol. 38, no. 8, pp. 9105-9111, 2011.
[11] K. G. Lovejoy, P. I. Cross, and P. S. Tippett, "Object-oriented method, system and medium for risk management by creating inter-dependency between objects, criteria and metrics," ed: Google Patents, 2010.
[12] O. Zwikael, R. D. Pathak, G. Singh, and S. Ahmed, "The moderating effect of risk on the relationship between planning and success," *International Journal of Project Management,* vol. 32, no. 3, pp. 435-441, 2014.
[13] M. Urbański, A. U. Haque, and I. Oino, "The moderating role of risk management in project planning and project success: evidence from construction businesses of Pakistan and the UK," *Engineering Management in Production and Services,* vol. 11, no. 1, pp. 23-35, 2019.
[14] J.-S. Chou, N. Irawan, and A.-D. Pham, "Project management knowledge of construction professionals: Cross-country study of effects on project success," *Journal of construction engineering and management,* vol. 139, no. 11, p. 04013015, 2013.
[15] D. Baloi and A. D. Price, "Modelling global risk factors affecting construction cost performance," *International journal of project management,* vol. 21, no. 4, pp. 261-269, 2003.
[16] R. Takim and A. Akintoye, "Performance indicators for successful construction project performance," in *18th Annual ARCOM Conference*, 2002, vol. 2, no. 4.
[17] H. Kerzner, *Project management: a systems approach to planning, scheduling, and controlling*. John Wiley & Sons, 2017.
[18] A. Musta, "Impact of risk analysis related to time, quality and cost in construction projects," 2019.
[19] N. K. Nassar, "An integrated framework for evaluation of performance of construction projects," in *PMI® Global Congress*, 2009, pp. 10-13.
[20] A. Dziadosz and M. Rejment, "Risk analysis in construction project-chosen methods," *Procedia Engineering,* vol. 122, pp. 258-265, 2015.
[21] O. Gregory, M. Yusuf, and K. Asinza, "Effect of Risk Identification and Risk Analysis on Performance of Road Construction Projects in Kenya: A Case Study of Kakamega County."
[22] U. H. Issa, K. G. Marouf, and H. Faheem, "Analysis of risk factors affecting the main execution activities of roadways construction projects," *Journal of King Saud University-Engineering Sciences,* 2021.
[23] J. M. Nzioki and M. N. Mwenda, "Promoting Performance of the Building Construction Industry through Risk Identification: A Case of Exchequer Funded Building Construction Projects in Machakos County, Kenya," 2020.
[24] E. Kinyua, K. Ogollah, and D. K. Mburu, "Effect of risk management strategies on project performance of small and medium information communication technology enterprises in Nairobi, Kenya," *International Journal of Economics, Commerce and Management,* vol. 3, no. 2, pp. 1-30, 2015.
[25] S. Nidumolu, "The effect of coordination and uncertainty on software project performance: residual performance risk as an intervening variable," *Information systems research,* vol. 6, no. 3, pp. 191-219, 1995.
[26] M. M. d. Carvalho and R. Rabechini Junior, "Impact of risk management on project performance: the importance of soft skills," *International Journal of Production Research,* vol. 53, no. 2, pp. 321-340, 2015.
[27] R. Rabechini Junior and M. Monteiro de Carvalho, "Understanding the impact of project risk management on project performance: An empirical study," *Journal of technology management & innovation,* vol. 8, pp. 6-6, 2013.
[28] L. Jun, W. Qiuzhen, and M. Qingguo, "The effects of project uncertainty and risk management on IS development project performance: A vendor perspective," *International Journal of Project Management,* vol. 29, no. 7, pp. 923-933, 2011.

APPENDIX A: THE QUESTIONNAIRE

EFFECT OF RISK ANALYSIS ON PERFORMANCE OF LARGE CONSTRUCTION PROJECTS IN KUWAIT

SOCIODEMOGRAPHIC INFORMATION

1. **Gender**
   - Male
   - Female
2. **Experience**
   - Less than 5 years
   - 5 to 10 years
   - More than 10 years
3. **Educational level**
   - Bachelor
   - Masters
   - PhD
4. **Working setting**
   - Public sector
   - Private sector
5. **Job title**
   - Project Manager
   - Assistant Project Manager
   - Civil Engineer
   - Building Inspector
   - Surveyor
   - Field Engineer
   - Construction Engineer
   - Planner

No.	Item	Strongly agree	Agree	Natural	Disagree	Strongly disagree
Risk Analysis Aspects						
1	Computer simulations and software were used					
2	The financial impacts of the different risks were identified and compared					
3	The organizational impacts of the different risks were identified and compared					
4	The gaps in the current safety procedures were identified					
5	The decision-making processes were					

	e-evaluated and enhanced					
6	The communication processes were e-evaluated and enhanced					
7	The employee awareness toward possible risks was evaluated and tested					
8	Risk assessment survey was conducted					
9	The word classifications for risks were used for risk consequences and likelihood description					
10	Likelihood analysis was conducted					
11	Consequences analysis was conduced					
12	Risk allocation analysis was performed					
13	Alternatives for risk mitigation were investigated					
14	All the involved parties of the project participated in the risk analysis processes					
Project Performance Indicators						
1	The project cost efficiency					
2	The project schedule efficiency					
3	The construction operations were carried out with minimum financing costs					
4	The project was profitable to date					
5	The site activities were safely carried out with minimal time incidents					
6	The project was delivered with a high quality					
7	Team satisfaction					
8	Client satisfaction					

.

APPENDIX B: THE INTERVIEW

1. Based on your experience as a project manager for a large construction project in Kuwait, can you mention the main risk analysis tools that are common in such projects?
2. On your opinion, what are the main effects of using the appropriate risk analysis tools on the performance of large construction projects in Kuwait?
3. What are the main steps or strategies that can be followed to reinforce risk analysis practices in large construction projects in Kuwait?

CIVIL ENGINEERING JOURNAL

Article no. 59

THE CIVIL ENGINEERING JOURNAL 3-2021

GEOPHYSICAL SURVEY AS A TOOL TO REVEAL SUBSURFACE STRATIFICATION AT WITHIN A SMALL AGRICULTURAL HEADWATER CATCHMENT: A CASE STUDY

Jakub Jeřábek and David Zumr

Czech Technical University in Prague, Faculty of Civil Engineering, The Department of Landscape Water Conservation, Prague, Thákurova 7/2077, 166 29, Praha 6 - Dejvice, Czech Republic; e-mail: jakub.jerabek@fsv.cvut.cz

ABSTRACT

Managers use the catchment as a basic spatial unit in landscape hydrology to estimate local water balance and manage water resources. The catchment drainage area is commonly delineated based on the surface topography, which is determined using a digital elevation model. Therefore, the surface outflow only is implicitly considered. However, a substantial portion of the rainfall water infiltrates and percolates through the soil profile towards the groundwater, where geological structures control the drainage area instead of the soil surface topography. The discrepancy between the surface topography-based and bedrock-based drainage area can cause larger discrepancies in water balance calculations. It this paper, we present the investigation of the subsurface media stratification within the headwater catchment, located in the central part of the Czech Republic using a geophysical survey method - electrical resistivity tomography (ERT). Results indicate that the complexity of the subsurface geological layers cannot be estimated solely from the land surface topography. Although the shallow layers follow the shape of the surface, the deeper layers do not. This finding has a strong implication on the water flow regime since it suggests that the deep drainage may follow different pathways and other preferential directions as compared to the water flow within the shallow subsurface.

KEYWORDS

Electrical resistivity tomography, Hydrology, Subsurface stratigraphy, Headwater catchment

INTRODUCTION

Catchment drainage area is a key concept in hydrology. It is defined by the catchment topographical boundaries which restrict the area from which all of the water flows to the common outlet. The catchment divide serves as a delineation between the adjacent catchments. Catchment drainage area also serves as a representative unit for water balance calculation. Water management is usually catchment-based as it is difficult to administrate the water resources within the landscape with politically designed boundaries where the water balance is not closed. The orographic divide is commonly used to delineate the catchment area. It is derived by means of topography (i.e. on a digital elevation model), therefore it is typically located at the ridge or a hilltop as is shown in Figure 1a. In some cases, the hydrogeological setting in the subsurface creates a low permeable geological layer in a way that the water which infiltrates towards this layer flows in opposite direction compared to the overlaying soil surface (Figure 1b). Knowledge about the subsurface stratification is important in order to be able to close or complete the water balance equation, since the water flow through the catchment orographic boundary may be affected by those layers [1]. However, the information about the subsurface settings at a catchment is not always available.

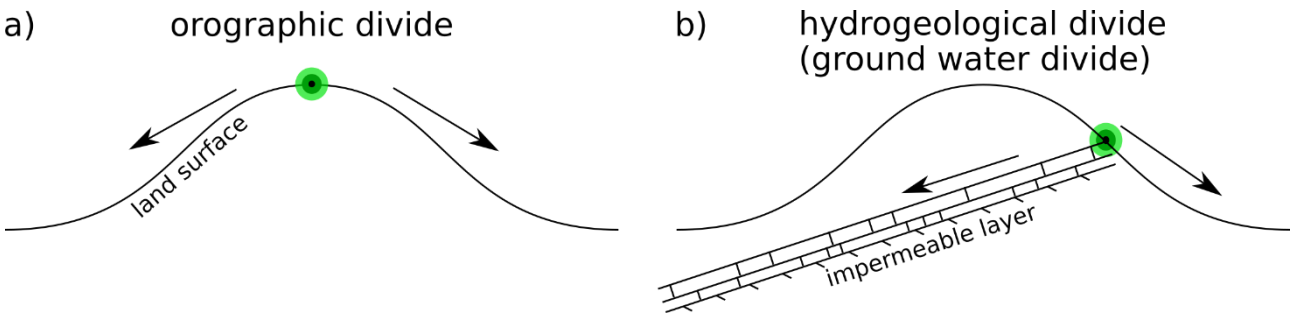

Fig. 1 – Difference between a) orographic and b) hydrogeological divide. Arrows indicate direction of the flowing water. Green dots indicate the divide.

Geophysical survey is a common option how to investigate the subsurface structures and the bedrock position. Number of geophysical techniques are available for practice and research purposes. The most common ones are: ground penetration radar, seismic refraction, magnetic methods, and electrical resistivity tomography [2]. Ground penetration radar (GPR), emits and detects electromagnetic pulses. The pulses are reflected from contrasted dialectical properties. Although GPR provides the best spatial resolution, it is not a suitable technique for materials with low contrast dielectric properties and in general for materials with lower el. resistivity than ca. 50 – 100 Ωm [2]. Seismic reflection uses geophones to detect a velocity of seismic waves introduced with sledgehammer (or earthquake). Although this method is well suited for bedrock detection and can reach deeper depths, it requires an increasing density of subsurface layers with depth. Magnetic methods are based on measuring of the magnetic properties (magnetic susceptibility) which reflect upon different concentrations of various ferromagnetic materials in the subsurface. Electrical resistivity tomography has shown to be a promising tool for its versatility and ease to obtain the field data. The depth ranges and spatial resolution can be easily set by the user. However, the technique requires good connection between the material and electrodes (principle explained bellow) and does not provide good results within a blocky subsurface structure [2].

In this study, we utilize the electrical resistivity tomography method (ERT), as described e.g. by Samouëlian et al. [3]. In principle, ERT can be used to detect the spatial distribution of electrical resistivity in the subsurface by introducing electrical current to the soil and detecting the resulting voltage of the subsurface media (more details are provided in the Methods section). Distinct soil layers or various rock materials, as well as soils of various water saturation, have different electrical resistivity [3], and therefore different subsurface structures can be detected and delineated.

ERT has been widely used in many fields of research and practical applications in various spatial scales, such as investigation of landslide to design protection measures (e.g. [4]), identification and delineation of soil contamination e.g. [5], [6], investigation of leachate from a landfill [7] or mixing of fresh and seawater in the coastal areas [8], [9]. ERT has been used to delineate individual soil layers above the bedrock [10] or even to study the shallow part of the soil profile (topsoil) where the tillage takes place [11], [12], and it is also commonly used in archaeology [13]. Furthermore, ERT has also been successfully used to identify the bedrock position in karst areas, where the heterogeneous bedrock (caused by uneven dissolution of the limestone) makes such a task very challenging [14], [15]. The representatives of the ERT method was successfully evaluated when compared with soil layers stratification observed in excavated trenches [14].

In this study we utilize electrical resistivity tomography (ERT) to observe and delineate subsurface structures and the bedrock, within a small agricultural headwater catchment. The main objective is to improve the understanding of the geological layering at the catchment in order to be able to assess movement of water e.g. via hydrological models [16].

METHODS

Study area

The study was performed at the experimental catchment Nučice which is located at the central part of the Czech Republic (Figure 2). The catchment area is 53 ha with a mean slope of 3.9%. The majority of the catchment is covered with arable land (96.4%). The soils are classified as Cambisols and Haplic Luvisols with sandy loam texture. The bedrock consists of layers of sandstone, siltstone and conglomerate from Carboniferous and Permian geological period (geological map CR, Figure 2). The Czech Geological Survey classifies the whole catchment area as "Alternating sandstone and claystone – permeability low to moderate". For more information about the catchment and instrumentation at the catchment we refer to [17].

The deep ground water level was observed at 355 m a.s.l. (57.7 m below ground surface) within a nearby borehole survey. The borehole survey was performed in the southern direction at a distance of 700 meters (m) from the west-south edge of the catchment. The borehole survey showed sandstone and conglomerate layers with thickness up to 10 meters.

The shallow groundwater level (GWL) of the quaternary alluvial aquifer was measured at two locations in the catchment (Figure 2). Generally, the shallow GWL dropped 3 m below the soil surface during prolonged dry periods in the summer. During heavy rain events GWL almost reached the surface. For most of the year the groundwater is between 2 and 3 m below the ground. The shallow and deep groundwater indicate a complex hydrogeological situation within the catchment, where the proposed ERT survey may help to understand the system.

There are 3 separated fields at the catchment: the top field (Figure 2) and bottom fields (fields 2 and 3 in Figure 2). The asphalt road separates the top and bottom fields. An ephemeral stream is located between the fields 2 and 3. The stream starts at the lowest part of the top field where outlet from tile drain is located. The tile drain then continues in thalweg to the other side of the field 1 where the main road is located near the catchment boundary.

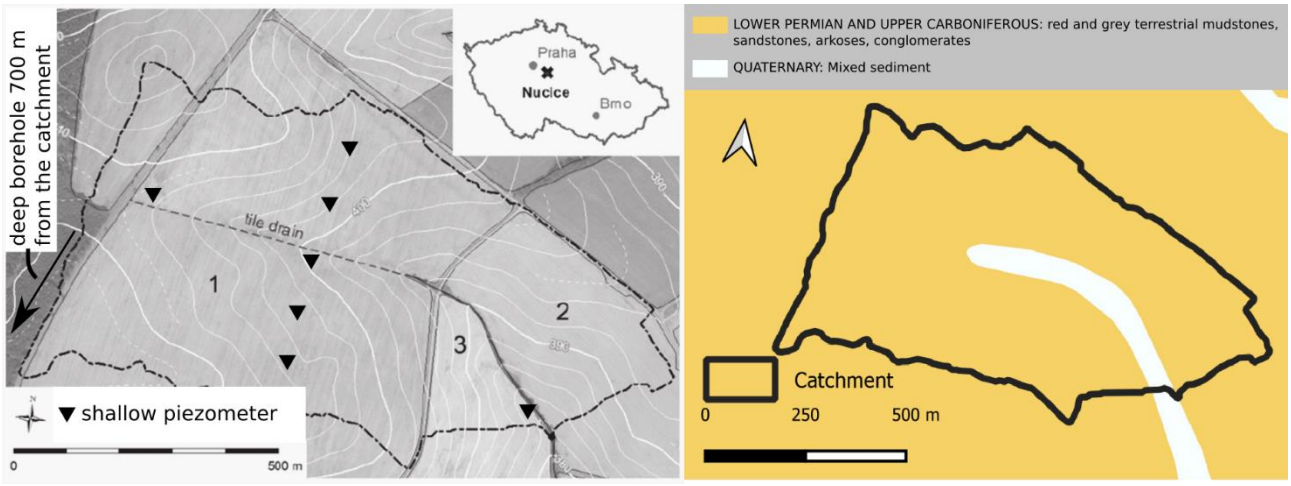

Fig. 2 - .The experimental catchment (left). The numbers stand for three different fields. Location of the shallow groundwater level monitoring and the location of borehole are indicated in the map. Geological map of the experimental catchment (right) © ČGS.

Soils and rocks of different composition and water saturation have distinct electrical properties. The electrical resistivity of the shallow soil layers (down to 1 meter from the surface) was measured at the same catchment by Jerabek et al. [11], the values ranged between 20 – 50 Ωm. The electrical resistivity of the sedimentary rocks is usually considerably higher, the literature reports values in a wide range of 10 – 10^4 Ωm order of magnitude [18], [19]. According to [20] the electrical resistivity of relevant media is shown in Table 1.

Tab. 1: overview of materials and their electrical resistivity (based on [20])

		electrical resistivity Ωm	
origin	material	from	to
shield un-weathered rocks	massive sulfides, graphite	0.01	10
	Igneous and metamorphic rocks	1000	100000
weathered layered		1	10000
glacial sediments	clays	3	100
	tills	30	3000
	gravel and sand	30	10000
sedimentary rocks	shales	50	300
	sandstone and conglomerate	50	10000
	lignite, coal	10	700
	dolomite, limestone	1000	100000
water, aquifers	salt water	0.3	1
	fresh water	2	100

Electrical resistivity tomography

The electrical resistivity tomography (ERT) survey consists of several steps. The so-called apparent electrical resistivity data is collected in the field. In this step, a number of electrodes are inserted into the soil surface along the line (in the case of a 2D profiling). An electrical field is introduced by a pair of electrodes (current electrodes) in the soil, while another pair of electrodes (potential electrodes) measures the voltage caused by the electrical field in the subsurface structure. Configuration of current and potential (voltage) electrodes, commonly called ERT array, exhibits varying horizontal or vertical spatial resolution, and sensitivity to the vertical (e.g. buried boulders) or horizontal (e.g. soil horizons or groundwater level) structures [3, 21]. Based on the geometry of the ERT array a hemisphere with a given apparent electrical resistivity is constructed.

The apparent electrical resistivity data collected has to be processed by inverse numerical modelling in order to obtain real electrical resistivity at a given location in the measured transect [22]. In the inversion procedure, the electrical resistivity is optimized based on the given ERT array and the apparent electrical resistivity data. In some cases, thousands of values need to be optimized which makes the process nontrivial and computationally intensive [22]. The numerical inversion also introduces a certain degree of uncertainty in the results and has to be considered during the data interpretation.

ERT survey design

Five independent ERT transects were performed within this study. An overview of the measured transects is shown in Table 2. Each of the ERT profiles consisted of several individual overlapping sub-transects which were merged before inversion. Most of the measurements were performed with the electrode spacing of 5 m, except the measurements BFC3 and TFC3 with 3 m electrode spacing. Location and orientation of each transect is shown in Figure 3. Two transects follow the thalweg and brook of the catchment, three transects cross the catchment perpendicularly to the catchment thalweg and the stream (Figure 3). There were three interceptions of the ERT transects; two in the field 1 and one in bottom fields 2 and 3.

Tab. 2: Overview of all measured ERT transects.

Date mm/yyyy	Measurement ID	Transect length [m]	Electrode spacing [m]	Location at the catchment – orientation
04/2012	BFC3	540	3	Bottom fields – cross
12/2016	TFC3	444	3	Top field – cross
08/2019	BFB5	395	5	Bottom fields – brook
10/2019	TFC5	620	5	Top field – cross
10/2019	TFT5	580	5	Top field – thalweg

Automatic resistivity system (ARES, GF Instruments, Brno, Czech Republic) was used to obtain the apparent resistivity data. Wenner-Schlumberger array was used for all the measurements. Res2DInv software was used for the data inversion to calculate the electrical resistivity profiles [22]. Total of 1233 (in case of BFB5) to 3161 (in case of BFC3) data points were inverted with the Res2DInv. The software reached the values of the absolute error between the measured end inverted data below 1.5% after 5 – 6 iterations. The robust inversion method (which is more suitable for layers detection) was used for all transects. The topography of each transect was extracted from the digital elevation model with 1 m spatial resolution.

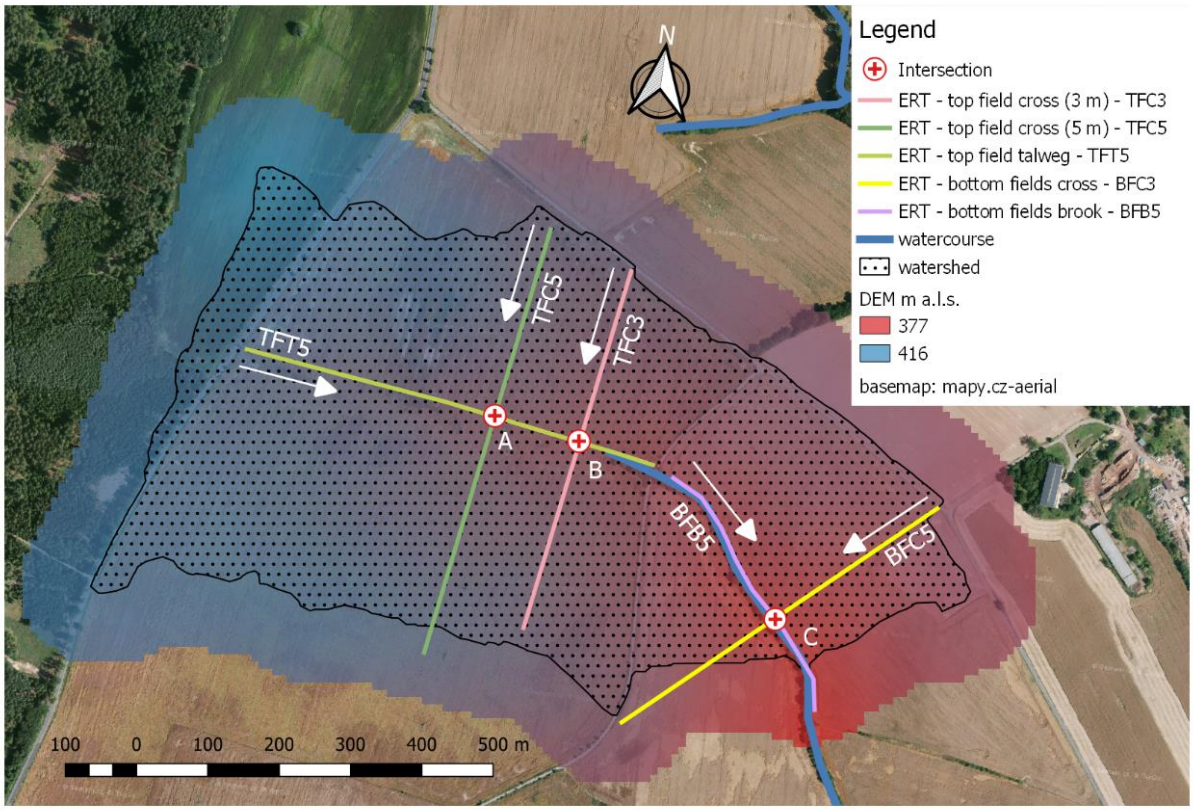

Fig. 3 - The location and intersections of the measured transects. Arrows indicate start and direction of each transect. Digital elevation model provided (C) ČÚZK.

RESULTS

ERT transects

All ERT profiles show electrical resistivity (ρ) in a range of 20 – 150 Ωm. The highest ρ was observed either in the layer located 4 to 6 m below the soil surface or in the deeper layer which is located 15 to 20 m below the soil surface. Soil layer of lower ρ (30 to 50 Ωm) is found in between these regions. Such a layering is clearly visible in the field 1 on transects TFT5, TFC5 and TFC3. Although the same pattern was observed in the bottom fields (field 2 and 3; transects BFB5 and BFC3) the alteration with the regions of different resistivity is less clear. Low electrical resistivity was also observed close to the surface in some cases. The resistivity variability of the upper soil layers (only few meters of a depth) could be attributed to varying soil properties which may differ in organic matter and clay content, and in the actual soil moisture conditions.

The thalweg (TFT5) and along-the-brook (BFB5) transects are both shown in Figure 4. Several spots with high electrical resistivity (ρ) are aligned in the depth of approximately 4 to 10 m. The bottom half of the profile also exhibits higher ρ at the transect TFT5. The area with high ρ was also observed within the BFB5 transect, which appears closer to the soil surface.

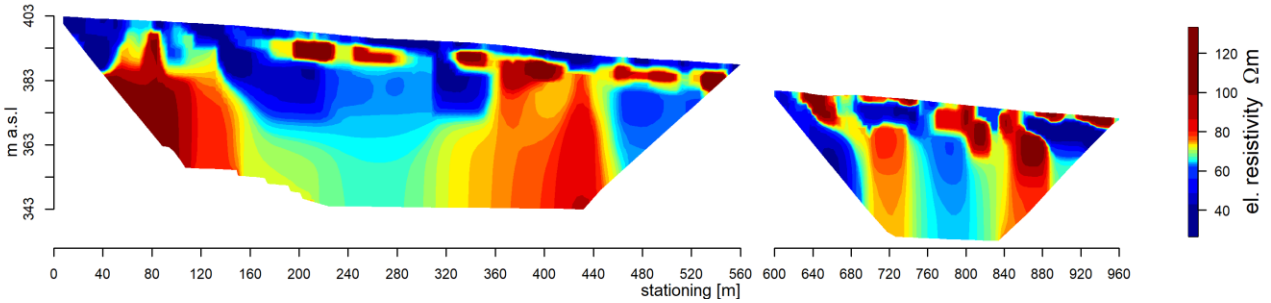

Fig. 4 – ERT transects TFT5 and BTB5 shown in single plot with elevation and stationing starting at the western boundary of the catchment.

The field 1 ERT transects were oriented in the orthogonal direction to the thalweg (TFC transects) and are as shown in Figure 5. Both transects exhibit lower electrical resistivity ρ near the soil surface. High ρ zone near the soil surface areas are restricted only to a limited part of both the transects. Both profiles also exhibit low ρ (below 50 Ωm) in the upper half of each transect. The bottom half of both these transects exhibited higher ρ. Both transects also exhibited the same pattern of the low and high ρ layers despite the different electrode spacing.

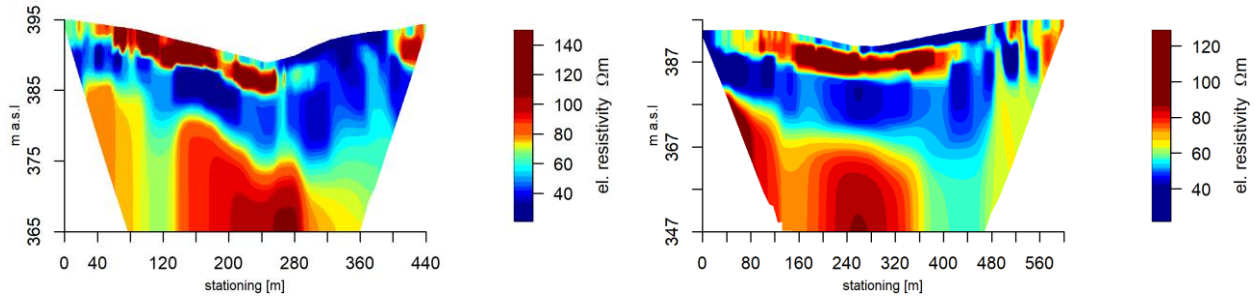

Fig. 5 – ERT transects TFC3 (left) and TFC5 (right).

The ERT profile in the orthogonal direction to the brook (BFC3) transecting the lower fields 2 and 3 is shown in Figure 6. The bottom of the valley is at the stationing of 260 m. The lower ρ was measured only in the shallow part of the field 2 (right hillslope in Figure 6). Below the field 3 (left hillslope in Figure 6) the low ρ layer reaches the depth of approximately 20 m below the soil surface.

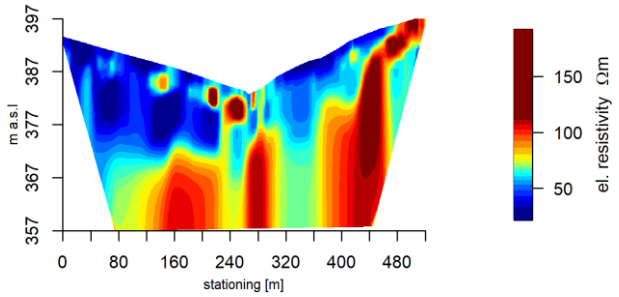

Fig. 6 – BFC3 ERT transects.

ERT transects intersections

The ERT transects were intersected at 3 locations (Figure 7). Intersections A and B were located in the field 1, the intersection C in the field 2 close to the valley. 1D graphs of electrical resistivity ρ with corresponding depth for the 3 intersections are shown in Figure 7. The intersection of transects TFT5 and TFC5 is shown in Figure 7 intersection A. The high ρ values near the soil surface are recognizable in the same depth at both the transects. Also, the second increase of ρ values which can be observed at an altitude of 375 m a.s.l. appeared at a similar depth. The ρ to depth graph of the intersection B (TFT5 and TFC3 ERT transects) exhibited difference in the onset of the shallower high ρ region (Figure 7 intersection B). The difference of the onset was about 2.5 m. The high ρ area which can be observed in the TFC3 profile at an altitude 370 m a.s.l. (approximately 15 m deep) did not appear in the TFT5 transects. Similar results were observed in the intersection of transects BFB5 and BFC3, where onset of the high ρ in near soil surface were also shifted (Figure 7 intersection C). The BFB5 transect exhibited oscillation of the electrical resistivity which could be caused by an error in the measurement or created as an artifact during the mathematical inversion.

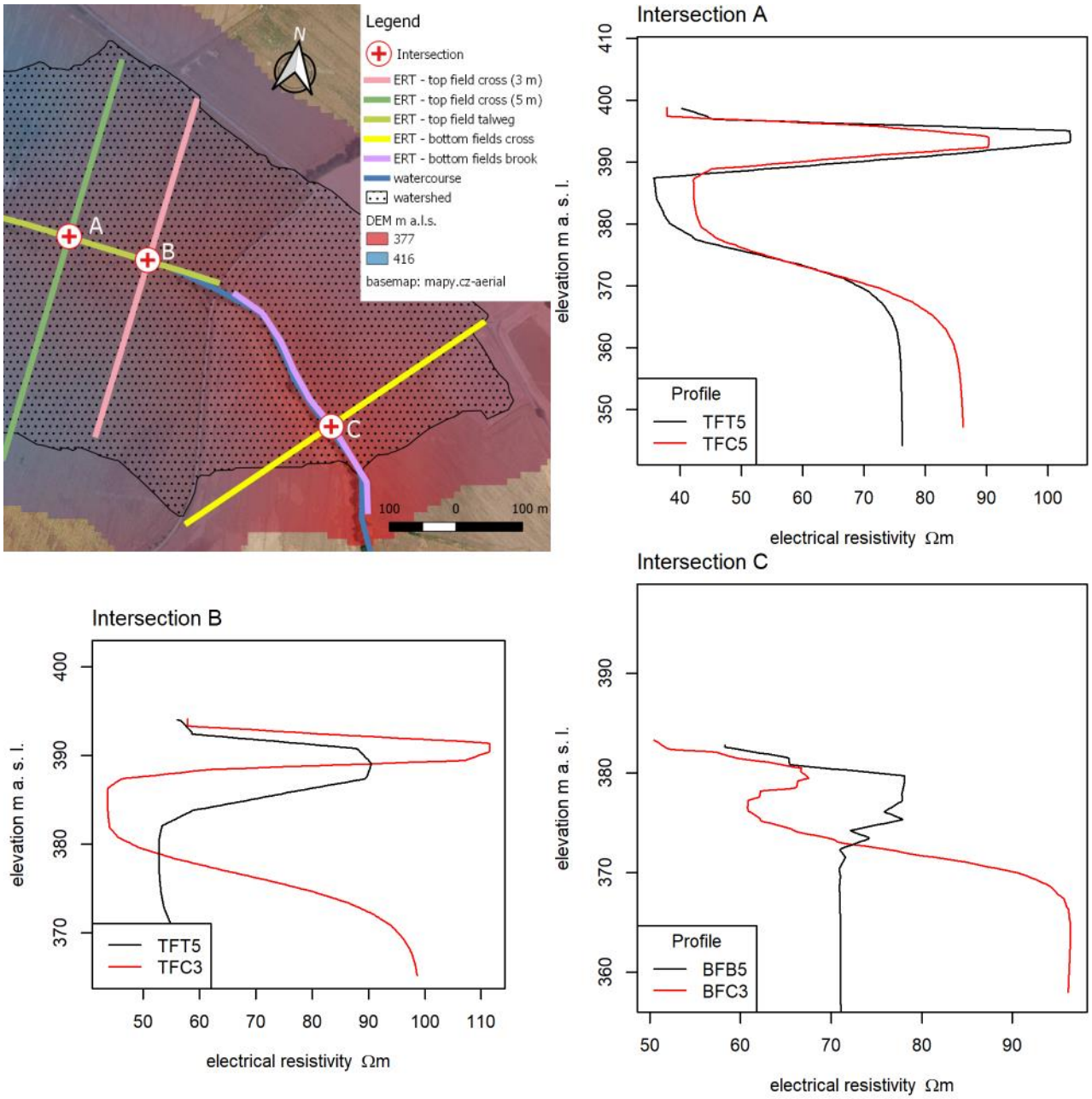

Fig. 7 – Map of intersections and comparison of ERT intersections: intersection A of transects TFT5 and TFC5, intersection B of transects TFT5 and TFC3, and intersection C of transects BFB5 and BFC3.

Hydraulic conductivity of the subsurface structures

Electrical resistivity transects were recalculated with the use of Archie's law [23] to hydraulic conductivity for investigating the hydrological behavior of the subsurface (Figure 8). A high conductive layer is presented at the transects TFC5 and TFC3 overlaid with multiple orders of magnitude lesser conductive layer, probably an aquitard. Presence of a confined aquifer can be hypothesized in this high conductive layer. However, no clear aquitards or aquifers are visible at the perpendicular transects TFT5 and BFB5 or the transect BFC5 at the bottom field. Shallow ground water levels (1 – 3 meter depth) which were recorded in the piezometers indicate an unconfined aquifer on the top of the low-conductivity layer which is visible few meters below the surface. The usage of Archie's law in this context has to be considered only as qualitative metrics, since we cannot

distinguish amongst the various factors affecting the electrical resistivity changes (e.g. soil water content).

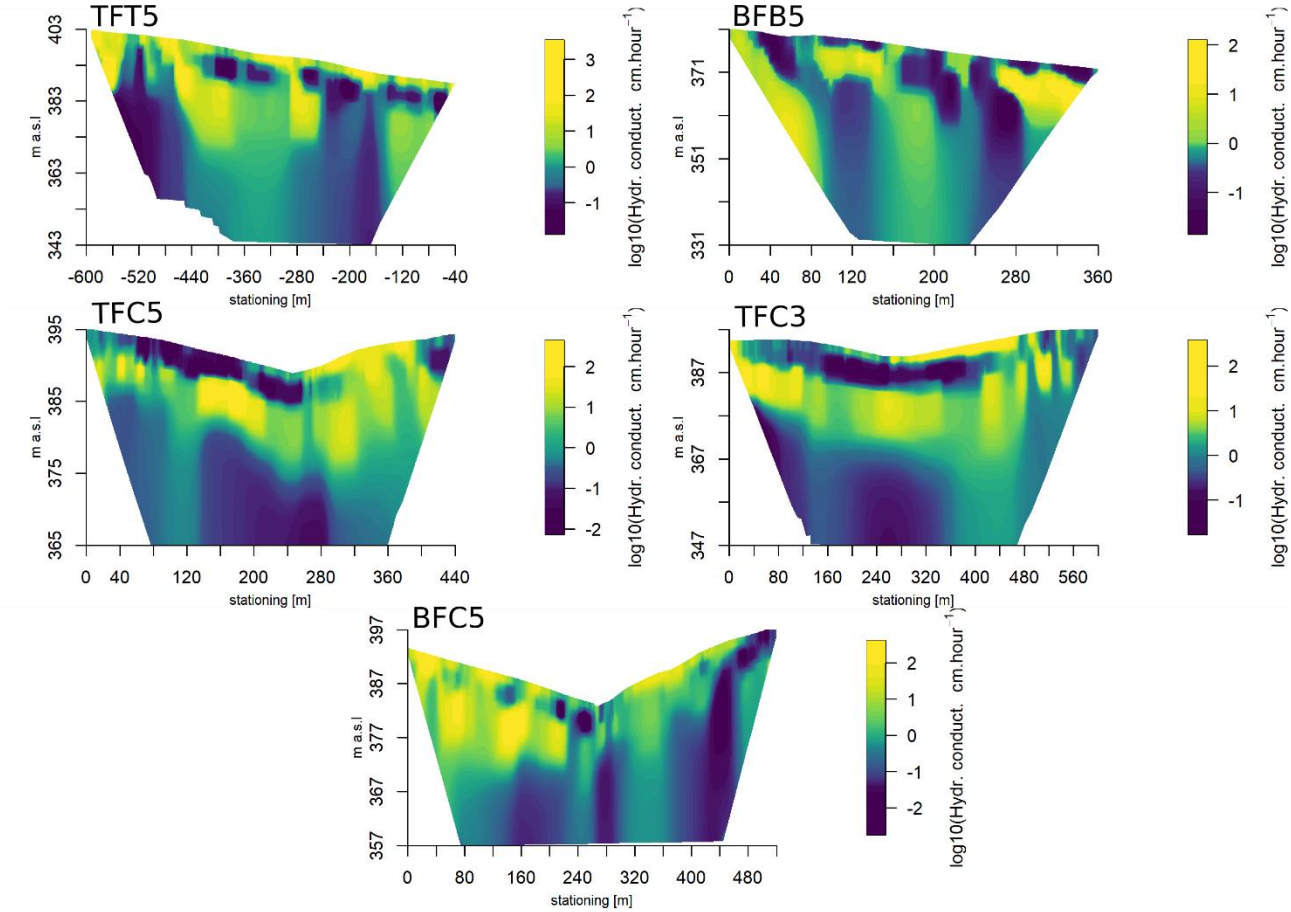

Fig. 8 -The hydraulic conductivity calculated with Archie's law for all the ERT transects.

DISCUSSION

ERT transects

Four distinct layers were distinguished in all ERT transects based on the electrical resistivity values. The layers are shown in Figure 9 (profile TFC5 is shown for illustration):

Layer L1: Low electrical resistivity (ρ) values up to 60 Ω m. Close to the surface - down to the depth of 1 – 2 meters. This layer is not continuous in some transects.

Layer H1: Higher ρ layer. All the transects exhibited areas of higher ρ (up to 150 Ω m) which are located below the layer L1 and reaches the depth of 5 – 10 meters below the soil surface. This layer is more developed at the field 1 compared to fields 2 and 3.

Layer L2: Low ρ layer. This layer exhibit varying thickness and ρ around 40 Ω m. The layer reaches depths down to 25 m below the soil surface.

Layer H2: The bottom of the measured profiles are formed by an area with higher ρ of values above 60 Ω m. Layer H2 is however very heterogeneous, locally reaching resistivity values above 150 Ω m at some transects. It also has to be noted that the ERT profiles exhibit a high degree of uncertainty and lower resolution in the deeper regions.

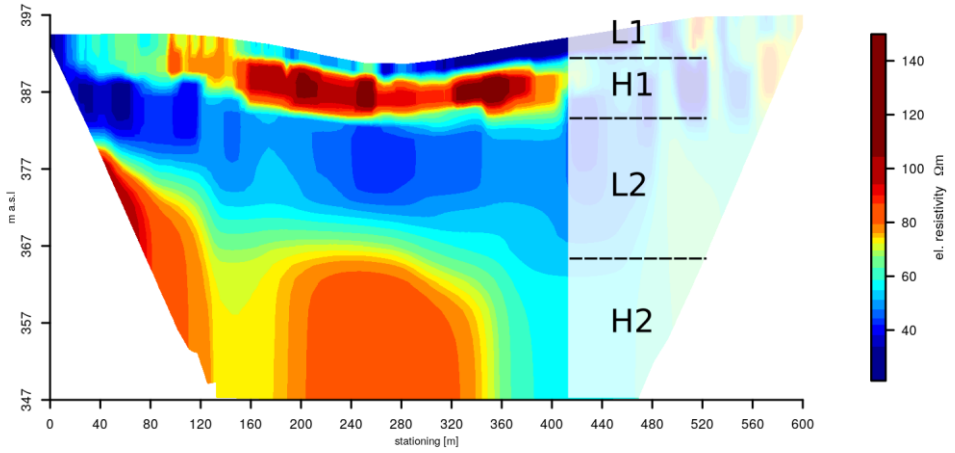

Fig. 9 - The profile TFC5 with clearly developed 4 distinct subsurface layers. Similar stratification is to some extend visible at all measured ERT transects. The TFC5 transect is used here as an example.

The layer L1 is not present in all transects as it is shown in Figure 10. However, in Jeřábek et al. [11], it was shown that the top 1 – 2 meters consist of soil material with ρ around 40 Ωm. The fact that the low ρ layer is not present in all profiles could also be caused by uncertainty in the measured resistivity closer to the surface. The median depth of investigation starts at 2.5 m and 1.55 m for the 5 and 3 m electrode spacing in case of the Wenner-Schlumberger array [18]. The H1 layer was presented mainly below the field 1. It was visible especially in the transects crossing the valley thalweg (TFC5 and TFC3). The ERT transect TFT5 exhibited H1 layer only within a limited area. A key property of the H1 layer is that its shape copies the topography of the surface (compared to the H2 layer as described later). The L2 layer, which is characteristic by its comparatively low resistivity, has a variable thickness and even reaches the soil surface at the BFC3 transect. The delineation between the layers L2 and H2 is not very sharp, as compared to the divide between layers H1 and L2. This may be caused by more gradual transition between geological layers, but also by artifact of inversion, which was not successful in recognizing areas below high ρ layers (such as H1 in this case) [18] . The interface, even though not very sharp, between L2 and H2 layers clearly declines in a southern direction, the inclination does not mirror the topography of the land surface.

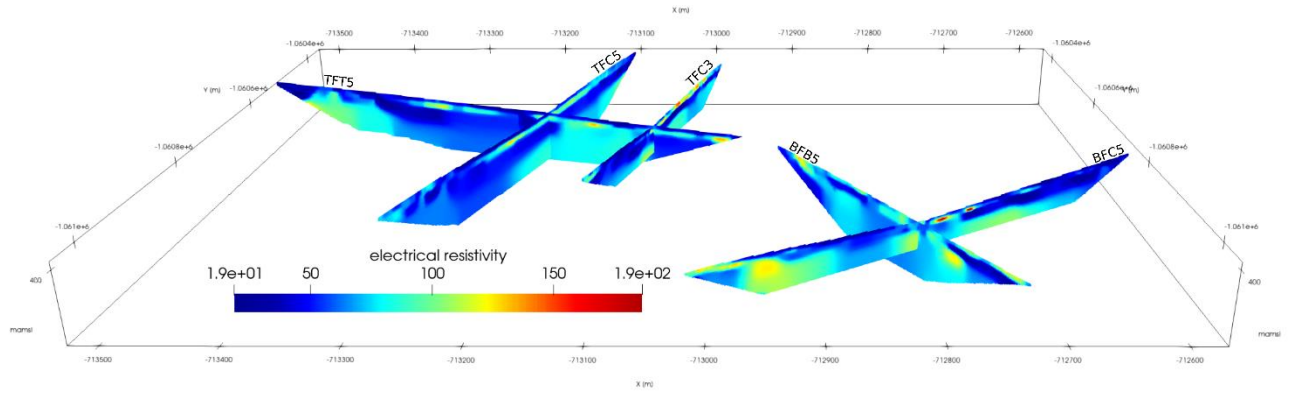

Fig. - 10. All ERT profiles shown at its real positions. Profiles coding is shown in the Figure.

The declination of the layer H2 differed for the area below field 1, and below fields 2 and 3. This difference indicates a large geological complexity in the area. At the same time, the electrical resistivity of the layers are not very different which suggest similarities within the geological layers.

The shallow and deep groundwater levels qualitatively correspond to the ERT measurements. The shallow GWL is likely positioned above the impermeable H1 layer while the deeper one above the H2 layer. The high electrical resistivity indicates rocks or less water-saturated

areas. The low electrical resistivity in layers L1 and L2 may be caused by ions dissolved in the ground water. The deep GWL derived from the borehole data was observed deeper compared to the ERT. However, the borehole was located further from the catchment in the direction of thickening of the L2 layer. It is therefore possible that the less permeable H2 layer is even deeper at the location of the borehole.

ERT transects intersections

Intersections of the ERT profiles served as cross-validation of the highly qualitative measurement which the ERT is. The transects were measured under different topsoil moisture and vegetation conditions, which may have affected the results. Also, the 2D transects which are perpendicular to each other can capture the 3D structures differently. For instance, the presence of the brook may result in differences in the transects BFB5 and BFC3 and cause the discrepancies in the intersection C [24]. The highly variable geology of the catchment and inclinations of the subsurface layers may also manifest differently to the perpendicular cross-sections. The perpendicular transects B and C exhibited larger differences. Here the differences may be also caused by different electrode spacings, where one of the transects had electrode spacing 3 and the other 5 meters. Besides these factors ERT measurement loses its sensitivity with depth and suffer various artifacts due to inversion during data processing which may also have led to deviations between profiles [25].

CONCLUSION

In this paper, we present and discuss results of a geophysical survey performed at a small headwater agricultural catchment. The survey aimed to extend the knowledge about the subsurface stratification. This information helps to interpret the water transport in the catchment and can be used for setting up the hydrological models. Results indicated a complex geology within the area. The ERT identified at least four layers with distinct electrical resistivity. Interestingly, the shallow layers (approximately 5 m below surface) corresponded to the topography of the soil surface, however, the deeper layers interface did not. These results confirm the hypothesis that portion of the water which percolates into the deep horizon can be transported from the catchment through the flow paths which do not correspond to the drainage paths inferred from the digital elevation model. Also, the shape and declination of the deep layers are different in the upper and bottom parts of the catchment which indicates heterogeneous geological setting even in a relatively small area. Although the indirect ERT method is hard to interpret quantitatively, the information presented in the manuscript increase understanding of the water transport regime within the catchment.

ACKNOWLEDGEMENTS

We would like to thank Nina Noreika, Tailin Li, Tomáš Laburda and Jáchym Jeřábek for an assistance during the labor-intensive field surveys and to Saunak Sinha Ray for the proofreading. The field work, data analysis, and manuscript preparation were funded by the Horizon 2020 research and innovation program project 773903 - “Shui - Soil Hydrology research platform underpinning innovation to manage water scarcity in European and Chinese cropping systems,” funded by the European Union, and by the Grant Agency of the Czech Technical University in Prague project no. SGS20/157/OHK1/3T/11 - “Experimentání výzkum a modelování komplexních fyzikálních procesů v půdním prostředí”.

REFERENCES

[1] Beven, K. 2006. Searching for the Holy Grail of scientific hydrology: Q_t=(S, R, Δt)A as closure. Hydrology and Earth System Sciences. Vol. 10, No. 5, p. 609–618. DOI 10.5194/hess-10-609-2006.

[2] Schrott, L., Sass, O. 2008. Application of field geophysics in geomorphology: Advances and limitations exemplified by case studies. Geomorphology. Vol. 93, No. 1–2, p. 55–73.

DOI 10.1016/j.geomorph.2006.12.024.
[3] Samouëlian, A., Cousin, I., Tabbagh, A., Bruand, A., Samouëlian, A., Cousin, I., Tabbagh, A., Bruand, A., Electrical, G.R. 2006. Electrical resistivity survey in soil science : a review . To cite this version : HAL Id : hal-00023493. .
[4] Colangelo, G., Lapenna, V., Loperte, A., Perrone, A., Telesca, L. 2008. 2D electrical resistivity tomographies for investigating recent activation landslides in Basilicata Region (Southern Italy). Annals of Geophysics. Vol. 51, No. 1, p. 275–285. DOI 10.4401/ag-3048. ze se pouziva na landslide
[5] Abudeif, A.M. 2015. Integrated electrical tomography and hydro-chemical analysis for environmental assessment of El-Dair waste disposal site, west of Sohag city, Egypt. Environmental Earth Sciences. Vol. 74, No. 7, p. 5859–5874. DOI 10.1007/s12665-015-4610-5.
[6] Wang, T.P., Chen, C.C., Tong, L.T., Chang, P.Y., Chen, Y.C., Dong, T.H., Liu, H.C., Lin, C.P., Yang, K.H., Ho, C.J., Cheng, S.N. 2015. Applying FDEM, ERT and GPR at a site with soil contamination: A case study. Journal of Applied Geophysics. Vol. 121, p. 21–30. DOI 10.1016/j.jappgeo.2015.07.005.
[7] Audebert, M., Clément, R., Moreau, S., Duquennoi, C., Loisel, S., Touze-Foltz, N. 2016. Understanding leachate flow in municipal solid waste landfills by combining time-lapse ERT and subsurface flow modelling – Part I: Analysis of infiltration shape on two different waste deposit cells. Waste Management. Vol. 55, p. 165–175. DOI 10.1016/j.wasman.2016.04.006.
[8] Sherif, M., Mahmoudi, A. El, Garamoon, H., Kacimov, A., Akram, S., Ebraheem, A., Shetty, A. 2006. Geoelectrical and hydrogeochemical studies for delineating seawater intrusion in the outlet of Wadi Ham, UAE. Environmental Geology. Vol. 49, No. 4, p. 536–551. DOI 10.1007/s00254-005-0081-4.
[9] Satriani, A., Loperte, A., Imbrenda, V., Lapenna, V. 2012. Geoelectrical surveys for characterization of the coastal saltwater intrusion in metapontum forest reserve (Southern Italy). International Journal of Geophysics. Vol. 2012. DOI 10.1155/2012/238478.
[10] Chambers, JE , Wilkinson, PB , Uhlemann, S , Sorensen, JPR , Roberts, C , Newell, AJ , Ward, WOC , Binley, Andrew , Williams, PJ , Gooddy, DC, O. 2014. Derivation of lowland riparian wetland deposit architecture using geophysical image analysis and interface detection. Water Resources Research. DOI 10.1111/j.1752-1688.1969.tb04897.x. ze se pomic ert pokouseli rozdelit jednotlive vrstby (ne jen bedrock a soil profile)
[11] Jeřábek, J., Zumr, D., Dostál, T. 2017. Identifying the plough pan position on cultivated soils by measurements of electrical resistivity and penetration resistance. Soil and Tillage Research. Vol. 174, p. 231–240. DOI 10.1016/j.still.2017.07.008.
[12] Besson, A., Cousin, I., Samouëlian, A., Boizard, H., Richard, G. 2004. Structural heterogeneity of the soil tilled layer as characterized by 2D electrical resistivity surveying. Soil and Tillage Research. Vol. 79, No. 2 SPEC.ISS., p. 239–249. DOI 10.1016/j.still.2004.07.012.
[13] Haskins, N. 2010. Book Review - A Field Guide to Geophysics in Archaeology. Archaeological Prospection. Vol. 62, No. December 2009, p. 61–62. DOI 10.1002/arp.
[14] Zhou, W., Beck, B.F., Stephenson, J.B. 2000. Reliability of dipole-dipole electrical resistivity tomography for defining depth to bedrock in covered karst terranes. Environmental Geology. Vol. 39, No. 7, p. 760–766. DOI 10.1007/s002540050491.
[15] Cheng, Q., Tao, M., Chen, X., Binley, A. 2019. Evaluation of electrical resistivity tomography (ERT) for mapping the soil–rock interface in karstic environments. Environmental Earth Sciences. Vol. 78, No. 15, p. 1–14. DOI 10.1007/s12665-019-8440-8.
[16] Noreika, N., Li, T., Zumr, D., Krasa, J., Dostal, T., Srinivasan, R. 2020. Farm-scale biofuel crop adoption and its effects on in-basin water balance. Sustainability (Switzerland). Vol. 12, No. 24, p. 1–15. DOI 10.3390/su122410596.
[17] Li, T., Jeřábek, J., Noreika, N., Dostál, T., Zumr, D. 2021. An overview of hydrometeorological datasets from a small agricultural catchment (Nučice) in the Czech Republic. Hydrological Processes. DOI 10.1002/hyp.14042.
[18] Loke, M.H. 1999. Electrical imaging surveys for environmental and engineering studies. A practical guide to 2-D and 3-D surveys. . No. 1999, p. 59.
[19] Samouëlian, A., Cousin, I., Tabbagh, A., Bruand, A., Richard, G. 2005. Electrical resistivity survey in soil science: A review. Soil and Tillage Research. Vol. 83, No. 2, p. 173–193. DOI 10.1016/j.still.2004.10.004.
[20] Palacky, G.J. 3. Resistivity Characteristics of Geologic Targets. In : Electromagnetic Methods in Applied Geophysics. 1988. p. 52–129.
[21] Furman, A., Ferré, T.P.A., Warrick, A.W. 2003. A Sensitivity Analysis of Electrical Resistivity Tomography Array Types Using. Vadose Zone Journal. Vol. 2, p. 416–423.
[22] Loke, M.H. 1998. “Res2dInv.” Rapid 2D resistivity and IP inversion using the least-squares method.

User Manual, Austin Tex, Advanced Geoscience Inc.
[23] Archie, G.E. 1942. The electrical resistivity log as an aid in determining some reservoir characteristics. Transactions of the AIME. Vol. 146, No. 01, p. 54–62.
[24] Hung, Y.C., Lin, C.P., Lee, C.T., Weng, K.W. 2019. 3D and boundary effects on 2D electrical resistivity tomography. Applied Sciences (Switzerland). Vol. 9, No. 15. DOI 10.3390/app9152963.
[25] Loke, M.H. 2004. Tutorial: 2-d and 3-d electrical imaging surveys, Geotomo Software, Malaysia. . No. July, p. 136.